

# **An Analysis of the Factors Influencing Electrochemical Measurements of the Condition of Reinforcing Steel in Concrete Structures**

by

Amirreza Esmaeilpoursaee

A thesis  
presented to the University of Waterloo  
in fulfilment of the  
thesis requirement for the degree of  
Doctor of Philosophy  
in  
Mechanical Engineering

Waterloo, Ontario, Canada 2007

©Amirreza Esmaeilpoursaee 2007

I hereby declare that I am the sole author of this thesis. This is a true copy of the thesis, including any required final revisions, as accepted by my examiners.

I understand that my thesis may be made electronically available to the public.

## ABSTRACT

Electrochemical assessment of the condition of the steel reinforced concrete structures is being carried out increasingly and more regularly, both in the laboratory and in the field. It is important to have enough information about the factors that may affect these measurements. In this way, results obtained from different tests can be interpreted in more reliable manner and the condition of the embedded reinforcing steel bars in concrete structures can be evaluated with more confidence. The main goals of this project were:

- to determine the causes of the errors in electrochemical measurements that may mislead the researchers,
- to determine factors that may affect the measurements,
- to attempt to manifest better interpretation of the results,
- to avoid the problematic pitfalls and overcome them as much as possible.

To this end, two types of concrete specimens were prepared for performing gravimetric and electrochemical tests: beams with four pre-weighed sections of rebars, and prisms with a single rebar and with different variables (cracked in two directions, carbonated and different cover depth). These have been exposed to de-icing salt for more than 2.5 years. The condition of the rebar in the beams and prisms was evaluated over this period by (i) half-cell potential measurements, (ii) galvanostatic pulse measurements (using the GalvaPulse™ and the potentiostat), (iii) potentiostatic linear polarisation resistance measurements (LPR), (iv) electrochemical impedance spectroscopy (EIS) and (v) potentiodynamic cyclic polarisation.

Also, specimens were prepared to determine the amount of required time for steel to passivate itself in pore solution and mortar.

Results from corrosion measurements in the laboratory show that:

- Steel bar in mortar and pore solution needs time for passivation: about 7 days for steel embedded in mortar and about 3 days for steel in simulated pore solution.
- Data from gravimetric tests were compared with the values calculated from electrochemical tests and results show that, in the laboratory condition, values obtained from potentiostatic LPR technique are more realistic and closer the actual mass loss than those obtained by galvanostatic techniques.
- It was observed that, in most cases, when the steel bars were corroding actively, the half-cell potential values were more negative than -350 mV vs. CSE, in agreement with ASTM guidelines.
- When performing the half-cell potential measurements, it was found that it is essential provide sufficient time after wetting the surface to allow the potential to stabilise. A minimum of about 15-20 minutes was found to be required.
- One of the most informative electrochemical tests is the cyclic polarisation technique. The half-cell potential, corrosion rate, susceptibility to pitting, severity of corrosion, protecting potential, concentration limitations and, with appropriate procedures, Tafel constants, can be obtained by this technique. However, it is essential to choose the appropriate scan rate for the particular system, otherwise the achieved data mislead the researcher. The appropriate scan rate can be determined by using the Bode plot obtained from the EIS experiment.

- To measure the concrete resistance, the galvanostatic pulse technique and EIS are suggested. Wenner four probe technique measures only the surface resistance and is, therefore, very dependant on the surface condition and is not recommended.
- The guard ring in the GalvaPulse™ instrument which is designed to limit the polarised area was found to be working in reverse and, in fact, it polarises the steel even more than when it is not used. It is recommended that the guard ring electrode not be used during the measurements.
- Another limitation of the GalvaPulse™ is its lack of capability to measure the high corrosion rates.
- It was found that the GalvaPulse™ pulse generator unit must be calibrated every month, or before each measurement, whichever is longer period.

In addition to the experiments in the laboratory, four locations were chosen for field measurements in collaboration with the Ministry of Transportation of Ontario. These measurements show that:

- The half-cell potential of galvanised steel is much more negative than that in the black steel. This emphasises the importance that the ASTM C876 recommended guideline should not be used for other types of reinforcing bars.
- It is recommended that half-cell potential contour map rather than the absolute values of potential be used for condition analysis. However, it is found that these maps are not constant varying with time and ambient conditions. Based on this experience, it is recommended that half-cell potential measurements be made

exactly at the same time and date in different years. The results might be closer and more readily interpretable.

- The measured half cell potential is a function, not only of the state of corrosion, but also of environmental factors. The temperature and relative humidity of both the atmosphere and inside the concrete play a role. The permittivity of concrete is dependent on all these factors and needs to be taken into account.
- To measure the corrosion current density in the field, galvanostatic and galvanodynamic LPR and galvanodynamic polarisation can be used. The potentiostatic LPR, potentiodynamic LPR and EIS techniques appear to be limited by the size of full-scale structures and are also very sensitive to extraneous electrical noise. Consequently, they cannot be performed in the field.

## **ACKNOWLEDGEMENT**

I would like to express my sincere appreciation to my supervisor, Professor Carolyn Hansson, whose invaluable advice, assistance and support made this work possible. Her diligent effort, thoughtful guidance, encouragements and supports helped me to learn precious lessons in my life which are not forgettable. Working with Professor Hansson was one of the most wonderful opportunities that I have ever had. I admire her as an exceptional supervisor and as an excellent friend and I am truly honoured to work under her supervision.

I would like to thank the members of my PhD examination committee: Dr. Alberto Sagues, Dr. John Straube, Dr. Jeff West and Dr. Michael Mayer, for their expertise, helpful comments and assistance.

The achievement of this work was not possible without great collaborations of my colleagues and friends. I am especially thankful to Dr. Laura Mammoliti, Miss Shahzma Jaffer and Mr. Ramtin Movassaghi for their valuable support.

I am grateful to Mr. John Potzold, Mr. Norval Wilhelm and Mr. Fred Baker for their co-operations. I also thank Mr. Frank Pianca from the Ministry Transportation, Ontario (MTO) for his great helps, encouragements and support during this study.

Finally, I must thank my parents and my brothers for their support and patience. To you my family, I dedicated this thesis.

Ministry of Transportation Ontario provided the financial support of this work.

# TABLE OF CONTENT

|  |            |
|--|------------|
| <b>ABSTRACT .....</b>  | <b>iii</b> |
| <b>ACKNOWLEDGEMENT .....</b>   | <b>vii</b> |
| <b>TABLE OF CONTENT .....</b>  | <b>vii</b> |
| <b>LIST OF TABLES .....</b>  | <b>xi</b>  |
| <b>LIST OF FIGURES .....</b>   | <b>xiv</b> |
| <b>CHAPTER 1, INTRODUCTION .....</b>   | <b>1</b>   |
| <b>CHAPTER 2, LITERATURE REVIEW .....</b>  | <b>3</b>   |
| <b>2.1. CONCRETE.....</b>  | <b>3</b>   |
| 2.1.1. <i>Ordinary Portland Cement (OPC) concrete.....</i>                           | <i>3</i>   |
| 2.1.3. <i>Curing of concrete.....</i>  | <i>7</i>   |
| <b>2.2. CORROSION OF STEEL IN CONCRETE .....</b>                                     | <b>8</b>   |
| 2.2.1. <i>Reinforcing steel passivation time.....</i>                                | <i>10</i>  |
| 2.2.1.1. <i>Raman spectroscopy.....</i>  | <i>11</i>  |
| 2.2.2. <i>Chloride induced corrosion .....</i>                                       | <i>12</i>  |
| 2.2.2. <i>Carbonation induced corrosion .....</i>                                    | <i>13</i>  |
| 2.2.2.1. <i>Carbonation depth measurement .....</i>                                  | <i>13</i>  |
| 2.2.3. <i>The influence of concrete parameters on rebar corrosion .....</i>          | <i>14</i>  |
| 2.2.4. <i>Mechanism of corrosion in reinforced concrete .....</i>                    | <i>16</i>  |
| <b>2.3. CORROSION EVALUATION TECHNIQUES .....</b>                                    | <b>18</b>  |
| 2.3.1. <i>Half-cell potential technique.....</i>                                     | <i>19</i>  |
| 2.3.1.1. <i>Interpretation difficulties with half-cell potential technique .....</i> | <i>21</i>  |
| 2.3.2. <i>Linear Polarisation Resistance (LPR).....</i>                              | <i>29</i>  |
| 2.3.2.1. <i>Potentiostatic LPR.....</i>  | <i>33</i>  |
| 2.3.2.2. <i>Galvanostatic pulse technique .....</i>                                  | <i>34</i>  |
| 2.3.2.2.1. <i>GalvaPulse™ .....</i>  | <i>37</i>  |
| 2.3.3. <i>Electrochemical Impedance Spectroscopy (EIS) .....</i>                     | <i>41</i>  |
| 2.3.3.1. <i>Data presentation.....</i>   | <i>48</i>  |



|  |            |
|--|------------|
| 2.3.3.2. <i>Application of EIS in steel reinforced concrete structures</i> .....             | 55         |
| 2.3.4. <i>Cyclic polarization</i> .....  | 56         |
| <b>2.4. CONCRETE ELECTRICAL RESISTIVITY</b> .....  | <b>61</b>  |
| 2.4.1. <i>Concrete resistivity measurement techniques</i> .....                              | 62         |
| <b>CHAPTER 3, EXPERIMENTAL PROCEDURES</b> .....  | <b>66</b>  |
| <b>3.1. MATERIALS</b> .....  | <b>66</b>  |
| <b>3.2. SPECIMEMNS PREPARATION</b> .....   | <b>67</b>  |
| 3.2.1. <i>Beams with segmented steel bars</i> .....  | 67         |
| 3.2.2. <i>Specimens with different variables</i> .....                                       | 72         |
| 3.2.2.1. <i>Electrode configuration</i> .....  | 78         |
| 3.2.3. <i>Samples for determining the passivation time</i> .....                             | 82         |
| <b>3.3. MEASUREMNTS</b> .....  | <b>84</b>  |
| 3.3.1. <i>Laboratory measurements</i> .....  | 84         |
| 3.3.1.1. <i>Corrosion measurements</i> .....   | 84         |
| 3.3.1.1.1. <i>Automated Corrosion Monitoring Programme (ACMP) and measurement unit</i> ..... | 85         |
| 3.3.1.2. <i>Chloride content analysis</i> .....  | 89         |
| 3.3.2. <i>Field measurements</i> .....   | 91         |
| 3.3.2.1. <i>Bridge at the University of Waterloo</i> .....                                   | 92         |
| 3.3.2.2. <i>Victoria Street Bridge, Wingham, Ontario</i> .....                               | 94         |
| 3.3.2.3. <i>Barrier walls, Renfrew</i> .....   | 96         |
| 3.3.2.4. <i>Island Park Avenue bridge, Ottawa</i> .....                                      | 97         |
| <b>CHAPTER 4, EXPERIMENTAL RESULTS AND DISCUSSION</b> .....                                  | <b>100</b> |
| <b>4.1. RESULTS FROM LABORATORY MEASUREMENTS</b> .....                                       | <b>100</b> |
| 4.1.1. <i>Beams with segmented steel bars</i> .....  | 100        |
| 4.1.1.1. <i>Electrochemical corrosion measurements</i> .....                                 | 100        |
| 4.1.1.1.1. <i>Half-cell potential</i> .....  | 101        |
| 4.1.1.1.2. <i>Potentiostatic and galvanostatic LPR</i> .....                                 | 105        |
| 4.1.1.1.3. <i>Electrochemical impedance spectroscopy</i> .....                               | 110        |
| 4.1.1.1.4. <i>Cyclic polarisation</i> .....  | 117        |
| 4.1.1.1.5. <i>Galvanodynamic LPR</i> .....   | 119        |

|   |            |
|---|------------|
| 4.1.1.1.6. Comparison between different corrosion measurements.....                   | 121        |
| 4.1.1.3. Electrical resistance of concrete .....                                      | 122        |
| 4.1.1.4. Gravimetry .....   | 125        |
| 4.1.1.4.1. Actual corroded area and whole surface area.....                           | 129        |
| 4.1.2. Specimens with different variables.....  | 132        |
| 4.1.2.1. Electrochemical corrosion measurements .....                                 | 132        |
| 4.1.2.1.1. Half-cell potential.....   | 133        |
| 4.1.2.1.1.1. Distance of reference electrode to the steel bar.....                    | 134        |
| 4.1.2.1.2. Potentiostatic and galvanostatic LPR .....                                 | 137        |
| 4.1.2.1.3. Electrochemical impedance spectroscopy .....                               | 143        |
| 4.1.2.2.4. Cyclic polarisation .....  | 146        |
| 4.1.2.2.5. Galvanodynamic LPR.....  | 149        |
| 4.1.2.3. Electrical resistance of concrete .....                                      | 150        |
| 4.1.3. Chloride content.....  | 152        |
| 4.1.4. Effect of the wetness of the surface on half-cell potential measurements ..... | 153        |
| 4.1.5. The effect of different counter electrodes on corrosion measurements.....      | 155        |
| 4.1.6. Function of the GalvaPulse™.....   | 158        |
| 4.1.7. Reinforcing steel passivation time.....  | 166        |
| 4.1.8. Stern-Geary constant (B).....  | 176        |
| <b>4.2. RESULTS FROM FIELD MEASUREMENT .....</b>                                      | <b>179</b> |
| 4.2.1. Bridge at the University of Waterloo .....                                     | 179        |
| 4.2.2. Victoria Street Bridge, Wingham, Ontario .....                                 | 186        |
| 4.2.2.1. Visual inspection .....  | 186        |
| 4.2.2.2. Delamination.....  | 188        |
| 4.2.2.2. Corrosion measurement.....   | 189        |
| 4.2.2.3. Chloride ion content .....   | 192        |
| 4.2.2.4. Microscopic observation.....   | 192        |
| 4.2.3. Barrier walls, Renfrew .....   | 197        |
| 4.2.4. Island Park Avenue Bridge, Ottawa.....   | 200        |
| 4.2.5. General observations for the field tests.....                                  | 204        |
| <b>CHAPTER 5, SUMMARY, CONCLUSIONS, RECOMMENDATIONS AND FUTURE WORKS .....</b>        | <b>206</b> |

|  |            |
|--|------------|
| <b>5.1. SUMMARY AND CONCLUSIONS.....</b> | <b>206</b> |
| <b>5.2. RECOMMENDATIONS .....</b>        | <b>211</b> |
| <b>5.3. FUTURE WORK .....</b>            | <b>212</b> |
| <b>REFERENCES .....</b>                  | <b>215</b> |
| <b>Appendix (A).....</b>                 | <b>235</b> |
| <b>Appendix (B) .....</b>                | <b>242</b> |
| <b>Appendix (C).....</b>                 | <b>247</b> |
| <b>Appendix (D).....</b>                 | <b>251</b> |
| <b>Appendix (E) .....</b>                | <b>258</b> |
| <b>Appendix (F) .....</b>                | <b>261</b> |
| <b>Appendix (G).....</b>                 | <b>267</b> |

## LIST OF TABLES

|  |    |
|--|----|
| Table 2. 1. Bogue composition of normal Portland cement clinkers.....  | 4  |
| Table 2. 2. Approximate chemical composition limits of Portland cement.....  | 4  |
| Table 2. 3. Applications and potential compound composition of commonly used cements.....  | 4  |
| Table 2. 4. Portland cement compound hydration reaction.....   | 5  |
| Table 2. 5. Typical composition of pore solution from concrete made of OPC (w/c=0.5) .....                                       | 7  |
| Table 2. 6. The pH is revealed by the following illustrated colours.....   | 14 |
| Table 2. 7. Probability of corrosion according to half-cell potential reading .....  | 20 |
| Table 2. 8. Effect of the various factors on half-cell potential shift and corrosion probability ....                            | 27 |
| Table 2. 9 Quick evaluation of corrosion rate, recommended by FORCE Technology and<br>measure by the GalvaPulse™ .....           | 40 |
| Table 2. 10 Relationship between corrosion current density measured with guard ring device<br>(Gecor6™) and corrosion risk ..... | 40 |
| Table 2. 11. Simple circuit elements with their impedance expression.....  | 47 |
| Table 2. 12. Comparison of relationship between concrete resistivity and corrosion risk of<br>reinforcing steel .....            | 64 |
| Table 3. 1. Concrete mixture proportion for making 1m <sup>3</sup> concrete.....   | 66 |
| Table 3. 2. Composition of synthetic pore solution, Type 10 .....  | 67 |
| Table 3. 3. Concrete specimens with different variables .....  | 72 |
| Table 3. 4. . Mortar mixture .....   | 82 |

|  |     |
|--|-----|
| Table 4. 1. Comparison between half-cell potential and corrosion current density of one of the carbonated specimens, using three different locations for the reference electrode. .... | 136 |
| Table 4. 2. Results of chloride content analysis .....   | 153 |
| Table 4. 3. Material, shape and the size of the counter electrodes, used to determine the effect of counter electrode on the measurements.....   | 155 |
| Table 4. 4. Comparison between concrete resistance and corrosion current density, calculated using the data in Figures 4.65 and 4.66 and PSION unit .....                              | 161 |
| Table 4. 5. Calculation of the corrosion current density and concrete resistance, by using actual applied current; pre-set current: $I=100\mu\text{A}$ , guard ring off and on .....   | 165 |
| Table 4. 6. Main bands of reference iron oxide compounds (in $\text{cm}^{-1}$ ).....   | 171 |
| Table 4. 7. Value of B, calculated for different specimens.....  | 178 |
| Table 4. 8. Total chloride ions content in Victoria St. Bridge, Wingham .....  | 192 |
| Table 4. 9. Results of the corrosion measurements of the steel bars in barrier wall in HWY 17, Renfrew .....   | 198 |
| Table 4. 10. Comparison between corrosion current density and concrete resistance, measured by different techniques and equipment .....  | 199 |
| Table 4. 11. Half-cell potential and corrosion current density, obtained by the 3LP, of the selected points of the east abutment of Island Park Bridge, Ottawa.....                    | 202 |
| Table D. 1. Corrosion current density values of steel segments in beams A and B.....   | 254 |
| Table D. 2. Corrosion current density values of steel segments in beams C and D.....   | 255 |
| Table D. 3. Corrosion current density values of steel segments in beam C.....  | 256 |
| Table D. 4. Corrosion current density values of the specimens with different variables .....   | 257 |

|  |     |
|--|-----|
| Table E. 1. Mass loss determined by gravimetry and calculated by using electrochemical data,<br>beam A ..... | 260 |
| Table E. 2. Mass loss determined by gravimetry and calculated by using electrochemical data,<br>beam B.....  | 260 |
| Table E. 3. Mass loss determined by gravimetry and calculated by using electrochemical data,<br>beam C.....  | 260 |
| Table E. 4. Mass loss determined by gravimetry and calculated by using electrochemical data,<br>beam D ..... | 260 |
| Table E. 5. Mass loss determined by gravimetry and calculated by using electrochemical data,<br>beam E.....  | 260 |

## LIST OF FIGURES

|   |    |
|---|----|
| Figure 2. 1. Relative volume of the major compounds in the microstructure of hydrating Portland cement paste (left) as a function of time and (right) as a function of the degree of hydration for $w/c=0.5$ .....  | 6  |
| Figure 2. 2. Influence of moist curing on the strength of concrete with a water/cement ratio of 0.5.....  | 8  |
| Figure 2. 3. Pourbaix diagram for Fe-H <sub>2</sub> O at 25°C .....   | 9  |
| Figure 2. 4. Schematic illustration of the corrosion of reinforcement steel in concrete.....  | 17 |
| Figure 2. 5. Schematic diagram showing spalling of concrete due to corrosion damage.....  | 18 |
| Figure 2. 6. Apparatus for half-cell potential method described in ASTM C 876 to measure surface potential associated with corrosion current. ....  | 20 |
| Figure 2. 7. Half-cell potential contour map, measured by CSE; Lower Elk Creek Bridge #2531, British Columbia.....  | 21 |
| Figure 2. 8. Schematic active-passive corrosion behaviour .....   | 22 |
| Figure 2. 9. Experimental potentiostatic polarisation curves for steel in OPC mortar ( $w/c = 0.5$ ) at 22 °C. Curve (a) is for passivated steel and curve (b) for corroding steel due to chloride ion attack ..... | 23 |
| Figure 2. 10. Anodic and cathodic reactions and their variations in concrete .....  | 25 |
| Figure 2. 11. Comparison of corrosion current with half-cell potential .....  | 26 |
| Figure 2. 12. Linear polarisation curve .....   | 30 |
| Figure 2. 13. Applied potential and current response during LPR measurement.....  | 33 |
| Figure 2. 14. Set up of the galvanostatic pulse technique.....  | 34 |
| Figure 2. 15. Schematic illustration of galvanostatic pulse results .....   | 35 |

|   |    |
|---|----|
| Figure 2. 16 Schematic illustration of eq. 2.18.....  | 36 |
| Figure 2. 17. Schematic plan of the GalvaPulse™ measurement cell. ....  | 37 |
| Figure 2. 18. Schematic plan of the GalvaPulse™ with guarding to limit the polarised area while performing the corrosion measurement. ....                                | 38 |
| Figure 2. 19 The schematic illustration of the change of potential over time: (a) for active areas and (b) for passive areas .....  | 39 |
| Figure 2. 20. Sinusoidal AC voltage and current in a circuit with one resistor .....  | 42 |
| Figure 2. 21. Sinusoidal AC voltage and current with a capacitor .....  | 42 |
| Figure 2. 22. Sinusoidal AC voltage and current with an inductor .....  | 43 |
| Figure 2. 23. Relationship between vectors of voltage and current in a circuit with (a) resistor, (b) capacitor and (c) inductor .....                                    | 43 |
| Figure 2. 24. . Relationship between sinusoidal AC current and rotating vector representation ..  | 44 |
| Figure 2. 25. Equivalent circuit for a simple electrochemical system.....   | 48 |
| Figure 2. 26. Nyquist plot for a simple electrochemical system .....  | 49 |
| Figure 2. 27. Equivalent circuit for a system with Warburg impedance .....  | 50 |
| Figure 2. 28. Nyquist plot for a system with Warburg impedance.....   | 50 |
| Figure 2. 29. Experimental impedance diagram. System: Fe/0.5 M H <sub>2</sub> SO <sub>4</sub> , aerated .....   | 51 |
| Figure 2. 30. Equivalent circuit for system used in Figure 2.31 .....   | 52 |
| Figure 2. 31. Bode plot for the same system used in Figure 2.27. ....   | 53 |
| Figure 2. 32. Bode plots of the frequency response for the an electrochemical system with R <sub>Ω</sub> = 10Ω, R <sub>p</sub> =1000 Ω and C <sub>dl</sub> =93.8 μF ..... | 58 |
| Figure 2. 33. Variation of uncompensated potential with conductivity for different current densities .....  | 59 |



|  |    |
|--|----|
| Figure 2. 34. Schematic of pitting and passivation potentials on cyclic polarisation curve .....   | 61 |
| Figure 2. 35. Wenner technique for measuring resistivity .....   | 63 |
| Figure 2. 36. (a) Simple schematic model of steel-concrete interface, (b) equivalent circuit of the model and (c) schematic Nyquist plot for the model. ....   | 65 |
| Figure 3. 2. (a) one tapped steel segment with a threaded rod, (b) two segments with two PVC pieces for isolation. ....  | 70 |
| Figure 3. 3. Concrete beams in a container filled with water. A stainless steel sheet is kept at the bottom of the container as counter electrode.....   | 70 |
| Figure 3. 4. Schematic plan of a concrete specimen for determining the effect of different variables of the half-cell potential value (50 mm cover depth), (a) side view, (b) end view. ....                               | 73 |
| Figure 3. 5. Ponding well attachment to a concrete specimen with 50 mm cover depth.....  | 73 |
| Figure 3. 6. Carbonation depth versus time of exposure .....   | 74 |
| Figure 3. 7. Carbonation depth measurement. Phenolphthalein used to determine the pH of the concrete. The high pH of the concrete made the solution purple while carbonated area (the low pH area) remained unchanged..... | 75 |
| Figure 3. 8. View of the glove box used in this project to carbonate the concrete specimens.....   | 75 |
| Figure 3. 9. Longitudinal crack, parallel to the steel rebar, created by expansion of the plastic rod (a) longitudinal view, (b) end view. ....  | 76 |
| Figure 3. 10. Three point bending test configuration and (b) resultant transverse crack.....   | 77 |
| Figure 3. 11. A schematic plan of ERE 20 Mn/MnO <sub>2</sub> reference electrode.....  | 77 |

|  |    |
|--|----|
| Figure 3. 12. A sample with embedded Mn/MnO <sub>2</sub> reference electrode. The rather messy epoxy on the ponding well is due to the need to make the well leak-tight..... | 78 |
| Figure 3. 13. Schematic plan of setup, used for checking the stability of graphite in different solutions.....   | 79 |
| Figure 3. 14. Potential difference between calomel reference electrode and graphite in 3% salt solution over an eight hour period. ....                                      | 79 |
| Figure 3. 15. Potential difference between calomel reference electrode and graphite in synthetic pore solution over an eight hour period.....                                | 80 |
| Figure 3. 16. Schematic plan of the electrode holder, (a) top view, (b) end view.....  | 81 |
| Figure 3. 17. Schematic isometric of the immersed steel bars in synthetic pore solution. ....  | 83 |
| Figure 3. 18. Schematic section of the mortar sample with embedded steel bars. ....  | 83 |
| Figure 3. 19. Schematic diagram of the connections between different components of the automatic measurement system. ....  | 87 |
| Figure 3. 20. A view of Automated Corrosion Monitoring Programme (ACMP). ....  | 88 |
| Figure 3. 21. Comparison between potentiostatic LPR measurements, measured by two different setups: designed setup and conventional setup.....                               | 89 |
| Figure 3. 22. (a) A view of the bridge at the University of Waterloo, (b) some of the deteriorated spots on one of the approaches. ....                                      | 92 |
| Figure 3. 23. Schematic plan of the bridge at the University of Waterloo. ....   | 93 |
| Figure 3. 24. Epoxy coated steel bar used in the deck of the bridge at the University of Waterloo<br>.....   | 93 |
| Figure 3. 25. Location of the Victoria street Bridge, Wingham town, Ontario, Canada .....  | 95 |
| Figure 3. 26. Location of the barriers walls, Renfrew, Ontario .....   | 96 |

Figure 3. 27. (a) a view of the barriers wall, from the road, (b) the other side of the wall. .... 96

Figure 3. 28. The setup consisted of PARSTAT<sup>®</sup> 2263 potentiostat, reference and counter electrodes and the computer, used for performing electrochemical tests of the steel bars in the barrier walls, Renfrew, Ontario..... 97

Figure 3. 29. Island Park bridge, Ottawa, Ontario..... 98

Figure 3. 30. Photograph from Island Park Bridge, Ottawa, Ontario (a) corrosion of the steel bars of one of the approaches of the bridge, (b) repaired areas of the bridge, (c) corrosion underneath the bridge deck and (d) severely corroded spot on one of the approaches..... 98

Figure 4. 1. Segments designation for each beam. .... 101

Figure 4. 2. Half-cell potential values of the segmented steel bars, chloride-free section. .... 102

Figure 4. 3. Half-cell potential values of segmented steel bars, chloride-contaminated section. 102

Figure 4. 4. Half-cell potential values of segmented steel bars, measured by Ag/AgCl and converted to CSE, chloride free section. .... 104

Figure 4. 5. Half-cell potential values of segmented steel bars, measured by Ag/AgCl and converted to CSE, chloride contaminated section. .... 104

Figure 4. 6. Corrosion current density of the segmented steel bars, measured by potentiostatic LPR, chloride-free section. .... 106

Figure 4. 7. Corrosion current density of the segmented steel bars, measured by potentiostatic LPR, chloride-contaminated section. .... 106

Figure 4. 8. Corrosion current density of the segmented steel bars, measured by GalvaPulse<sup>™</sup>, chloride-free section. .... 107

|  |     |
|--|-----|
| Figure 4. 9. Corrosion current density of the segmented steel bars, measured by GalvaPulse™, chloride-contaminated section. ....   | 107 |
| Figure 4. 10. Nyquist (a) and Bode (b) plots for the steel segments of beam C, 88 weeks after casting.....   | 110 |
| Figure 4. 11. Extrapolated Nyquist plot for segment C1 in chloride-free concrete.....  | 112 |
| Figure 4. 12. Extrapolated Bode plot for segment C1 in chloride-free concrete.....   | 112 |
| Figure 4. 13The extrapolated Nyquist plot for segment C4 in chloride-contaminated concrete.  | 113 |
| Figure 4. 14. The extrapolated Bode plot for segment C4 in chloride-contaminated concrete...   | 113 |
| Figure 4. 15. Extrapolated Nyquist plot for segment A1 in chloride-free concrete. ....   | 115 |
| Figure 4. 16. Extrapolated Bode plot for segment A1 in chloride-free concrete. ....  | 115 |
| Figure 4. 17. Cyclic polarisation curve for segment A1, 118 weeks after casting, with the scan rate of 0.006 mV/s. Arrow shows the direction when the potential in returning.....      | 117 |
| Figure 4. 18. Cyclic polarisation curve for segment A1, 119 weeks after casting, with the scan rate of 0.1 mV/s. Arrow shows the direction when the potential in returning. ....       | 118 |
| Figure 4. 19. Galvanodynamic LPR results for the steel segments in beam A. ....  | 119 |
| Figure 4. 20. Galvanodynamic LPR results for the steel segments in beam B. ....  | 120 |
| Figure 4. 21. Comparison between different corrosion measuring techniques. Segments 1 and 2 are in chloride-free concrete; segments 3 and 4 are in chloride-contaminated concrete. ... | 121 |
| Figure 4. 22. Concrete resistance of the beams with segmented steel bars, measured by the GalvaPulse™, with the guard ring on, in chloride-free sections. ....                         | 122 |
| Figure 4. 23. Concrete resistance of the beams with segmented steel bars, measured by GalvaPulse™, with the guard ring on, in chloride-contaminated sections. ....                     | 122 |

|   |     |
|---|-----|
| Figure 4. 24. Concrete resistance of beams A, B and C, measured by GalvaPulse™(guard ring off), EIS and potentiostatic LPR, 65 weeks after casting. Segments 1 and 2 are in chloride-free concrete; segments 3 and 4 are in chloride-contaminated concrete..... | 123 |
| Figure 4. 25. Concrete resistance, measured by GalvaPulse™ and Wenner technique. Segments 1 and 2 are in chloride-free concrete; segments 3 and 4 are in chloride-contaminated concrete.....  | 124 |
| Figure 4. 26. Comparison between mass loss determined by gravimetry and calculated from electrochemical measurements, beam A .....  | 126 |
| Figure 4. 27. Comparison between mass loss determined by gravimetry and calculated from electrochemical measurements, beam B .....  | 126 |
| Figure 4. 28. Comparison between mass loss determined by gravimetry and calculated from electrochemical measurements, beam C .....  | 127 |
| Figure 4. 29. Comparison between mass loss determined by gravimetry and calculated from electrochemical measurements, beam D .....  | 127 |
| Figure 4. 30. Comparison between mass loss determined by gravimetry and calculated from electrochemical measurements, beam E.....   | 128 |
| Figure 4. 31. Calculated corrosion current density of the last measurement of segments in beam A, using actual corroded area and whole surface area. ....   | 129 |
| Figure 4. 32. Calculated corrosion current density of the last measurement of segments in beam B, using actual corroded area and whole surface area. ....   | 130 |
| Figure 4. 33. Calculated corrosion current density of the last measurement of segments in beam C, using actual corroded area and whole surface area. ....   | 130 |

Figure 4. 34. Calculated corrosion current density of the last measurement of segments in beam D, using actual corroded area and whole surface area. .... 131

Figure 4. 35. Calculated corrosion current density of the last measurement of segments in beam A, using actual corroded area and whole surface area. .... 131

Figure 4. 36. Half-cell potential values, measured by Cu/CuSO<sub>4</sub> reference electrode, of the specimens with different variables. .... 133

Figure 4. 37. Average half-cell potential values, measured by Cu/CuSO<sub>4</sub> reference electrode, of the specimens with different variables. Green dash lines represent the ASTM C876 recommended guideline. .... 133

Figure 4. 38. Comparison between half-cell potential values obtained by embedded Mn/MnO<sub>2</sub> reference electrodes and measured by Cu/CuSO<sub>4</sub> reference electrode from the top surface of the specimens. .... 135

Figure 4. 39. Schematic views of one of the carbonated concrete samples with a hole drilled on its top and its side. .... 136

Figure 4. 40. Corrosion current densities of the specimens with different variables, measured by potentiostatic LPR. .... 138

Figure 4. 41. Average values of the corrosion current densities, specimens with different variables, measured by potentiostatic LPR. .... 138

Figure 4. 42. Corrosion current densities of the specimens with different variables, measured by GalvaPulse™. .... 140

Figure 4. 43. Average values of corrosion current densities of the specimens with different variables, measured by GalvaPulse™. The blue arrow shows that the corrosion current

|   |     |
|---|-----|
| densities of the specimens with longitudinal cracks are more than $150\mu\text{A}/\text{cm}^2$ and the values are out of the scale of the graph. ....   | 140 |
| Figure 4. 44. Corrosion current density, measured by the GalvaPulse™. Assumed polarised length of rebar = 500mm .....   | 142 |
| Figure 4. 45. Extrapolated Nyquist plot for one of the carbonated specimens (S1), 27 weeks after exposure to salt solution. ....  | 144 |
| Figure 4. 46. Extrapolated Bode plot for one of the carbonated specimens (S1), 27 weeks after exposure to salt solution. ....   | 144 |
| Figure 4. 47. . Extrapolated Nyquist plot for one of the carbonated specimens (S1), 78 weeks after exposure to salt solution. ....  | 145 |
| Figure 4. 48. . Extrapolated Nyquist plot for one of the carbonated specimens (S1), 78 weeks after exposure to salt solution. ....  | 145 |
| Figure 4. 49. Cyclic polarisation curve with the scan rate of 0.006mV/s, one of the specimens with a longitudinal crack. Solid arrows show the direction of increasing the potential and dotted arrows show the direction of return potential. .... | 147 |
| Figure 4. 50. Cyclic polarisation curve with the scan rate of 1mV/s, one of the specimens with a longitudinal crack. Solid arrows show the direction of increasing the potential and dotted arrows show the direction of return potential. ....     | 147 |
| Figure 4. 51. Cyclic polarisation curves with different scan rates for one of the samples with transverse crack. Arrows show the direction of the return potential.....   | 148 |
| Figure 4. 52. Galvanodynamic LPR curves for one of the specimens of each variable. ....   | 149 |
| Figure 4. 53. Comparison of the values of corrosion current density of one of the specimens of each variable, measured by three different techniques. ....  | 149 |

|   |     |
|---|-----|
| Figure 4. 54. Concrete resistance of all specimens with different variables, measured by the GalvaPulse™, guard ring on.....  | 151 |
| Figure 4. 55. Average values of concrete resistance, specimens with different variables, measured by the GalvaPulse™, guard ring on. ....   | 151 |
| Figure 4. 56. Comparison between concrete resistance, measured by GalvaPulse™ (guard on and off), EIS, galvanostatic pulse technique and Wenner technique, 49 weeks after exposure to salt solution. The shown values are the average of the measured concrete resistances of multiple specimens of each variable. .... | 152 |
| Figure 4. 57. Setup used to monitor the half-cell potential to determine the effect of surface wetness of the measured values; (a) side view and (b) top view.....  | 154 |
| Figure 4. 58. Half-cell potential of the steel bar in a concrete beam, monitored for 90 minutes. ....   | 155 |
| Figure 4. 59. The effect of counter electrode on the corrosion current density values, measured by potentiostatic LPR.....  | 156 |
| Figure 4. 60. The effect of counter electrode on the corrosion current density values, measured by the GalvaPulse™.....   | 156 |
| Figure 4. 61. The effect of counter electrode on the concrete resistance values, measured by the GalvaPulse™ and EIS.....   | 157 |
| Figure 4. 62. Measured current on the counter electrode of the GalvaPulse™ measuring unit with three pre-set applied current. ....  | 158 |
| Figure 4. 63. Measured current on the guard ring of the GalvaPulse™ measuring unit with three pre-set applied current.....  | 159 |



|  |     |
|--|-----|
| Figure 4. 64. Measured current on the guard ring, while the guard was off. The measured values are almost zero. ....   | 159 |
| Figure 4. 65. Potential changes, measured by the HP multimeter; guard ring on; applied current =100 $\mu$ A. ....  | 160 |
| Figure 4. 66. Potential changes, measured by the HP multimeter; guard ring off; applied current =100 $\mu$ A. ....   | 160 |
| Figure 4. 67. Setup used to estimate the polarised length of the rebar. ....   | 162 |
| Figure 4. 68. Potential differences between before and at the end of applying the current by GalvaPulse™, guard ring on. Concrete resistance is compensated. ....  | 163 |
| Figure 4. 69. Potential differences between before and at the end of applying the current by GalvaPulse™, guard ring off. Concrete resistance is compensated. .... | 163 |
| Figure 4. 70. Schematic plan of the setup, used to determine the influence of the guard ring on the current under the counter electrode. ....                      | 164 |
| Figure 4. 71. Corrosion current density of steel embedded in mortar for 300 hours. ....  | 167 |
| Figure 4. 72. Corrosion current density of steel in synthetic pore solution for 300 hours. ....  | 167 |
| Figure 4. 73. Half-cell potential values of steel embedded in mortar for 300 hours. ....   | 168 |
| Figure 4. 74. Half-cell potential values of steel immersed in synthetic pore solution for 300 hours. ....  | 168 |
| Figure 4. 75. Mortar resistance, measured every 30 minutes for 300 hours. ....   | 169 |
| Figure 4. 76. Raman spectra of steel with mill scale, as received. ....  | 170 |
| Figure 4. 77. Raman spectra of steel with mill scale , immersed in pore solution for 2 months. ....  | 170 |
| Figure 4. 78. Raman spectra of sand blasted steel , immersed in pore solution for 2 months. ...  | 171 |
| Figure 4. 79. Permittivity of young concrete with ordinary Portland cement. ....   | 175 |

|  |     |
|--|-----|
| Figure 4. 80. Schematic illustration of obtaining $i_a$ , from $i_c$ and $i_{app, c}$ .....  | 177 |
| Figure 4. 81. A view of the bridge at the University of Waterloo. Approached are labelled A and B.....   | 179 |
| Figure 4. 82. Some of the rust spots (marked by black circles) on approach B of the bridge at campus of the University of Waterloo. ....   | 180 |
| Figure 4. 83. Location of the delaminations and cracks on two approaches.....  | 180 |
| Figure 4. 84. Contour map of the half-cell potential measurements of the approaches A and B of the bridge at the University of Waterloo; March 06, 2005; T = -10°C, RH = 72%, cloudy ..... | 181 |
| Figure 4. 85. Contour map of the half-cell potential measurements of the approaches A and B of the bridge at the University of Waterloo; May 25, 2005; T = +19°C, RH = 58%, sunny...       | 181 |
| Figure 4. 86. Contour map of the half-cell potential measurements of the approaches A and B of the bridge at the University of Waterloo; August 22, 2005; T = +16°C, RH = 91%, sunny ..... | 182 |
| Figure 4. 87. Contour map of the half-cell potential measurements of the approaches A and B of the bridge at the University of Waterloo; April 11, 2006; T = +17°C, RH = 40%, sunny..      | 182 |
| Figure 4. 88. Contour map of the half-cell potential measurements of the approaches A and B of the bridge at the University of Waterloo; May 17, 2006; T = +14°C, RH = 92%, sunny...       | 183 |
| Figure 4. 89. Contour map of the half-cell potential measurements of the approaches A and B of the bridge at the University of Waterloo; August 22, 2006; T = +19°C, RH = 90%, sunny. .... | 183 |
| Figure 4. 90. Corrosion current density (a) of the steel bars and concrete resistance (b) of approach B, measured by GalvaPulse™, August 22, 2005.....                                     | 184 |

|  |     |
|--|-----|
| Figure 4. 91. Corrosion current density (a) of the steel bars and concrete resistance (b) of approach B, measured by GalvaPulse™, April 11, 2006.....  | 184 |
| Figure 4. 92. Corrosion current density (a) of the steel bars and concrete resistance (b) of approach B, measured by GalvaPulse™, August 22, 2006..... | 185 |
| Figure 4. 93. Longitudinal cracks on bridge deck. ....   | 187 |
| Figure 4. 94. Pop-outs on the surface of the bridge deck.....  | 187 |
| Figure 4. 95. Corroded steel rebar in the one of the sidewalks. ....   | 187 |
| Figure 4. 96. Progression of delaminations on the Victoria St. bridge, Wingham.....  | 188 |
| Figure 4. 97. Grid map, used for corrosion measurements.....   | 189 |
| Figure 4. 98. Half-cell potential contour map of galvanised steel rebars, measured vs. CSE, Victoria St Bridge, Wingham, June 16, 1998.....            | 190 |
| Figure 4. 99. Half-cell potential contour map of galvanised steel rebars, measured vs. CSE, Victoria St Bridge, Wingham, November 22, 2004.....        | 190 |
| Figure 4. 100. Comparison between half-cell potential measurements (with CSE) in 1998 and 2004.....  | 191 |
| Figure 4. 101. Half-cell potential, corrosion current density and concrete resistance, measured by the GalvaPulse™, row C, November 2004. ....         | 191 |
| Figure 4. 102. Average corrosion potentials of Victoria St. Bridge, Wingham.....   | 192 |
| Figure 4. 103. Galvanised steel rebar under optical microscope (a) overview of the galvanised layer (b) different phases. ....                         | 193 |
| Figure 4. 104. Galvanised steel rebar under SEM, (a) Back Scattered Electron (BSE) mode and (b) secondary electron (SE) mode.....                      | 194 |

|   |     |
|---|-----|
| Figure 4. 105. Cyclic polarisation curve for spot S9. Arrow shows the direction of the return part of the curve. ....   | 199 |
| Figure 4. 106. Schematic illustration of the location of the selected points on the east abutment of Island Park Bridge.....  | 201 |
| Figure 4. 107. Cyclic polarisation curves for point B-32 with the scan rate of 5mV/s; assumed polarised length of the steel rebar = 70 mm. Based on the obtained curves, the approximated corrosion current densities for both dates are $\sim 2\mu\text{A}/\text{cm}^2$ . .... | 203 |
| Figure A. 1. General symbol of an optional amplifier [184].....   | 236 |
| Figure A. 2. Schematic plan of an optional amplifier (op-amp), when the inverting input and output are connected. The output of this circuit will be the input voltage. ....  | 237 |
| Figure A. 3. Using an optional amplifier as potentiostat [182].....   | 238 |
| Figure A. 4. A potentiostat with potential control [182].....   | 239 |
| Figure A. 5. Complete scheme of a simple potentiostat [182].....  | 240 |
| Figure A. 6. A standard potentiostat circuit [185].....   | 241 |
| Figure D. 1. Resultant current curve after performing potentiostatic LPR test on segment A4 (active corrosion); 120 weeks after casting. ....   | 252 |
| Figure D. 2. Resultant current curve after performing potentiostatic LPR test on segment A4 (passive corrosion); 120 weeks after casting. ....  | 252 |
| Figure F. 1. Steel segments after cleaning the corrosion products, removed from beam A. ....  | 262 |
| Figure F. 2. Steel segments after cleaning the corrosion products, removed from beam B. ....  | 263 |

Figure F. 3. Steel segments after cleaning the corrosion products, removed from beam C. .... 264

Figure F. 4. Steel segments after cleaning the corrosion products, removed from beam D. .... 265

Figure F. 5. Steel segments after cleaning the corrosion products, removed from beam E..... 266

Figure G. 1. Half-cell potential values of the Victoria Street Bridge deck, Wingham, measured in  
June 16, 1998; T= 24°C. Hatched regions represent the delaminated areas..... 268

Figure G. 2. Half-cell potential values of the Victoria Street Bridge deck, Wingham, measured in  
Nov 24, 2004; T= 5°C ..... 269

# CHAPTER 1, INTRODUCTION

Low cost, readily available raw materials and ease of forming at ambient temperatures make steel reinforced concrete the most widely used structural material. Concrete provides corrosion resistance to the steel reinforcement physically, by acting as a barrier and chemically, due to its high pH. However, reinforcing steel does corrode. The two most common causes of reinforcement corrosion are localised breakdown of the passive film on the steel by chloride ions and general breakdown of passivity due to neutralization of the concrete by reaction with atmospheric carbon dioxide. Corrosion of reinforcing steel in concrete is a serious problem from the point of view of both safety and economy. Therefore, it is essential to have reliable measurement techniques to evaluate the corrosion condition of the steel bars in the reinforcing concrete.

The half cell potential measurement technique is the most widely non-destructive method of evaluating the corrosion activity of embedded reinforcement. In 1980, the test was approved as a standard by ASTM: C 876 Standard Test Method for Half-Cell Potentials of Uncoated Reinforcing Steel in Concrete” and was modified in 1987 [1]. Potentiostatic and potentiodynamic polarisation techniques, galvanostatic and galvanodynamic polarisation methods and electrochemical impedance spectroscopy are the mostly commonly measuring techniques, mostly used in the laboratory, to identify the corrosion behaviour of steel rebars. However, each of these techniques needs specific requirements, such as the appropriate applied current or potential, the appropriate scan rate, frequency range and polarised area. If any of these parameters is ignored in the experiments, it can cause errors and consequently, mislead the researcher(s).

The aim of this project was to determine the factors that influence the electrochemical measurements (half-cell potential and corrosion current density) of the condition of the steel bars in reinforced concrete structures.

For this purpose, reinforced concrete specimens were cast and exposed to salt solution and the effect of cover-depth, carbonation depth, and distance of the electrodes from the surface of the steel bar on the corrosion measurement was investigated by different electrochemical techniques. Also, instrument variability and electrochemical techniques were evaluated and their limitations, advantages and disadvantages were determined. The effectiveness of a guard ring, in the instrument with guard electrode, in limiting the polarised length of the steel bar is the other issue which has been studied.

In addition to the laboratory experiments, measurements were performed in the field, with the assistance of the Ministry of Transportation of Ontario (MTO) staff, and attempts were made to find a correlation between the results obtained from the laboratory measurements and those obtained from the field measurement. The advantages, difficulties and limitations of each electrochemical technique in the field, were also determined.

## CHAPTER 2, LITERATURE REVIEW

### 2.1. CONCRETE

Concrete is a composite material which consists primarily of three main components: cement, aggregates (coarse and fine) and water. It is the most widely used structural material because of its low cost, readily available raw materials and ease of forming at ambient temperatures. Most of the cements used in making concrete are Ordinary Portland Cement (OPC).

#### 2.1.1. Ordinary Portland Cement (OPC) concrete

Portland cements are hydraulic cements containing calcium silicates that set and harden by a chemical reaction with water (hydration). The process of cement manufacturing starts by grinding the raw materials, which basically are: lime, silica, alumina and iron oxide, mixing them in certain proportions and burning them in a rotary kiln at a temperature of about 1450°C. This results in the formation of clinker. Clinker is cooled, ground to fine powder and, by adding some gypsum ( $\text{CaSO}_4 \cdot 2\text{H}_2\text{O}$ ), the resulting product is the commercial OPC. The four major components of cement are: tricalcium silicate ( $3\text{CaO} \cdot \text{SiO}_2$  or  $\text{C}_3\text{S}$ ), dicalcium silicate ( $2\text{CaO} \cdot \text{SiO}_2$  or  $\text{C}_2\text{S}$ ), tricalcium aluminate ( $3\text{CaO} \cdot \text{Al}_2\text{O}_3$  or  $\text{C}_3\text{A}$ ) and tetracalcium aluminoferrite ( $4\text{CaO} \cdot \text{Al}_2\text{O}_3 \cdot \text{Fe}_2\text{O}_3$  or  $\text{C}_4\text{AF}$ ) (Table 2.1)<sup>1</sup>. Gypsum is added to cement to provide sulphate to

---

<sup>1</sup> The calculation of the potential composition of Portland cement is based on work on R. H. Bogue and is often referred to as Bogue composition



react with  $C_3A$ , without which, cement would set rapidly (flash set). In addition to the main components, the minor components of cement include  $MgO$ ,  $TiO_2$ ,  $Mn_2O_3$ ,  $K_2O$  and  $Na_2O$  (Table 2.2). Their amounts are usually not more than a few percent of the cement weight. It should be mentioned that the term of ‘minor components’ refers to their quantity not necessarily to their importance [1-3].

Table 2. 1. Bogue composition of normal Portland cement clinkers [1].

| Phase   | Compound composition, percent |
|---------|-------------------------------|
| $C_3S$  | 50-70                         |
| $C_2S$  | 15-30                         |
| $C_3A$  | 5-10                          |
| $C_4AF$ | 5-15                          |

Table 2. 2. Approximate chemical composition limits of Portland cement [3].

| Oxide     | Content, percent |
|-----------|------------------|
| $CaO$     | 60-67            |
| $SiO_2$   | 17-25            |
| $Al_2O_3$ | 3-8              |
| $Fe_2O_3$ | 0.5-6            |
| $MgO$     | 0.1-4            |
| Alkalis   | 0.21.3           |
| $SO_3$    | 1-3              |

Different types of Portland cement can be used based on the chemical and physical exposure conditions. Table 2.3 shows the different types of Portland cement and their Bogue composition.

Table 2. 3. Applications and potential compound composition of commonly used cements [4].

| Type of Portland cement    | Application                                      | Potential compound composition (mean), wt % |        |        |         |
|----------------------------|--|---|--------|--------|---------|
|                            |  | $C_3S$                                      | $C_2S$ | $C_3A$ | $C_4AF$ |
| 10 (Normal)                | General use                                      | 54  | 18     | 10     | 8       |
| 20 (Moderate)              | Moderate sulphate attack, early formwork removal | 55  | 19     | 6      | 11      |
| 30 (High strength)         | Shorter curing time                              | 55  | 17     | 9      | 8       |
| 40 (Low-heat of hydration) | Massive concrete structures                      | 42  | 32     | 4      | 15      |
| 50 (Sulphate resistance)   | Severe sulphate attack                           | 54  | 22     | 4      | 13      |

### 2.1.2. Hydration of cement

The chemical reaction between cement and water is called hydration. In this process, the two calcium silicates,  $C_3S$  and  $C_2S$ , which constitute about 75% of the mass of Portland cement, react with water and form calcium silicate hydrate (C-S-H) and calcium hydroxide (CH). Hydrated Portland cement contains about 50% C-S-H and 15% to 25% CH. The strength of hydrated cement is due to C-S-H while CH controls the pH of the pore solution. The added gypsum reacts with  $C_3A$  and forms ettringite. In addition to controlling the setting time, the sulphate also helps control the drying shrinkage and can influence strength [5]. Table 2.4, shows the summary of the hydration reactions of Portland cement.

Table 2. 4. Portland cement compound hydration reaction [5].

|         |   |                       |   |
|---------|---|-----------------------|---|
| $2C_3S$ | + 11H <sub>2</sub> O                                    |                       | = C-S-H + CH  |
| $2C_2S$ | + 9 H <sub>2</sub> O                                    |                       | = C-S-H + CH  |
| $C_3A$  | + 3 CaO.SO <sub>3</sub> .2 H <sub>2</sub> O<br>(Gypsum) | + 26 H <sub>2</sub> O | = 6CaO.Al <sub>2</sub> O <sub>3</sub> .3SO <sub>3</sub> .32 H <sub>2</sub> O<br>(Ettringite)                                  |
| $2C_3A$ | + Ettringite  | + 4 H <sub>2</sub> O  | = 3 (4CaO.Al <sub>2</sub> O <sub>3</sub> .SO <sub>3</sub> .12H <sub>2</sub> O)<br>(Calcium Monosulphoaluminate)               |
| $C_3A$  | + CH  | + 12 H <sub>2</sub> O | = 4CaO.Al <sub>2</sub> O <sub>3</sub> .13H <sub>2</sub> O<br>(Tetracalcium aluminate hydrate)                                 |
| $C_4AF$ | + 10 H <sub>2</sub> O                                   | + CH                  | = 6CaO.Al <sub>2</sub> O <sub>3</sub> .Fe <sub>2</sub> O <sub>3</sub> .12H <sub>2</sub> O<br>(Calcium aluminoferrite hydrate) |

Figure 2.1 shows the relative volume of the major compounds in the hydrated Portland cement paste as a function of time and degree of hydration.

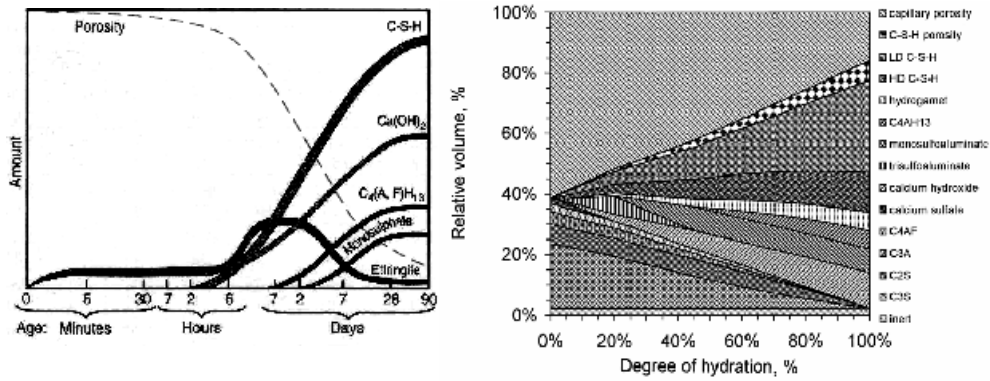
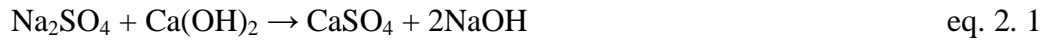


Figure 2. 1. Relative volume of the major compounds in the microstructure of hydrating Portland cement paste (left) as a function of time and (right) as a function of the degree of hydration for  $w/c=0.5$  [6, 7].

As shown in Table 2.4, one of the of hydration reactions is calcium hydroxide (CH). Some of CH reacts with sodium and potassium salts (minor components in Table 2.2) and forms very soluble potassium and sodium hydroxide.



These hydroxide compounds (potassium, sodium and calcium hydroxide) are found in the solution in the pores in the cement paste phase of the concrete, commonly called pore solution, and they are responsible for high alkaline environment in concrete. Table 2.5 shows the typical composition of pore solution [8].

Table 2. 5. Typical composition of pore solution from concrete made of OPC (w/c=0.5) [8].

| <b>Compound</b>              | <b>Pore Water (mol/litre)</b> |
|------------------------------|-------------------------------|
| Na <sup>+</sup>              | 0.3                           |
| K <sup>+</sup>               | 0.6                           |
| Ca <sup>++</sup>             | 0.002                         |
| OH <sup>-</sup>              | 0.85                          |
| SO <sub>4</sub> <sup>-</sup> | 0.03                          |
| pH (calculated)              | 13.9                          |

### 2.1.3. Curing of concrete

In order to obtain a good quality concrete, it should be cured in suitable environment during the early stages of hardening. Curing describes the procedures used to help the hydration of cement. It consists of controlling the temperature and the moisture movement from and into the concrete. The objective of curing is to keep concrete saturated or as nearly saturated as possible. It helps the originally water-filled space in the fresh cement paste to be filled out to the appropriate extent by the products of hydration of cement [3]. The hydration of cement occurs in capillaries which are filled with water. By evaporation of this water, the hydration rate would be decreased or stopped. Therefore, in fresh concrete while the hydration process is in its early stage, this evaporation should be prevented. In addition, during hydration, some internal water would be consumed and should be replaced from outside. So, better curing means more hydration reaction and this gives higher strength to the concrete. Figure 2.7 shows the influence of wet curing on the strength of concrete.

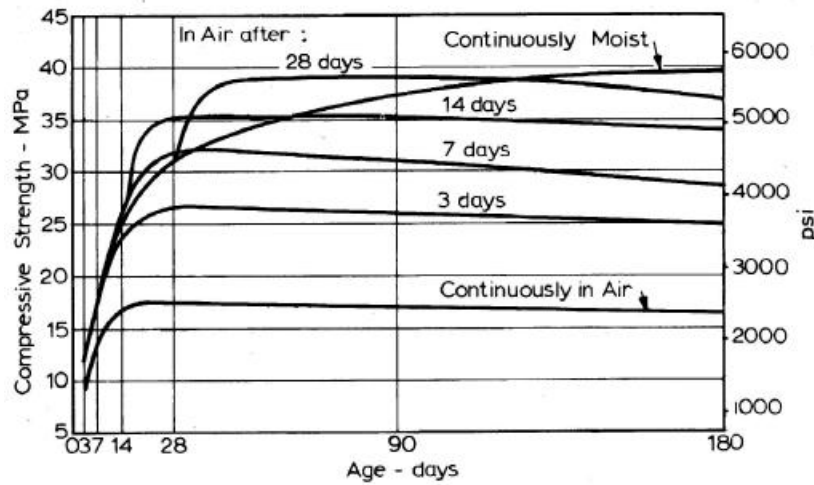


Figure 2. 2. Influence of moist curing on the strength of concrete with a water/cement ration of 0.5 [9].

## 2.2. CORROSION OF STEEL IN CONCRETE

Concrete gives corrosion resistance to steel reinforcement because it provides both a physical barrier and chemical protection. Steel is thermodynamically unstable in atmosphere and tends to revert to a lower energy state such as an oxide or hydroxide by reaction with oxygen and water. Concrete that is not exposed to any external influences usually has a pH between 12.5 and 13.5 [10]. As shown in the Pourbaix diagram (Figure 2.3), which defines the range of electrochemical potential and pH, for H<sub>2</sub>O-Fe system in the alkaline environment and at the potentials normally existing in the concrete, a protective passive layer forms on the surface of steel. This layer is an ultra-thin (<10nm), protective oxide or hydroxide film that decreases the anodic dissolution rate to negligible levels [11-14]. Formation of passive film on iron begins with dissolution of the metal which produces electrons and the reduction of oxygen that uses

those electrons. The ferrous ions from the anodic dissolution of iron are attracted to the cathodic part of the steel and combined with hydroxide ions from the cathodic reaction of oxygen and form the ferrous hydroxide. If this film exposed to the oxygen, other passive oxide layers such as  $\text{Fe}_3\text{O}_4$  or  $\text{Fe}_2\text{O}_3$  may form on the outer surface of the film. Therefore, the passive film can be consisted of layers of ion hydroxide or oxides based on different oxygen content [15-17].

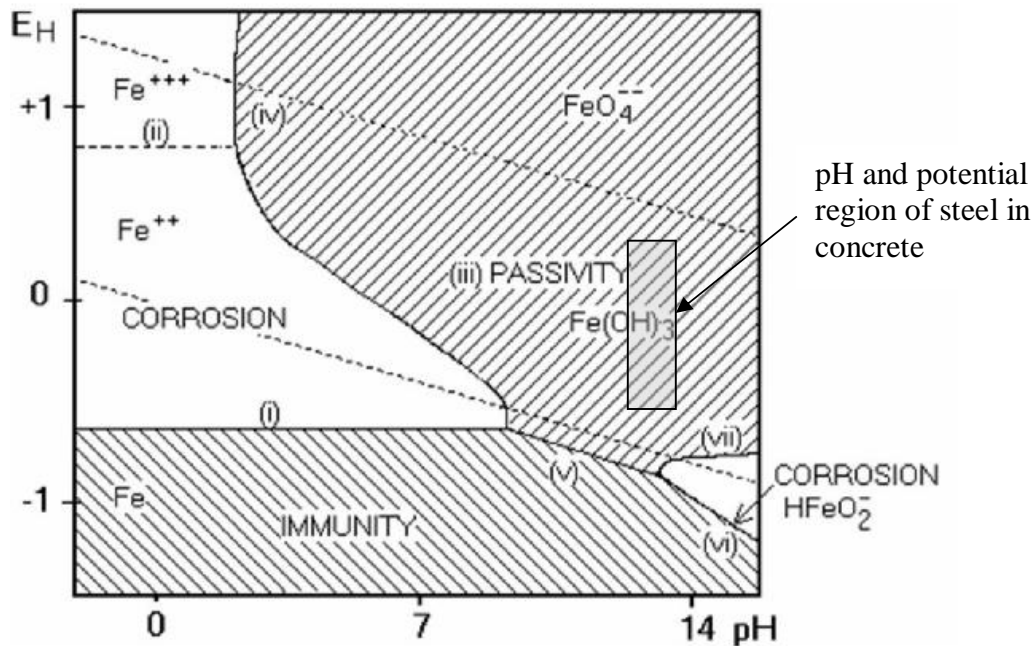


Figure 2. 3. Pourbaix diagram for Fe-H<sub>2</sub>O at 25°C [18].

The protective nature of this layer can be reduced and the result would be active corrosion of steel in concrete. Chloride ions, mostly from de-icing salts or seawater, and carbon dioxide, from atmosphere, are two major factors that can break the passive film on the surface of steel and initiate corrosion and the mechanism will be discussed in the next sections. Insufficient oxygen to preserve the passive film, galvanic cell formation from the contact of different metals and

stray currents are the other factors that may cause active corrosion in reinforcing steel structures which are not discussed in this literature review.

### **2.2.1. Reinforcing steel passivation time**

As mentioned in Table 2.5, Portland cement concrete pore solution mainly consists of saturated  $\text{Ca}(\text{OH})_2$  (pH=12.6), but presence of NaOH and KOH increases the pH to more than 13. Under normal field conditions, in which reinforcing steel is embedded in the concrete for many years before chlorides penetrate the cover, this high alkalinity allows the steel to develop a stable passive film. In laboratory studies, however, the steel is not generally given much time to passivate. Indeed, there are many studies in which steel is embedded in concrete with admixed chlorides or exposed to synthetic pores solution containing chlorides and, therefore, never has a chance to passivate. While, there are many studies concerning the nature and the composition of the passive film in pore solution and concrete [17, 19], there does not appear to have been any investigation of the time required for steel to be passivated in concrete or in pore solution. This is particularly critical when the study is being done in pore solution and there is an increasing tendency for such studies in order to obtain results in shorter period of time. In a number of these studies, [20-23] it appears that insufficient time was provided for passivation before the steel was exposed to chlorides and, in some case the chloride was added to the pore solution at the beginning of the experiment. Because of these unrealistic conditions, the application of such results, for example, to the prediction of the corrosion behaviour of steel in structures may be misleading. Therefore, the time required for deformed black steel reinforcing bar to be passivated in mortar and in synthetic pore solution has been determined. The passivation time

was measured for specimens in the as-received condition (with the mill scale intact) and specimens of the same bar after removal of the mill scale by sandblasting. Potentiostatic LPR and half-cell potential techniques were used to determine the time required for passivation. The surface condition of the steel bars, after immersion in pore solution, was studied by Raman spectroscopy. Results are given in Chapter 4.

### **2.2.1.1. Raman spectroscopy**

Raman scattering is a powerful light scattering technique used to identify the internal structure of molecules and crystals. This technique is based on Raman effect named for Sir Chandrasekhara Venkata Raman, who discovered it in 1928 [24]. When light is scattered from a molecule most photons are elastically scattered. The scattered photons have the same energy (frequency) and, therefore, wavelength, as the incident photons. However, a small fraction of light is scattered at optical frequencies different from the frequency of the incident photons. This is called the Raman effect. The difference in energy between the incident photon and the Raman scattered photon, which is called the Raman shift, is equal to the energy of a vibration of the scattering molecule or crystal. A plot of intensity of scattered light versus energy difference is a Raman spectrum. Typically, a sample is illuminated with a laser beam. Light from the illuminated spot is collected with a lens and sent through a monochromator. Wavelengths close to the laser line are filtered out and those in a certain spectral window away from the laser line are dispersed onto a detector.



### 2.2.2. Chloride induced corrosion

Chloride ions can be present in the concrete due to the use of chloride contaminated components or the use of  $\text{CaCl}_2$  as an accelerator when mixing the concrete, or by diffusion into the concrete from the outside environment [25]. Use of de-icing salts during the winter time is the largest source of chlorides in Ontario.

A localised breakdown of the passive layer occurs when sufficient amount of chlorides reach reinforcing bars, and the corrosion process is then initiated. Chlorides in concrete can be either dissolved in the pore solution (free chlorides) or chemically and physically bound to the cement hydrates and their surfaces (bound chlorides). Only the free chlorides dissolved in the pore solution are responsible for initiating the process of corrosion [26].

There are three theories about the chloride attack [27]:

1. Penetration of chloride ions to the oxide film on steel through pores or defects in the film is easier than the penetration of other ions.
2. Chloride ions are adsorbed on the metal surface in competition with dissolved  $\text{O}_2$  or hydroxyl ions.
3. Chloride ions compete with hydroxyl ions for the ferrous ions produced by corrosion and a soluble complex of iron chloride forms which can diffuse away from the anode, destroying the protective layer of  $\text{Fe}(\text{OH})_2$  permitting corrosion to continue.

### **2.2.2. Carbonation induced corrosion**

When concrete is exposed to air, the calcium hydroxide reacts with water and carbon dioxide in the air:



The effect of carbonation is to reduce the pH value of the surface layer of the concrete to less than 8.3. This pH is sufficient to make the passive layer on the reinforcement rebar, unstable [28]. The process of carbonation can be summarised in the following steps:

1. CO<sub>2</sub> diffuses into concrete.
2. In the presence of moisture, it reacts with CH (Calcium Hydroxide).
3. The pH decreases from about 12.6 to 8.3.
4. In this pH, steel is not passive.

#### **2.2.2.1. Carbonation depth measurement**

Carbonation depth is the average distance, from the surface of concrete or mortar where the carbon dioxide has reduced the alkalinity of the hydrated cement [29]. Depending on the concrete quality and curing condition, the carbonation depth is different. The depth of carbonation can be determined by different techniques. Microscopic observation of CaCO<sub>3</sub>,

which is the main chemical product of carbonation, in one of the techniques that can be used for this purpose [30]. As mentioned before, carbonation reduces the pH, therefore examination the internal pH of concrete by applying pH sensitive liquid indicators such as phenolphthalein to a freshly fractured or freshly cut surface of concrete can be used to estimate the depth of carbonation. Upon application of phenolphthalein, noncarbonated areas turn red or purple while carbonated areas remain colourless. Maximum colour change to deep purplish red occurs at pH of 9.8 or higher. Below 9.8 the colour may be pink and at pH of 8, colourless [31]. The Rainbow Indicator® [32] is a combination of specific chemicals which produce a range of colour based on the different pH when sprayed on a freshly broken concrete surface [33]. The manufacturer reported the following colours and detectable pH values as followings:

Table 2. 6. The pH is revealed by the following illustrated colours [32].

| Colour          | pH |
|-----------------|----|
| Red             | 5  |
| Yellow          | 7  |
| Green           | 9  |
| Purple          | 11 |
| Violet to black | 13 |

### 2.2.3. The influence of concrete parameters on rebar corrosion

As described, chloride ions or carbon dioxide penetrate the concrete cover depth to reach the surface of the reinforcing steel by a number of mechanisms. The surface of the concrete may be dry, allowing the dissolved chlorides or carbon dioxide to be absorbed by capillary action together with moisture through the interconnected pores in the cement paste. At deeper levels, concrete rarely dries out in the atmosphere [34] and so continued penetration of

the aggressive ions is by diffusion through the pores, which is a much slower process than absorption.

Porosity in cement paste consists of capillary pores, gel pores and calcium silicate hydrate (C-S-H) interlayers [35]. Capillary pores are the remains of originally water-containing spaces between cement particles that have not been filled up by products of hydration [36]. They are the largest (diameter > 5 nm [37]), and their number and interconnectivity control the ingress of chloride ions, carbon dioxide, oxygen and moisture into concrete [38]. Gel pores and interlayer spaces are believed to be too small and disconnected to contribute to transport. Two factors that significantly influence capillary porosity in concrete are the water to binder (w/b) ratio [39] and the use of supplementary cementing materials (SCMs) [40]. Theoretically, a w/b ratio of 0.42 is required for the complete hydration of cement. However, hydration is a gradual process and the unused mixing water is retained in the capillary pores [41]. Higher w/b ratios, traditionally used to give a workable mixture, increase the amount and interconnectivity of capillary porosity in the cement paste allowing greater diffusion. With the advent of high range water reducing agents, much lower w/b ratios are now possible and significantly limit the penetration of chloride ions and carbon dioxide.

There other factors that can affect the diffusion of the chloride ions and carbon dioxide [31]:

- Inadequate cover provides shorter path for diffusion and is regularly associated with areas of high corrosion risk due to both carbonation and chloride ingress.

- Age of concrete is the other factor that affects the diffusion of aggressive ions. By passing time, the curing process continues and the diffusion becomes harder. In addition to that, diffusion is the function of time and its rate decrease with time.
- Curing is the other parameter that changes the diffusion of chloride ions and carbon dioxide into the concrete [42, 43]. Better curing causes lower permeability, better hydration, more CH and consequently, less carbonation and chloride diffusion.
- Temperature and relative humidity are the other factors that can affect diffusion of aggressive species into concrete [44-47]. Diffusion is a function of temperature. For carbonation, there is critical point which allows evaporation of the water, released by carbonation reactions, but does not dry out the concrete enough to stop the reaction. Relative humidity [48], wind and direction of sunlight, and the type environment (e.g. pollutant and costal regions) are the other effective factors.

#### **2.2.4. Mechanism of corrosion in reinforced concrete**

Corrosion is an electrochemical reaction which consists of anodic and cathodic half-cell reactions. Micro-cell corrosion is the term given to the situation where active dissolution and the corresponding cathodic half-cell reaction take place at adjacent parts of the same metal part. For a steel reinforcing bar (rebar) in concrete, this process always occurs in practice. The surface of the corroding steel can act as a mixed electrode containing both anode and cathode regions which are connected by the bulk steel. Macro-cells corrosion can also form on a single bar exposed to different environments within the concrete or where part of the bar extends outside

the concrete. In both cases, concrete pore solution functions as an electrolyte. Figure 2.4 shows a schematic illustration of corrosion in reinforcing concrete.

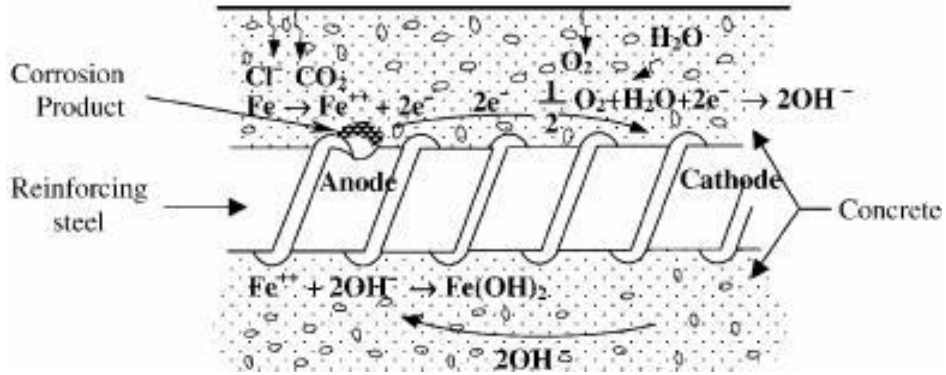


Figure 2. 4. Schematic illustration of the corrosion of reinforcement steel in concrete [49]

For steel embedded in concrete, based on the pH of the concrete (electrolyte) and presence of aggressive ions, the following would be the possible anodic reactions [10, 49]:



The possible cathodic reactions depend on the availability of  $\text{O}_2$  and on the pH near the steel surface. The most likely reactions are as follows [10, 49]:



The corrosion products occupy a greater volume than the steel itself, and this causes an internal expansion and stress. The stress can destroy the concrete and expose the steel to more aggressive factors. Figure 2.5 shows a schematic illustration of a damaged concrete by corrosion of reinforcement steel.

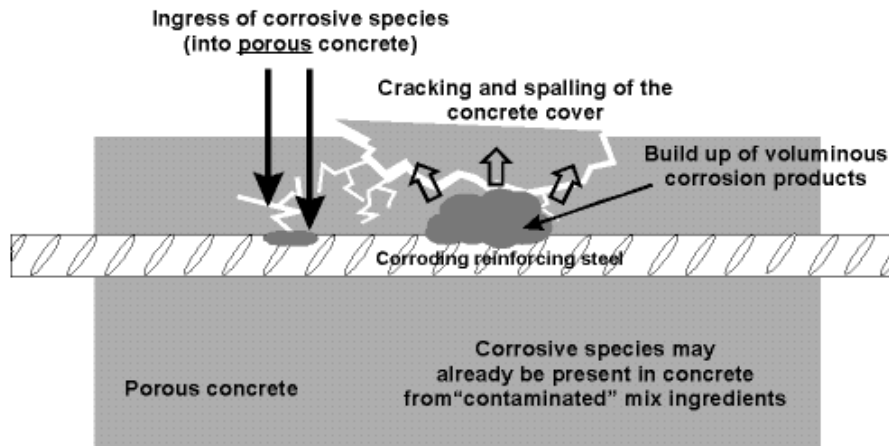


Figure 2. 5. Schematic diagram showing spalling of concrete due to corrosion damage [50].

### 2.3. CORROSION EVALUATION TECHNIQUES

As mentioned, corrosion consists of electrochemical reactions at the interface between the metal and an electrolyte solution. During the anodic reaction, a metal is oxidised and releases electrons. These electrons are consumed by the cathodic reaction in which the reduction occurs. By equating these two reactions, a corrosion current,  $I_{\text{corr}}$ , which is the absolute value of corrosion rate, and half-cell potential (also called corrosion potential or open circuit potential),  $E_{\text{corr}}$ , which is the probability of corrosion, can be found.

$E_{\text{corr}}$  is equivalent to the voltage of a cell or battery versus a reference electrode under no-load conditions and can be measured with a high impedance voltmeter or potentiometer [51, 52].

However,  $I_{\text{corr}}$  cannot be measured directly but it can be estimated by using electrochemical techniques while  $E_{\text{corr}}$  must be determined as the potential difference between that of the metal surface and a reference electrode.

As mentioned, corrosion occurs via electrochemical reactions. Therefore, electrochemical techniques are ideal for the study of the corrosion processes. Usually, in electrochemical measurements, a cell consists of a working electrode (the corroding metal), a counter electrode, a reference electrode and electrolyte. All of the electrodes are connected to a potentiostat (Appendix A) which allows the potential of the metal to be changed in a controlled manner and the resultant current flow to be measured as a function of potential. This changing of the potential is called “polarisation”. When the polarisation is done potentiostatically (controlled by potential), the current is measured, and when it is done galvanostatically (controlled by current), the potential is measured [53-55].

### **2.3.1. Half-cell potential technique**

The half-cell potential technique is the most widely used technique of corrosion measurement of the steel rebars in concrete. It was introduced in the 1970s by Richard F. Stratfull in North America and by the Danish Corrosion Centre in Europe [56-58]. In 1980, the test was approved as a standard by ASTM: C 876 “Standard Test Method for Half-cell Potentials of Uncoated Reinforcing Steel in Concrete”. This technique is based on measuring the electrochemical potential of the steel rebar with respect to a standard reference electrode placed



on the surface of the concrete and can provide an indication of the corrosion risk of the steel. The suggested reference electrode by ASTM is a copper/copper sulphate electrode (CSE). A wet sponge should be placed between the electrode and the concrete to provide a low electrical resistance i.e. good contact between the electrode and the concrete. Figure 2.6, shows the basics of half-cell potential measurement.

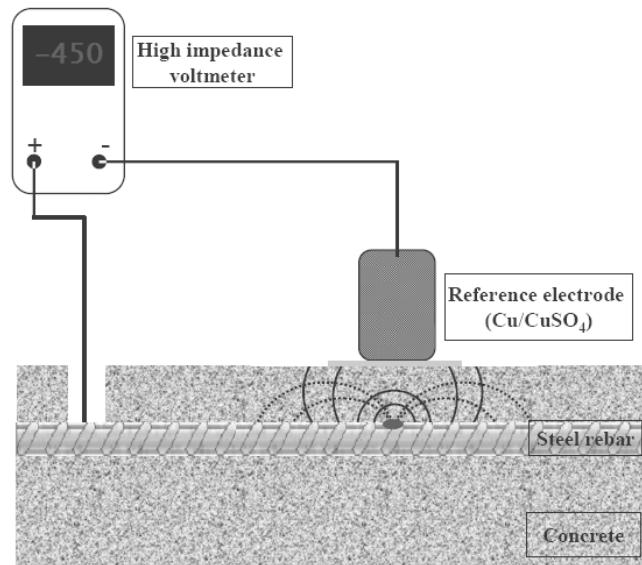


Figure 2. 6. Apparatus for half-cell potential method described in ASTM C 876 to measure surface potential associated with corrosion current.

According to the ASTM Standard, the recommended guidelines for interpretation are as follows:

Table 2. 7. Probability of corrosion according to half-cell potential reading [59].

| Half-cell potential reading vs. Cu/CuSO <sub>4</sub> | Corrosion activity                   |
|--|--------------------------------------|
| More positive than -200 mV                           | 90% probability of no corrosion      |
| Between -200 and -350 mV                             | An increase probability of corrosion |
| More negative than -350 mV                           | 90% probability of corrosion         |

The most common way of presenting the half-cell potential data is plotting the potential distribution or potential mapping contour as shown in Figure 2.7.

|              |          |
|--------------|----------|
| -200 to -349 | Yellow   |
| -350 to -499 | Red      |
| -500         | Dark Red |



Figure 2. 7. Half-cell potential contour map, measured by CSE; Lower Elk Creek Bridge #2531, British Columbia [60].

### 2.3.1.1. Interpretation difficulties with half-cell potential technique

Since half-cell potential value is defined as the thermodynamic measure of the ease of removing electrons from the metal in steady state condition, it can not be used as direct measurement of corrosion rate. It should be noted that half-cell potential is the probability of corrosion activity while  $i_{\text{corr}}$  is the direct measurement of corrosion rate.

The measured half-cell potentials can be affected by several factors which should be considered in their interpretation.

Steel in concrete has active-passive corrosion behaviour. Figure 2.8 shows typical active-passive corrosion behaviour [54]. The half-cell potential,  $E_{\text{corr}}$ , and corrosion current density,  $i_{\text{corr}}$ , are the values of potential and current at the intersections of the anodic and cathodic reaction

lines. Figure 2.9 shows experimental curves obtained potentiostatically for steel in OPC [10]. It should be noted that the curves in Figure 2.9 are the net current density which is  $i_{net} = i_{anodic} - i_{cathodic}$  in the anodic part and  $i_{net} = i_{cathodic} - i_{anodic}$  in the cathodic part.

This means that, at more negative potentials, the corrosion rate which is measured by corrosion current density is high and increases with potential in the active state. At potential more positive than a certain value (primary passive potential,  $E_{pp}$ ) the passive film becomes stable and the corrosion rate falls to very low values in the passive state. By increasing the potential further to more positive values, the passive film eventually breaks down and the anodic rate increases in the transpassive state.

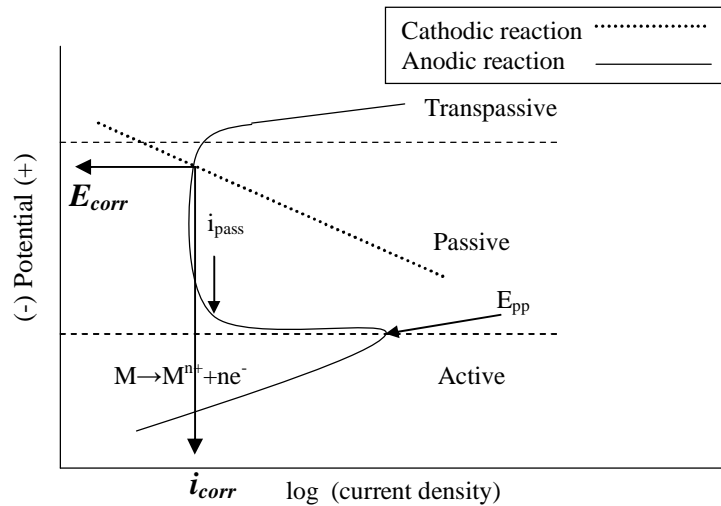


Figure 2. 8. Schematic active-passive corrosion behaviour [54].

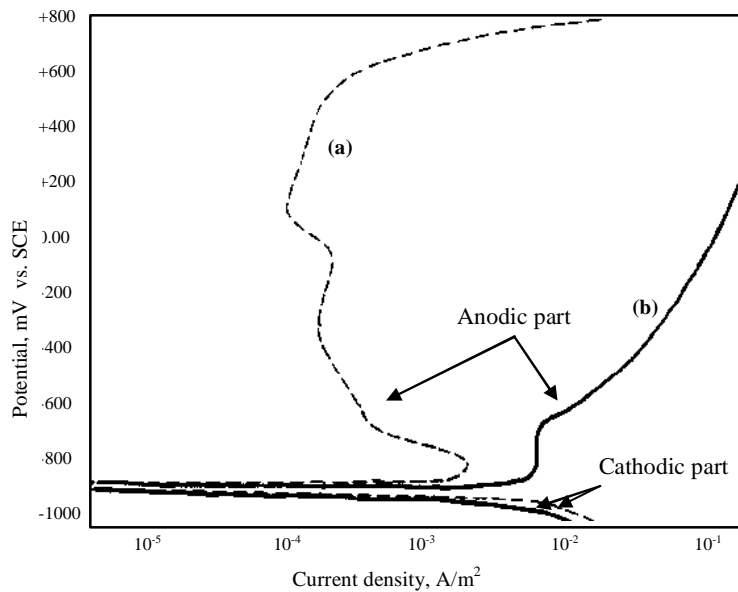


Figure 2. 9. Experimental potentiostatic polarisation curves for steel in OPC mortar ( $w/c = 0.5$ ) at  $22\text{ }^{\circ}\text{C}$ . Curve (a) is for passivated steel and curve (b) for corroding steel due to chloride ion attack [10].

In concrete, the anodic reaction is oxidation of iron, eqs. 2.4 to 2.7, and the cathodic reaction is normally reduction of oxygen, eq. 2.8. These two reaction rates must be equal and where the cathodic and anodic lines intersect in Figure 2.8 and 2.10, gives the value of half-cell potential and corrosion current. The following circumstances may occur in concrete:

1. When the steel is in its passive state, Figure 2.10(a), the corrosion current is low and the half-cell potential more positive.
2. If the passive film breaks down, the corrosion current will increase and the potential will become more negative compared with (1) (Figure 2.10(b)). This is the principal on which ASTM recommendations are based.

3. If access to oxygen increases (for example by cracking of the concrete cover), the cathodic reaction line moves to more positive potentials and the new line intercepts the anodic curve at point 3, instead of point 2 (Figure 2.10 (c)). While  $i_2 < i_3$ , the potential value for point 2 is more negative than point 3 which is opposite of ASTM recommended guidelines.
4. If the position of the cathodic line changes to more negative potentials (as an example: a decrease in the concentration of oxygen) the new cathodic line intercepts the anodic curve at point 3, instead of point 2 (Figure 2.10(d)). Comparing points 2 and 3 shows that  $i_2 > i_3$  while  $E_3$  is more negative than  $E_2$  which appear to be in contradiction with ASTM recommended interpretations.

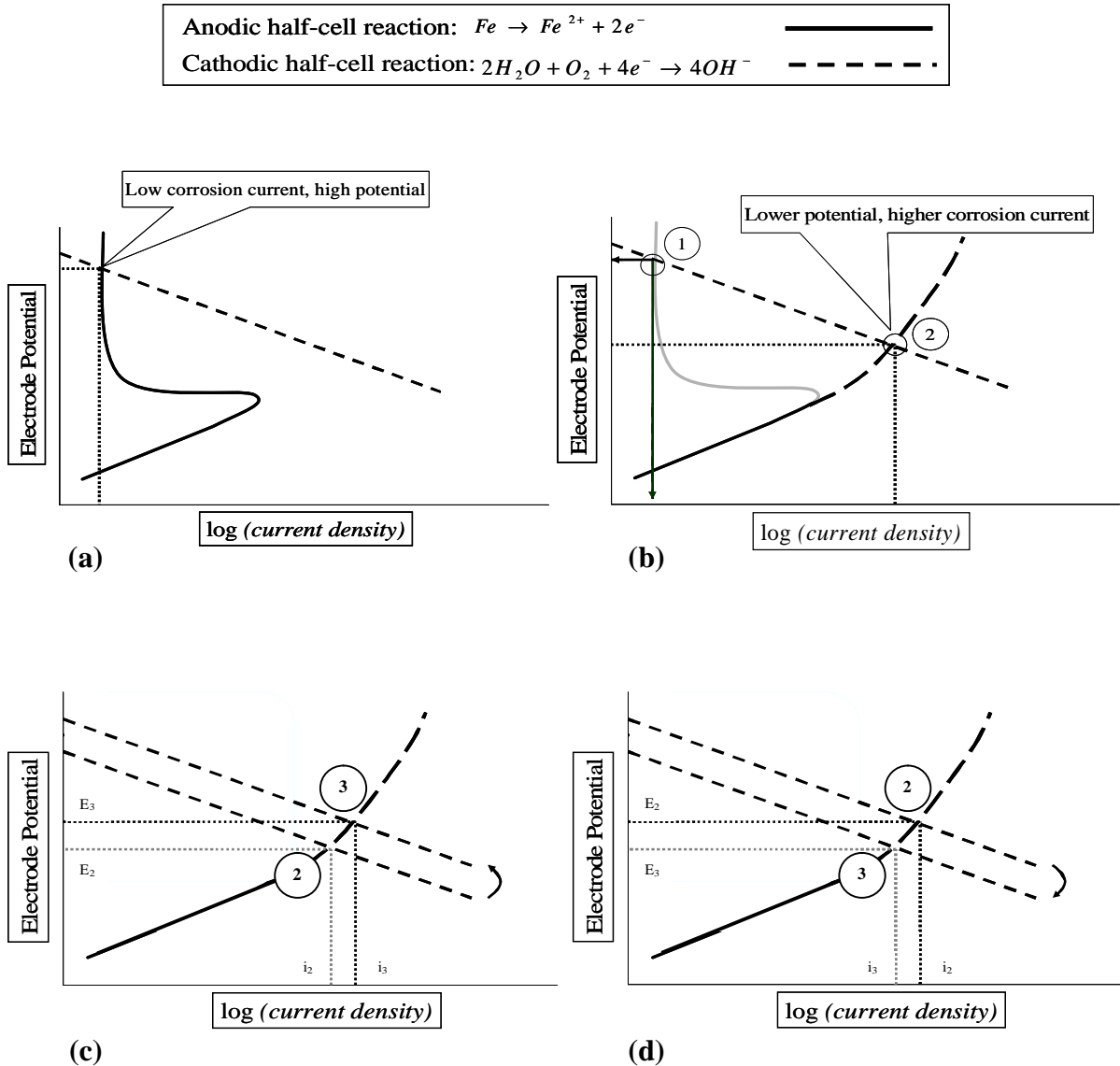


Figure 2. 10. Anodic and cathodic reactions and their variations in concrete.

Therefore, a simple comparison of the half-cell potential data with the ASTM guidelines on steel reinforcement corrosion probability could cause mistakes in the evaluation of the structure. It has been accepted by the people who work in the field that a more negative reading of potential means a higher probability of corrosion. But as explained above, this general rule may not always be correct. Some precautions are necessary in interpreting the data from half-cell potential measurements because there are many factors that may affect the magnitude of the potentials. For example, a surface layer with high resistance gives less negative surface potential which may cover underlying corrosion activity [52]. On the other hand, cathodic polarisation due to the lack of oxygen results in more negative potentials while the corrosion rate is reduced [61]. Soleymani et al. [62], mentioned that very high moisture content can decrease the half-cell potential to -1000 mV vs. CSE, while corrosion does not exit at all. Feliu et al. [63], found that generally there is a poor correlation between half-cell potential values and corrosion current density measured by polarisation resistance method (Figure 2.11).

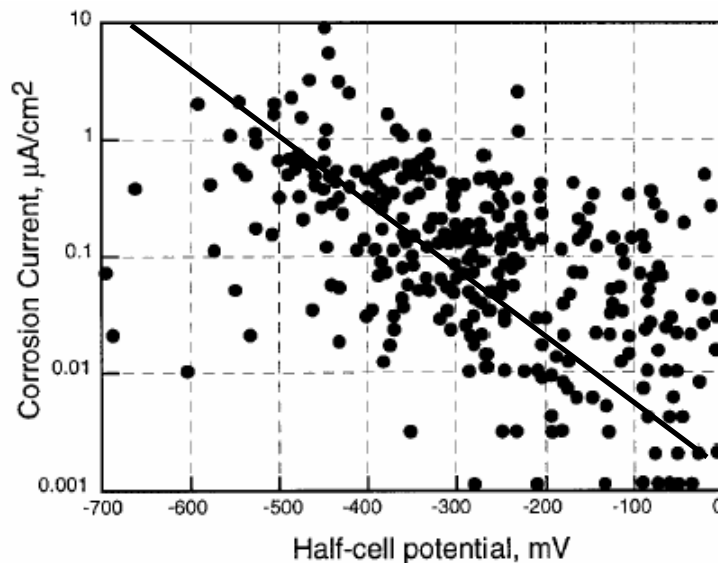


Figure 2. 11. Comparison of corrosion current with half-cell potential [63].

Gu and Beaudoin [61], reviewed and summarised some factors that may affect half-cell potential readings and the results are shown in Table 2.8.

Table 2. 8. Effect of the various factors on half-cell potential shift and corrosion probability [61].

| <b>Situation</b>                   | <b>Half-cell potential shift</b>          | <b>Corrosion of steel reinforcement</b> | <b>Applicable to ASTM C876</b> |
|------------------------------------|---|---|--------------------------------|
| Decrease in oxygen concentration   | to negative                               | may not increase                        | no                             |
| Carbonation/decrease in pH         | to negative                               | increase                                | yes                            |
| Increase in chloride concentration | to negative                               | increase                                | yes                            |
| Anodic corrosion inhibitor         | to positive                               | decrease                                | yes                            |
| Cathodic corrosion inhibitor       | to negative                               | decrease                                | no                             |
| Mixed corrosion inhibitor          | to positive or negative                   | decrease                                | no                             |
| Epoxy-coated rebar                 | to positive                               | not related                             | no                             |
| Galvanized rebar                   | to negative                               | not related                             | no                             |
| Dense concrete cover               | to negative                               | not related                             | no                             |
| Concrete resistance                | to positive                               | not related                             | no                             |
| Dry concrete                       | to positive                               | not related                             | no                             |
| Reference electrode position       | to positive                               | not related                             | no                             |
| Coatings and sealers               | to positive                               | not related                             | no                             |
| Concrete repair patch              | to positive or negative                   | not related                             | no                             |
| Cathodic protection                | to negative                               | not related                             | no                             |
| Stray current                      | Fluctuating between positive and negative | not related                             | no                             |

On the other hand, other results have been in agreement with the ASTM interpretation. For example, Kliethermes [64] reported the results of the inspection of 120 exposed concrete decks from 33 states in US. He found that, for bridges in good condition, 90% of all potential readings were more positive than -0.22 volts vs. Saturated Calomel Electrode (SCE) (-294 mV vs. Cu/CuSO<sub>4</sub>). Also, he reported that for bridge decks in poor condition, i.e., spalled and cracked, the 100 % of the potential readings were more negative than -0.32 volts vs. SCE. (-394



mV vs. Cu/CuSO<sub>4</sub>). Novokshchenov [65], found good correlation between results of the potential survey on pre-stressed bridge girders using a copper-copper sulphate half-cell and other corrosion detection methods, including the visual inspection, concrete cover survey, rapid chloride permeability test, and determination of the amount of Cl<sup>-</sup> at the level of the tendons. Romagnoli et al.[66] measured the half-cell potential values of steel in mortar with different w/c ratios and related the measured values to the rebar surface condition through Scanning Electron Microscopy (SEM) and they found that SEM observations confirms the ASTM guidelines. Moreover, in contrast to observations of Browne et al. [67] and Elsener and Bohni [68], Cairns and Melville [69], surprisingly reported that half-cell potential measurements using the high impedance equipment were not affected by the presence of a surface treatment (such as waterproof membrane) and it remains a valid method for the detection of corrosion activity in reinforced concrete even where the concrete is coated; on the other hand they found that the presence of surface coatings in concrete have a significant influence on measured corrosion rate determined by the linear polarisation resistance technique (describe in the next section).

This difference between results emphasises the need of more in-depth study about half-cell potential and other corrosion measurements techniques used in concrete structures.

As mentioned above, many factors including those listed in Table 2.8, can shift the half-cell potential readings to more positive or negative values, but this may not be related to the severity or extent of the corrosion of the steel bars. On the basis of this literature review and the observations of the current project, carbonation depth, chloride concentration and gradient, quality of concrete, concrete resistivity, cover depth, cracks, ambient conditions and oxygen concentration are the most important factors that are predicted to affect the half-cell potential readings.

### 2.3.2. Linear Polarisation Resistance (LPR)

Figure 2.12 shows a schematic plot of the relationship between potential and current in the region of the open circuit potential. The curve plots the applied potential versus measured current or vice versa. As shown in Figure 2.12, there is an approximately linear region in the region of the open circuit potential. LPR measurements are performed by applying a potential in the range of  $\pm 20\text{mV}$  about the  $E_{\text{corr}}$ , either as a constant pulse (potentiostatic) or a potential sweep (potentiodynamic) and measuring the current response. Alternatively, a current pulse (galvanostatic) or a current sweep (galvanodynamic) can be applied, and potential response is measured. Polarisation resistance ( $R_p$ ) is the resistance of the specimen to oxidation while an external potential is applied and the corrosion rate which is inversely related to the  $R_p$  can be calculated from it [70].

$R_p$  is determined by calculating the slope of this linear region:

$$R_p = \frac{\Delta E}{\Delta I} \qquad \text{eq. 2. 10}$$

where,  $\Delta E$  = change in potential and  $\Delta I$  = change in current.

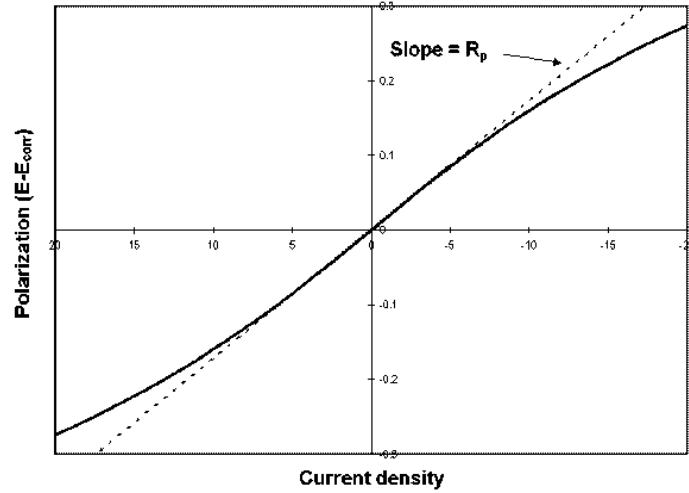


Figure 2. 12. Linear polarisation curve [51].

The Stern-Geary equation relates corrosion current to  $R_p$  [71]:

$$I_{\text{corr}} = \frac{B}{R_p} \quad \text{eq. 2. 11}$$

$$B = \frac{\beta_a \beta_c}{2.3(\beta_a + \beta_c)} \quad \text{eq. 2. 12}$$

B is Stern-Geary constant and  $\beta_a$  and  $\beta_c$  are anodic and cathodic Tafel constants, respectively. The value of B is empirically determined and has been measured as 0.026V for active and 0.052V for passive corrosion of steel in concrete [72, 73]. These values are used in the calculations for corrosion of steel in concrete for many years without questioning them. In this project, the value of B was calculated and the results are given in chapter 4.

The resistance measured by LPR is actually is the sum of the polarisation resistance,  $R_p$ , and the electrolyte resistance,  $R_\Omega$ . Normally,  $R_p \gg R_\Omega$  and the resistance which is measured by LPR is close enough to the polarisation resistance that can be used as the actual value. However, in some environments with low conductivity, and/or high corrosion rates, the  $R_\Omega$  is significant and should be considered [54].

The corrosion current density,  $i_{\text{corr}}$ , can be calculated by dividing the corrosion current ( $I_{\text{corr}}$ ) by the surface area of the polarised area (A):

$$i_{\text{corr}} = \frac{B}{R_p A} \quad \text{eq. 2. 13}$$

The relationship between  $I_{\text{corr}}$  and m, mass reacted, in an electrochemical reaction is given by Faraday's law:

$$m = \frac{I_{\text{corr}} \times t \times a}{n \times F} \quad \text{eq. 2. 14}$$

where:

m = mass (g)

t = time (seconds)

a = atomic weight (g/mol)

n = number of equivalents exchanged

F = Faraday's constant (96500 coulomb/equivalent)

The penetration depth (d) can be calculated by dividing m by density and the corroding area:

$$d = \frac{m}{\rho A} \quad \text{eq. 2. 15}$$

For iron,  $a = 55.845 \text{ g/mol}$ ,  $\rho = 7875 \text{ kg/m}^3 = 7.875 \text{ g/cm}^3$ , and  $n = 2$ , therefore:

$$\text{Corrosion rate (in } \mu\text{m/year)} = 11.6 i_{\text{corr}} \text{ (in } \mu\text{A/cm}^2\text{)} \quad \text{eq. 2. 16}$$

According to some researchers, corrosion current densities over  $\sim 1 \mu\text{A/cm}^2$  are identified as the level of high corrosion risk and corrosion current density below  $0.1 \mu\text{A/cm}^2$  are characterised as passive corrosion in the system [74-76]. However, it seems that the equipment used by these researchers generally gives lower values than the other commercial equipment [77]. Therefore, applying such definitions may over or under-estimate the corrosion rate and cause errors in evaluations and life predictions.

Interpreting the corrosion current density values of embedded steel bars in concrete, obtained from the LPR technique is difficult in large part because determining the actual corroding area of steel is almost impossible and usually causes underestimation of the actual corrosion current density in the areas of active corrosion.

LPR has some advantages over the other measurement techniques which make it popular in the evaluation of the corrosion rate in reinforced concrete: it is a non-destructive technique; it is a simple method and it usually needs only a few minutes for corrosion rate determination. Because of its rapidity, it can effectively be used in kinetic studies of corrosion monitoring [54].

### 2.3.2.1. Potentiostatic LPR

In potentiostatic LPR technique, a constant potential signal (usually  $\pm 10\text{mV}$  or  $\pm 20\text{mV}$ ) is applied for a certain period of time, which is determined by time for current to reach steady state, in the form of square wave between the working electrode (steel bar in concrete) and reference electrode and the response current ( $\Delta I$  in Figure 2.13) is measured. By using eq. 2.10, the  $R_p$  and consequently, corrosion current density and corrosion rate can be calculated.

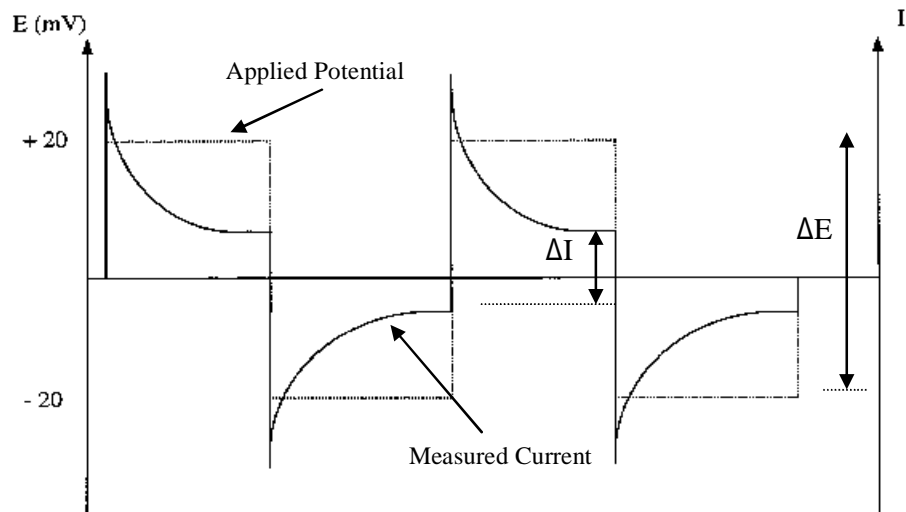


Figure 2. 13. Applied potential and current response during LPR measurement

### 2.3.2.2. Galvanostatic pulse technique

The galvanostatic pulse technique was introduced for field application in 1988 [78]. This method is a rapid non-destructive polarisation technique

A short-time anodic current pulse is applied galvanostatically between a counter electrode placed on the concrete surface and the rebar. The applied current is usually in the range of 10 to 100  $\mu\text{A}$  and the typical pulse duration is between 5 to 30 seconds. The reinforcement is anodically polarised and the resulting change of the electrochemical potential of the reinforcement is measured with a reference electrode, which is usually in the centre of the counter electrode and recorded as a function of polarisation time [79, 80]. Figure 2.14 shows a schematic setup for the test and a typical potential response for a corroding reinforcement is shown in the Figure 2.15.

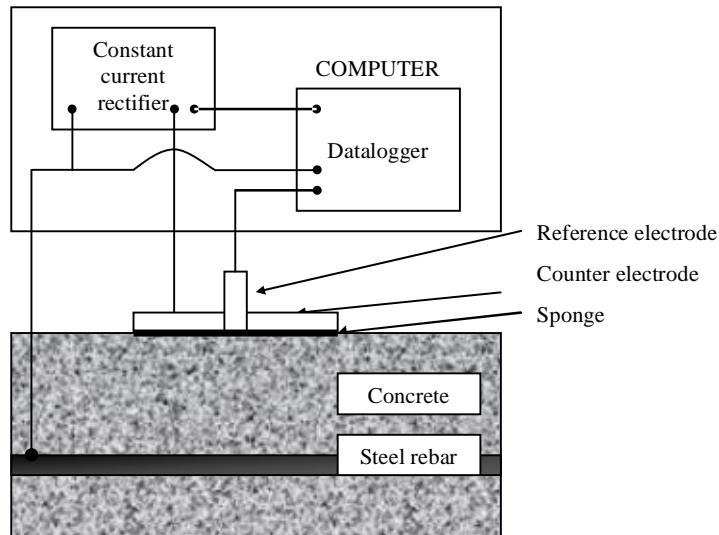


Figure 2. 14. Set up of the galvanostatic pulse technique (adapted from [80]).

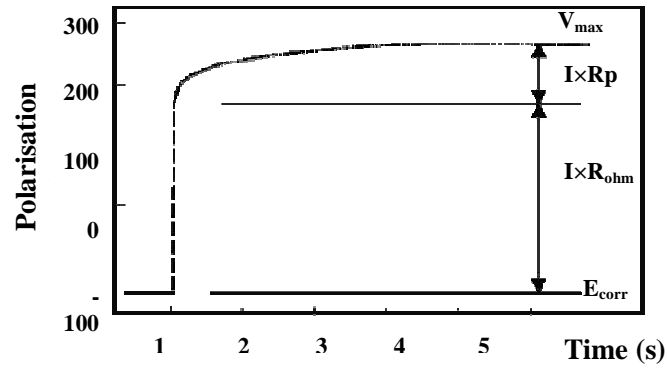


Figure 2. 15. Schematic illustration of galvanostatic pulse results [81].

When the constant current,  $I_{app}$ , is applied to the rebar, the polarisation of the rebar,  $\eta_t$ , at given time  $t$  can be expressed as [82]:

$$\eta_t = I_{app} \times \left[ R_p \times \left[ 1 - e^{\left( \frac{-t}{R_p C_{dl}} \right)} \right] + R_{\Omega} \right] \quad \text{eq. 2. 17}$$

where:

$R_p$  = polarisation resistance

$C_{dl}$  = double layer capacitance

$R_{\Omega}$  = ohmic resistance of the concrete cover

By transferring eq. 2.17 to logarithmic form, the values of  $R_p$  and  $C_{dl}$ , can be calculated as following [78]:



$$\ln(h_{\max} - h_t) = \ln(I_{\text{app}} \times R_p) - \left(\frac{t}{R_p C_{\text{dl}}}\right) \quad \text{eq. 2. 18}$$

where  $\eta_{\max}$  is the final steady state potential value. Figure 2.16 plots eq. 2. 18.

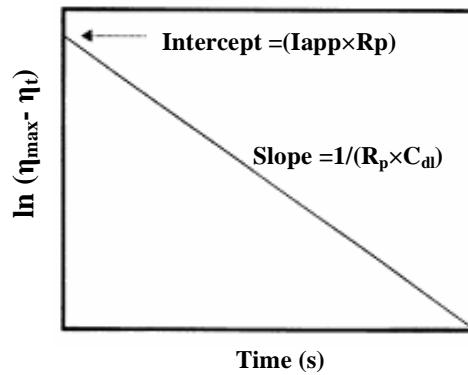


Figure 2. 16 Schematic illustration of eq. 2.18 [78].

If this straight line is extrapolated to  $t = 0$ , it will give an intercept of  $I_{\text{app}} \times R_p$  and the slope of the line in  $1/R_p C_{\text{dl}}$ . The remaining overpotential corresponds to  $I_{\text{app}} \times R_{\Omega}$  which is the ohmic voltage drop across the concrete cover. After determining the polarisation resistance ( $R_p$ ) by using the above method, the corrosion current  $I_{\text{corr}}$  can be calculated from Stern-Geary formula [71, 78]; eq. 2.11.

### 2.3.2.2.1. GalvaPulse™

The GalvaPulse™ system was developed by FORCE Technology in Denmark. It is based on the galvanostatic pulse technique and it is a non-destructive instrument for measuring the electrical resistance of the concrete, the half-cell potential, and corrosion rate of the steel rebars in concrete. The instrument consists of a handheld PSION computer which generates a small galvanostatic pulse. It also controls the pulse duration and processes the data. The measuring cell has a Ag/AgCl reference electrode at the centre with a zinc counter electrode and a zinc guard ring. Figure 2.17 shows a schematic illustration of the measuring cell.

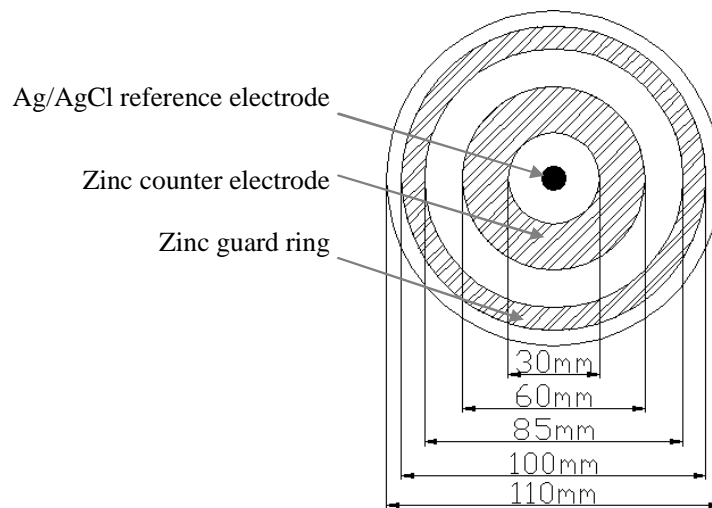


Figure 2. 17. Schematic plan of the GalvaPulse™ measurement cell.

As mentioned before, the actual polarised area of steel embedded in concrete is difficult to determine. In order to deal with the problem of confining the current to a predetermined area and to obtain a uniformly polarized area, the use of a second auxiliary guard ring electrode surrounding the inner auxiliary electrode has been developed [83-86]. The current applied from

the guard ring tends to repel the lines of current from the central counter electrode and confining them to an area of the structure located approximately under the counter electrode. Figure 2.18, shows the schematic plan of the measurement by the GalvaPulse™ using guard ring to confine the polarised area.

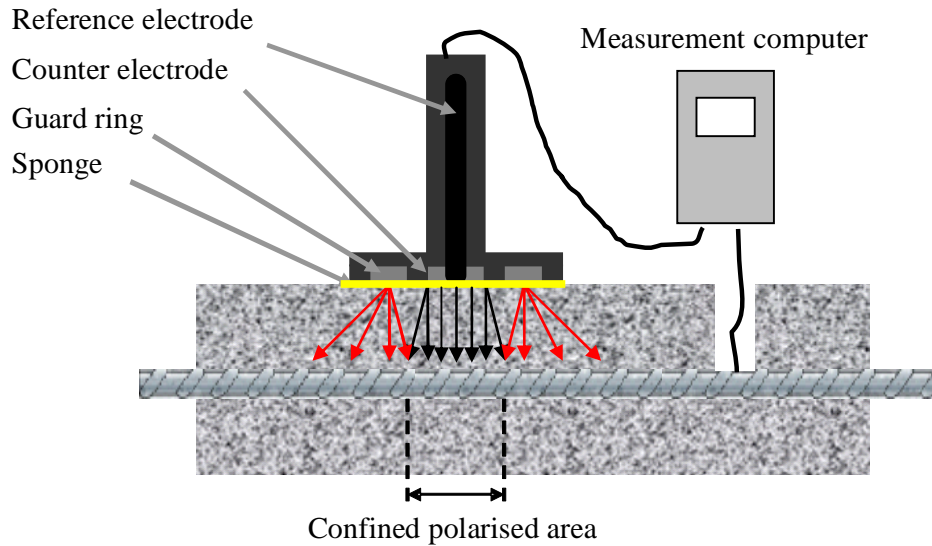


Figure 2. 18. Schematic plan of the GalvaPulse™ with guarding to limit the polarised area while performing the corrosion measurement.

Based on the suggestion of the manufacturer, 10-20  $\mu\text{A}$  for 5-10 seconds, in passive areas, should give a reasonable polarisation of the reinforcement. The recommended applied current pulse in active areas is 80-100  $\mu\text{A}$  for 5-10 seconds. The changes in the potential over time should display the general shape shown in Figure 2.19. Thus, it is important to make sure, from the polarisation graph on PSION that there is no irregularity; otherwise the measurement should be repeated with an increased current.

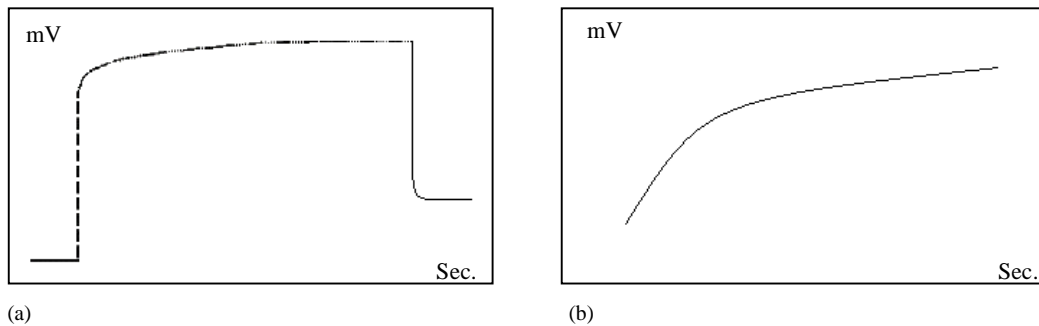


Figure 2. 19 The schematic illustration of the change of potential over time: (a) for active areas and (b) for passive areas [87].

The important concern is that the graph should increase with time without any large scatter. A decrease in potential indicates a false reading (e.g., problem with electrical contact). A large amount of scatter may be because of bad connections and/or insufficient applied current and/or the short time duration [87].

According to the manufacturer, the advantages of this system can be summarised as follows [88]:

- Estimation of the corrosion rate in the reinforcement can be made in less than 10 seconds.
- Reliable evaluation of reinforcement corrosion also in wet, carbonated or inhibitor treated concrete.
- Half-cell potential of the steel and electrical resistance of the concrete cover layer are given.
- Lightweight electrode/hand held computer and easy to operate software.
- Durable Guard Ring system for focusing the current field to the reinforcement.

- Measurements possible on uneven and curved surfaces.

For easy and quick evaluation, FORCE Technology suggested the following threshold values to categorise the risk of the corrosion rate:

Table 2. 9 Quick evaluation of corrosion rate, recommended by FORCE Technology and measure by the GalvaPulse™ [88].

| Measurement ( $\mu\text{A}/\text{cm}^2$ ) | Corrosion rate |
|---|----------------|
| Less than 0.5                             | Negligible     |
| Between 0.5 and 5                         | Slow           |
| Between 5 and 15                          | Moderate       |
| More than 15                              | High           |

Table 2.9 is based on experience and there is no standard guideline for interpreting the corrosion rate, measured by guard ring devices. Andrade and Alonso [89] and Feliu´ et al. [63], recommend the following interpretation based on their experience with the Gecor6™ instrument which employs galvanodynamic LPR and also uses a guard ring.

Table 2. 10 Relationship between corrosion current density measured with guard ring device (Gecor6™) and corrosion risk [63, 89].

| Measurement ( $\mu\text{A}/\text{cm}^2$ ) | Corrosion risk |
|---|----------------|
| Less than 0.1                             | Negligible     |
| Between 0.1 and 0.5                       | Low            |
| Between 0.5 and 1                         | Moderate       |
| More than 1                               | High           |

As can be seen, there are significant differences between the two recommended guidelines given in Tables 2.9 and 2.10, which indicates that these recommended values for interpreting the corrosion rates can not be used directly and need further study.

### 2.3.3. Electrochemical Impedance Spectroscopy (EIS)

EIS studies the system response to the application of a small amplitude alternating potential signal at different frequencies. The popularity of EIS or AC impedance methods for reinforced concrete has increased remarkably in recent years, because analysis of the system response provides information about the double-layer capacitance, interface, structure, reactions which are taking place, corrosion rate and electrolyte (environment) resistance [54, 90, 91].

An electrochemical process can be considered as an electrical circuit with basic elements such as resistors, capacitors and inductors. Therefore, in interpreting the response to an AC current, the AC circuit theory can be used successfully to demonstrate of a corrosion process and also it may be used to understand the behaviour of the corrosion process and prediction of the corrosion rates.

In direct current, the Ohm's law is as following:

$$V=IR \qquad \text{eq. 2. 19}$$

(V= Potential, I = Direct current, R= Actual resistor)

In the AC condition, Ohm's law becomes:

$$V=IZ \qquad \text{eq. 2. 20}$$

(V= Potential, I = Alternative current, Z= Impedance)

Direct current can be viewed as alternating current at zero frequency. In this case, the resistance is composed of only one or more actual resistors. When the frequency is not zero, all circuit elements that can affect the flow of current, e.g., resistors, capacitors, and inductors cause the resistance. The created resistance by capacitors and inductors depends on frequency while that created by a resistor is not dependant on frequency [92]. When an AC sinusoidal voltage is applied through a circuit with just a resistor, the resultant current will have the same frequency with no phase shift (Figure 2.20). If the circuit consists of capacitors and inductors, the resulting current will differ in time and it will have a phase shift ( $\theta$  = phase shift in radian), Figures 2.21 and 2.22 [93].

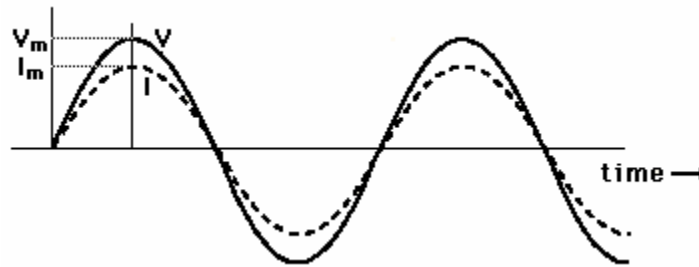


Figure 2. 20. Sinusoidal AC voltage and current in a circuit with one resistor [93].

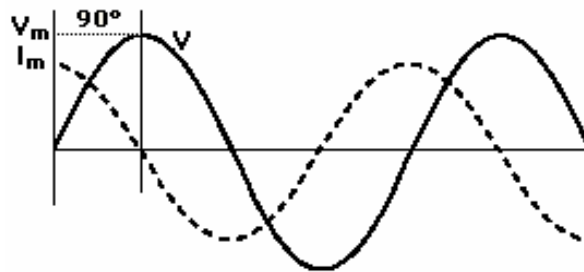


Figure 2. 21. Sinusoidal AC voltage and current with a capacitor [93].

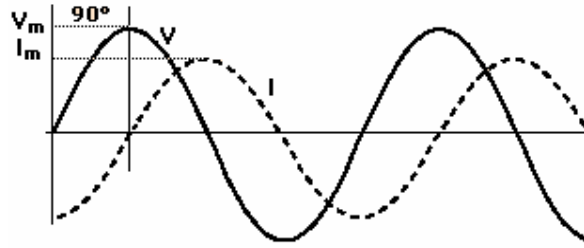


Figure 2. 22. Sinusoidal AC voltage and current with an inductor [93].

Using sines and cosines are mathematically inconvenient. Vector analysis provides an easier method of describing the equivalent circuit in mathematical terms (Figure 2.23) [92].

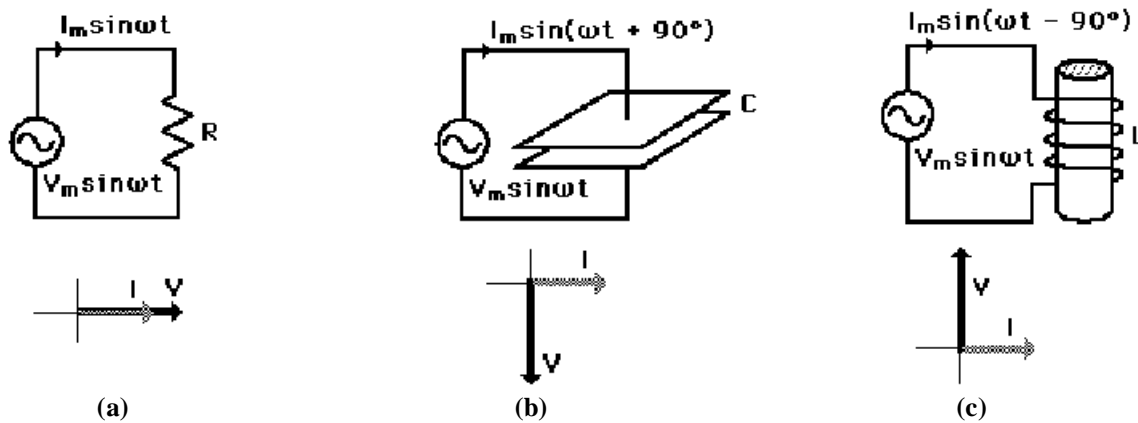


Figure 2. 23. Relationship between vectors of voltage and current in a circuit with (a) resistor, (b) capacitor and (c) inductor [93].



AC impedance analysis is based on the relationship between such vectors. A sinusoidal current or voltage can be represented as a rotating vector as shown in Figure 2.24. In this Figure, the x component shows the observed current so it becomes the real component of the rotating vector while the y component is a contribution that is not observed; therefore it is named the imaginary component of the rotating vector.

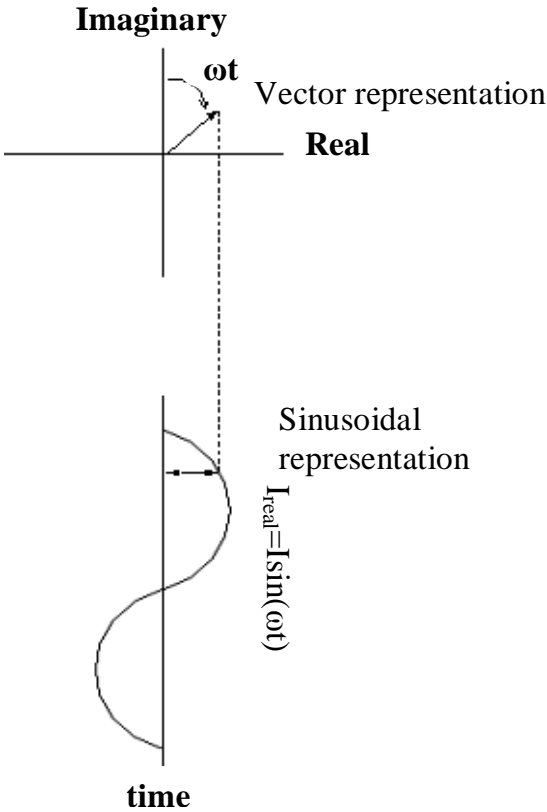


Figure 2. 24. . Relationship between sinusoidal AC current and rotating vector representation (adapted from [92]).

The mathematical descriptions of the two components are as followings:

$$\text{Real current} = I_x = |I| \cos(\omega t) \quad \text{eq. 2. 21}$$

$$\text{Imaginary current} = I_y = |I| \sin(\omega t) \quad \text{eq. 2. 22}$$

where  $t$  = time and  $\omega$  = frequency in radians per second =  $2\pi f$  ( $f$  = frequency in Hertz)

To separate the real (x) and imaginary (y) components, the magnitude of the imaginary part should be multiplied by  $j = \sqrt{-1}$ <sup>1</sup> and then the real and imaginary values can be reported separately. The equations for AC impedance become:

$$E_{\text{total}} = E_{\text{real}} + E_{\text{imaginary}} = E' + jE'' \quad \text{eq. 2. 23}$$

$$I_{\text{total}} = I_{\text{real}} + I_{\text{imaginary}} = I' + jI'' \quad \text{eq. 2. 24}$$

$$Z_{\text{total}} = Z' + jZ'' = \frac{E' + jE''}{I' + jI''} \quad \text{eq. 2. 25}$$

Absolute amplitude of the impedance (that is the length of the vector) and the phase angle are defined by [94]:

---

<sup>1</sup> Mathematicians use  $i$  to stand for  $\sqrt{-1}$ , but electrochemists use  $j$  to avoid confusion with  $i$ , the symbol for current.

$$|Z| = \sqrt{Z'^2 + Z''^2} \quad \text{eq. 2. 26}$$

$$\tan\theta = \frac{Z''}{Z'} \quad \text{eq. 2. 27}$$

The goal of AC impedance is to measure the impedance  $Z$  as  $Z'$  and  $Z''$ , and then model the response by using an equivalent simple circuit [92].

Table 2.11 shows the impedance expression for some simple circuit elements. As can be seen, there is no imaginary component for the impedance of a resistor and the phase shift is zero which means that the current is in phase with the potential. On the other hand, the impedance of the capacitor has no real component and its imaginary component is a function of both capacitance and frequency. The current through a capacitor is 90 degree out of phase with potential across it (Figure 2.21). As shown in Table 2.11, the impedance of a capacitor changes inversely with frequency, therefore, at high frequencies a capacitor acts as a short circuit and its impedance is close to zero. Conversely, at low frequencies (coming close to dc) a capacitor behaves as an open circuit, and the impedance tends toward infinite. The third simple electrical component is the inductor the current through an inductor is always 90 degrees out of phase with the potential drop across it. However, the phase shift is in the opposite direction (Figure 2.22). Also, as the frequency increases, the impedance of an inductor increases. An inductor acts as a short circuit at low frequencies and as large impedance at high frequencies [94].


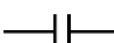
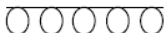
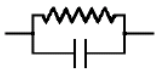
To determine the total impedance of a combination of simple elements, the impedance values of the individual components should be combined according to the following rules. For two circuit elements in series, the combined impedance is simply the vector sum of the

individual impedance values (eq. 2.28) and for circuit elements in parallel, the admittance values (the inverse of impedance) must be added together (eq 2.29):

$$Z_s = Z_1 + Z_2 \quad \text{eq. 2. 28}$$

$$\frac{1}{Z_p} = \frac{1}{Z_1} + \frac{1}{Z_2} \quad \text{eq. 2. 29}$$

Table 2. 11. Simple circuit elements with their impedance expression [94].

| Circuit element   | Impedance equation   |                     |
|---|--|---------------------|
|  | $Z = R + 0j$   | $(j = \sqrt{-1})$   |
|  | $Z = 0 - \frac{j}{\omega C}$   | $(\omega = 2\pi f)$ |
|  | $Z = 0 + j \omega L$   | $(\omega = 2\pi f)$ |
|  | $Z = \frac{R}{1 + \omega^2 C^2 R^2} - \frac{j \omega C^2}{1 + \omega^2 C^2 R^2}$ |                     |

### 2.3.3.1. Data presentation

As discussed in previous section, the expression for  $Z$  is composed of a real and an imaginary part (eq. 2.25). There are different ways to illustrate the response of an electrochemical system to an applied AC potential or current. The most common plots are Nyquist plot and Bode plots.

If, at each excitation frequency, the real part is plotted on the x-axis and the imaginary part is plotted on the y-axis of a chart, a "Nyquist plot" is formed.

A simple corroding system can be assumed as: solution resistance, in series with a combination of a resistor and a capacitor, which represent the polarisation resistance and double layer capacitance, respectively. This simple representation is called Randles cell and is shown in Figure 2.25.

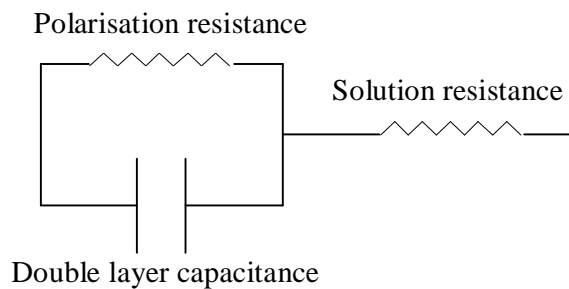


Figure 2. 25. Equivalent circuit for a simple electrochemical system.

Figure 2.26 is the Nyquist plot for a simple electrochemical system corresponding to the analogue circuit in Figure 2.25. It should be noted that each point on the Nyquist plot is the impedance at one frequency. Also it is important to mention that low frequency data are on the

right side of the plot and higher frequencies are on the left. On the Nyquist plot, the impedance can be represented as a vector of length  $|Z|$  and the angle between this vector and the x-axis, is the phase angle “ $\theta$ ” [94, 95].

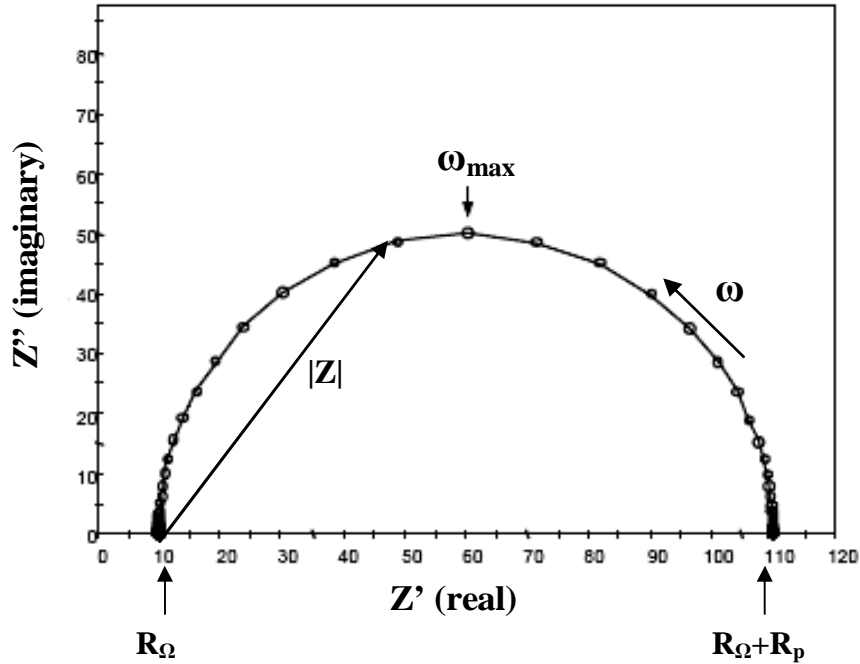


Figure 2. 26. Nyquist plot for a simple electrochemical system (adapted from [94]).

At high frequencies, at the leftmost end of the semicircle, where the semicircle touches the x-axis, the impedance of the Randles cell is entirely produced by the ohmic resistance,  $R_\Omega$ . The frequency reaches its low limit at the rightmost end of the semicircle. At this frequency, the Randles cell also approximates a pure resistance, but now the value is  $(R_\Omega + R_p)$  [94].

If the diffusion in the electrolyte (concentration polarisation) or a surface film or coating controls the system, an additional resistive element called the “Warburg impedance”,  $W$ , must be

included in the Randles circuit (Figure 2.27).  $W$  is shown at low frequencies on the Nyquist plot by a straight line superimposed at  $45^\circ$  to both axes, as shown schematically in Figure 2.28 [54].

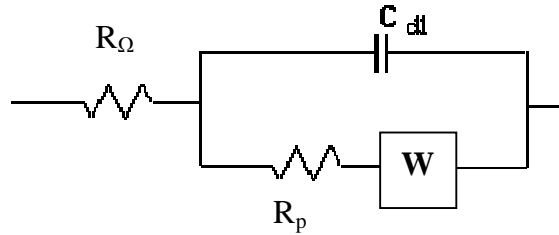


Figure 2. 27. Equivalent circuit for a system with Warburg impedance.

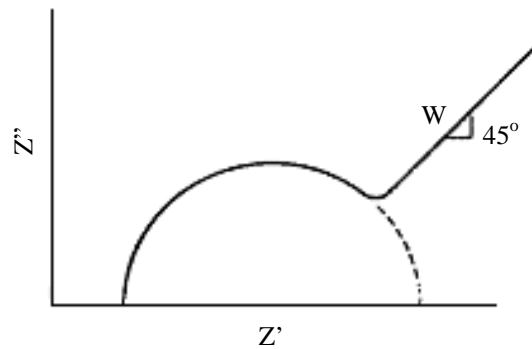


Figure 2. 28. Nyquist plot for a system with Warburg impedance.

The Nyquist plot has some limitations [94]: (i) the frequency is not clearly shown on the plot and it is not possible to determine, for a specific point, the frequency used to record that point; (ii) as mentioned before, the ohmic and polarization resistances can be directly determined from the plot but the electrode capacitance can be only calculated if the frequency information is

known. In Figure 2.26, the maximum frequency and the value of  $R_p$  can be used to calculate the capacitance by using the following equation:

$$C = \frac{1}{\omega_{\max} \times R_p} \quad \text{eq. 2. 30}$$

(iii) if there are high and low impedance components in the circuit, the larger impedance controls plot scaling and distinguishing the low impedance semicircle would probably be impossible.

Impedance spectra are often more complex than that shown in the in Figures 2.26 and 2.28. The semicircle maybe distorted, and the centre is usually moved below the horizontal axis. These complexities occur because the simple equivalent circuits do not completely explain the physical phenomena of an electrochemical system. Several computer programs have been written to fit experimental data to an equivalent circuit model. However, due to the complexity of this problem, all of these programs require some initial assumptions for the circuit parameters. Figure 2.29 shows a Nyquist plot for Marz grade iron (high purity) in aerated 0.5 M  $H_2SO_4$  for a frequency range of 10 kHz to 10 mHz [96].

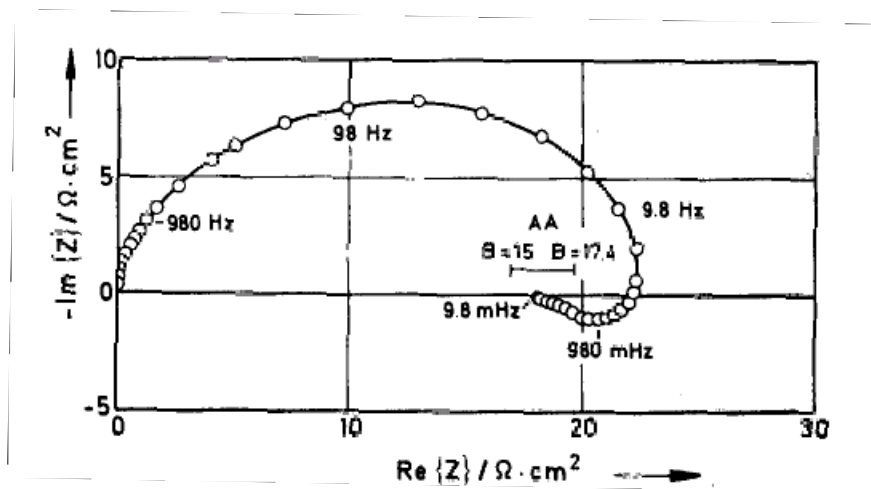


Figure 2. 29. Experimental impedance diagram. System: Fe/0.5 M  $H_2SO_4$ , aerated [96].



It is clear that it is not a perfect semicircle and an additional loop appears at low frequencies. It is believed that this distortion is due to the inductive behaviour of the electrochemical system [97, 98]. Most researchers believe that it is incorrect to interpret the actual low frequency  $Z'$  axis intercepts as  $R_{\Omega}+R_p$ . Instead, curve-fitting techniques should be used to obtain these values [99]. There is another complexity in Figure 2.29. In this plot, the centre of the semicircle does not lie on the  $Z'$  axis and is shifted to negative  $Z''$  values. To explain this phenomenon, some researchers use models that assume that the surface of the electrode is not homogeneous and, since the impedance data do not produce a simple semicircle in the capacitive half plane, more than one time constant must determine the corrosion behaviour [96]. These models can characterise different areas of the surface with different time constants. In this case, the total impedance of the surface would be the parallel combination of these areas and by using several Resistor-Capacitor-Inductor sub-circuits, the equivalent circuit for the system can be illustrated. Figure 2.30, show the circuit for the electrochemical system used in Figure 2.29.

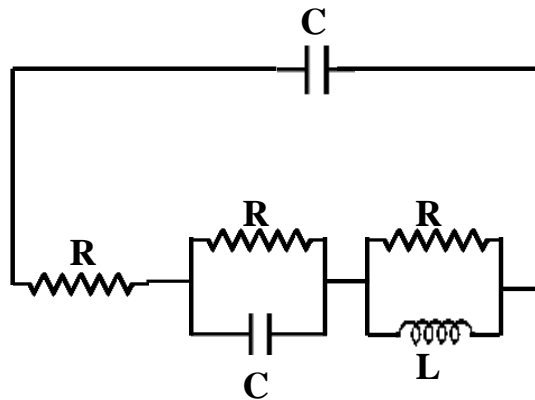


Figure 2. 30. Equivalent circuit for system used in Figure 2.31 (adapted from [96]).

A Bode plot is another popular presentation method for the impedance data. In the Bode plot, the data are plotted with log of frequency on the abscissa and both the log of absolute value of the impedance ( $|Z|$ ) and phase-shift ( $\theta$ ) on the ordinate [100]. Figure 2.31 shows a Bode Plot for the same data presented in the Nyquist plot in Figure 2.26 [94]. Since the frequency appears in as one of the axes in the Bode plot, it is easy to understand the dependence of impedance to the frequency from the plot. The  $\log |Z|$  vs.  $\log \omega$  curve can be used to determine the values of  $R_p$  and  $R_\Omega$ . As shown in Figure 2.29, at very high and very low frequencies,  $|Z|$  becomes independent of frequency. At the highest frequencies the ohmic resistance controls the impedance and  $\log (R_\Omega)$  can be read from the high frequency horizontal level. On the other hand, at the lowest frequencies, polarisation resistance contributes, and  $\log (R_p + R_\Omega)$  can be read from the low frequency horizontal portion.

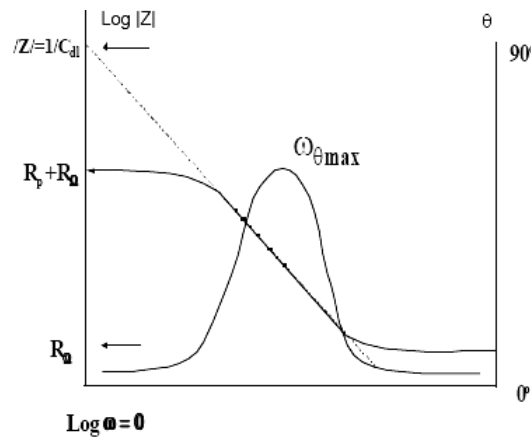


Figure 2. 31. Bode plot for the same system used in Figure 2.27.

For an intermediate frequency range, absolute values of the impedance is inversely proportion to frequency and a straight line with a slope of -1 is observed in  $\log |Z|$  vs.  $\log \omega$  curve. Extrapolating this straight line to  $\omega=1$ , the capacitance can be calculated by using eq. 2.31 [94, 99]:

$$|Z| = \frac{1}{C_{dl}} \quad \text{eq. 2. 31}$$

The Bode plot also shows the phase angle,  $\theta$ . At high and low frequencies, the Randles circuit behaves like a pure resistor and the phase angle is nearly zero. At intermediate frequencies,  $\theta$  increases and reaches its maximum value where the phase shift of the response is maximum. In case where the  $|Z|$  vs.  $\log \omega$  plot does not show the horizontal section, the double layer capacitance can be calculated from eq. 2.32 [94]:

$$\omega_{(\theta=\max)} = \sqrt{\left(\frac{1}{C_{dl} \times R_p}\right) \times \left(1 + \frac{R_p}{R_{\Omega}}\right)} \quad \text{eq. 2. 32}$$

The Bode format is advantageous when data scatter prevents satisfactory fitting of the Nyquist semicircle. In general, the Bode plot provides a more understandable description of the frequency-dependent behaviour of electrochemical system than does the Nyquist plot, which frequency values are not clear [94].

### **2.3.3.2. Application of EIS in steel reinforced concrete structures**

EIS is being used as a power tool to obtain information about metal/concrete systems and it seems that its applications in such systems are increasing. The following are some examples of such applications.

Lemoine et al [101] used EIS to study the precipitation of calcium hydroxide on the steel surface after setting of the mortar. Also, they tried to detect the corroded area on large beams, under and above water and they claimed that impedance measurements are feasible with large reinforced structure dipped in water or out of water. Pruckner et al. [102] used EIS to monitoring the efficiency of the cathodic protection of reinforced concrete. They found that changes in the corrosion rates of steel in different chloride contaminated concrete specimens with applied potential were detectable. Due to the ability of EIS to study the surface phenomena, many researchers such as Dhouibi et al [103], Monticelli et al. [104] Trabanelli et al. [105] Gu et al. [106], Hope and Ip [107], used EIS to determine the long-term effectiveness of concrete inhibitors for steel in concrete. Shi and his colleagues [108] used EIS to determine the chloride diffusivity in concrete. Aldea et al. [109] studied the microstructural changes during rapid chloride permeability test, using ac impedance technique. Hansen and his colleagues [110] studied the chloride permeability of of high performance concrete and used EIS. Peled et al [111] used EIS to monitor damage during tensile loading of cement composites. Andrade et al. [112] performed EIS to study the cement paste hardening process. Perron et al. [113] studied the freezing of water in Portland cement paste and in their study the authors have developed a method to measure the impedance characteristics of cement paste on cooling and warming.

#### **2.3.4. Cyclic polarization**

Cyclic potentiodynamic polarisation technique is a relatively non-destructive measurement that can provide information about the corrosion rate, corrosion potential, susceptibility to pitting corrosion of the metal and concentration limitation of the electrolyte in the system. The original test standard, ASTM G 5 [114], was expanded from a stepped potentiostatic test to a potentiodynamic test as electronics developed, and consequently to a cyclic experiment (ASTM G 61 [115]) [116]. The technique is built on the idea that predictions of the behaviour of a metal in an environment can be made by forcing the material from its steady state condition and monitoring how it responds to the force as the force is removed at a constant rate and the system is reversed to its steady state condition. Applied potential is the force and is raised at a continuous, often slow, rate by using potentiostat [117]. This rate is called polarization scan rate and is an experimental parameter.

It is very important to choose the proper scan rate otherwise the result does not reflect the corrosion behaviour and the result could be an incorrect polarisation scan and an incorrect prediction from it. As mentioned in section 2.3.3.1, the surface of the metal/electrolyte can be considered solution resistance, in series with a combination of a resistor and capacitor, which represent the polarisation resistance and double layer capacitance, respectively (Figure 2.25). To ascertain that the current/voltage relationship reflects only the interfacial corrosion process at every potential of the polarization scan, the effect of capacitance should be minimised. For this purpose, the capacitor should remain fully charged; otherwise, some of the current generated would reflect charging of the surface capacitance in addition to the polarisation resistance and the measured current would then be greater than the current actually produced by the corrosion

reactions. To reduce the effect of the capacitance, the scan rate should be slow enough in a way that the capacitance remains fully charged during the experiment. In this case, the current-potential relationship just reflects the polarisation resistance (interfacial corrosion process) at every potential of the polarisation scan [117].

Because, the capacitance and resistance are functions of the material, environment and the applied potential, choosing the appropriate scan rate is not an easy decision.

An outline of an approach to determine the maximum scan rate is given by Mansfeld [118]. The principle of the method is based on Bode plot, Figure 2.31, represented by Randles circuit (Figure 2.25). At low frequencies,  $|Z| = R_{\Omega} + R_p$ , therefore, in order to determine the polarisation resistance accurately, the frequency characterisation of the scan rate should be less than the  $f_{max}$  in the low frequency portion of the Bode plot (Figure 2.32).

$\omega = 2\pi f$ , where  $f$  is the frequency of the applied sine wave, and  $E$  can be calculated by using eq. 2.33:

$$E = E_o \sin(\omega t) = \frac{1}{2} \Delta E e^{j2\pi f t} \quad \text{eq. 2. 33}$$

$\Delta E$  is the peak to peak amplitude and is equal to  $2E_o$ .  $\Delta E$  is usually taken  $\sim 10$  mV. This assures the linear response of the system to the applied potential [71]. The rate of change of potential can be calculated by taking derivative of eq. 2.33:

$$dE/dt = \frac{1}{2} \Delta E \times (j2\pi f t) \times (e^{j2\pi f t}) \quad \text{eq. 2. 34}$$

and the maximum rate of change would be:

$$E_{\max} = \pi f \Delta E \quad \text{eq. 2. 35}$$

This maximum rate of change corresponds to scan rate,  $S$ , and by using  $f_{\max}$  in eq. 2.34, the maximum scan rate,  $S_{\max}$ , can be calculated as following:

$$S_{\max} = \Delta E \cdot \pi \cdot f_{\max} \quad \text{eq. 2. 36}$$

The value of  $f_{\max}$  can be found from Bode plot as shown in Figure 2.32 as one decade slower than the lower break-point<sup>2</sup>,  $f_2$ .

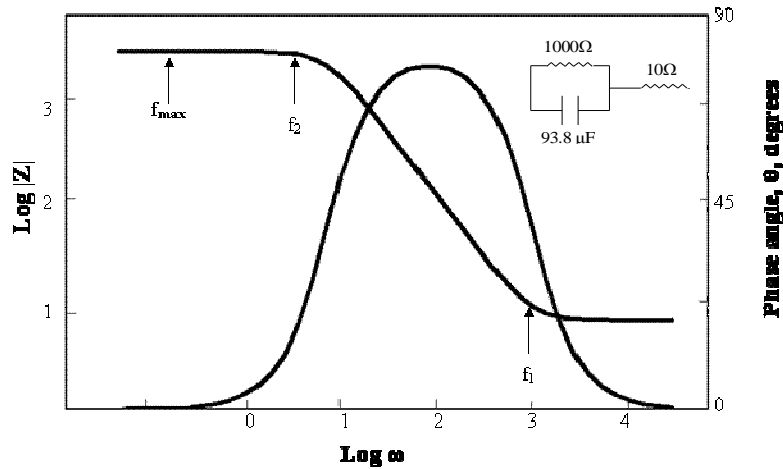


Figure 2. 32. Bode plots of the frequency response for the an electrochemical system with  $R_{\Omega} = 10\Omega$ ,  $R_p = 1000\Omega$  and  $C_{dl} = 93.8\mu F$  (adapted from [118]).

2. Break point is the point where low frequency behaviour starts to change to high frequency behaviour and vice versa [119].

For example in Figure 2.32,  $f_2$  is  $\sim 1.7$  Hz, consequently:

$$S_{\max} = \pi \cdot \Delta E \cdot f_{\max} < \frac{\pi \cdot \Delta E \cdot f_2}{10} = 5.3 \text{ mV/s}$$

To obtain a frequency in the horizontal portion of the Bode plot,  $f_2$  is divided by 10. Therefore, for a system shown in Figure 2.30, a scan rate lower than 5.3 mV/s has to be used for an accurate result.

Cyclic polarisation measurement is carried out with three electrodes: the specimen (working electrode which in present case, is the reinforcing steel), a counter electrode and a reference electrode. The potential of the specimen is changed continuously while the resulting current is monitored and then the applied potential is plotted versus the logarithm of the resulting current density. The conductivity of the electrolyte (environment) is very important factor that should be considered in all electrochemical experiments, especially in cyclic polarisation technique. The electrolyte resistance causes a potential drop between the working electrode and reference electrode and can cause errors. This effect has important impact on the interpretation, and should be compensated. Figure 2.31 shows how the uncompensated potential might vary with conductivity for different current densities [117].

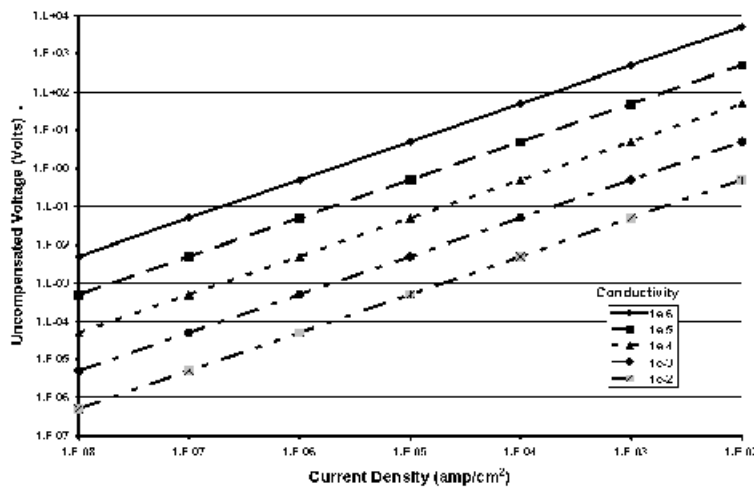


Figure 2. 33. Variation of uncompensated potential with conductivity for different current densities [117].



The effects of a significant potential drop are summarised as followings [117, 120]:

1. The applied potential can be much greater than the potential that is actually affecting the corrosion processes.
2. The applied scan rate can be much greater than the intended scan rate.
3. More importantly, the differences will be a function of the magnitude of the current passed between the working and counter electrodes, becoming greater as the current increases. If the metal is passive, this effect is not significant.

The shape of the curve indicates if the sample is in the passive or active state, and can also show the pitting potential and the re-passivation or protection potential. In a passive system, the potential at which the current sharply increases is defined as the pitting potential ( $E_{pit}$ ) and where the loop closes on the reverse scan is the protection or re-passivation potential ( $E_{pro}$ ). If these two potentials are the same, there is a little tendency to pitting. If  $E_{pro}$  is more positive than  $E_{pit}$ , there is no tendency to pitting. On the other hand if  $E_{pro}$  is more negative than  $E_{pit}$ , the pitting could happen. Further more, the size of the pitting loop can be used as an indication of pitting tendency. The larger loop shows more tendency to pit [121]. Figure 2.32 shows how the pitting or nucleation potential and re-passivation or protection potential can be deduced from the potentiodynamic cyclic polarisation curves.

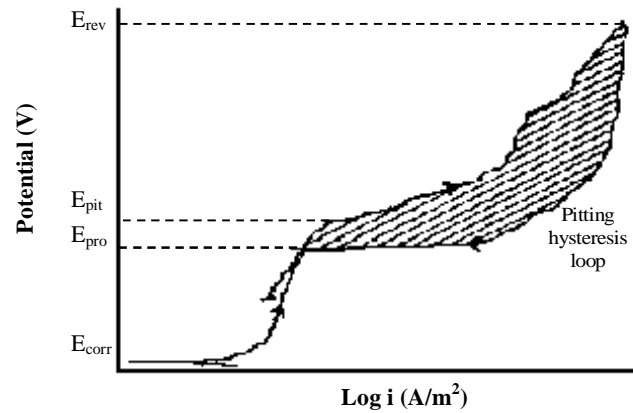


Figure 2. 34. Schematic of pitting and passivation potentials on cyclic polarisation curve (adapted from [121]).

## 2.4. CONCRETE ELECTRICAL RESISTIVITY

Electrical resistivity of concrete is considered an important parameter for evaluating the quality of concrete. There are many studies on the relationship between concrete resistivity and corrosion of reinforcing steel [122-128] and the effect of resistivity on the initiation of corrosion of embedded bars [127, 129]. Many investigators have tried to correlate the concrete resistivity to different characteristics, properties and composition of concrete such as: w/c ratio [130-132], age [127, 130-135], porosity [136], cement paste volume content [130, 132] and chloride diffusion coefficient [137, 138].

### 2.4.1. Concrete resistivity measurement techniques

Many techniques have been used for measuring concrete resistivity and they can be categorised into two methods: AC, those using alternating current or potential, and DC, those using direct current. In this project, both AC and DC methods were used.

The four-probe method is one of the most widely used technique for field measurement of concrete resistivity. This method was originally developed by F. Wenner [139] to measure the resistivity of soil. As shown in Figure 2.34, four electrodes are equally spaced. A small alternating current is applied between the outer electrodes while potential is measured between the inner electrodes. The resistivity is then calculated by using the following equation:

$$\rho = \frac{2 \cdot p \cdot a \cdot V}{I} \quad \text{eq. 2. 37}$$

where  $\rho$  is the resistivity ( $\Omega \cdot \text{cm}$ ),  $a$  is the distance between inner electrodes (cm) and  $V$  and  $I$  are RMS<sup>3</sup> values or maximum values of voltage (volts) and current (amps), respectively.

---

3. The value of an AC voltage is continually changing from zero up to the positive peak, through zero to the negative peak and back to zero again. Clearly for most of the time it is less than the peak voltage, so this is not a good measure of its real effect. Instead the root mean square value (RMS) which is 0.7 of the peak voltage or current is normally used.

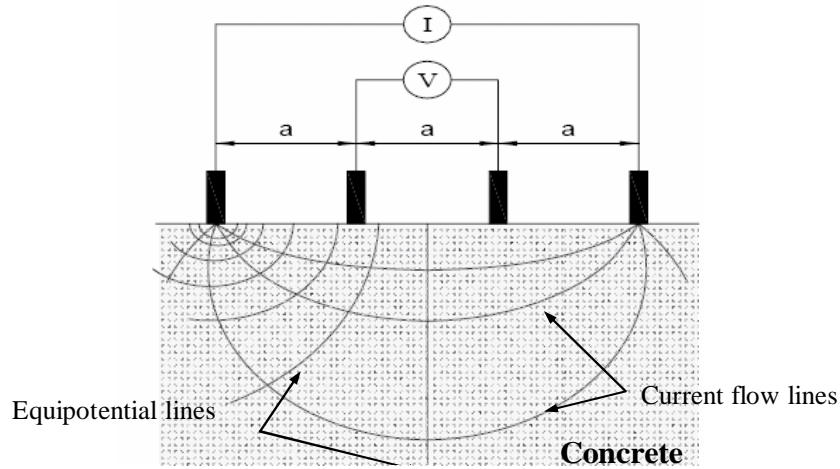


Figure 2. 35. Wenner technique for measuring resistivity (adapted from [122]).

There are several factors that may affect the results of four probe technique measurement.

Gowera and Millard studied these factors and summarized them as [122, 140]:

1. geometrical constraints,
2. surface contact,
3. concrete non-homogeneity,
4. the presence of steel reinforcing bars,
5. surface layers having different resistivity from the bulk of the concrete, and
6. ambient temperature.

Another way to measure the concrete resistance or resistivity is using electrochemical techniques. Galvanostatic pulse and EIS are two techniques which were used in this project and the theory behind each of them was explained in previous sections.

In reinforced concrete, at least two semicircles appear in the Nyquist plot, in which the first semicircle is usually representative of concrete resistance. Sometimes, there is just one semicircle in Nyquist plot but, it does not start from zero on x-axis. That shift is considered as concrete resistance. Figure 2.35 (a) illustrates the simple model of the steel-concrete interface and the equivalent circuit and Nyquist plot are shown in Figures 2.35 (b) and (c), respectively. There are some recommendations for correlating the corrosion of steel to concrete resistivity (Table. 2.12) [141, 142]. Dissimilarity seen in Table 2.12, shows that using concrete resistivity as an indicator for steel corrosion activity can not be used with confidence and needs more investigation.

Table 2. 12. Comparison of relationship between concrete resistivity and corrosion risk of reinforcing steel.

| <b>Resistivity (kΩ.cm)</b>                  | <b>Corrosion risk</b>                                |
|---|--|
| <b>Feliu et al [141]</b>                    |  |
| >100-200                                    | Negligible corrosion; concrete is too dry            |
| 50-100                                      | Low corrosion rate                                   |
| 10-50                                       | Moderate to high corrosion rate when steel is active |
| <10   | Resistivity does not control corrosion rate          |
| <b>Bungey (nonsaturated concrete) [142]</b> |  |
| >20   | Low  |
| 10-20                                       | Low/moderate   |
| 5-10  | High   |
| <5  | Very high  |

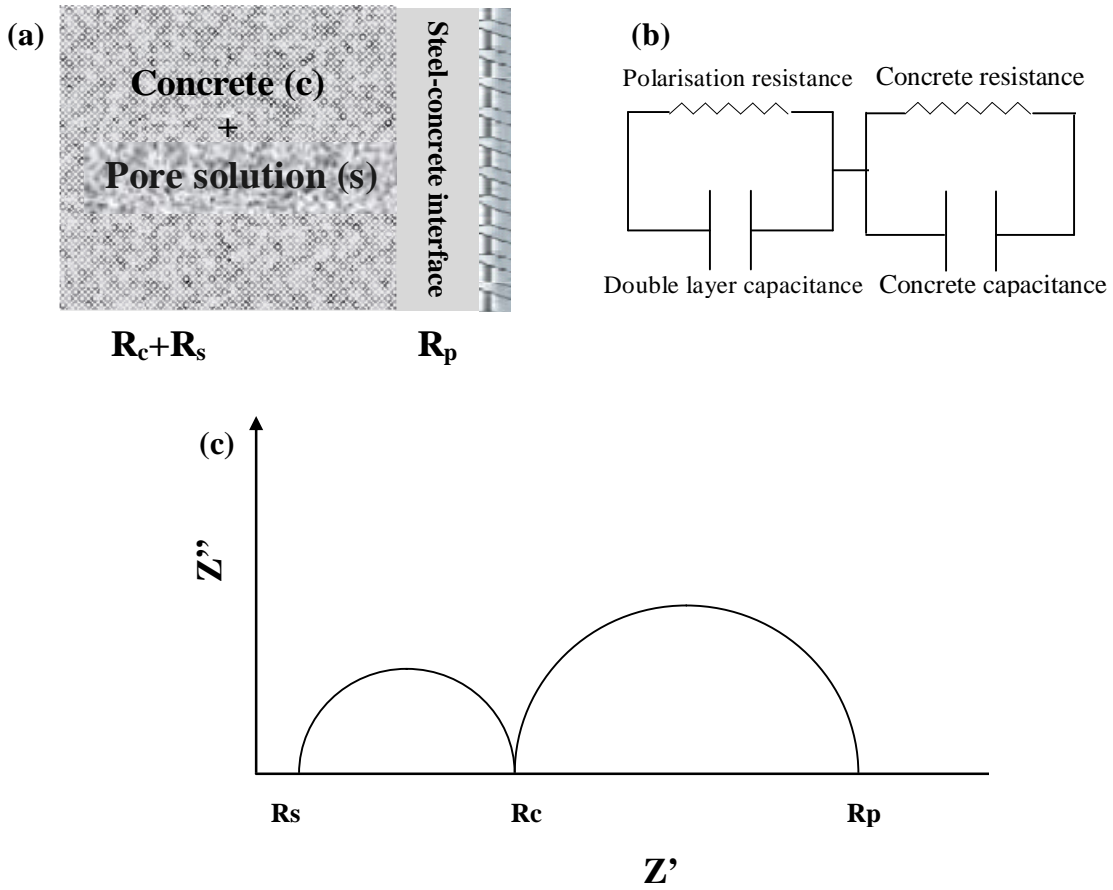


Figure 2. 36. (a) Simple schematic model of steel-concrete interface, (b) equivalent circuit of the model and (c) schematic Nyquist plot for the model.

## CHAPTER 3, EXPERIMENTAL PROCEDURES

### 3.1. MATERIALS

Many variables are involved in the electrochemical behaviour of steel in concrete and because of time and the number of measurements, it was impossible to consider all of them in this project. Therefore, for the purpose of this study, OPC concrete and plain carbon steel (black steel) bars, which are the most common combination in reinforced concrete structures, were chosen. It should also be noted that ASTM C 876 guidelines are only recommended for black steel and it cannot be applied to any other type of steel such as stainless steel or galvanised steel.

Table 3.1 shows the concrete mixture proportion used for preparing the 1 m<sup>3</sup> concrete.

Table 3. 1. Concrete mixture proportion for making 1m<sup>3</sup> concrete

| <b>Component</b>          |                     |
|---------------------------|---------------------|
| Type 10 Portland, kg      | 355                 |
| Sand. Kg                  | 770                 |
| Stone 20 mm, kg           | 1070                |
| Water, l                  | 160                 |
| Eucon MRC air entrainment | 40 ml/100 kg cement |
| W/CM                      | 0.43                |

In addition to concrete specimens, some experiments were carried out in synthetic pore solution. The expression of pore solution from hardened cement pastes and mortars is based on the work of Barneyback and Diamond in 1981 [143]. For this purpose, hardened paste cylinders, made with OPC, were subjected to high pressure to extract the pore solution in the porosity of the cement paste. The expressed pore solution was chemically analysed and the results are given in Table 3.2 and the synthetic solution was prepared based on the obtained results [144].

Table 3. 2. Composition of synthetic pore solution, Type 10

| <b>Material</b>                         | <b>Volume</b> |
|---|---------------|
| NaOH, g                                 | 9.17          |
| KOH, g                                  | 31.4          |
| CaSO <sub>4</sub> .2H <sub>2</sub> O, g | 0.96          |
| Ca(OH) <sub>2</sub> , g                 | 4.2           |
| Water, g                                | 1750          |

## **3.2. SPECIMEMNS PREPARATION**

Three sets of samples were used in this project: Beams with segmented steel bars, concrete specimens with different variables and steel in synthetic pore solution.

### **3.2.1. Beams with segmented steel bars**

It was necessary to identify a second technique with which to verify the values of half-cell potential consistent with either active corrosion or passivity. The obvious parameter to act as a correlation is corrosion rate determined electrochemically. However, recent research [77] has shown that commercially available instruments designed to determine the corrosion rate of steel in concrete can give very different values for the same structure tested at the same time. Consequently, the first phase of this project was to determine which technique gives the most accurate and reproducible corrosion rate measurements.

For this purpose, five beams with one segmented 10M rebar in each were cast as illustrated in Figures 3.1 and 3.3. To separate and isolate the steel segments, a small plastic spacer made of PVC was used between each segment. Segments and plastic spacers were tapped



and they were connected together by a 6mm threaded rod (Figures 3.2). For electrical connection, copper wires were used and connected to each steel segment. The concrete for each beam was cast in two parts: for one half was as given in Table 3.1 while the concrete for the second half had the same mixture proportions but with 2.5% Cl<sup>-</sup> by weight of cement added to the mixing water as NaCl. Later in the process, a ponding well was installed on the Cl<sup>-</sup> contaminated part of each beam and filled with saturated sodium chloride solution to accelerate the corrosion on that side (Figures 3.3).

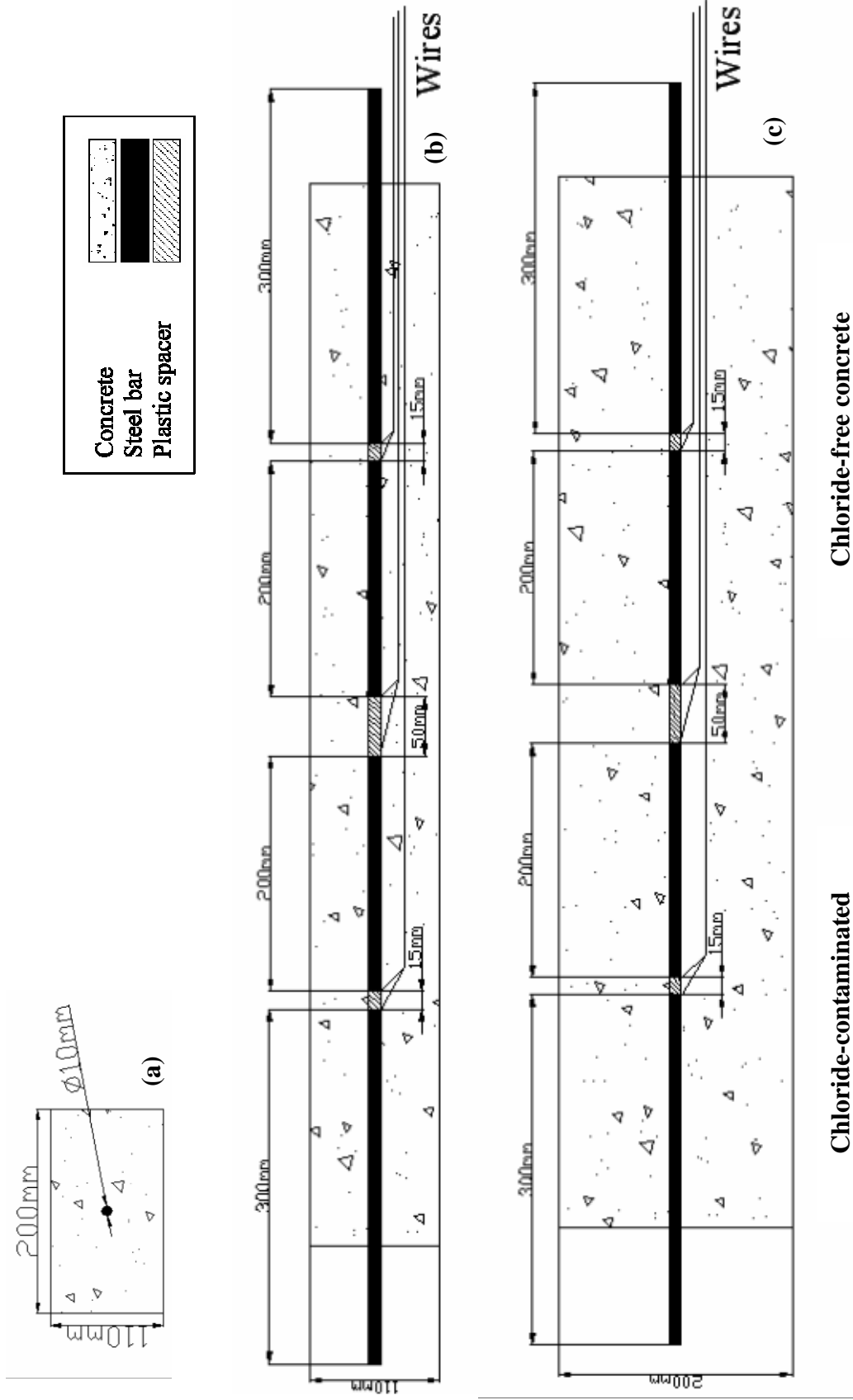


Figure 3. 1 Schematic plan of a beam with segmented steel bar embedded in concrete (a) end view, (b) side view and (c) top view.



Figure 3. 2. (a) one tapped steel segment with a threaded rod, (b) two segments with two PVC pieces for isolation.



Figure 3. 3. Concrete beams in a container filled with water. A stainless steel sheet is kept at the bottom of the container as counter electrode.

The corrosion activity along each bar was monitored using GalvaPulse™ (a commercial field instrument) as well as four laboratory techniques (LPR, Cyclic polarization, EIS and Galvanostatic LPR). Both half-cell potential,  $E_{\text{corr}}$ , and corrosion current,  $i_{\text{corr}}$ , were recorded as a function of time.

When the bars were deemed to have corroded sufficiently to allow gravimetric measurements of the mass loss due to corrosion, the specimens were autopsied and the extent and distribution of the corrosion recorded. The corrosion products were removed according to the ASTM G1 [145] standard procedure. Among the various compositions recommended by ASTM G1, for removing the corrosion products from iron and steel, the most commonly used and popular solution is as follows: 1000 ml hydrochloric acid solution (HCl, specific gravity [sp.gr.] = 1.19) + 20 g antimony trioxide ( $\text{Sb}_2\text{O}_3$ ) + 50 g stannous chloride ( $\text{SnCl}_2$ ). This solution, which is also called Clark solution, is effective in cleaning corrosion products at room temperature. The steel segments were immersed in Clark solution for about half an hour or until the corrosion products were entirely removed. The time is based on the extent of the corroded areas and could be more or less than 30 minutes. Due to the toxic nature of the Clark solution, the cleaning procedure must be carried out under fume hood with safety glasses and gloves.

The bars were then weighed and a comparison of the mass loss determined by gravimetry and that estimated by the cumulative values of  $i_{\text{corr}}$  was done. The results are given in next chapter.

### 3.2.2. Specimens with different variables

A second set of reinforced concrete specimens was cast to determine the effect of the variables given in Table 3.3, on the half-cell potential values. For this purpose, ~ 700 mm, 10 M steel rebar was used. One end of the rebar was tapped and a stainless steel screw was used for electrical connection. Both ends of the steel bar including the electric connection were epoxy coated. The coated length inside the concrete was equal to the cover depth. Therefore, the exposed area for the specimens with 30 mm cover depth was 440 mm, for 50 mm cover depth was 400 mm and for 70 mm cover depth was 360 mm. To expose the concrete specimens to salt solution, a ponding well, made of Plexiglas sheets, was installed on top of each specimen and filled with sodium chloride solution. A schematic plan of one of the samples with 50 mm cover depth is given in Figure 3.4 and Figure 3.5 shows how the ponding well was attached to a concrete specimen.

Table 3. 3. Concrete specimens with different variables.

| <b>Purpose</b>   | <b>Number of samples</b> |
|--|--------------------------|
| Cover depth-30 mm  | 5                        |
| Cover depth-50 mm  | 5                        |
| Cover depth-70 mm  | 5                        |
| Carbonation (cover depth 50 mm)  | 5                        |
| Cracks (longitudinal) (cover depth 50 mm)                              | 3                        |
| Cracks (transverse) (cover depth 50 mm)                                | 3                        |
| Distance of reference electrode to the steel rebar (cover depth 50 mm) | 3                        |

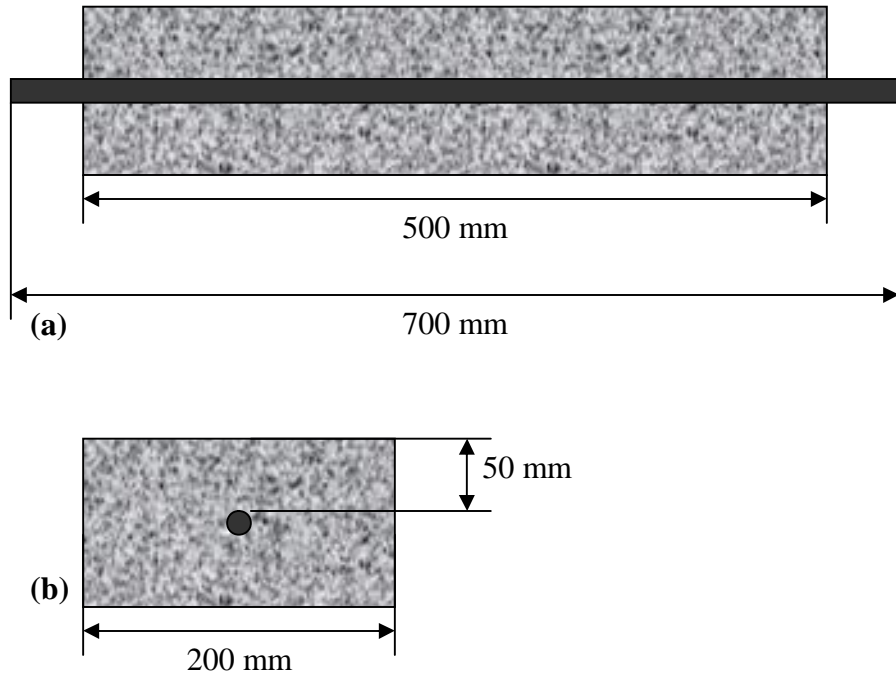


Figure 3. 4. Schematic plan of a concrete specimen for determining the effect of different variables of the half-cell potential value (50 mm cover depth), (a) side view, (b) end view.



Figure 3. 5. Ponding well attachment to a concrete specimen with 50 mm cover depth.

To determine the effect of the carbonation on the half-cell potential values, five samples with 50 cover depth and fifteen cylinders were kept in an AC Model HE-453-6 Dry-Lab glove box with high purity carbon dioxide (99.99%) atmosphere for three months at  $\sim 40^{\circ}\text{C}$  and the relative humidity of  $\sim 60\%$ . To control inside temperature of the glove box, an electrical heater was used and the temperature and the relative humidity of the glove box were monitored continuously. The cylinders were used to determine the carbonation depth as a function of exposure time. By applying the phenolphthalein solution to a freshly fractured or freshly cut surface of concrete, noncarbonated areas ( $\text{pH} \sim 12.5$ ) turn red or purple while carbonated areas ( $\text{pH} \sim 8.5$ ) remain colourless (Figure 3.8). The results of the carbonation depth measurement with time are given in Figure 3.6. The edge of the fracture surface of one the cylinders after carbonation and applying phenolphthalein solution and the glove box are shown in Figures 3.7 and 3.8, respectively.

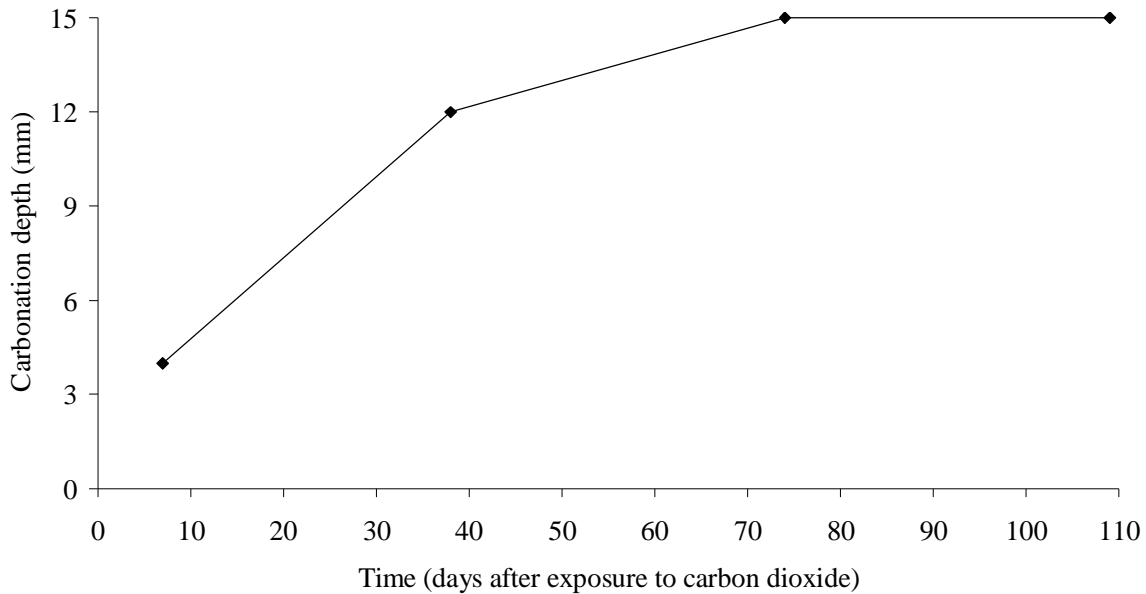


Figure 3. 6. Carbonation depth versus time of exposure

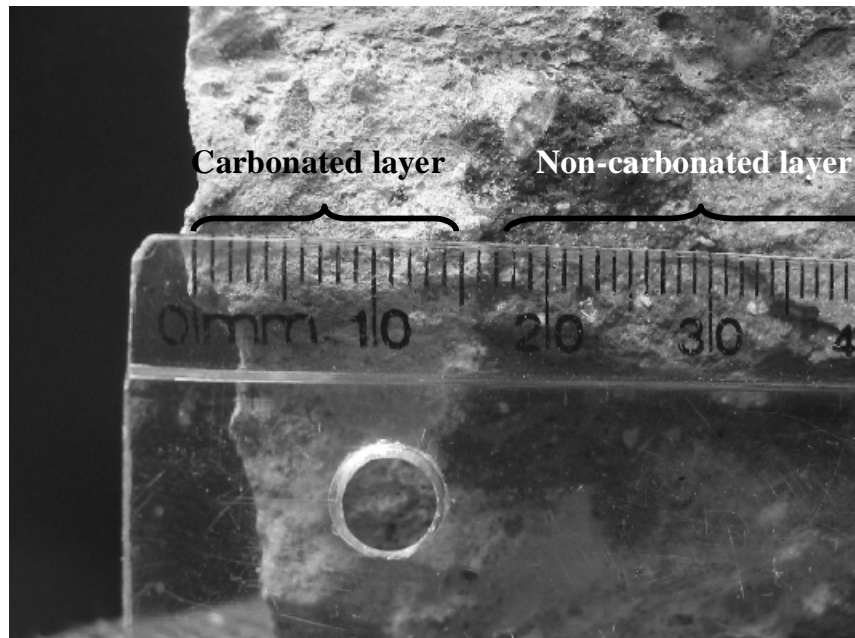


Figure 3. 7. Carbonation depth measurement. Phenolphthalein used to determine the pH of the concrete. The high pH of the concrete made the solution purple while carbonated area (the low pH area) remained unchanged.



Figure 3. 8. View of the glove box used in this project to carbonate the concrete specimens.



As mentioned in Table 3.3, two types of cracks were introduced to the samples: longitudinal and transverse. To cause longitudinal cracking (i.e. parallel to the steel rebar), a PMMA rod (polymethyl methacrylate) was positioned underneath of the steel rebar and the samples were kept outdoors from December 2005, to July 2005. The thermal expansion coefficient of the PMMA rod is between  $60-90 \times 10^{-6} \text{ }^\circ\text{C}^{-1}$  [146], and that of cement paste is around  $11-20 \times 10^{-6} \text{ }^\circ\text{C}^{-1}$  [3]. The temperature variations from  $-32$  to  $+34 \text{ }^\circ\text{C}$  during the exposure period was sufficient to create cracks parallel to the steel rebar (Figure 3.9).

For cracks transverse to the steel rebar, the beam was subjected to three point bending. Figures 3.9 shows three point bending configuration and the resultant transverse crack on one of the samples.

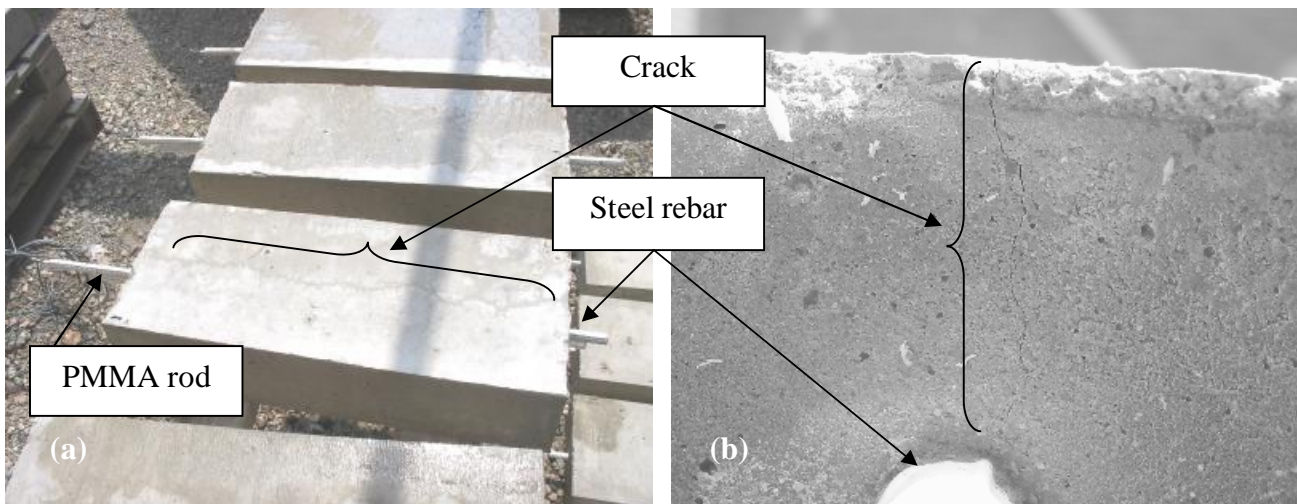


Figure 3. 9. Longitudinal crack, parallel to the steel rebar, created by expansion of the plastic rod (a) longitudinal view, (b) end view.

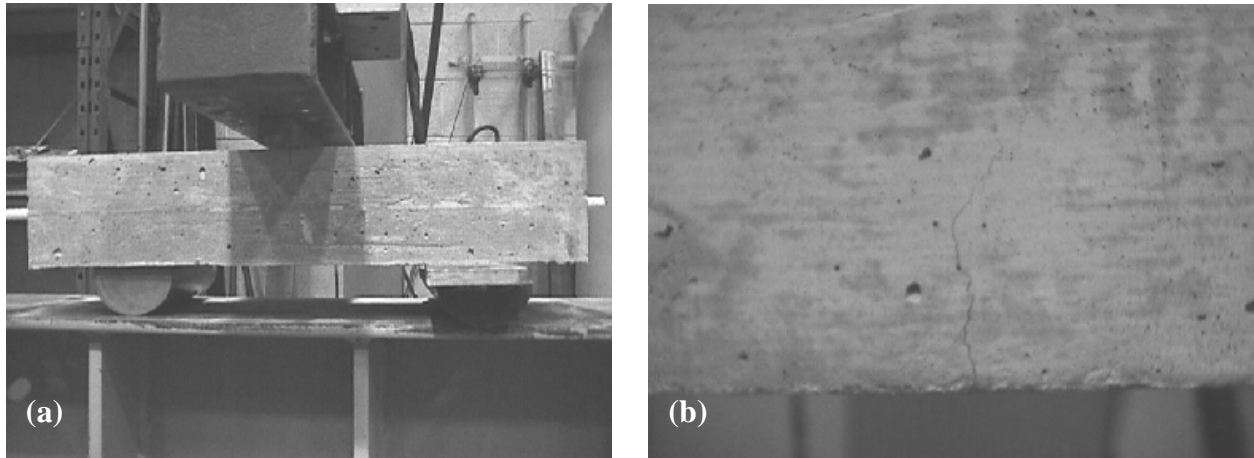


Figure 3. 10. Three point bending test configuration and (b) resultant transverse crack.

To study the effect of the distance of reference electrode from the surface of the steel rebar on half-cell potential values, embeddable Mn/MnO<sub>2</sub> reference electrodes, ERE 20 (Figure 3.10), from FORCE Technology [147] were used. For this purpose, a hole ( $\Phi = 20$  mm and  $L = 90$  mm, 5 mm from the surface of the steel rebar) was drilled perpendicular to the steel rebar on each sample and a Mn/MnO<sub>2</sub> reference electrode was installed in the hole. Each hole was filled with cement paste and cured for two days and then coated with Sika ® AnchoreFix ® 3<sup>CA</sup> anchoring gel. Figure 3.11 shows a schematic plan of ERE 20 Mn/MnO<sub>2</sub> reference electrode and Figure 3.12 shows a sample with the embedded electrode.

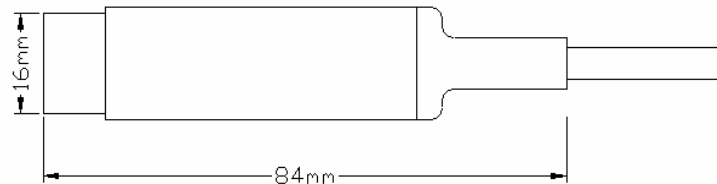


Figure 3. 11. A schematic plan of ERE 20 Mn/MnO<sub>2</sub> reference electrode.

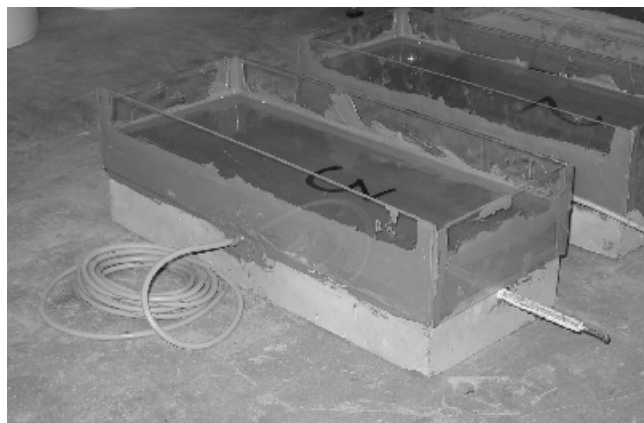


Figure 3. 12. A sample with embedded Mn/MnO<sub>2</sub> reference electrode. The rather messy epoxy on the ponding well is due to the need to make the well leak-tight

### 3.2.2.1. Electrode configuration

Due to the number of laboratory measurements in this project and the cost and difficulties because of the fragile nature of most commercially available reference electrodes, for this number of measurements, it was not feasible to use a single reference electrode for each measurement location. Therefore, another option was considered which was using graphite as reference electrode and the stability in two different environments: concrete synthetic pore solution, and salt solution was evaluated. For this purpose, a setup consisted of two beakers, one with saturated calomel electrode one with a graphite rod was used. The two solutions were connected together by a salt bridge (saturated KCl) which provided an ionic conductivity (Figure 3.13). Both electrodes were connected to an automated monitoring system, and the potential of graphite was monitored with respect to calomel for 8 hours. Results are shown in Figures 3.14 and 3.15.

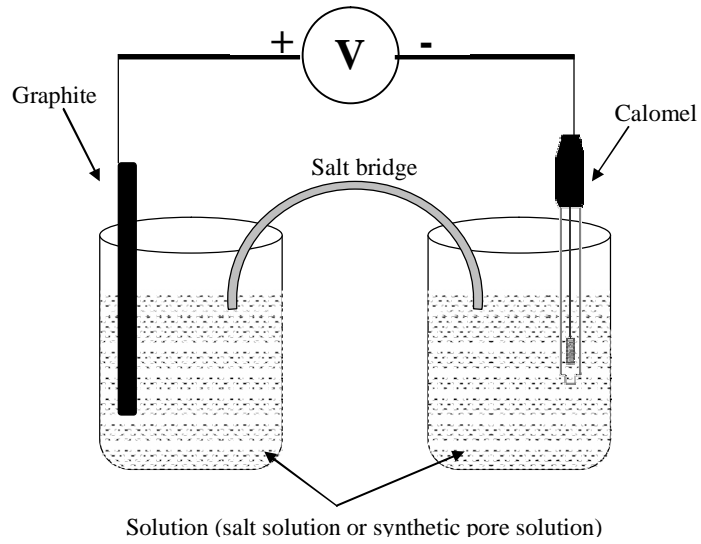


Figure 3. 13. Schematic plan of setup, used for checking the stability of graphite in different solutions.

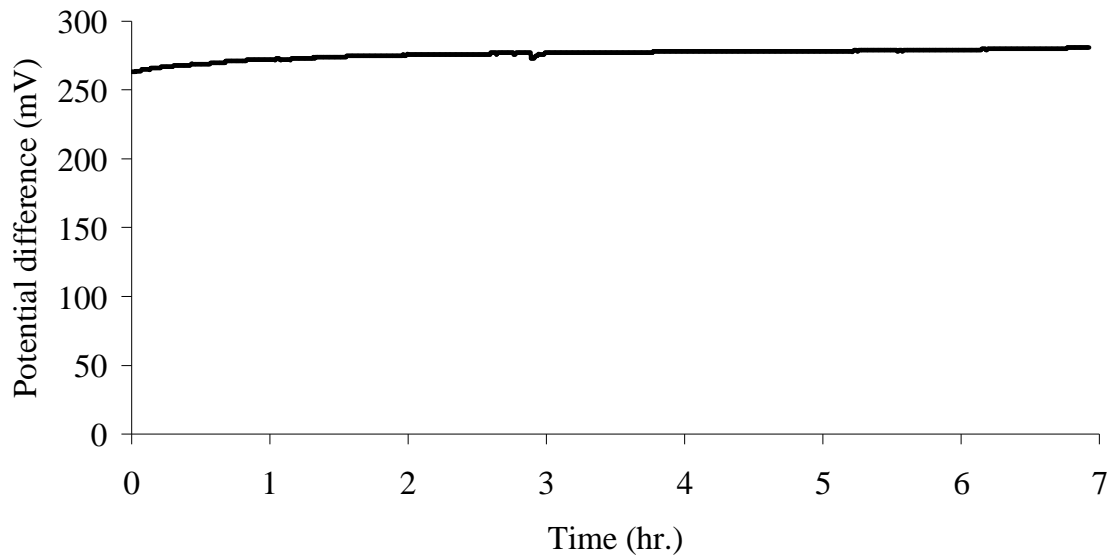


Figure 3. 14. Potential difference between calomel reference electrode and graphite in 3% salt solution over an eight hour period.

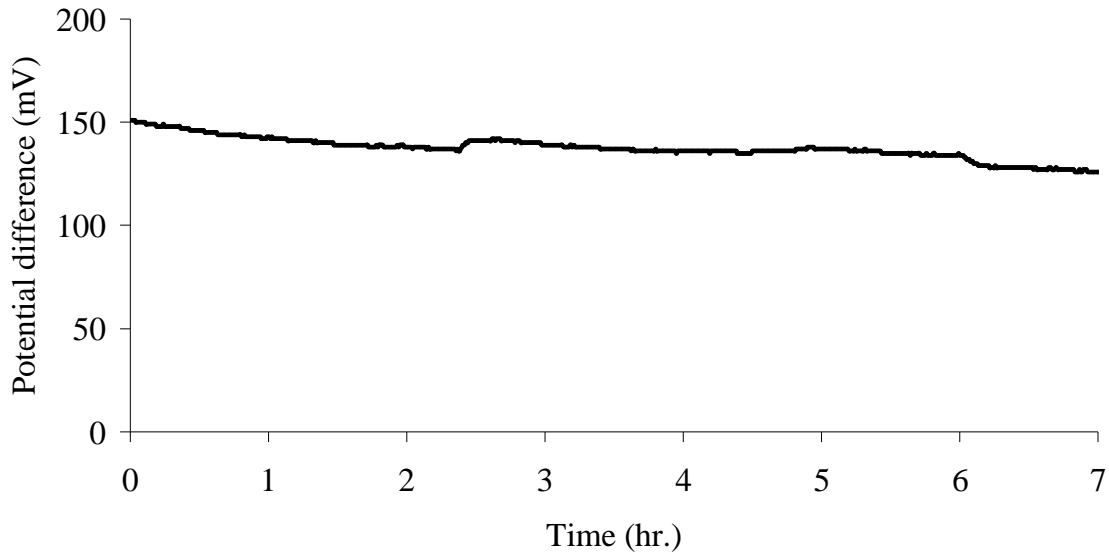


Figure 3. 15. Potential difference between calomel reference electrode and graphite in synthetic pore solution over an eight hour period.

The results show that graphite potential is reasonably stable for an interval of 15 to 20 minutes which is sufficient for most of the measurements made. Also, research conducted by Muralidharan et al. on three different embeddable reference electrodes (manganese dioxide (MnO<sub>2</sub>), metal-metal oxide (MMO) and graphite) in concrete and confirms the same behaviour for graphite [148]. It should be noted that the graphite stability may not be good for very sensitive measurements. In those applications, graphite should go through specific processes [149].

After choosing the materials for counter and reference electrodes, an electrode holder was designed specifically for the prism specimens and constructed from a PVC rod. As mentioned before, the length of each prism with different variable was 500 mm (Figure 3.4), and at least two measurements were needed for each sample. Based on these requirements, and ease of machining, a three section holder was designed: two for holding the graphite reference and

counter electrodes and one piece for keeping the constant distance between two other pieces.

Figure 3.16 shows a schematic plan of the design and the electrode holder.

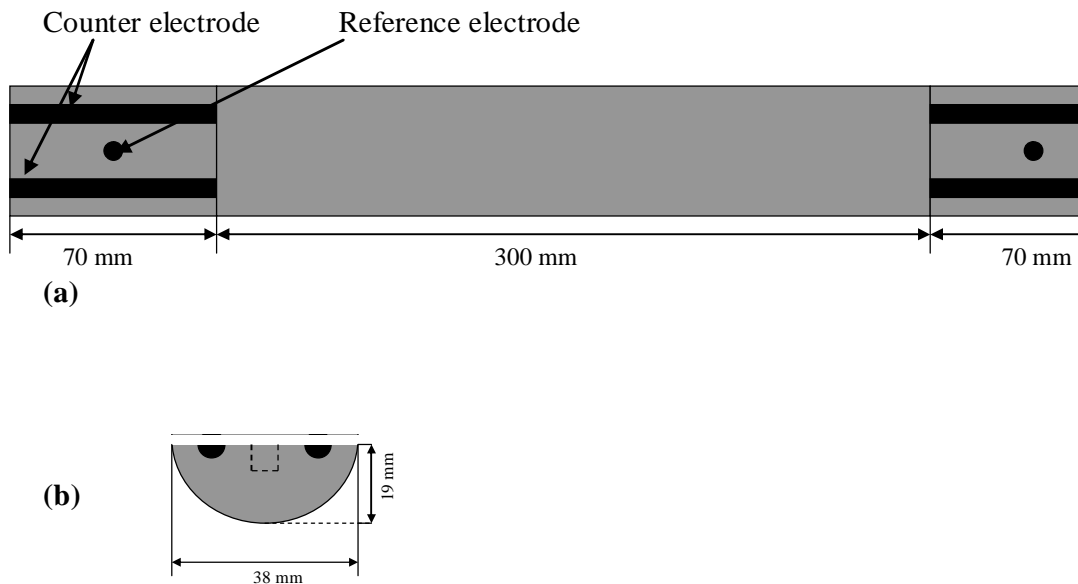


Figure 3. 16. Schematic plan of the electrode holder, (a) top view, (b) end view.

To ascertain that sufficient surface area is available for polarisation, two graphite rods were used as counter electrodes in each side. All graphite pieces were connected to the data acquisition system by wires.

### 3.2.3. Samples for determining the passivation time

For this experiment, two sets of samples have been made:

- a) Steel bars with two different surface conditions (as received with mill scale and sand blasted) embedded in mortar
- b) Steel bars with two different surface conditions (as received with mill scale and sand blasted) in synthetic pore solution.

The pore solution composition and the mortar proportions are given in Tables 2.5 and 3.4, respectively.

Table 3. 4. . Mortar mixture

| <b>Material</b>          | <b>Mass (kg)</b> |
|--------------------------|------------------|
| Cement, type 10 Portland | 250              |
| Sand                     | 750              |
| w/c ratio                | 0.45             |

Three sand-blasted and three as-received steel bars were used in each setup as illustrated in Figures 3.17 and 3.18. All samples were connected to an automatic data acquisition system (section 3.3.1.1.1) and the corrosion current density, using potentiostatic LPR, and half-cell potential of each steel bar, were monitored every hour. A Mn/MnO<sub>2</sub> electrode was used as a reference electrode and graphite rods were used as counter electrodes in both setups. In addition to electrochemical measurements, the surface condition of the steel bars, after immersion in pore solution for two months, was studied with Raman spectroscopy technique compared to the Raman spectra taken from a steel bar which had not been exposed to the solution. Results of the measurements are given in next Chapter.

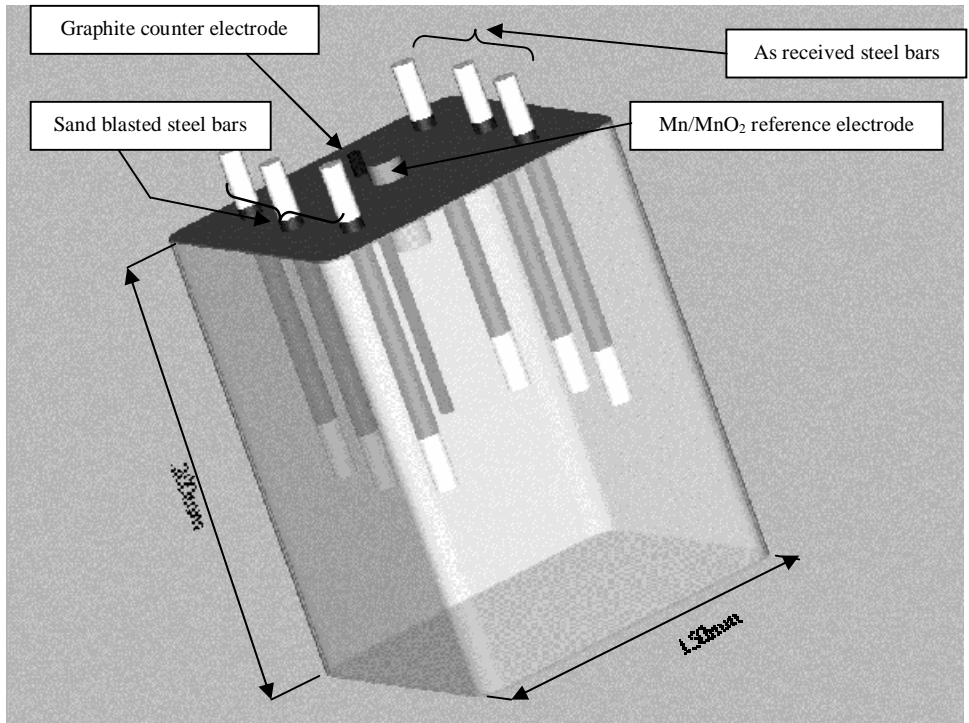


Figure 3. 17. Schematic isometric of the immersed steel bars in synthetic pore solution.

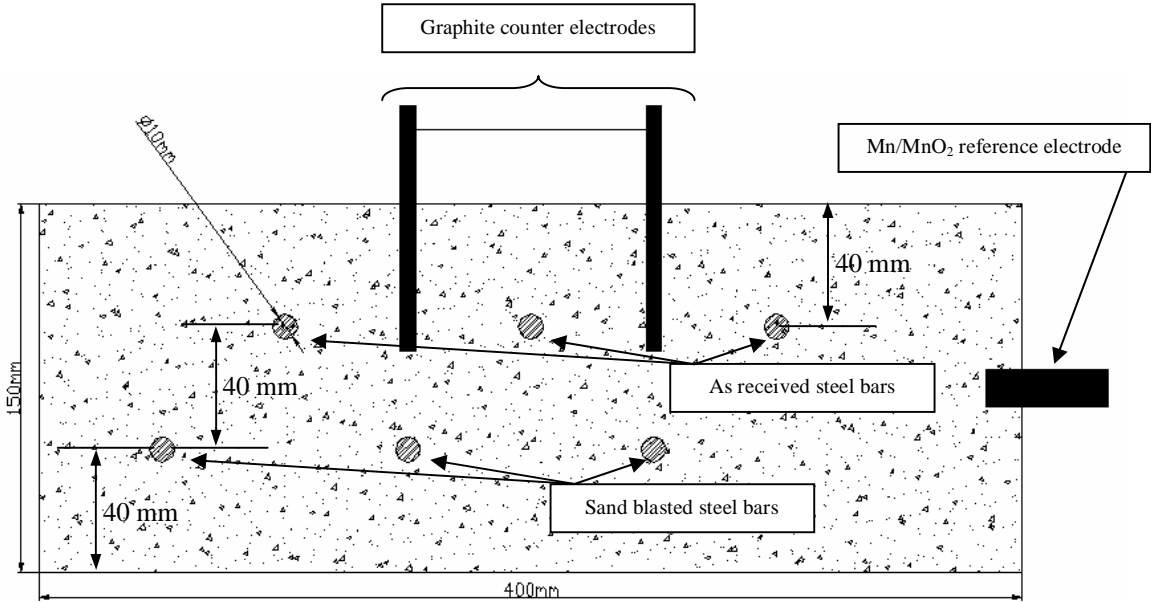


Figure 3. 18. Schematic section of the mortar sample with embedded steel bars.



### **3.3. MEASUREMENTS**

Two sets of measurements were made in this project: laboratory measurements and field measurements, as described below.

#### **3.3.1. Laboratory measurements**

The laboratory measurements were carried out on the steel reinforced concrete specimens described in the previous sections to identify the most accurate and reliable technique for determining the corrosion rate and to evaluate the effect of the different parameters on the half-cell potential values.

##### **3.3.1.1. Corrosion measurements**

To evaluate the corrosion activity of the steel bars in both sets of laboratory samples: beams with segmented steel bars and reinforced concrete specimens with different variables, potentiostatic LPR, galvanostatic LPR and half-cell potential measurements were carried out on the steel reinforced concrete specimens to identify the most accurate and reliable technique for determining the corrosion rate and to evaluate the effect of the different parameters on the half-cell potential values. The measurements were made about every two weeks for more than two and a half years. In addition to the previously mentioned techniques, cyclic polarisation and impedance spectroscopy were also performed on the specimens to verify the obtained results.

The theory and details of each of these techniques were explained in Chapter 2 and the results of the measurements are given in Chapter 4. Three potentiostats: PARSTAT<sup>®</sup> 2263, EG & G 273A and Solartron 1286 were used in this study. In addition, the Solartron 1260 impedance/gain analyser was used for EIS measurements and the GalvaPulse<sup>™</sup>, which was developed for field measurements, was used for measuring the corrosion rate and potential of steel in concrete.

#### **3.3.1.1.1. Automated Corrosion Monitoring Programme (ACMP) and measurement unit**

There are many commercially developed software programmes and hardware instruments for performing different electrochemical tests. However, for steel in concrete, large numbers of specimens must be tested (because of the inhomogeneity of concrete) over long periods of time (because of the changes in concrete with time). This can be tedious, leading to possible errors and less frequent measurements than would be desirable. To enhance and improve the accuracy by omitting the human errors and saving time, new user friendly software was developed and used in this study. In addition to the software, a measurement assembly unit for each specimen was designed and all specimens are connected to a data acquisition system through that measurement unit. The data acquisition system consisted of a computer, Keithley digital multi-metre and switcher models 2750, one of the above potentiostats and the new developed software which can communicate between all components of the system and gather the required data. The software is called Automatic Corrosion Monitoring Programme (ACMP) [150].

As described in Chapter 2, a counter electrode, is used to apply current to the working electrode (the rebar). The counter electrode is usually made of a relatively inert material, such as platinum, stainless steel or graphite to prevent it from dissolving in electrolyte. In this project,

for the concrete prisms with different variables, graphite is used as the counter electrode, because of low price, excellent conductivity, resistance to both salt solution and the high pH environment of concrete.

The potentiostats used are capable of performing only one measurement in a time. There are multi-channel units available on the market, but they have two limitations: first, most of the units are designed to do only maximum 16 measurements and secondly, a multi-unit system for the 58 measurements (two for 29 prisms) in this study would have been too expensive.

Keithley digital multi-metre and switcher were chosen for this project due to their sensitivity and high impedance. These models are robust and relatively easy to use. The Model 2750 mainframe has five slots for inserting the plug-in switch/control modules. Each slot can support a series of multiplexer, matrix, or control modules, and all the modules in a system operate simultaneously. Input modules can be mixed or matched to provide a broad range of measurement, acquisition, and control capabilities. In this project Module 7708 with 40 channels was used. The general features of Keithley 2750 and Module 7708 are given in Appendix B.

For each measurement, 3 channels were used, one for reference electrode, one for counter electrode and one for working electrode. Therefore, a Keithley 2750 mainframe with five 7708 modules can be used for 66 measurements. If more than 66 measurements are necessary, more Keithley mainframes can be joined together so provide the appropriate number of channels and there is no limitation for this purpose and this is one of the main advantages of this setup.

To combine the mentioned components, ACMP was developed, using LabVIEW 6.1. The computer was connected to Keithley by RS-232 serial port. If fast or real time data transfer

between Keithley and computer is required, a GPIB<sup>1</sup> card [151] should be used. The computer communicated with the potentiostat through a USB port or a GPIB board, based on the specific potentiostat. The role of ACMP is to control and switch the channels in 7708 module for each measurement, control and run the electrochemical software and potentiostat and save data to the computer for later analysis. This software is designed in a way to facilitate the use of electrochemical software. For this purpose, predefined configurations for techniques which were commonly used in the lab, were developed and appear on the main menu. These configurations can be modified based on the application. There are options which allow setting the number of samples, measurement frequency and the time between each set of measurements, if it is necessary. The display on the Keithley main frame can be also controlled by ACMP and a message can be shown on the display. The data are saved in MS-ACCESS<sup>®</sup> format and then can be transferred to Excel<sup>®</sup> or other graphical and mathematical software. Figure 3.19 shows a schematic diagram of the relationship between different parts of the measurement system and Figure 3.20 shows a view of the main page of the ACMP.

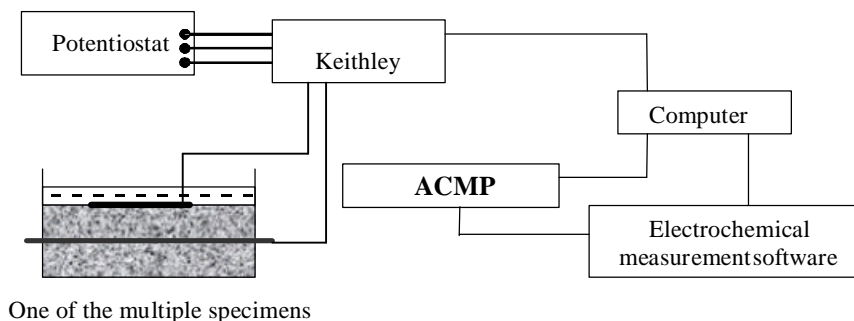


Figure 3. 19. Schematic diagram of the connections between different components of the automatic measurement system.

<sup>1</sup> “The General Purpose Interface Bus (GPIB) is an industry standard published by the Institute of Electrical and Electronic Engineers (IEEE) as ANSI/IEEE Standard 488. GPIB defines the electrical, mechanical, functional, and software specifications of an interfacing system to connect PCs to programmable instruments [11].

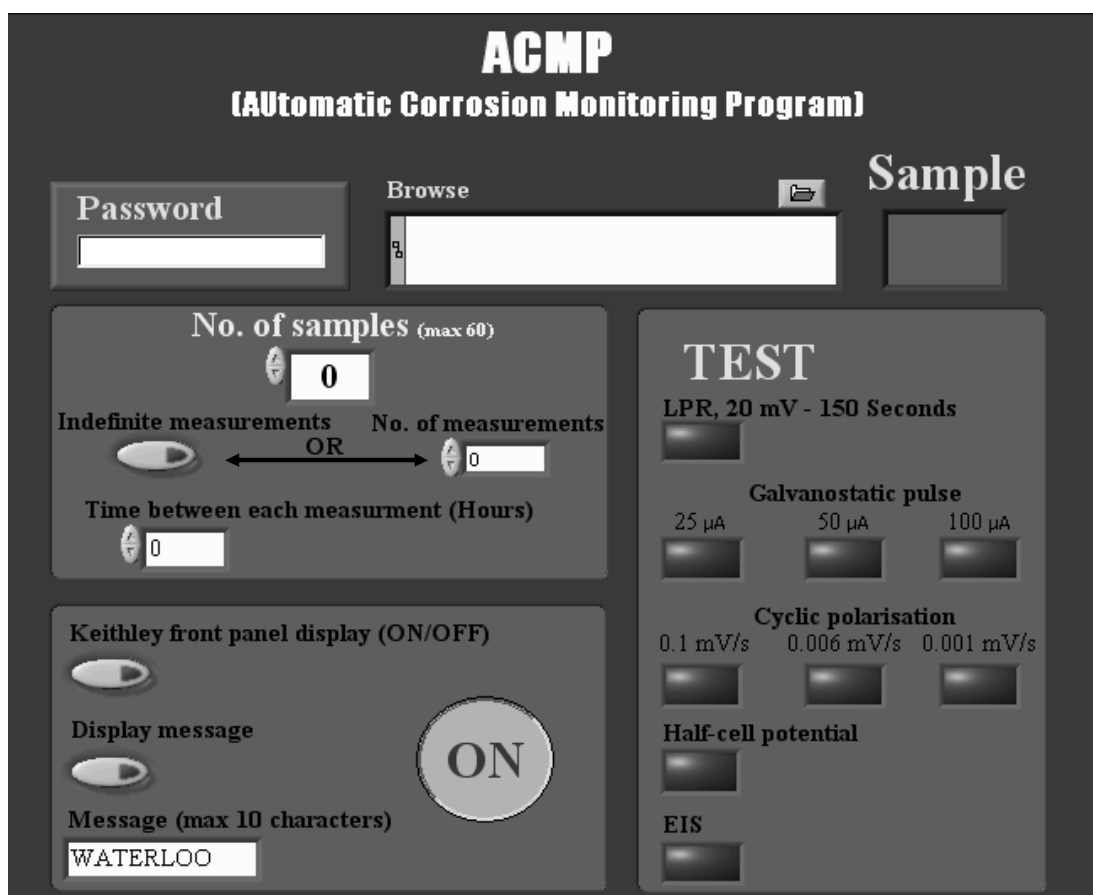


Figure 3. 20. A view of Automated Corrosion Monitoring Programme (ACMP).

Corrosion of some of the steel rebars was also measured by using the conventional measurement setup which is consisted of a calomel reference electrode and stainless steel counter electrode. Figure 3.21 is the comparison between, the results of potentiostatic LPR, measured by automated system and conventional setup. As can be seen, the differences between two setups are negligible. The automated measurement unit can be used effectively for a long time. The designed system, consisted of ACMP and measurement unit, is working without failure in this project for more than two years. Also, the programme has successfully been used in other projects at the University of Waterloo.

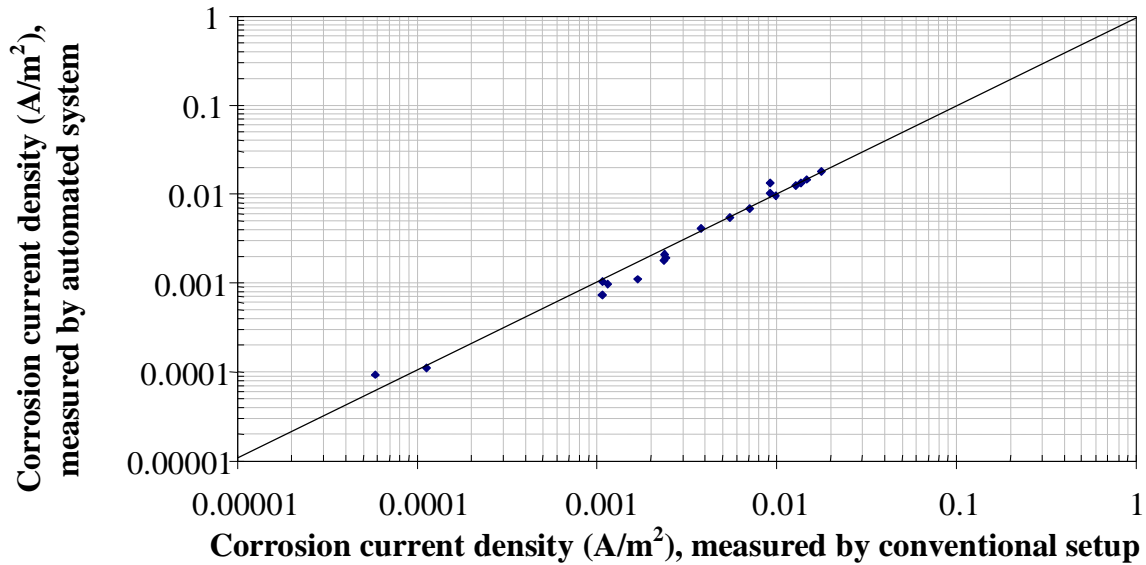


Figure 3. 21. Comparison between potentiostatic LPR measurements, measured by two different setups: designed setup and conventional setup.

### 3.3.1.2. Chloride content analysis

It was necessary to determine the chloride diffusion depth. For this purpose, a cylindrical-radius carbide drill bit was used to pulverise the concrete adjacent to the steel surface. The ASTM C1152 [152] standard with some modifications [144] was used to determine acid-soluble chlorides. Acid-soluble chloride consists of both free and chemically bound chlorides in the cement paste. The following procedures were performed to prepare the solution for the test:

1. Power was weighed to the nearest tenth of the milligram and transferred to a separate 250 ml beaker and then 120ml dilute nitric acid was added to the beaker.
2. Samples were dispersed thoroughly with a cleaned stirring rod.

3. Each beaker was covered with watch glass and heated on a hotplate until a soft boil was reached, then it was boiled for 5 minutes to release chlorides.
4. After boiling, the beakers were removed from hotplates and filtered through WHATMAN No. 541 filter paper into a 400 ml beaker. Beakers and stirring rods were rinsed by using hot distilled water at least three times into the filter until all residue was removed.
5. The filtrates were washed in the filter paper at least six times with hot distilled water to remove all chloride from solids. The filter paper was removed from the funnel and its exterior and the funnel rinsed three times into the beaker to remove any remaining chlorides.
6. Distilled water was added to the solution to increase its volume 250 ml. Then the filtrates cooled to room temperature.

After preparation, 50 ml of the solution was titrated against 0.1 M  $\text{AgNO}_3$  Using a Radiometer Copenhagen TIM 800 Titration Manager with ABU 901 Autoburette. One or two drops of methyl orange were added to the beaker to determine if the solution is acidic enough. If no colour change is observed, a few drops of concentrated nitric acid should be added to the prepared solution.

The titrant increments were added slowly to determine the equivalent point of chloride solutions which corresponds to the maximum change in millivolt occurring when the chloride solution is neutralised to a pH of about 7. To improve the accuracy of the chloride measurements, the amount of chloride was increased by adding 4ml of a sample with 0.025M NaCl to each solution.

The chloride concentration can be calculated by using the following equations:

$$V_{\text{sample}} = V_{\text{inf}} - \frac{V_s \times [\text{salt solution}]}{[\text{Titrant}]} \quad \text{eq 3. 1}$$

$$[\text{Cl}^-] = \frac{V_{\text{sample}} \times [\text{Titrant}]}{V_q} \quad \text{eq 3. 2}$$

where:

$V_{\text{sample}}$  = volume of titrant added for the sample (ml)

$V_{\text{inf}}$  = total volume of titrant added until inflection (ml)

$V_s$  = volume of salt standard added (ml)

[salt solution] = mean  $\text{Cl}^-$  standard concentration (mol/litre)

[Titrant] = molarity of  $\text{AgNO}_3$  titrant (mol/litre)

[ $\text{Cl}^-$ ] = concentration of chloride in the sample (mol/litre)

$V_q$  = original volume of the sample (ml)

### 3.3.2. Field measurements

With the cooperation of the Ministry of Transportation staff, both  $E_{\text{corr}}$  and  $I_{\text{corr}}$  measurements were made of the selected Ministry structures for validation of the laboratory observations.



### 3.3.2.1. Bridge at the University of Waterloo

A small bridge at campus of the University of Waterloo was chosen for the field measurements. Easy access to the bridge, the exposed deck and visible corrosion of the steel bars in both approaches were the main reasons for this choice. Figure 3.22 shows pictures of the bridge and Figure 3.23 is a schematic diagram of the bridge with its dimensions. Half-cell potential measurements and, at different times during about a three year period, galvanostatic pulse LPR technique using the GalvaPulse™ were performed on the bridge. Some attempts were made to use a conventional potentiostat to perform other electrochemical tests such as cyclic polarisation, EIS and potentiostatic LPR. Only the cyclic polarisation technique proved successful. For the measurements rebars were located by Micro Covermeter™ 7000-MC-89, made by Kolectric Ltd., rebar locator and all the results, which are given in the next chapter, were shown as the contour map. The actual values are given in Appendix C. It should be noted that the steel bars are located every foot (~30 cm), but the measurements were made every three feet.



Figure 3. 22. (a) A view of the bridge at the University of Waterloo, (b) some of the deteriorated spots on one of the approaches.

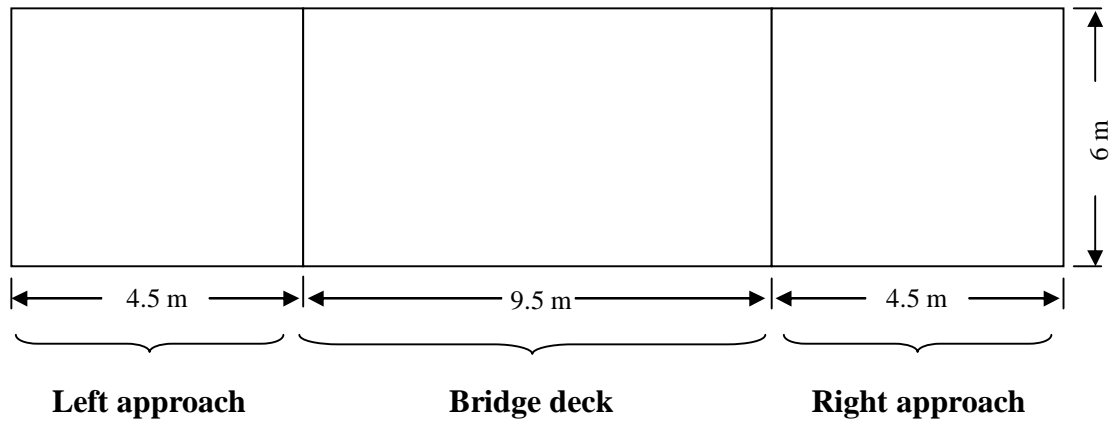


Figure 3. 23. Schematic plan of the bridge at the University of Waterloo.

In spite of the good appearance of the bridge deck, the potential values of the steel in the bridge deck were very negative while the corrosion current densities indicated that the steel bars are in good condition. Therefore, with the cooperation of the Ministry of Transportation staff, two cores were taken from two different locations and the visual observation of the reinforcing steel showed that epoxy coated bars were used (Figure 3.24). For that reason, the measurements were limited to the two approaches.



Figure 3. 24. Epoxy coated steel bar used in the deck of the bridge at the University of Waterloo.

### **3.3.2.2. Victoria Street Bridge, Wingham, Ontario**

The second field test location was a 37 year old bridge on Victoria Street in Wingham, Ontario over the Maitland River (Figure 3.25). This is a post-tensioned bridge with galvanized steel rebars. Visual observations showed no evidence of corrosion on the surface of the bridge deck. Half-cell potential measurements and galvanostatic LPR, using GalvaPulse™ were performed on the bridge and the results are given in Chapter 4.



Figure 3. 25. Location of the Victoria street Bridge, Wingham town, Ontario, Canada

### 3.3.2.3. Barrier walls, Renfrew

The third field tests were carried out on barrier walls in HWY 17 west of Ottawa, approximately 2 km east of Renfrew, Ontario (Figure 3.26). The walls were installed in 1975 and they have been repaired several times but corrosion products were visible in some spots. Figure 4.27 shows walls from two different views. The location of the repaired part can be seen in Figure 3.27 (a).



Figure 3. 26. Location of the barriers walls, Renfrew, Ontario



Figure 3. 27. (a) a view of the barriers wall, from the road, (b) the other side of the wall.



In addition to half-cell potential measurements using standard Cu/CuSO<sub>4</sub> reference electrode, GalvaPulse™ was used to determine the corrosion current density and corrosion potential of the reinforcing steel. Also attempts were made to perform EIS, cyclic polarisation resistance, potentiostatic LPR, galvanostatic LPR and galvanodynamic LPR tests on the steel bars using the PARSTAT® 2263 potentiostat. Galvanostatic LPR, using 3LP equipment provided by MTO, was also used. Figure 3.28 shows the setup used for electrochemical measurement techniques which were mentioned above. Results are given in the next chapter.



Figure 3. 28. The setup consisted of PARSTAT® 2263 potentiostat, reference and counter electrodes and the computer, used for performing electrochemical tests of the steel bars in the barrier walls, Renfrew, Ontario.

#### 3.3.2.4. Island Park Avenue bridge, Ottawa

The fourth field location was a bridge in HWY 417, on the Island Park Dr. overpass in Ottawa, Ontario. This bridge was constructed in 1961, rehabilitated in 1983 and is currently severely deteriorated due to rebar corrosion. Figure 3.29 illustrates the location of the bridge on the map and Figure 3.30 shows pictures of the some of the corroded areas.

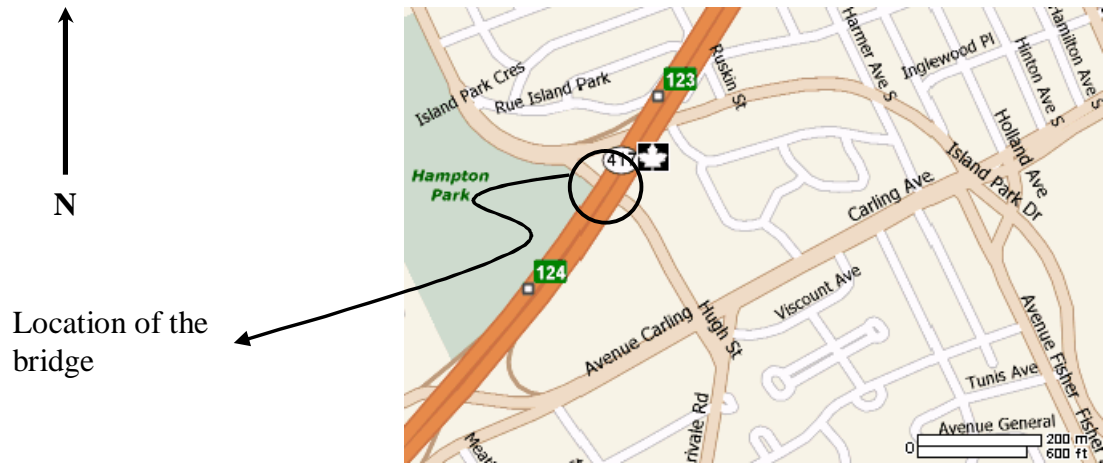


Figure 3. 29. Island Park bridge, Ottawa, Ontario.



Figure 3. 30. Photograph from Island Park Bridge, Ottawa, Ontario (a) corrosion of the steel bars of one of the approaches of the bridge, (b) repaired areas of the bridge, (c) corrosion underneath the bridge deck and (d) severely corroded spot on one of the approaches.

Half-cell potential test was made as an essential evaluation technique. Potentiostatic LPR, galvanostatic LPR (made with GalvaPulse™ and PARSTAT® 2263 potentiostat), EIS, cyclic polarisation, galvanodynamic LPR (made with 3LP) were used to evaluate the corrosion condition of the steel bars in this structure. Results are given in the next chapter.



## **CHAPTER 4, EXPERIMENTAL RESULTS AND DISCUSSION**

### **4.1. RESULTS FROM LABORATORY MEASUREMENTS**

#### **4.1.1. Beams with segmented steel bars**

Two sets of measurements were carried out on the beams with segmented steel bar: electrochemical corrosion measurements and gravimetry. The results are given in the following sections.

##### **4.1.1.1. Electrochemical corrosion measurements**

Corrosion activity of the segmented bars was monitored every two weeks by (i) half-cell potential, (ii) potentiostatic LPR and (iii) galvanostatic LPR using GalvaPulse™. In addition; cyclic polarization, EIS, galvanostatic LPR and galvanodynamic LPR (using PARSTAT® 2263 or Solartron 1286) were also used to confirm the results and provide more information about the techniques, equipment and corrosion behaviour of the embedded steel segments. In addition, the concrete resistance was measured by GalvaPulse™, with and without guard ring and the results were compared to those obtained from EIS, galvanostatic pulse technique and four-probe technique.

#### 4.1.1.1.1. Half-cell potential

In each prism, segments 1 and 2 are in chloride-free concrete and segment 3 and 4 are in chloride-contaminated concrete as shown in Figure 4.1.

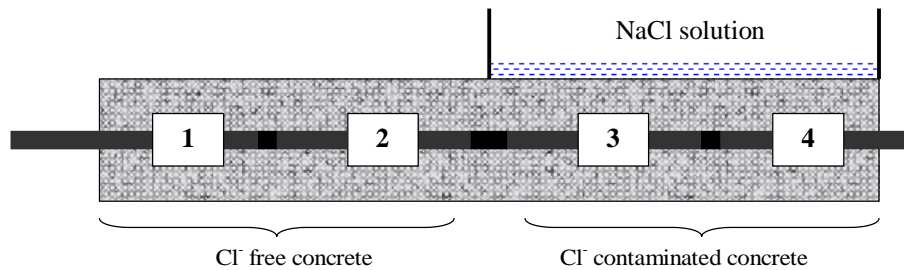


Figure 4. 1. Segments designation for each beam.

Figures 4.2 and 4.3 shows the half-cell potential values measured vs. Cu/CuSO<sub>4</sub> reference electrode for the chloride-free and chloride-contaminated sections of the beams, respectively. The blue lines indicate the ASTM C876 guidelines for interpretation of the data. It should be mentioned that all segments in beam D were short-circuited due to inadequate insulation or inappropriate vibration. Also, after 35 weeks, wire was disconnected from segments A3.

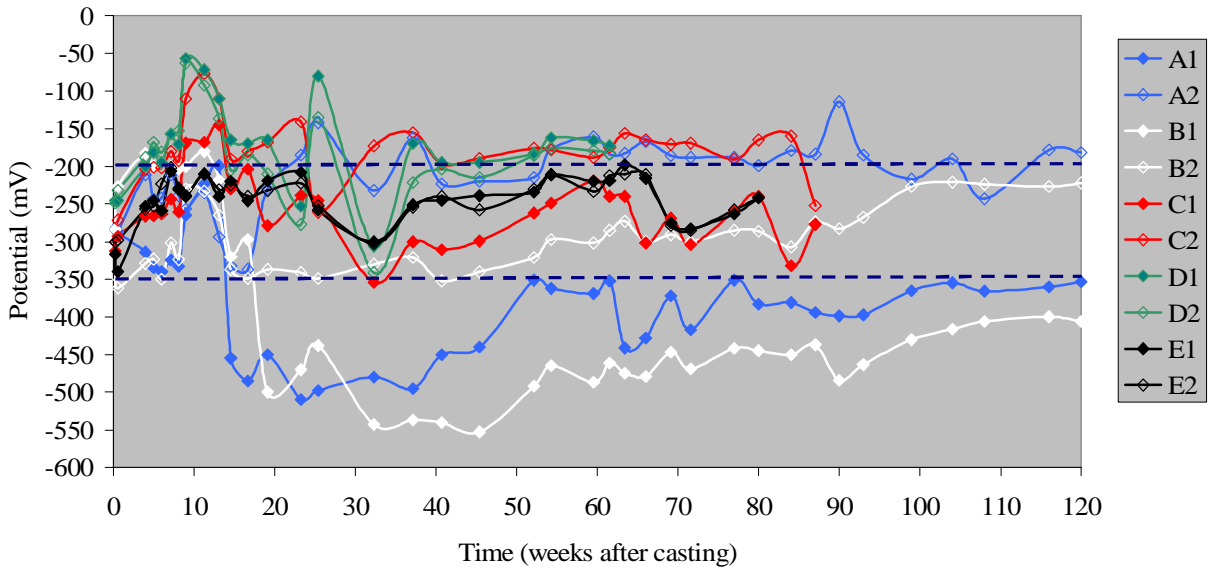


Figure 4. 2. Half-cell potential values of the segmented steel bars, chloride-free section.

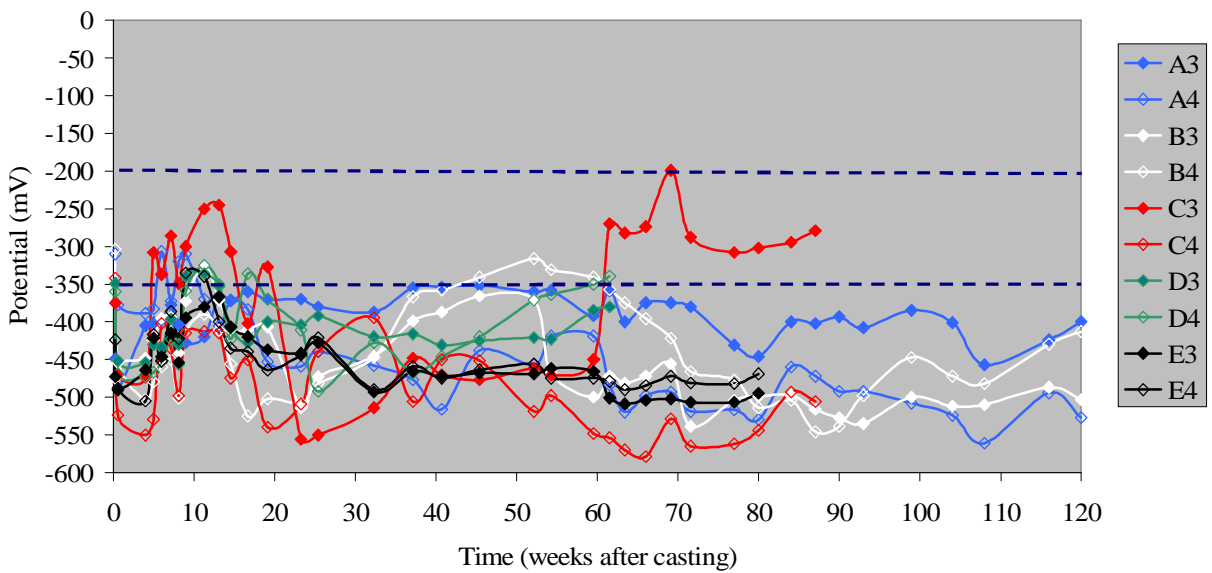


Figure 4. 3. Half-cell potential values of segmented steel bars, chloride-contaminated section.

As can be seen, in the chloride-contaminated concrete, most of the segments from the first measurement show the potential more negative than -350 mV vs. CSE indicating that there is a 90% probability of active corrosion according to ASTM C876. However, the potential of most segments in chloride-free concrete is in region between -200mV and -350mV vs. CSE for which the probability of active corrosion is uncertain. It should be noted that there was leakage from the ponding well on chloride-contaminated section to the  $\text{Ca(OH)}_2$  solution in the trough and therefore, the chloride-free section was also exposed to chloride ions but to a lower extent. There are major fluctuations in potential for all sections about 3 months after casting but, after that period, the potentials are more stable. The unusual behaviour of segment C3 is due to applying +300mV potential vs. SCE from week 19 for 4 weeks to that segment to accelerate the diffusion of chloride from the ponding well into the concrete. The beams were broken at different times and after that time, there are no points for that beam in the given Figures.

The potential of the segments was also monitored by Ag/AgCl reference electrode (embedded in GalvaPulse™ measurement unit) for the same period of time and the results are shown in Figures 4.4 and 4.5. It is clear that the half-cell potential values measured by two different reference electrodes shows similar behaviour.

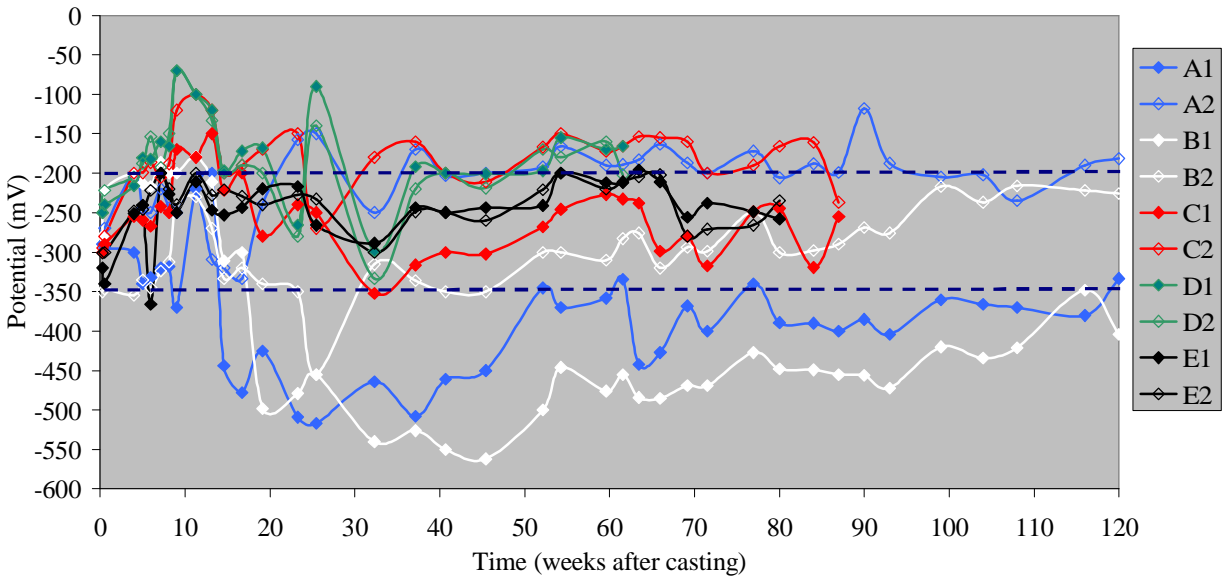


Figure 4. 4. Half-cell potential values of segmented steel bars, measured by Ag/AgCl and converted to CSE, chloride free section.

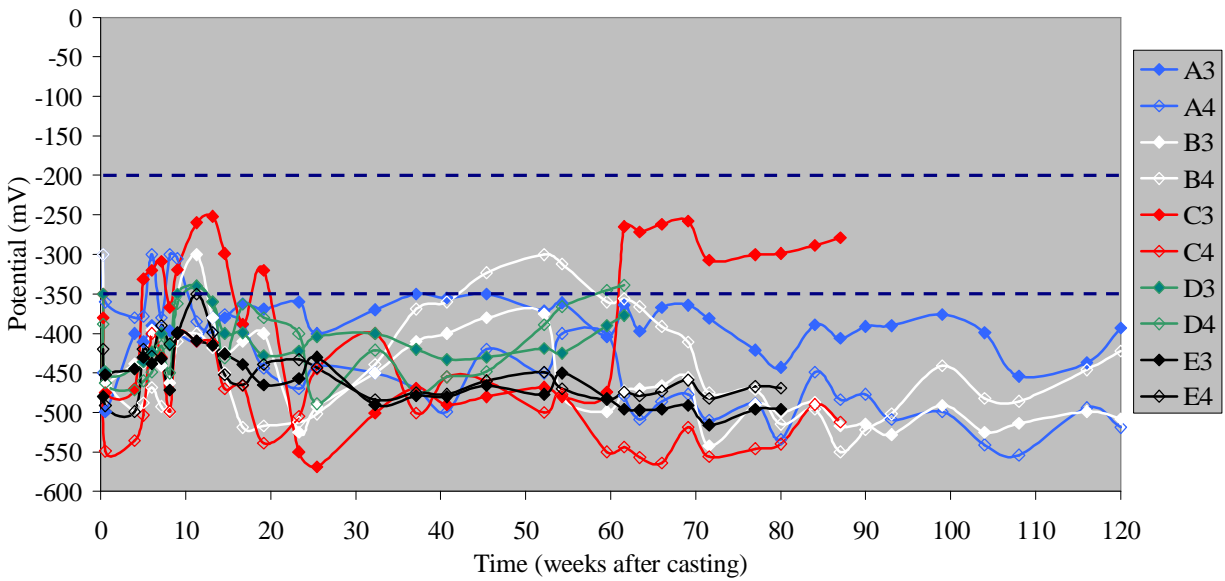


Figure 4. 5. Half-cell potential values of segmented steel bars, measured by Ag/AgCl and converted to CSE, chloride contaminated section.

The half-cell potential values of all bar segments, in chloride-free section of the beams, except A1 and B1, are more positive than -350 mV vs. CSE, which is in uncertainty region of the ASTM C876 recommendation. The potential fluctuated considerably at the beginning of the test (with the first ~6 months after casting); but were more constant after this time, implying the steel bars are in a more stable state. The isolation of all segments in Beam D and segments E2 and E3 was not good and the segments were electrically connected. This could have occurred during vibration of the concrete. As mentioned in Chapter 3, a ponding well was installed on top of the chloride-contaminated section of each to accelerate corrosion on that section. However, the ponding well of beams A and B leaked and the salt solution in the ponding well of those beams dropped into the trough underneath the beams. Therefore, the water in the trough of beams A and B was actually chloride-contaminated but not to the extent of salt solution in the well. The more negative potentials of segments A1 and B1 are attributed to this problem.

The half-cell potential of all the segments in chloride-contaminated sections, except for C3, are all more negative than -350 mV. The +300 mV potential with respect to half-cell potential after 60 weeks on segment C3 was the reason of such a behaviour. The similar half-cell potentials were obtained by using Ag/AgCl reference electrode confirming the accuracy of the measurements.

#### **4.1.1.1.2. Potentiostatic and galvanostatic LPR**

Figures 4.6 and 4.7 show the corrosion current densities of the steel segment, measured by potentiostatic LPR technique, using PARSTAT<sup>®</sup> 2263. For the calculations, 21.98 cm<sup>2</sup> was considered the surface area of each steel segment. This corresponds to 7 cm of the length of each 10M rebar segment which is the length width which the GalvaPulse<sup>™</sup> confines the

polarisation with the guard ring. The actual corrosion current density values are shown in Appendix D.

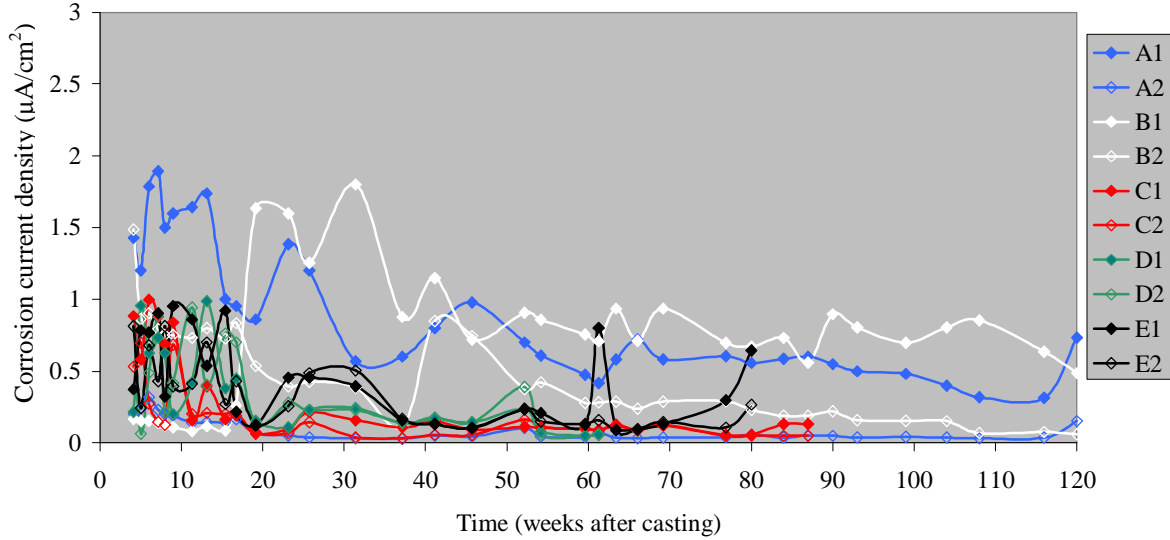


Figure 4. 6. Corrosion current density of the segmented steel bars, measured by potentiostatic LPR, chloride-free section.

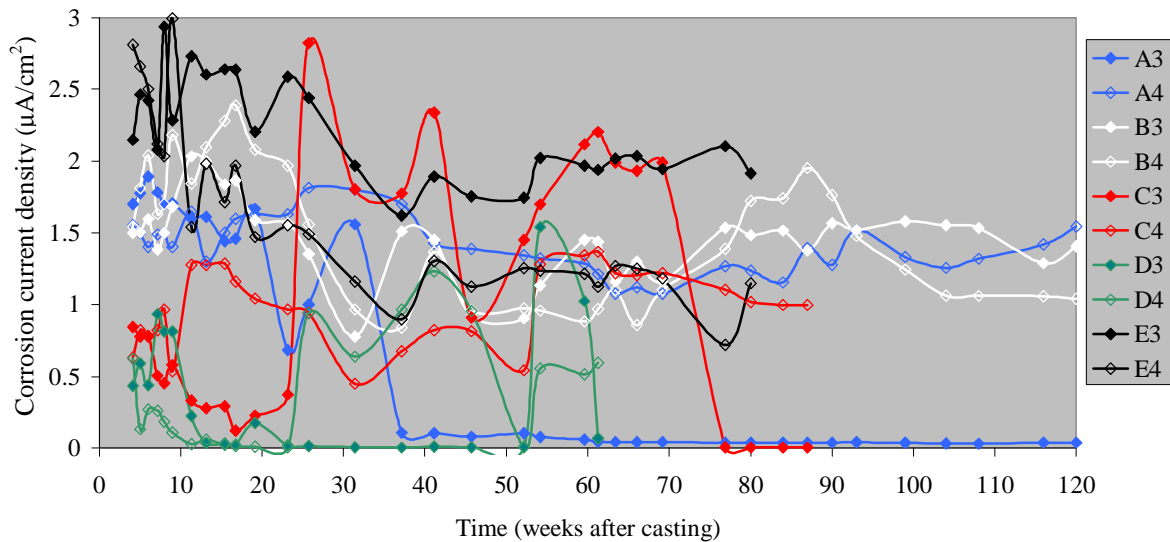


Figure 4. 7. Corrosion current density of the segmented steel bars, measured by potentiostatic LPR, chloride-contaminated section.

As can be seen, after 35 weeks, there is no measurement for segment A3 due to the connection problem.

Figure 4.8 and 4.9 show the corrosion current densities of the steel segments, measured by GalvaPulse™.

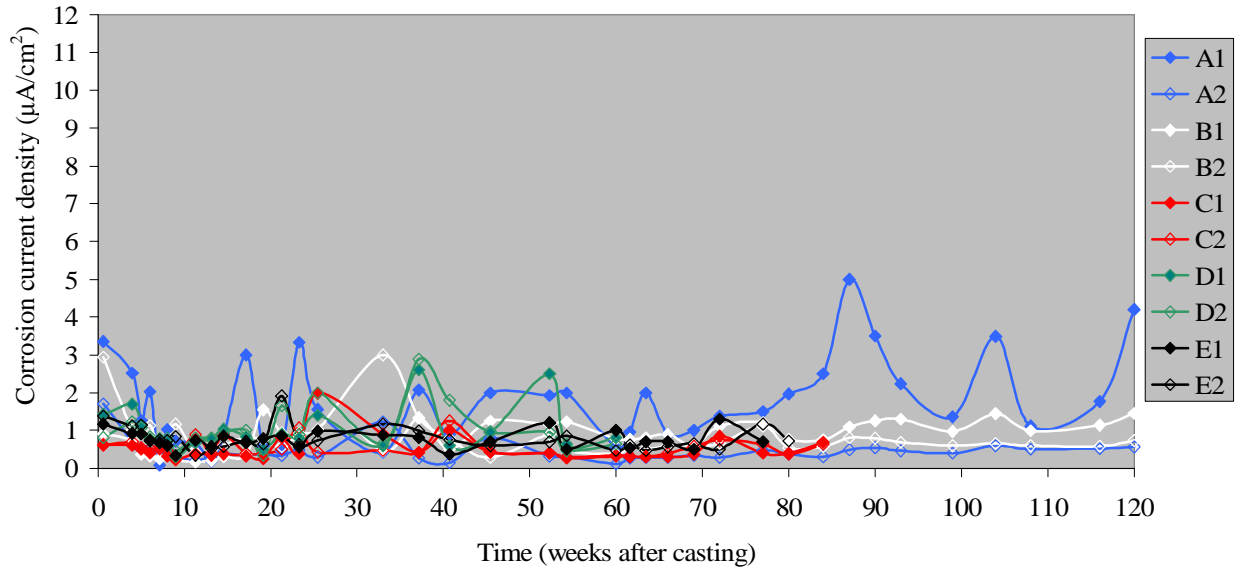


Figure 4. 8. Corrosion current density of the segmented steel bars, measured by GalvaPulse™, chloride-free section.

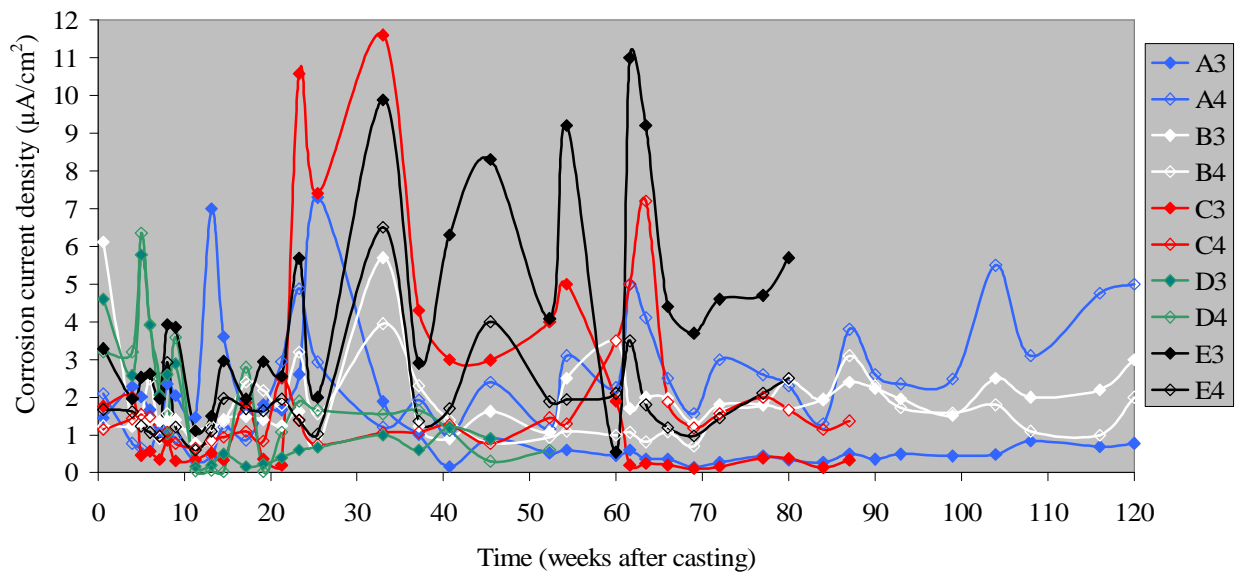


Figure 4. 9. Corrosion current density of the segmented steel bars, measured by GalvaPulse™, chloride-contaminated section.



It was realised that at the beginning of the measurement the corrosion current densities were higher than what was expected in high alkaline environment when the steel is expected to be in its passive state. This can be attributed to the fact that the measured  $R_p$  represents the current exchange of the redox process ( $Fe^{2+} \leftrightarrow Fe^{3+}$ ) in the passive layer [19, 153-155]. At potentials more positive than -200mV vs. CSE, two processes act together at the metal/concrete interface the corrosion process ( $Fe \rightarrow Fe^{2+} + 2e^-$ ) and the phase transformation in oxide layer according to the following process:



As the value of the corrosion potential becomes more positive, more  $Fe^{3+}$  presents in the oxide layer and consequently, the redox process contributes in whole process in more extend [153]. Therefore, due to the redox process, the measured corrosion current densities at the beginning of passivation of steel do not represent the actual steel dissolution. It should be noted that this fact is not noticed clearly when the steel is showing active corrosion. It seems that in active corrosion, the redox process is masked by faradaic process [155].

The corrosion current densities, measured by potentiostatic LPR technique, show that all of the segments in chloride-contaminated sections were actively corroding. The fluctuations observed for C3 are due to the application of the potential and for segments A3, D3 and D4 is due to electrical connections. It should be noted that because the chloride was mixed to the concrete in chloride-contaminated section, not enough time was provided to each steel segment to passivate itself and even at the beginning of the measurements, the bars show active corrosion rates. Corrosion measurements, performed by potentiostatic LPR, show that all the segments

except A1 and B1 were not actively corroded and the corrosion current density was about  $0.25 \mu\text{A}/\text{cm}^2$ . Measurements carried out by GalvaPulse™ show at least two times higher values than values obtained by the potentiostatic LPR for similar segments. It should be noted that in all the measurements, the guard ring in GalvaPulse™ was used and therefore this difference could be due to a higher current applied by the GalvaPulse™. Current densities measured by the GalvaPulse™ show more fluctuations. These behaviours could be attributed to the fact that, applying the appropriate current by GalvaPulse™ to stay in the linear region of the potential versus current curve is a difficult task, while in the potentiostatic LPR, the applied potential is constant and certainly is in the linearity range. These points will be discussed later in more detail.

### 4.1.1.1.3. Electrochemical impedance spectroscopy

Figure 4.10, shows the Nyquist plot for the steel segments in beam C, 88 weeks after casting. The frequency range was between 2MHz and 1mHz and the potential amplitude was 10mV.

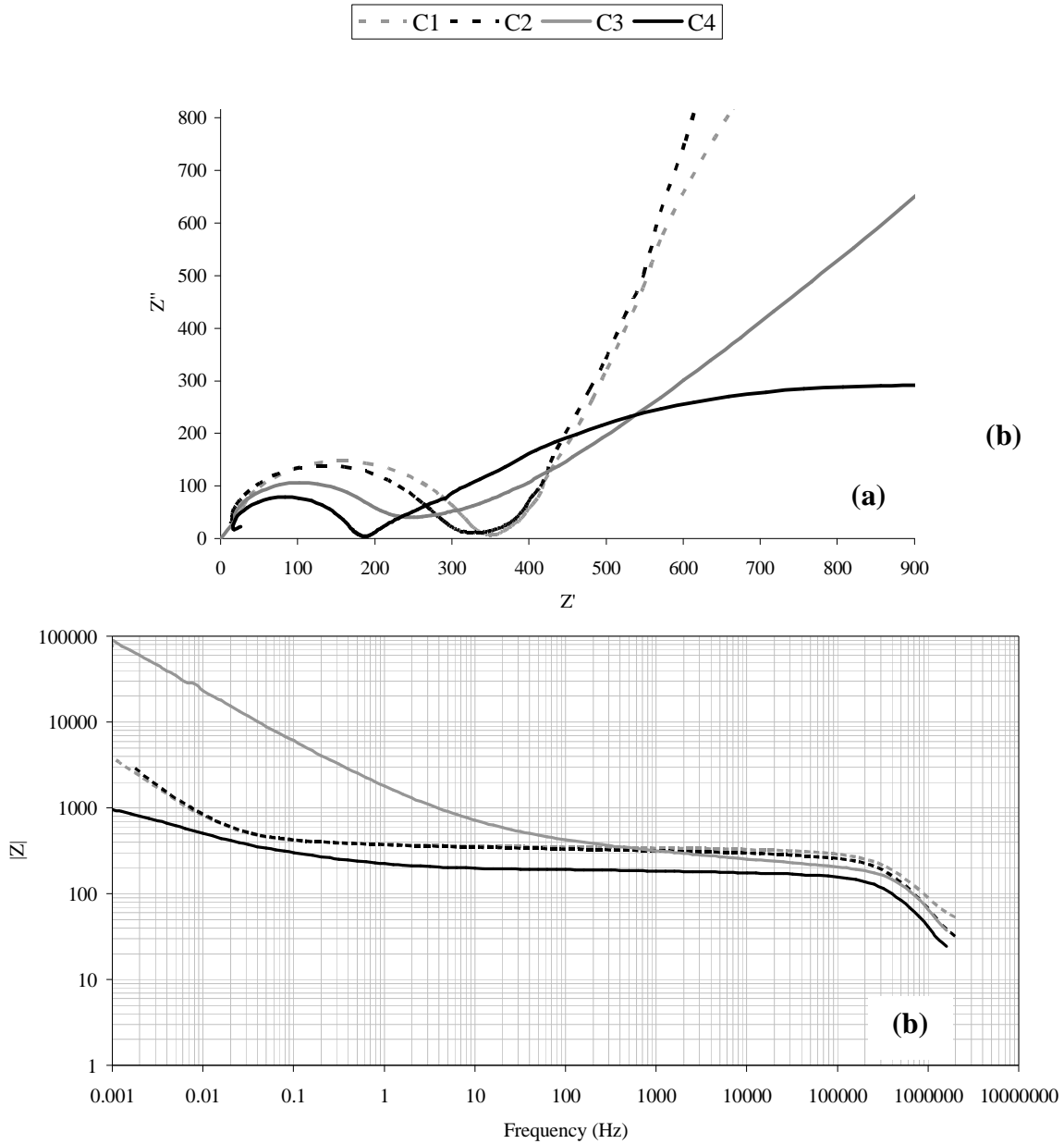


Figure 4. 10. Nyquist (a) and Bode (b) plots for the steel segments of beam C, 88 weeks after casting.

The diameter of the first semi-circle in each curve is considered to correspond to the concrete resistance and capacitance and the second, large, incomplete one represents the Helmholtz double layer and the polarisation resistance ( $R_p$ ). Therefore, Figure 4.10 shows that both concrete resistance and  $R_p$  for chloride-free concrete are higher than the same in chloride-contaminated concrete. Because the second semi circles are incomplete, the value of  $R_p$  can not be determined directly from plots in Figure 4.10 and the curves need to be extrapolated. Figures 4.11 and 4.14 show the extrapolated Nyquist and Bode plots for segments C1 and C4 respectively and it should be noted that the scales for plots differ by factor of 10. For extrapolation, the Kramers-Kronig [156, 157] method with ZSimpWin software was used. The solid points in each curve correspond to the calculated data and the open points are measured data. The difference between the experimental and the calculated (using Kramers-Kronig method) values ( $X$ ) of the real and imaginary impedance determines if the obtained results from the EIS test can be fitted to an equivalent circuit, and consequently, extrapolated or not. If  $X^2$  is less than  $10^{-6}$ , the experimental results show excellent agreement with the results calculated by the Kramers-Kronig method. If  $10^{-6} < X^2 < 10^{-5}$ , the agreement is reasonable;  $10^{-5} < X^2 < 10^{-4}$  shows marginal condition and  $X^2 > 10^{-4}$  indicates that the experimental results cannot be used to determine the equivalent circuit for extrapolation and if they used for the extrapolation, the results would show insufficient curvature or unreal loop(s). The reasons of getting such not valid data from the EIS experiment can be: high external noise during the experiment, measurement at non-stationary or non-stable electrodes, measurements at non-steady state, non-linear effects (using high amplitude potential) and instrumental limitations [157, 158].

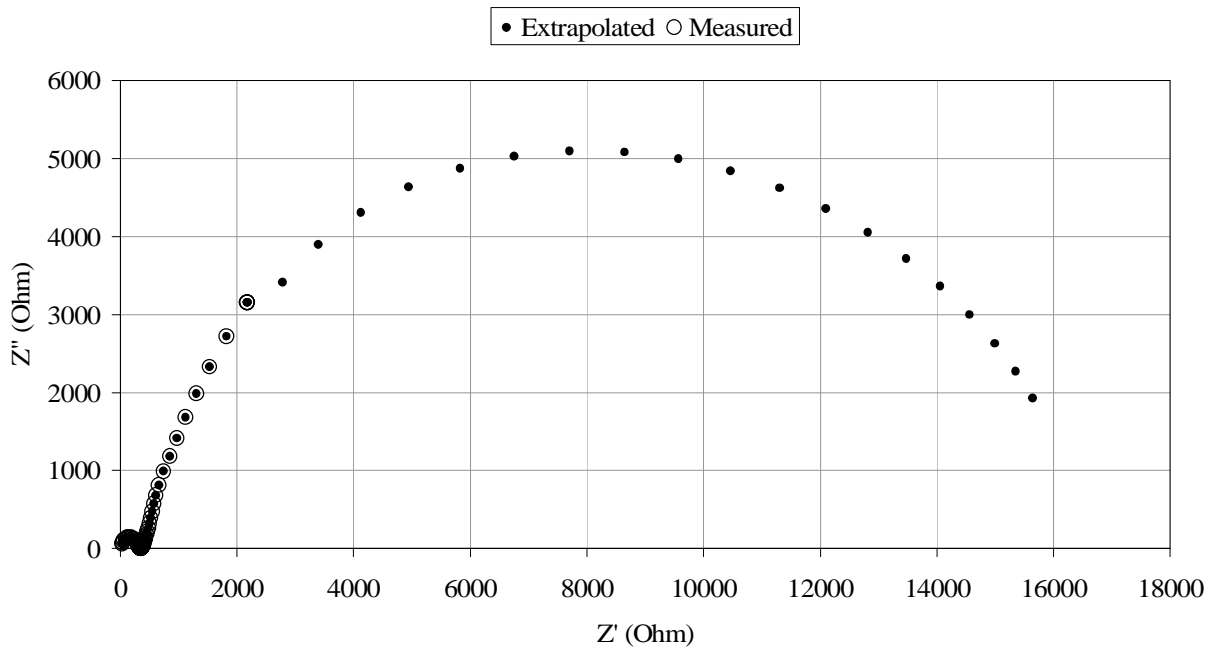


Figure 4. 11. Extrapolated Nyquist plot for segment C1 in chloride-free concrete.

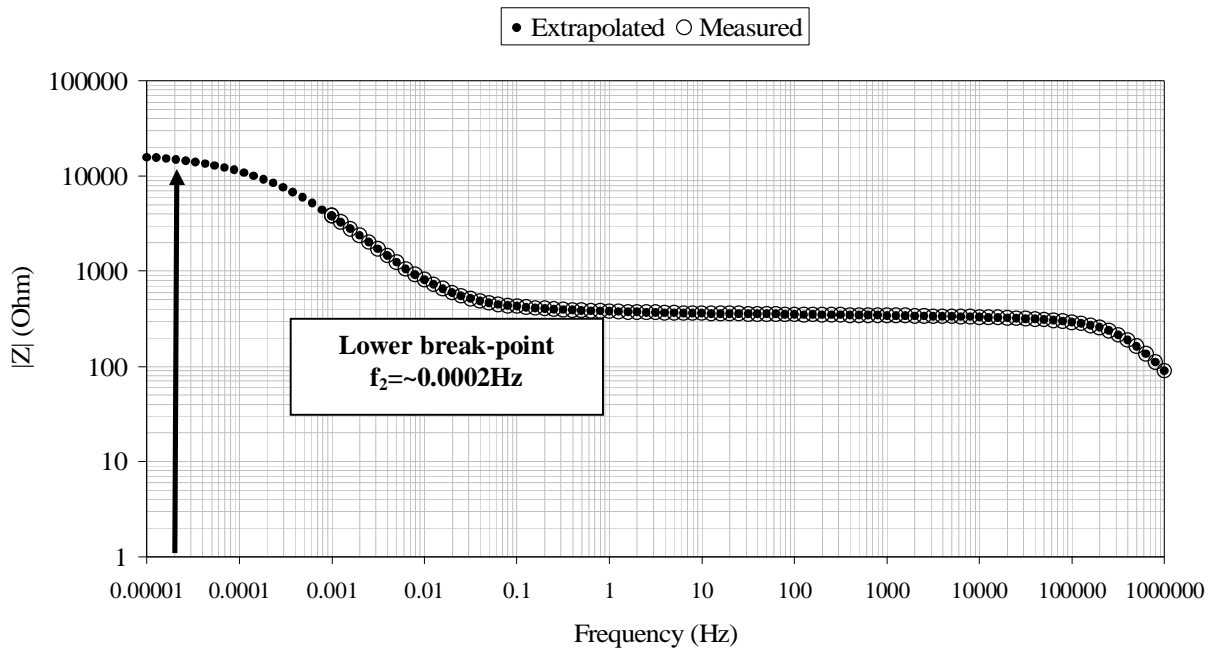


Figure 4. 12. Extrapolated Bode plot for segment C1 in chloride-free concrete.

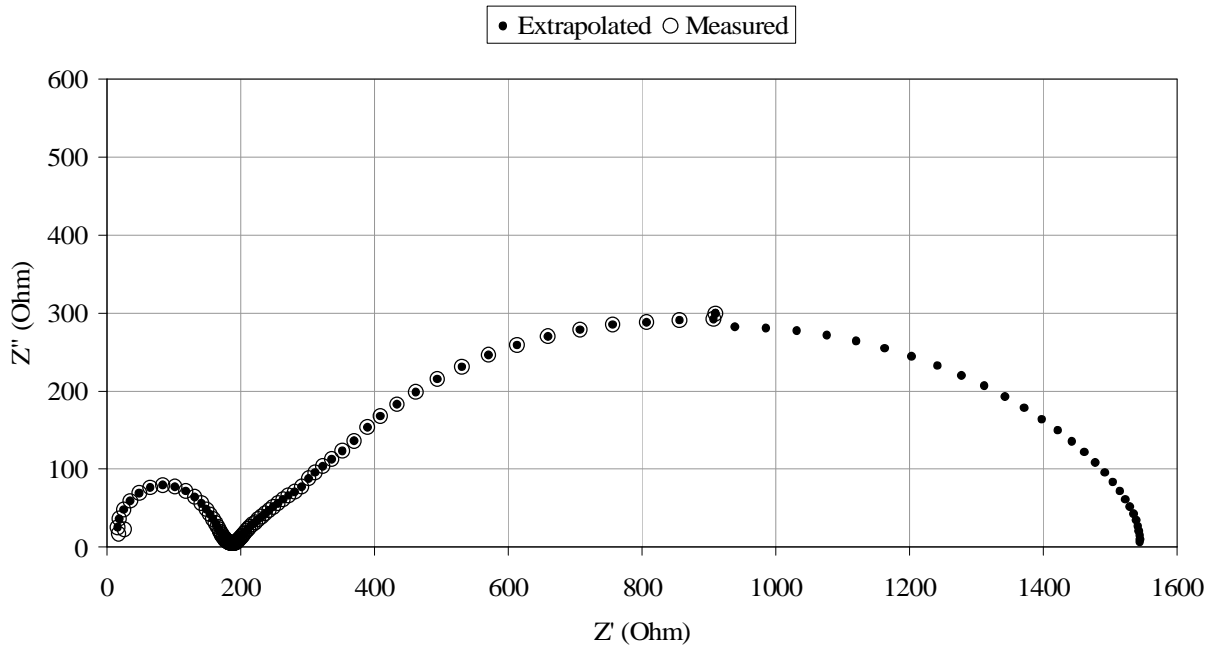


Figure 4. 13The extrapolated Nyquist plot for segment C4 in chloride-contaminated concrete.

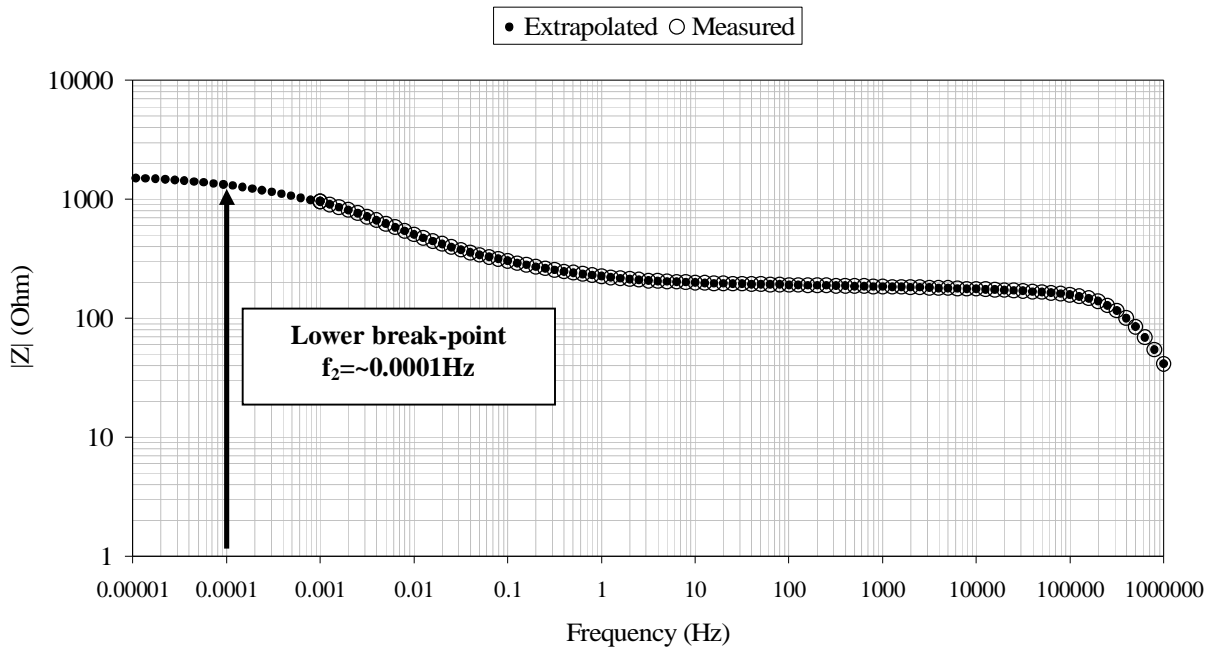


Figure 4. 14. The extrapolated Bode plot for segment C4 in chloride-contaminated concrete.

From Figures 4.12 and 4.14, the lower break point ( $f_2$ ) and consequently, the value of  $f_{\max}$  can be determined. These data have been used to determine the appropriate scan rate for potentiodynamic cyclic polarisation. By using eq. 2.36, the maximum scan rate,  $S_{\max}$ , can be calculated as following:

$$\text{C1: } S_{\max} = \pi \cdot \Delta E \cdot f_{\max} < \frac{\pi \cdot \Delta E \cdot f_2}{10} = \frac{3.14 \times 10 \times 0.0002}{10} \approx 0.0006 \text{ mV/s}$$

$$\text{C4: } S_{\max} = \pi \cdot \Delta E \cdot f_{\max} < \frac{\pi \cdot \Delta E \cdot f_2}{10} = \frac{3.14 \times 10 \times 0.0001}{10} \approx 0.0003 \text{ mV/s}$$

Where  $\Delta E$  is the peak-to-peak amplitude (usual 10mV). Figures 4.15 and 4.16 show the extrapolated Nyquist and Bode plots for segment A1. The test was carried out after 63 weeks after casting and the frequency range was between 1MHz and 0.05Hz. As can be seen in Figure 4.15, the experimental data could not be fitted in Kramers-Kronig method and at the end (low frequency) an inductance loop appears.

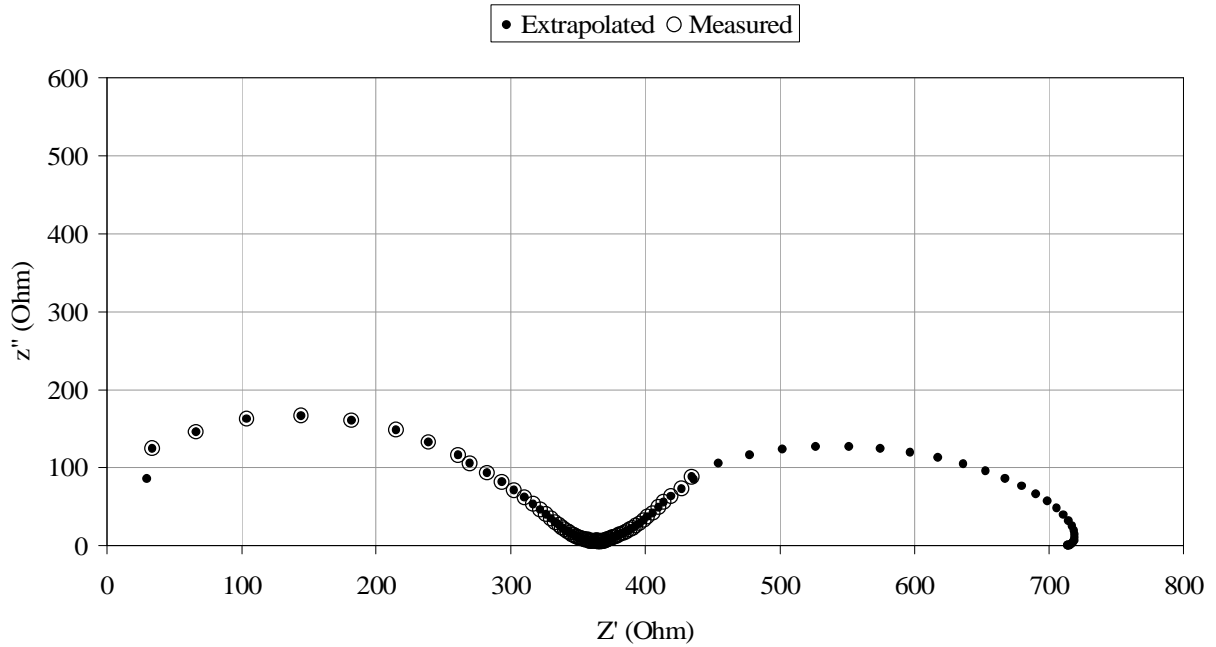


Figure 4. 15. Extrapolated Nyquist plot for segment A1 in chloride-free concrete.

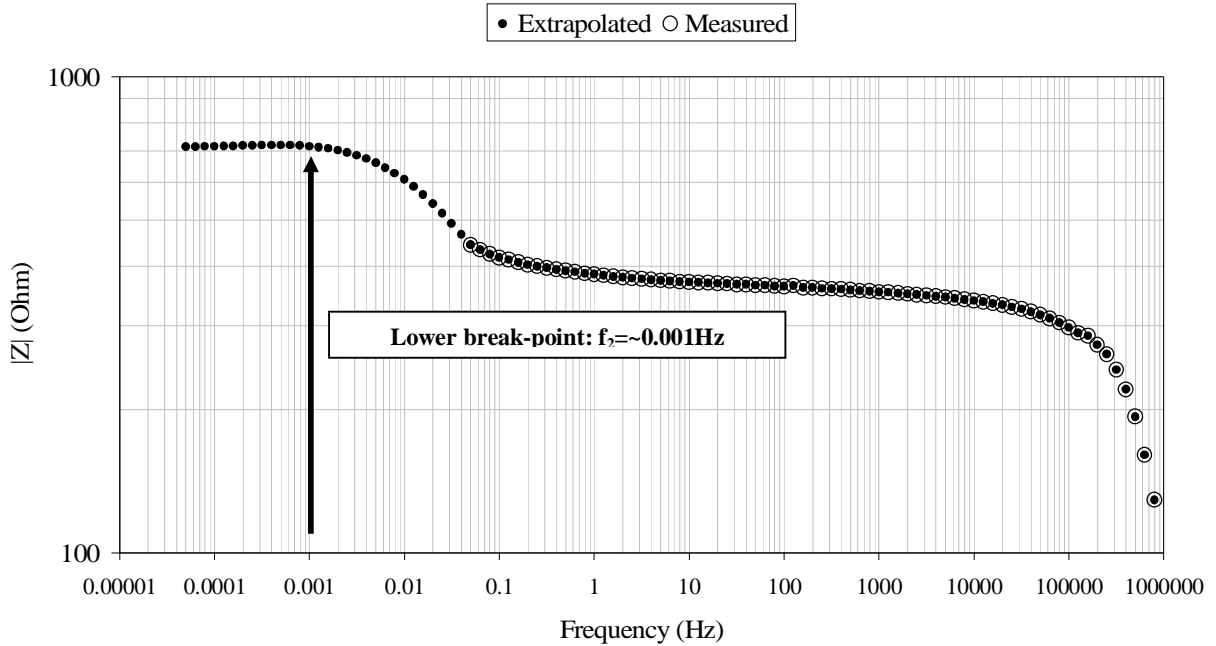


Figure 4. 16. Extrapolated Bode plot for segment A1 in chloride-free concrete.



From Figure 4.16, the lower break point ( $f_2$ ) and consequently, the value of  $f_{\max}$  can be determined for segment A1. By using eq. 2.36 the maximum scan rate,  $S_{\max}$ , for performing the cyclic polarization tests can be calculated as following:

$$\text{A1: } S_{\max} = \pi \cdot \Delta E \cdot f_{\max} < \frac{\pi \cdot \Delta E \cdot f_2}{10} = \frac{3.14 \times 10 \times 0.001}{10} \approx 0.003 \text{ mV/s}$$

The appropriate scan rate would be different because of the concrete environment and amount of corrosion of the steel bar. Using very slow scan rate, such as 0.0006 mV/s is not practical due to the length of the test. Assume that the cyclic tests starts at -100 mV vs. half-cell potential, and the potential increases to +900mV vs. reference and then reverses to -900 mV vs. reference electrode. The total potential changes for this test would be ~3400 mV which at a scan rate of 0.0006 mV/s would need at least 63 days to complete. During this period, the corrosion behaviour could change considerably. For this reason, the scan rate was chosen based on the lower-break point frequency not one decade slower than  $f_2$ . Thus, for the segmented steel bars, the scan rate of 0.006mV/s would be sufficient.

It should be noted that the lower scan rate is necessary if the steel is in passive state or if it is corroding at lower corrosion rate. This can be attributed to the fact that more corrosion is proportional to a lower polarisation resistance and, consequently easier path for current to pass. This means that shorter time is required to keep the double layer capacitance fully charged. From a practical perspective, the scan rate was chosen based on the lower-break point frequency not one decade slower than  $f_2$ .

#### 4.1.1.1.4. Cyclic polarisation

Figure 4.17, shows the cyclic polarisation curve for segment 1 of beam A 118 weeks after casting performed with the scan rate of 0.006mV/s. The scan started at -100mV vs. half-cell potential, increased to +500mV vs. SCE and returned -500 vs. SCE. Figure 4.18 shows the cyclic polarisation curve with the potential range for the same segment, one week later with the scan rate of 0.1mV/s, recommended by ASTM G5 [159]. Clearly, there is a considerable difference between the results shown in Figures 4.17 and 4.18. It needs to be noted that the ASTM G59 recommended scan rate is for tests in solution not an environment like concrete. This important point is sometimes missed by the researchers who are studying the behaviour of steel in concrete.

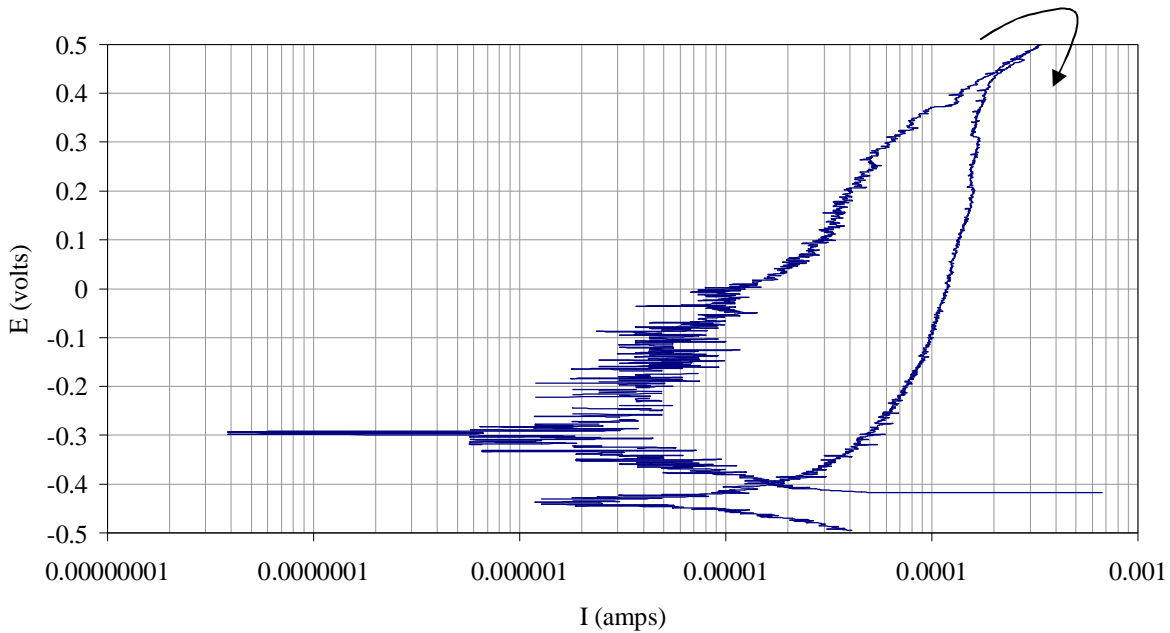


Figure 4. 17. Cyclic polarisation curve for segment A1, 118 weeks after casting, with the scan rate of 0.006 mV/s. Arrow shows the direction when the potential is returning.

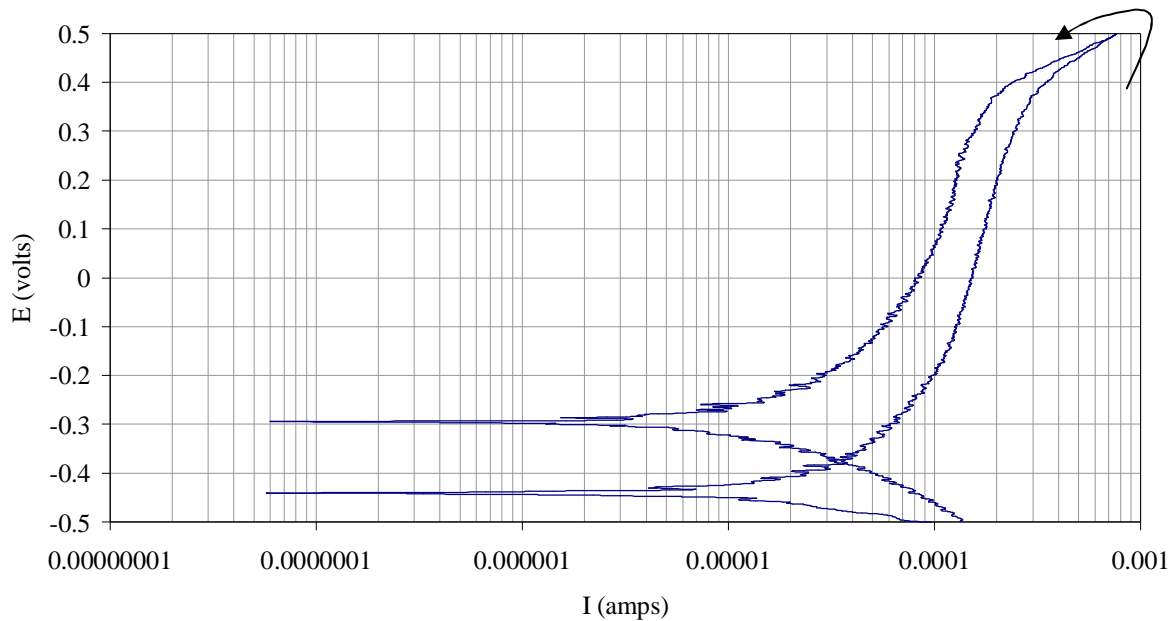


Figure 4. 18. Cyclic polarisation curve for segment A1, 119 weeks after casting, with the scan rate of 0.1 mV/s. Arrow shows the direction when the potential is returning.

The important difference is the direction of the curve in the portion corresponding to the decrease in anodic polarisation. The existence of the hysteresis is usually indicative of pitting, while the size of the loop is often related to the amount of pitting. In the case of the lower scan rate, the pitting potential can be observed while this potential is not shown in the curve obtained with faster scan rate.

#### 4.1.1.1.5. Galvanodynamic LPR

In galvanodynamic LPR, an applied current was raged continuously between  $-100 \mu\text{A}$  and  $100 \mu\text{A}$  at  $10 \mu\text{A/s}$  and the resultant potential was monitored. The value of  $R_p$  is the slope of the potential versus current curve at  $i = 0 \text{ amp}$ . Where there is hysteresis, as for segment A3 in Figure 4.19, the slope of the line between maximum values of the current is taken as  $R_p$ . The result of the galvanodynamic LPR for beams A and B are given in Figures 4.19 and 4.20, respectively.

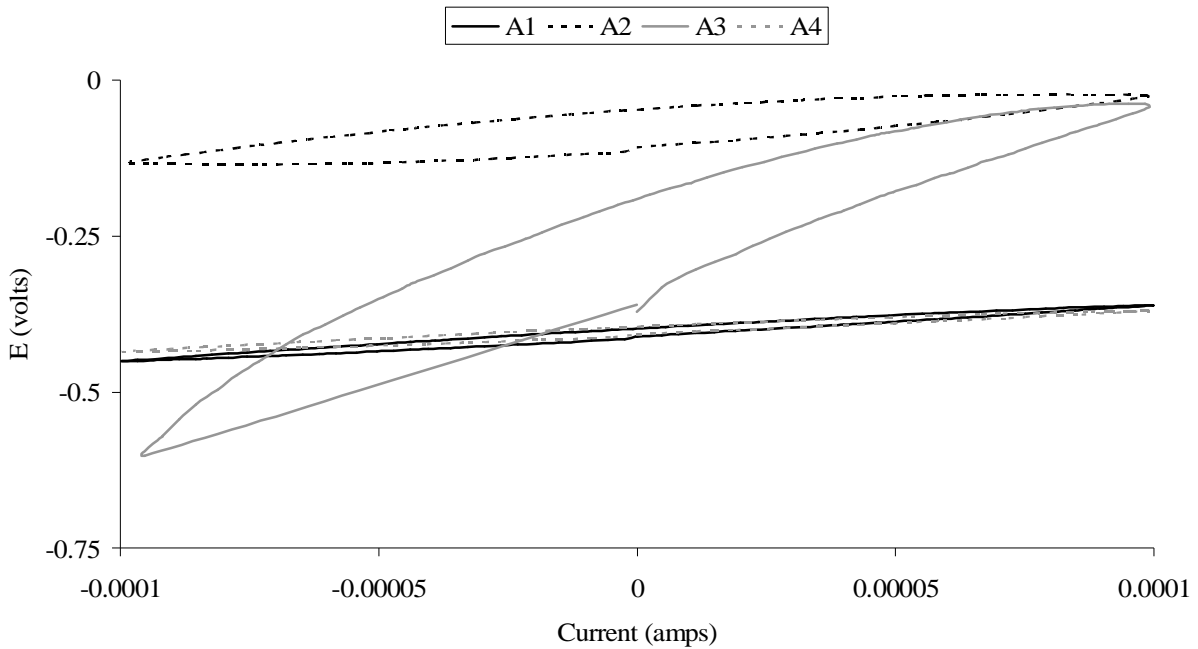


Figure 4. 19. Galvanodynamic LPR results for the steel segments in beam A.

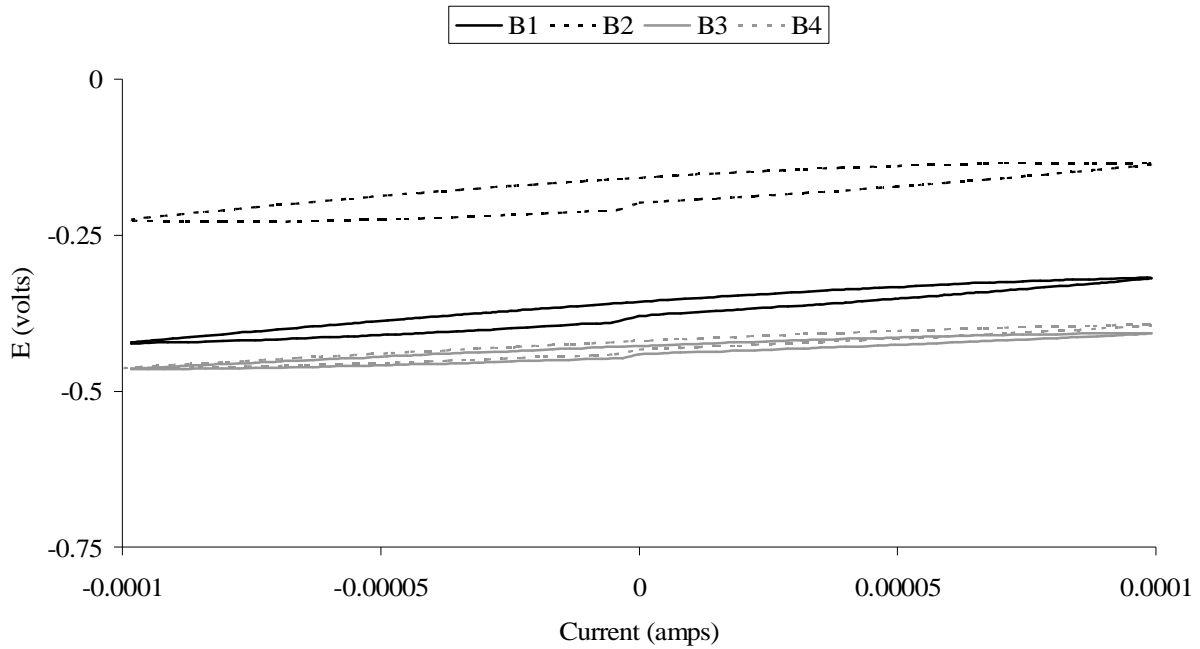


Figure 4. 20. Galvanodynamic LPR results for the steel segments in beam B.

The results, obtained from this test, compare to the other performed electrochemical measurements, show that this tests usually show higher values that the other methods. This test is relatively fast and can be performed in the field with no difficulties. In the field it is possible to compare the relative corrosion activity of different parts of the structure with each other with this technique; however it should be noted that the absolute corrosion rates cannot be determined using this technique.

#### 4.1.1.1.6. Comparison between different corrosion measurements

Figure 4.21, shows the comparison of corrosion current density determined by galvanostatic LPR, measured by GalvaPulse™ (with the guard ring on and off), potentiostatic LPR and galvanodynamic LPR.

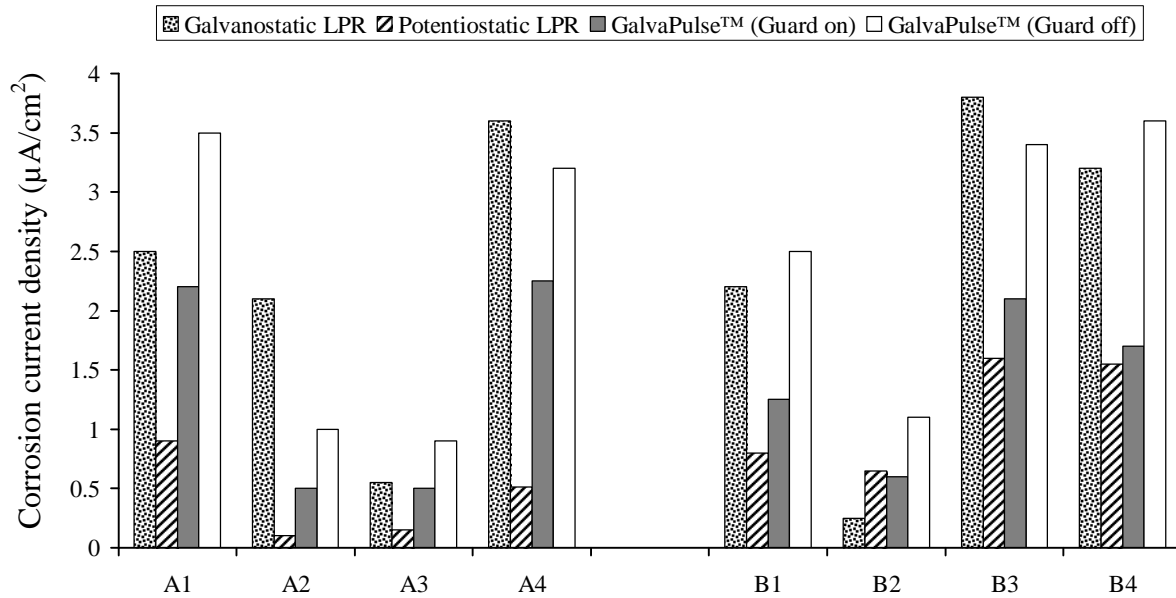


Figure 4. 21. Comparison between different corrosion measuring techniques. Segments 1 and 2 are in chloride-free concrete; segments 3 and 4 are in chloride-contaminated concrete.

As shown in Figure 4.21, potentiostatic LPR consistently shows the lowest corrosion current densities compared to the other techniques and galvanodynamic LPR in most cases gives the highest value. There is a significant difference between measurements performed with GalvaPulse™ when the guard ring is on and off. When the guard ring is off, the measured corrosion current density is almost two times higher than the measured values while the guard ring is on.

### 4.1.1.3. Electrical resistance of concrete

The electrical resistance of the concrete beams was measured by three different techniques and equipment. Figure 4.22 and 4.23, show the trend of concrete resistance of the different segments of the beams (chloride-free and chloride-contaminated), measured by GalvaPulse™ with the guard ring on. The different scale for the resistance values in D in Figures 4.22 and 4.23 is because of connection problem in steel segments in beam D.

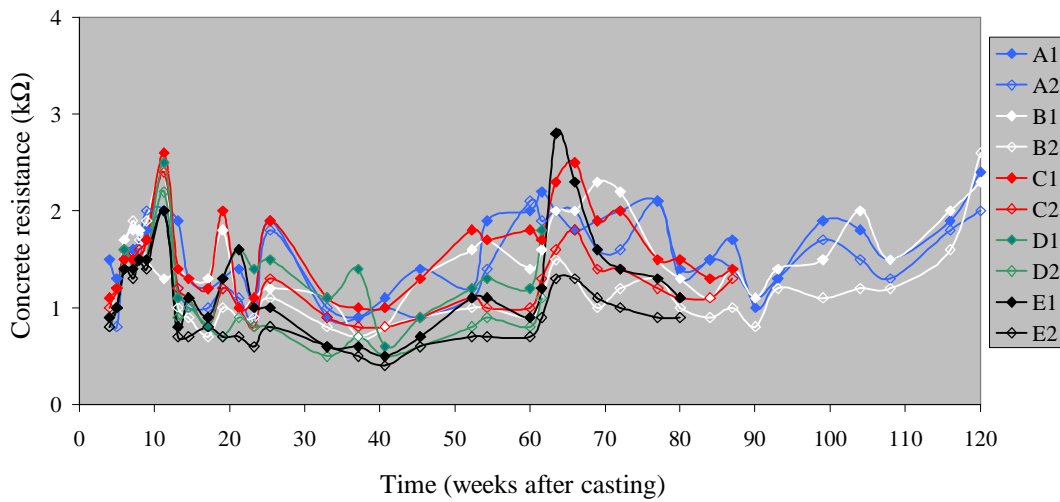


Figure 4. 22. Concrete resistance of the beams with segmented steel bars, measured by the GalvaPulse™, with the guard ring on, in chloride-free sections.

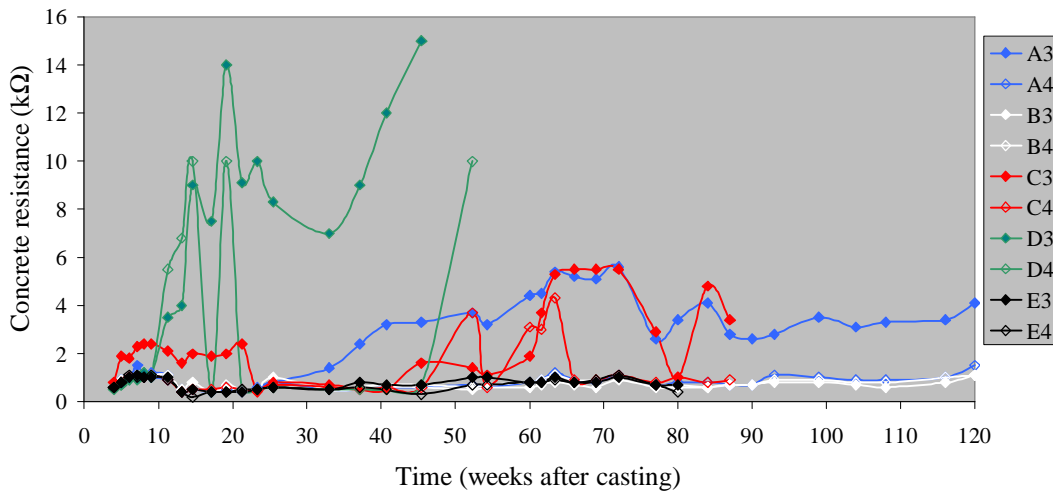


Figure 4. 23. Concrete resistance of the beams with segmented steel bars, measured by GalvaPulse™, with the guard ring on, in chloride-contaminated sections.

The first technique which was used to verify the concrete resistance values, obtained by the GalvaPulse™ was AC impedance spectroscopy. For this purpose, a frequency range between 1MHz to 1Hz was sufficient to obtain the first semi-circle in Nyquist plot, corresponding to the impedance of the concrete. Galvanostatic pulse technique, using potentiostat, was the second technique for determining the value of concrete resistance. Figure 4.24, shows the comparison between concrete resistances of beams A, B, and C, measured by the GalvaPulse™ (guard ring off), EIS and galvanostatic LPR, 65 weeks after casting.

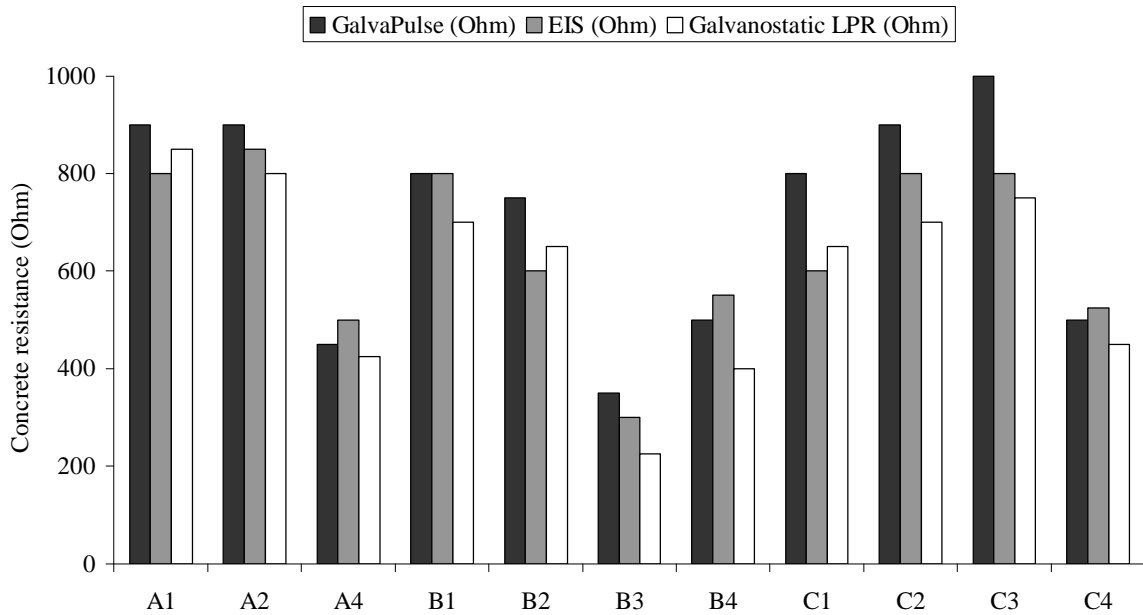


Figure 4. 24. Concrete resistance of beams A, B and C, measured by GalvaPulse™(guard ring off), EIS and potentiostatic LPR, 65 weeks after casting. Segments 1 and 2 are in chloride-free concrete; segments 3 and 4 are in chloride-contaminated concrete.



From Figures 4.24, it is obvious that, when the guard ring of the GalvaPulse™ is off, the concrete resistance value measured by all techniques and equipment are in a good agreement. However, when the guard ring is on, the measured resistance by GalvaPulse™ is two times higher than that measured with the guard ring off (Figure 2.25).

The final technique which was used to measure the concrete resistance was the four-probe method (Wenner technique). This is the most commonly used technique for measuring the concrete resistivity in the field. Figure 4.25 shows the comparison between the concrete resistance values obtained by the GalvaPulse™ (with and without guard ring) and the Wenner technique with two different conditions: with a wet sponge between the probes and the surface of the concrete and without a sponge but with a completely wet surface. All the values obtained by Wenner technique were in the resistivity format which was converted to resistance for comparison purpose.

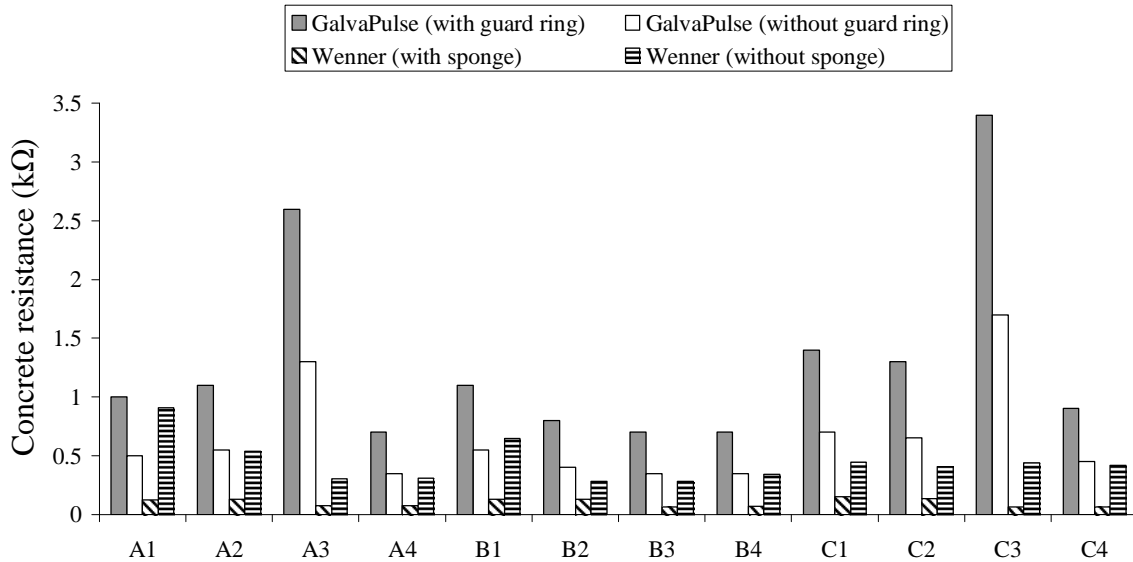


Figure 4. 25. Concrete resistance, measured by GalvaPulse™ and Wenner technique. Segments 1 and 2 are in chloride-free concrete; segments 3 and 4 are in chloride-contaminated concrete.

Concrete resistance of the beams and the specimens with different variables, measured by different techniques, shows that GalvaPulse™, with the guard ring on, gives higher values with respect to the other techniques. Results obtained from galvanostatic pulse technique and EIS, performed using the PARSTAT®, and galvanostatic pulse measured by the GalvaPulse™ while the guard ring was off, show relatively similar values. The Wenner technique was the other method used to measure the concrete resistance. Results show that this technique is very sensitive to surface condition of the concrete (wetness on the surface) and should be used very carefully.

Generally, there was a good consistency in concrete resistance of the specimens during the experiment. The laboratory conditions, relatively constant temperature and relative humidity and wetness of the specimens, were mostly responsible for the aforementioned consistency.

#### **4.1.1.4. Gravimetry**

To evaluate and determine the most accurate electrochemical corrosion measurement technique, all beams were autopsied and each segment was weighed and the amount of mass loss was determined. Then by using the area under the corrosion current density versus time curves, the cumulative mass loss was calculated and compared to the actual mass loss. The results are shown in Figures 4.26 to 4.30. The calculations and the photographs of the steel segments are given in Appendices E and F, respectively.

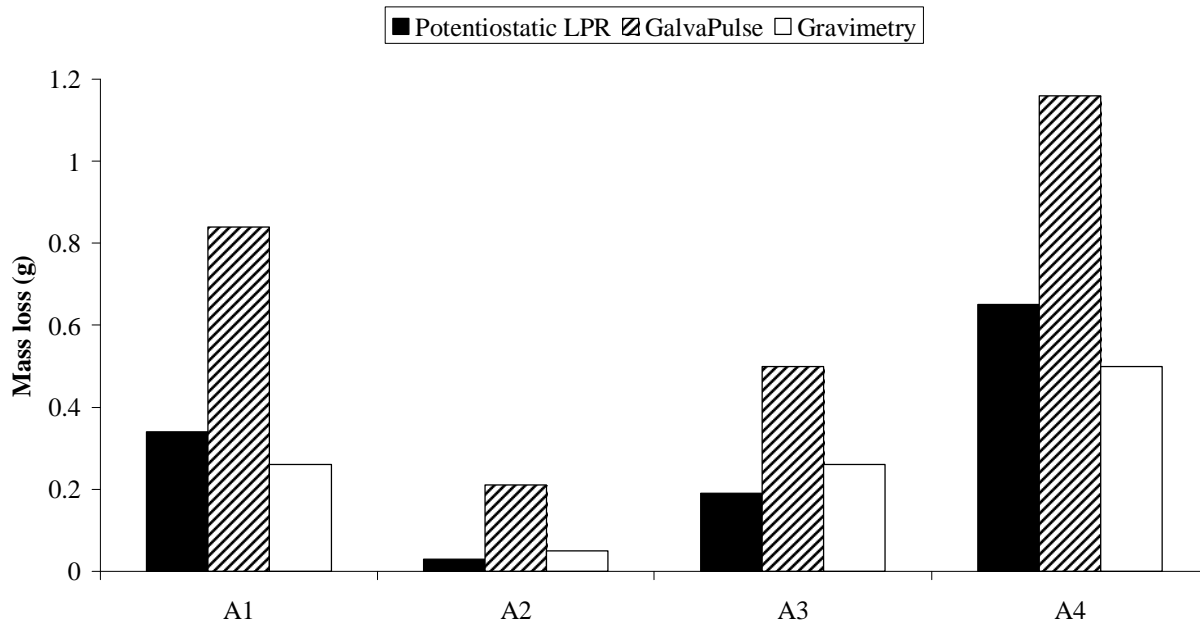


Figure 4. 26. Comparison between mass loss determined by gravimetry and calculated from electrochemical measurements, beam A

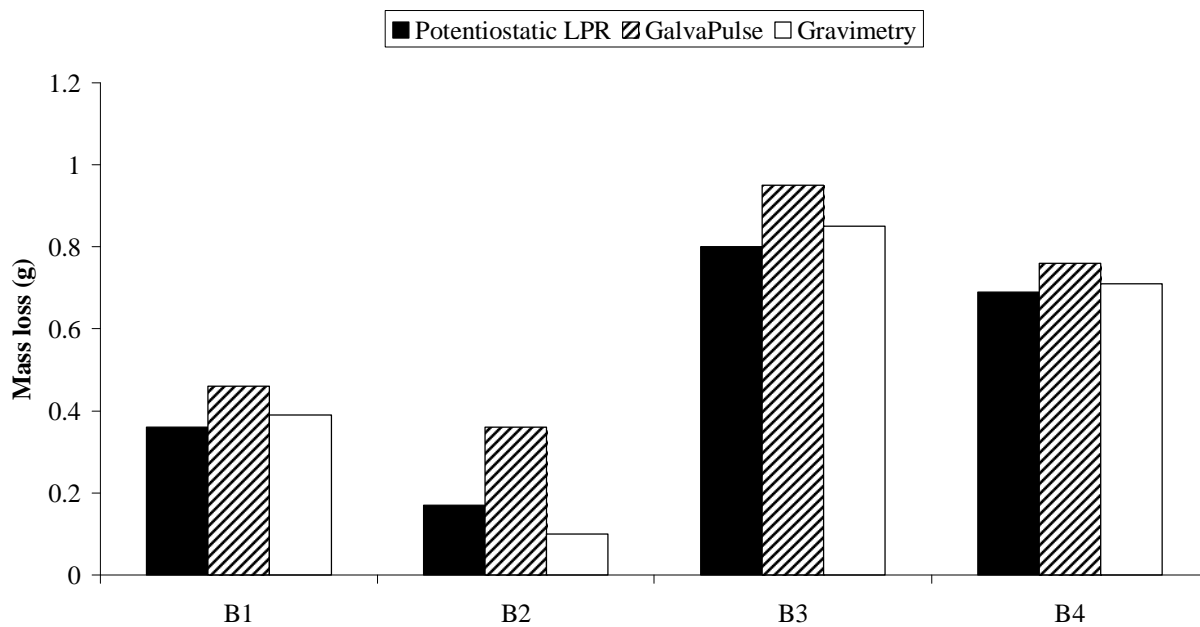


Figure 4. 27. Comparison between mass loss determined by gravimetry and calculated from electrochemical measurements, beam B

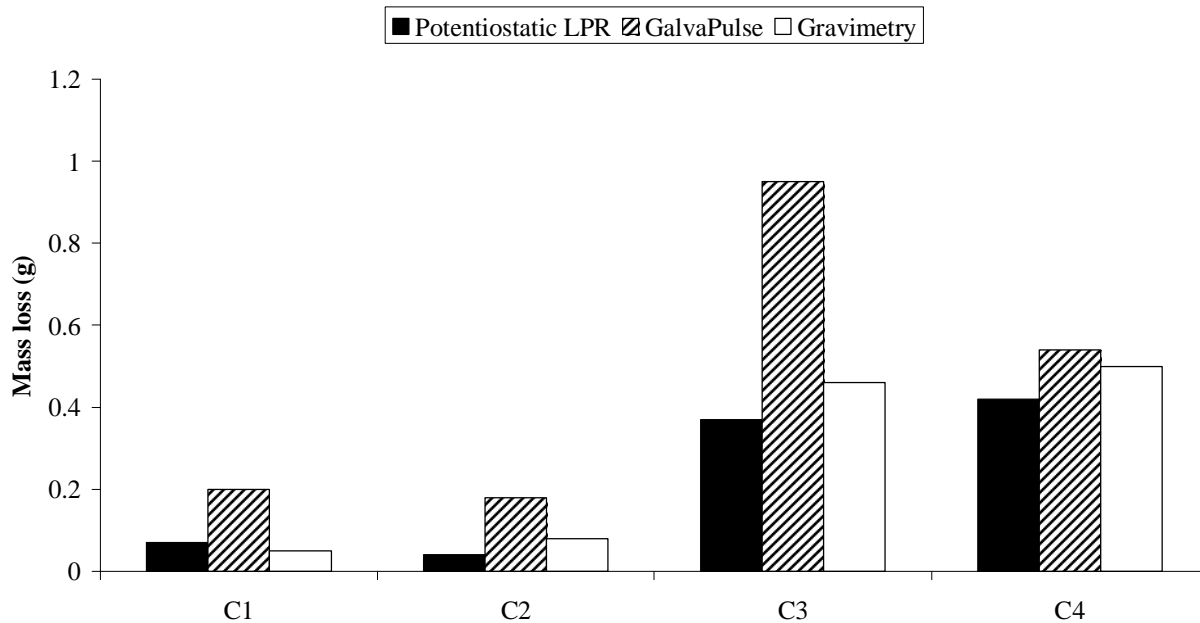


Figure 4. 28. Comparison between mass loss determined by gravimetry and calculated from electrochemical measurements, beam C

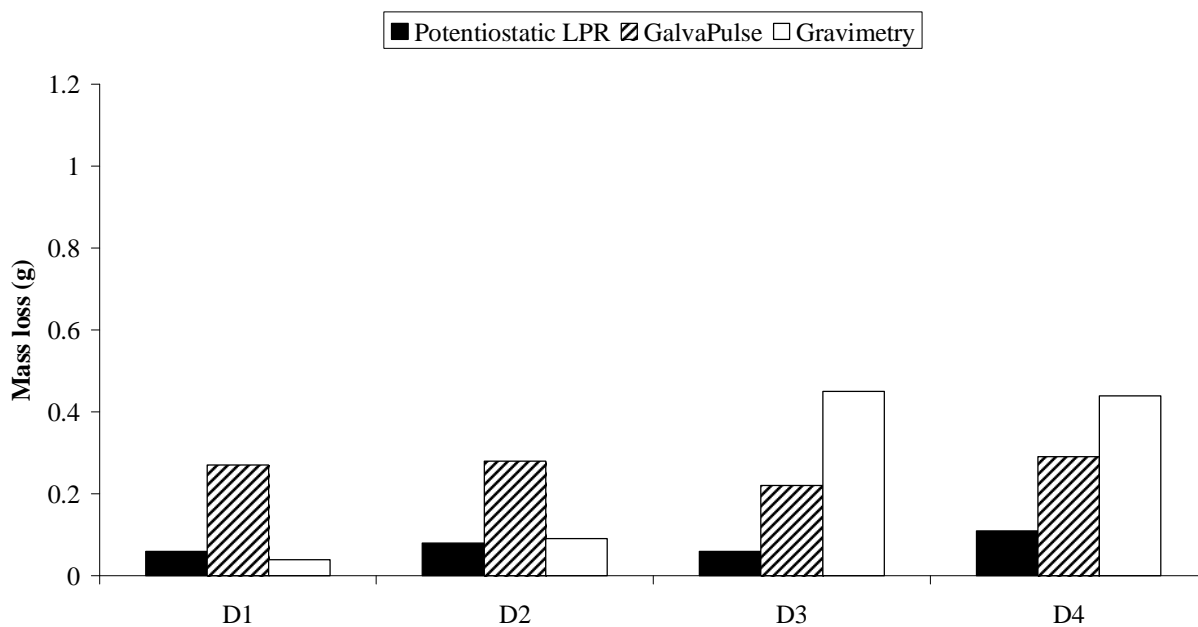


Figure 4. 29. Comparison between mass loss determined by gravimetry and calculated from electrochemical measurements, beam D

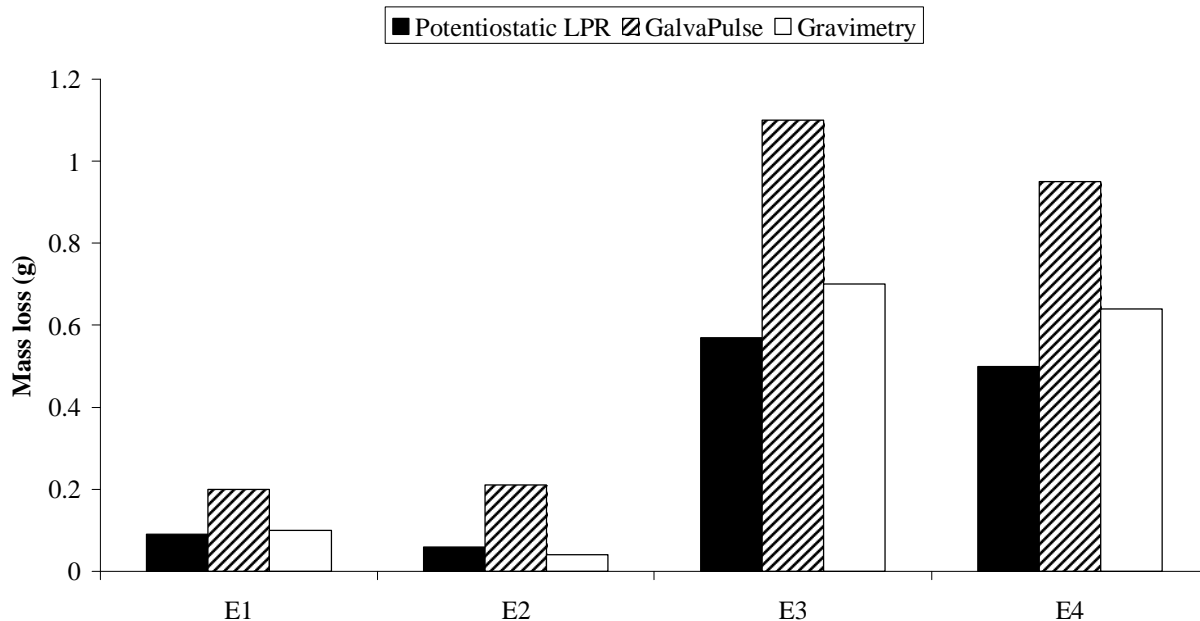


Figure 4. 30. Comparison between mass loss determined by gravimetry and calculated from electrochemical measurements, beam E.

The beams were autopsied at different times and the mass loss of each segment was measured. Comparison between the results from the gravimetry test and those obtained from electrochemical measurements shows that the potentiostatic LPR technique correspond best with gravimetry test and the values obtained by the GalvaPulse™ are higher than actual values. As will be discussed in Section 4.1.6 with more details, using guard ring polarised more area on surface of the steel bar. Due to applying more current than what was necessary, the resultant potential is out of the linear region and the calculated mass loss shows higher values. It is, therefore, concluded that the potentiostatic LPR technique is the most reliable corrosion measurement method for this particular project.

#### 4.1.1.4.1. Actual corroded area and whole surface area

After autopsying the beams, the corrosion current density of the last measurement of each steel segment, measured by potentiostatic LPR and the GalvaPulse™, calculated by using actual corroded area and the whole surface area of each segment and the results are given in Figure 4.31 to 4.35.

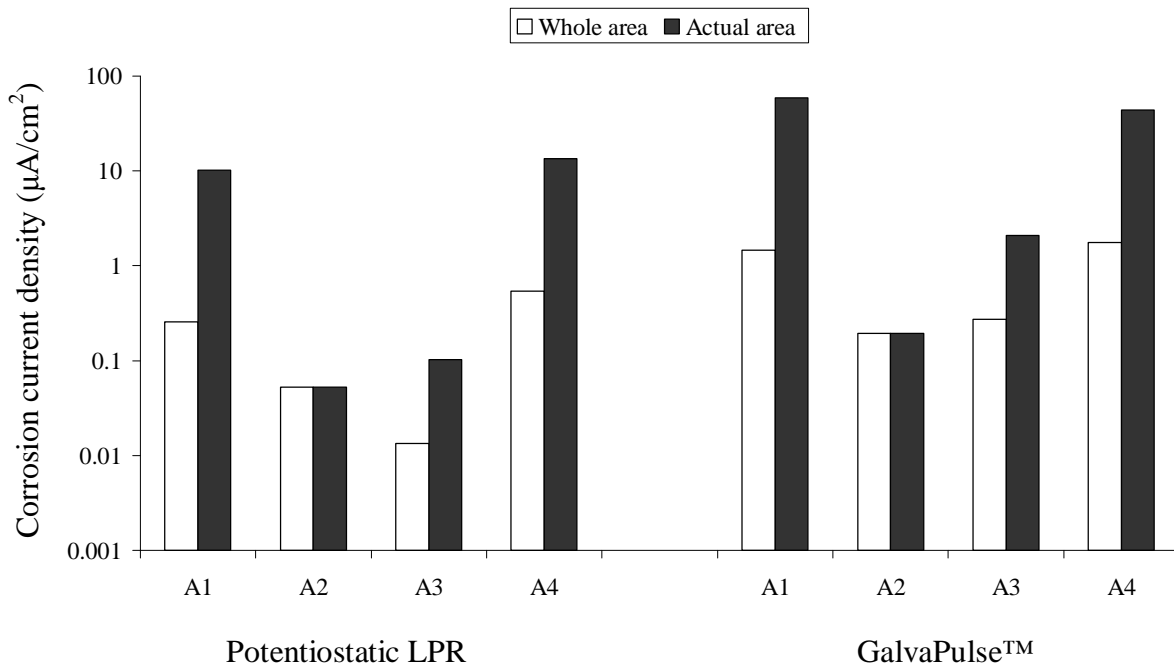


Figure 4. 31. Calculated corrosion current density of the last measurement of segments in beam A, using actual corroded area and whole surface area.

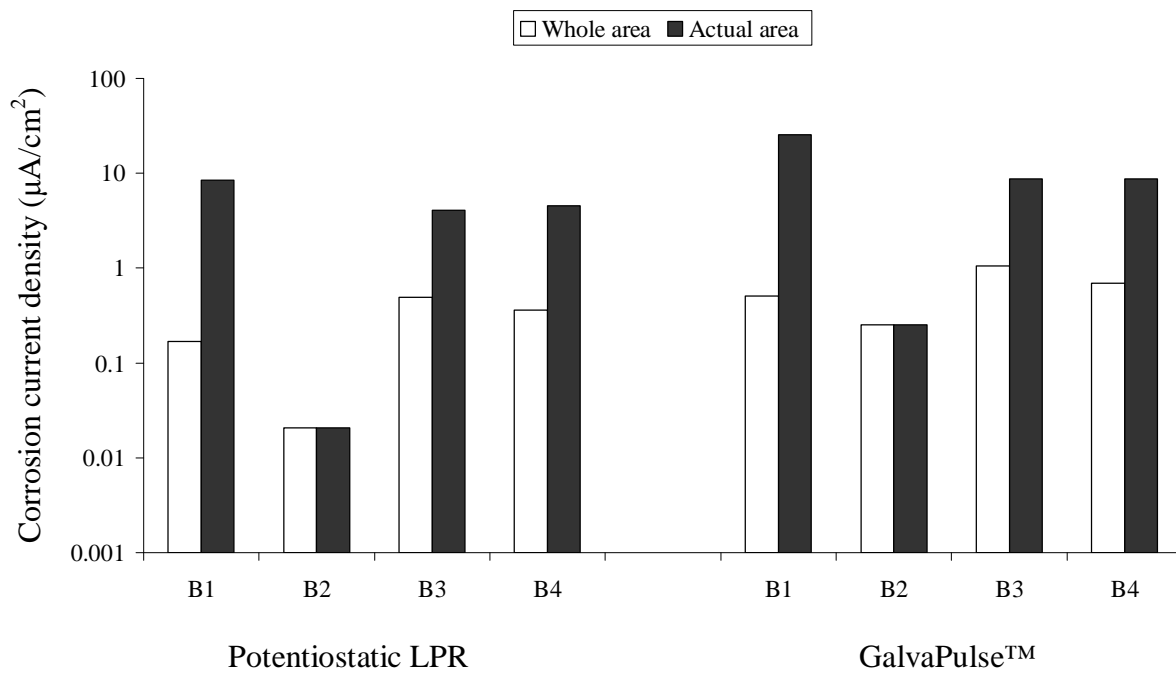


Figure 4. 32. Calculated corrosion current density of the last measurement of segments in beam B, using actual corroded area and whole surface area.

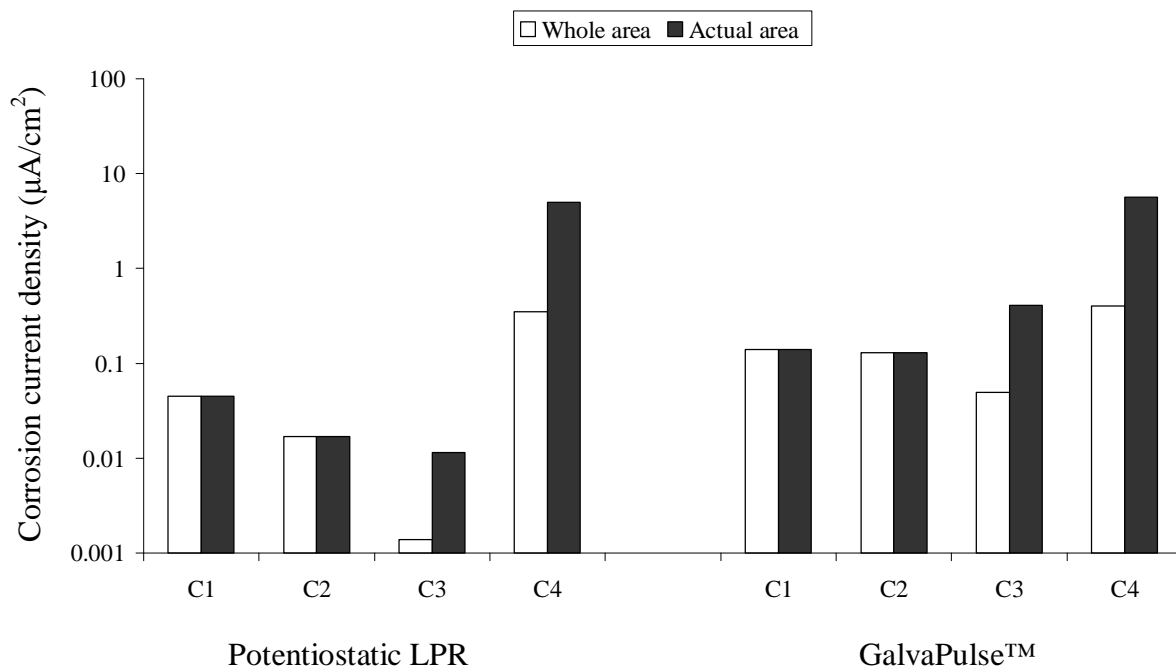


Figure 4. 33. Calculated corrosion current density of the last measurement of segments in beam C, using actual corroded area and whole surface area.

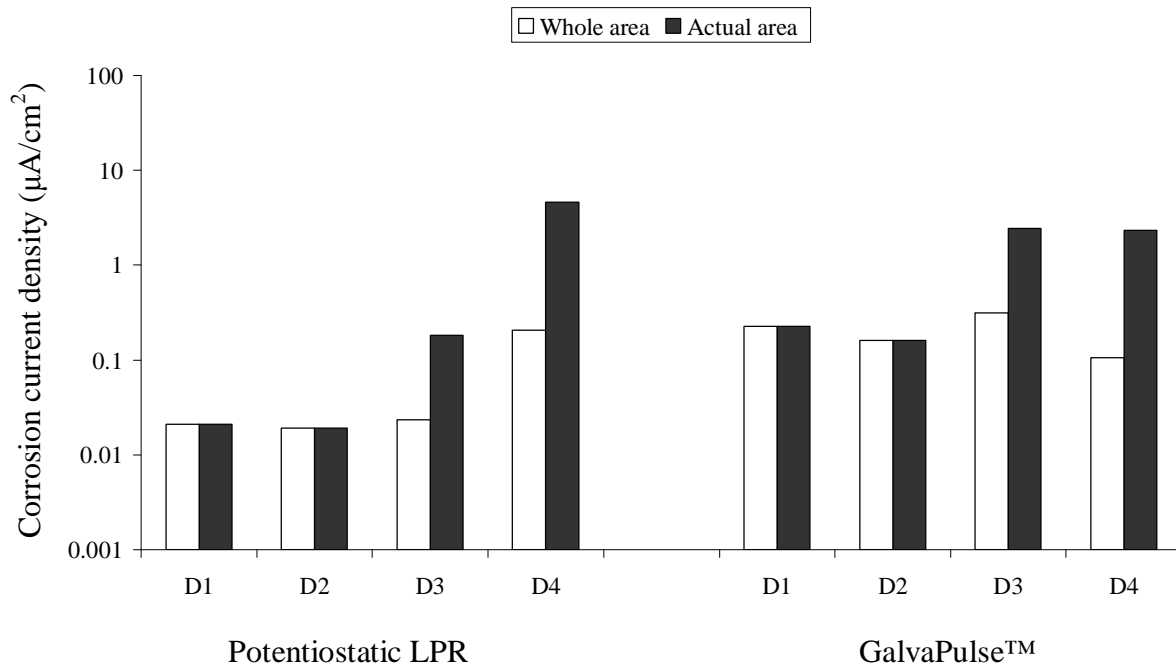


Figure 4. 34. Calculated corrosion current density of the last measurement of segments in beam D, using actual corroded area and whole surface area.

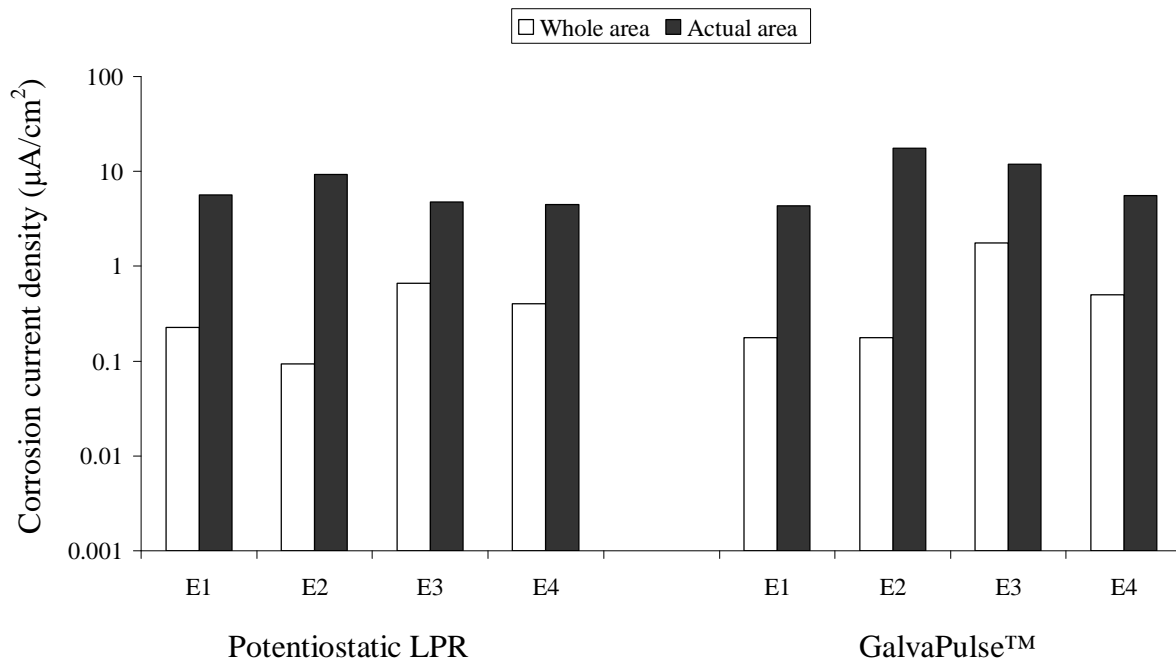


Figure 4. 35. Calculated corrosion current density of the last measurement of segments in beam A, using actual corroded area and whole surface area.



#### **4.1.2. Specimens with different variables**

The results obtained from electrochemical measurements of the reinforced concrete specimens with different variables are given in the following sections. It should be noted that these samples were cast in Dec 06, 2004 and exposed to salts solution in Feb 11, 2005 and all the measurements were carried out after exposure to chloride. An anodic potential of +500mV potential, with respect to SCE, was applied to all specimens during weeks 29 and 36 to accelerate the diffusion of chloride ions into concrete.

##### **4.1.2.1. Electrochemical corrosion measurements**

Corrosion activity of the steel bars in the concrete specimens with different variables was monitored primarily by half-cell potential, potentiostatic LPR and galvanostatic LPR (using the GalvaPulse™) techniques. These measurements were performed every two weeks. In addition; cyclic polarization, EIS and galvanostatic LPR (using PARSTAT® 2263 or Solartron 1286) were used to confirm the results of the biweekly monitoring and to provide more information about the techniques, equipment and corrosion behaviour of the embedded steel bars. Also, the concrete resistance was measured by the GalvaPulse™, with and with guard ring and the results were compared to those obtained from the EIS, galvanostatic pulse method and the Wenner technique.

### 4.1.2.1.1. Half-cell potential

The individual half-cell potential values for all the specimens are given in Figure 4.36 and the average values are given in Figure 4.37.

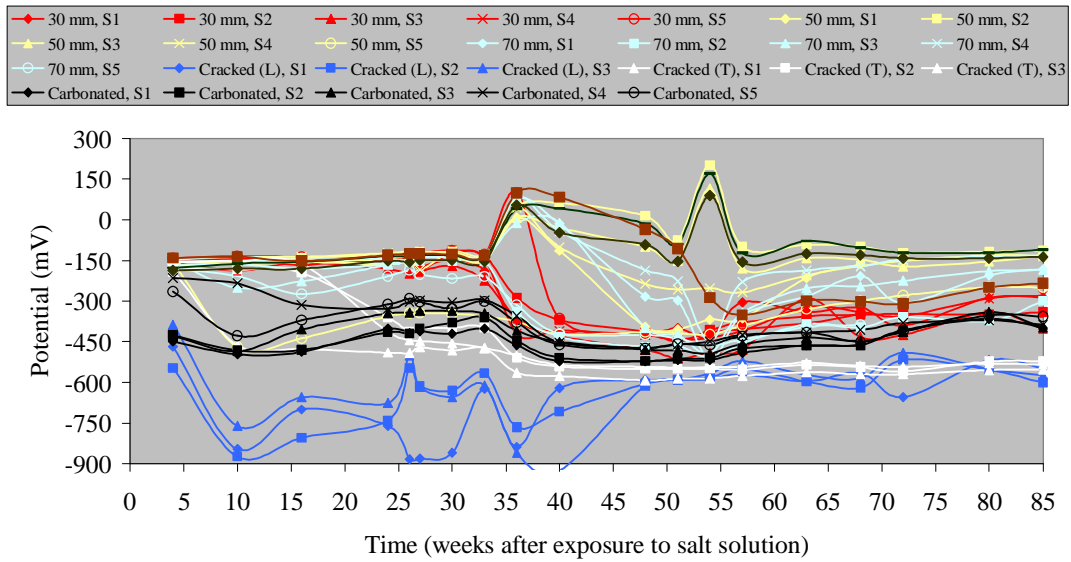


Figure 4. 36. Half-cell potential values, measured by Cu/CuSO<sub>4</sub> reference electrode, of the specimens with different variables.

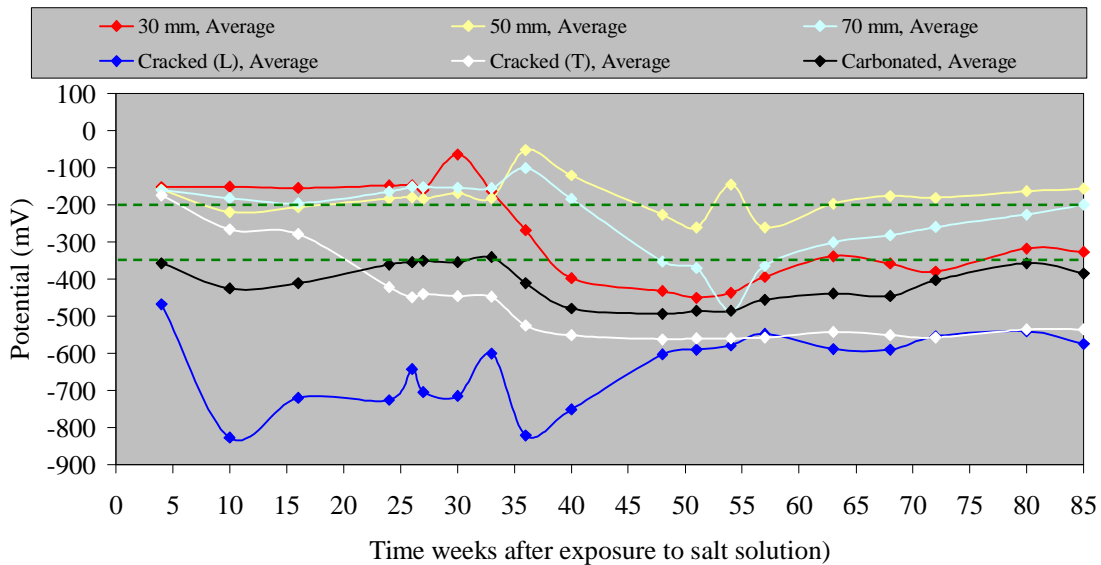


Figure 4. 37. Average half-cell potential values, measured by Cu/CuSO<sub>4</sub> reference electrode, of the specimens with different variables. Green dash lines represent the ASTM C876 recommended guideline.

The most negative half-cell potential values belong to cracked specimens and the most positive values are for specimens with 50 and 70 mm cover depth. Both carbonated specimens (with 50 mm cover) and samples with 30 mm cover depth show similar behaviour and their potentials are more negative than -350 mV vs. CSE.

The half-cell potential of the embedded steel bars was measured for 85 weeks (after exposure to salt solution). All the values are more negative than -350 mV except for specimens with 50 mm and 70 mm cover depth. As described before, to accelerate the diffusion of chloride into the concrete, +500 mV potential versus the half-cell potential was applied to each steel bar between weeks 29 and 36. The more positive potential in specimens with 50 mm and 70 mm cover depth during that period is due to the application of potential. Since specimens with cracks were actively corroding, no significant difference in potential values was observed during that period. The half-cell potential of the specimens with 30 mm cover depth, tended to be more negative. This can be attributed to the fact that chloride ions have reached the surface of steel and increasing the potentials caused more ions to reach the surface and consequently, more corrosion. These observations were confirmed by corrosion measurements.

#### **4.1.2.1.1.1. Distance of reference electrode to the steel bar**

As mentioned in Chapter 3, three specimens with cover depth of 50mm were cast with Mn/MnO<sub>2</sub> reference electrodes embedded 5 mm from the rebar, to determine the effect of distance of the reference electrode to the surface of the steel on the values on half-cell potential. Figure 4.38 shows the values by these electrodes and those measured by Cu/CuSO<sub>4</sub> on the

surface of the specimens. All the obtained results from Mn/MnO<sub>2</sub> electrodes were converted to Cu/CuSO<sub>4</sub> for comparison purpose.

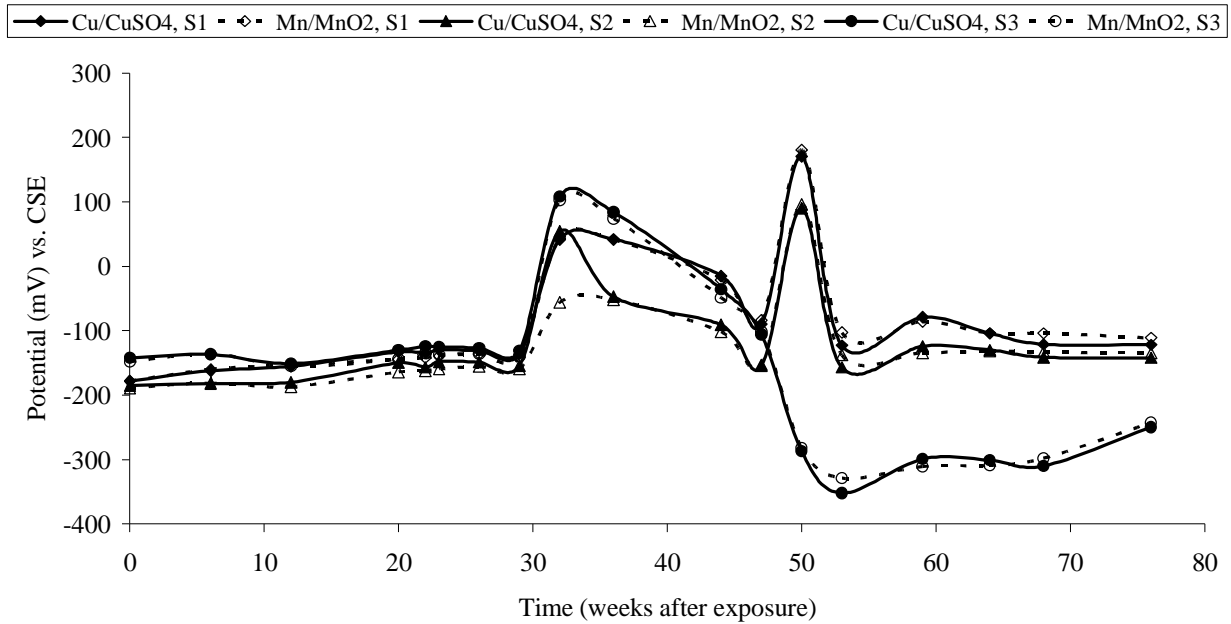


Figure 4. 38. Comparison between half-cell potential values obtained by embedded Mn/MnO<sub>2</sub> reference electrodes and measured by Cu/CuSO<sub>4</sub> reference electrode form the top surface of the specimens.

The half-cell potential values measured by Mn/MnO<sub>2</sub> reference electrode show similar variation, as those measured by Cu/CuSO<sub>2</sub> reference electrode. This means that the distance of the reference electrode to the surface of the steel bars has no significant effect on the measured potential values. This can be due to the fact that the steel rebars in those specimens were not actively corroding and the concrete specimens in the lab were most of the time wet, and consequently there will be little effect of IR drop.

To determine the effect of the distance of the carbonated layer on the half-cell potential values, a hole with 35 mm depth and 70 mm diameter (Figure 4.39) was made on the surface of the same specimen and the half-cell potential and corrosion current density, using potentiostatic LPR, was measured and the results are given in Table 4.3.

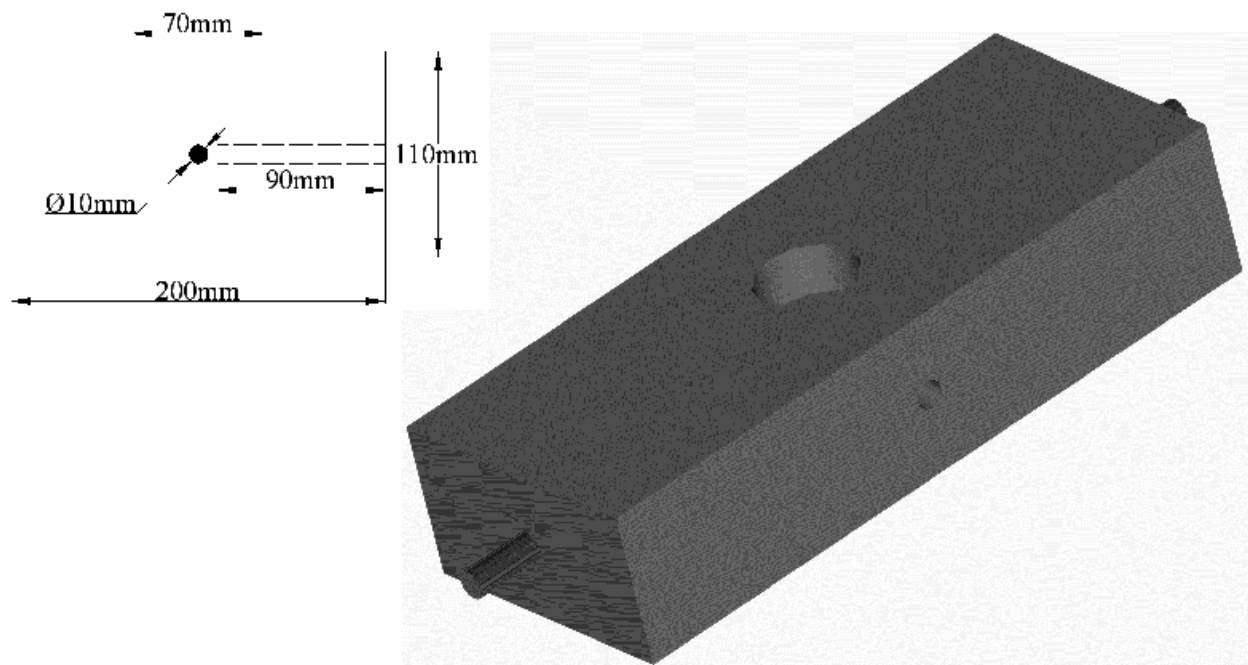


Figure 4. 39. Schematic views of one of the carbonated concrete samples with a hole drilled on its top and its side.

Table 4. 1. Comparison between half-cell potential and corrosion current density of one of the carbonated specimens, using three different locations for the reference electrode.

|   | Half-cell potential (mV) vs. Cu/CuSO <sub>4</sub> | Current density (μA/cm <sup>2</sup> ) |
|---|---|---------------------------------------|
| Ref. electrode on top surface                 | -356  | 0.31                                  |
| Ref. electrode in the perpendicular hole      | -341  | 0.29                                  |
| Ref. electrode in the hole on the top surface | -341  | 0.32                                  |

The potential measured from inside the hole was ~15 mV more positive than the one measured on the top of the concrete surface which is not significant. Therefore, half-cell potential values, measured on surface of the carbonated concrete can be considered valid.

#### **4.1.2.1.2. Potentiostatic and galvanostatic LPR**

Figures 4.40 shows the corrosion current densities of the embedded steel in the specimens with different variables, measured by potentiostatic LPR technique, using PARSTAT<sup>®</sup> 2263, and Figure 4.41, shows the average values of the corrosion densities. As mentioned before, for the calculations, 21.98 cm<sup>2</sup> was used as the surface area of steel. The actual corrosion current density values are shown in Appendix D.

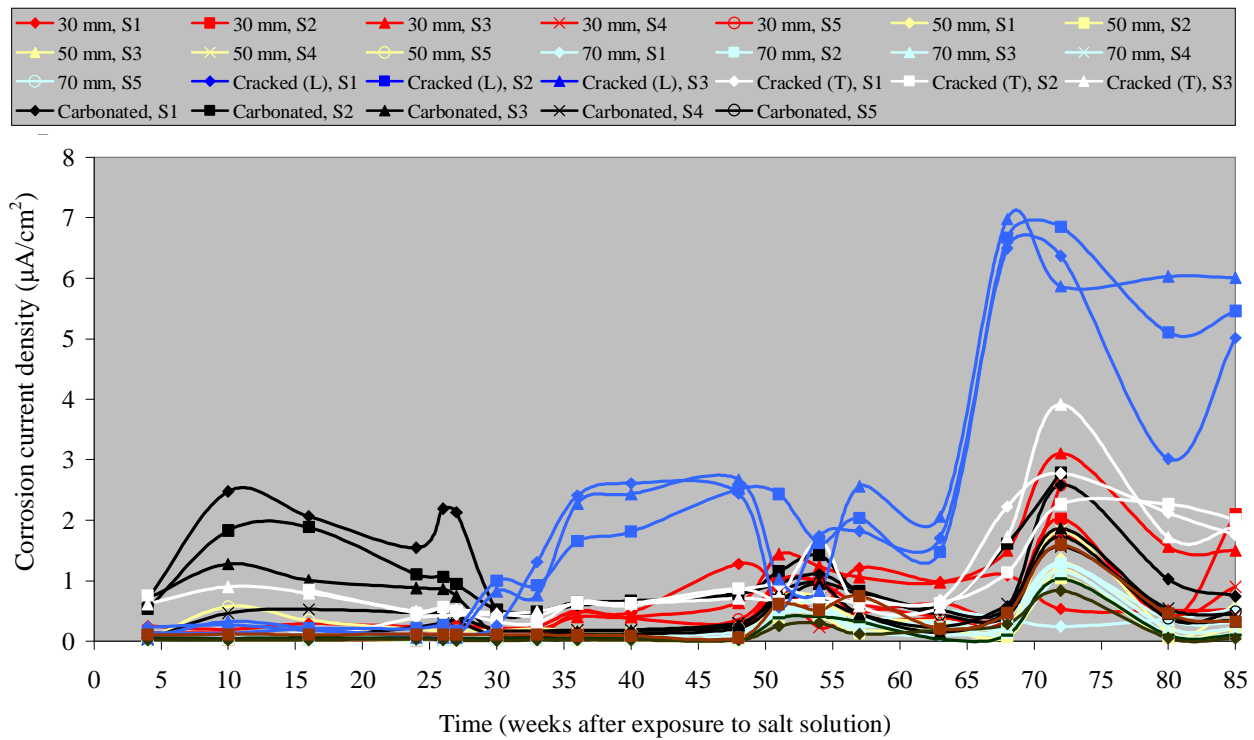


Figure 4. 40. Corrosion current densities of the specimens with different variables, measured by potentiostatic LPR.

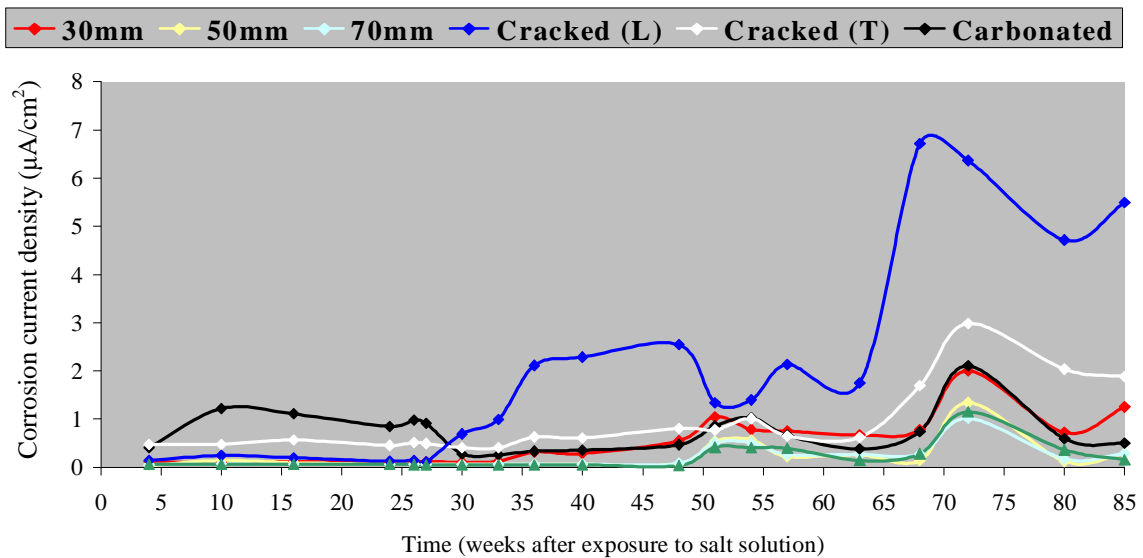


Figure 4. 41. Average values of the corrosion current densities, specimens with different variables, measured by potentiostatic LPR.

As can be seen, steel bars in cracked specimens have highest corrosion current densities while the lowest values belong to the steel bars in the specimens with 50 and 70mm cover depth. Also, corrosion densities of steel rebars in concrete with 30 mm cover depth and carbonated concrete are similar.

Figures 4.42 and 4.43 show the corrosion current densities for all specimens and the average values, measured by the GalvaPulse™, respectively.



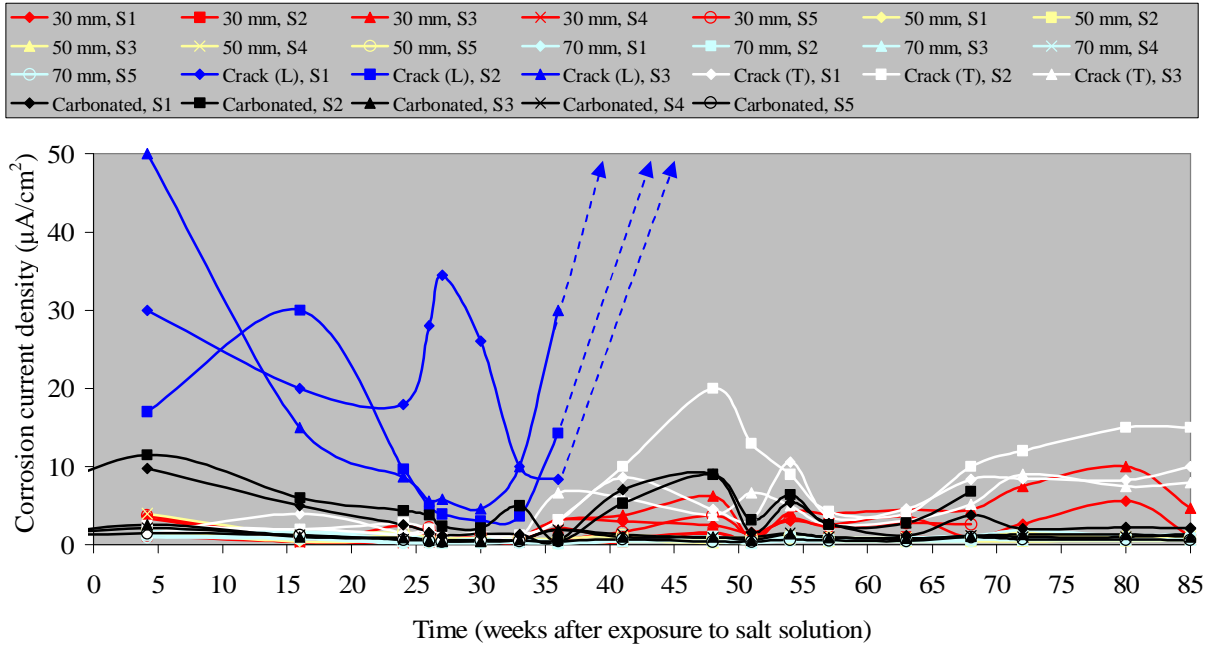


Figure 4. 42. Corrosion current densities of the specimens with different variables, measured by GalvaPulse™.

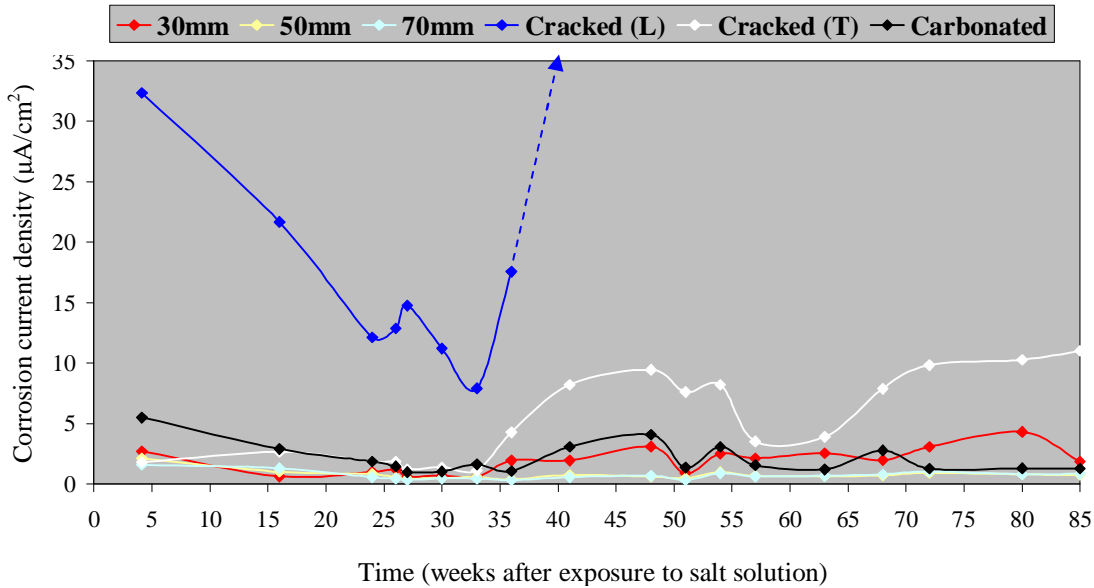


Figure 4. 43. Average values of corrosion current densities of the specimens with different variables, measured by GalvaPulse™. The blue arrow shows that the corrosion current densities of the specimens with longitudinal cracks are more than  $150\mu\text{A}/\text{cm}^2$  and the values are out of the scale of the graph.

From Figures 4.42 and 4.43, it is seen that the values of the corrosion current densities measured by the GalvaPulse™ have the same trend as those measured by potentiostatic LPR. However, the actual values with the GalvaPulse™ are more than three times higher than those measured by potentiostatic LPR. It should also be noted that when the corrosion rate is very high, such as the samples with longitudinal cracks, the GalvaPulse™ cannot make the measurement with the guard ring on and the measured values are far from the actual values. If the steel bars are highly corroded, the GalvaPulse™, even without guard ring, is not capable of performing the measurements at all. This observation was confirmed during the field measurements and the results of which are given later in this chapter.

The corrosion current density of the steel bars in specimens with different variables measured by the potentiostatic LPR show that those with longitudinal cracks had highest corrosion rate while those with 50 mm and 70 mm cover, remained passive throughout the test period. The carbonated specimens and those with 30 mm cover, showed active corrosion. One specimen with cover depth of 30 mm, 50 mm and 70 mm, and one carbonated specimen were broken and the embedded steel bars were visually inspected. Corrosion products were observed on the middle part of the steel bar in specimen with 30 mm cover. No corrosion product was found on the surface of the steel in the concrete with 50 mm cover. However, corrosion was observed on the steel bars in the carbonated specimen and concrete with 70 mm, but they were located at the border of epoxy coated and bare steel. Due to leakage from the ponding well on the top, the chloride ions diffused to the concrete from the sides, in addition to the top surface, and caused corrosion. Also, it was noticed that the steel bars in those specimens, had moved during casting compaction of the concrete and the distance from each end of steel was i.e. about

20 mm less than the cover depth. Chloride analysis confirmed the presence of chloride in all the corroded locations.

Corrosion measurement results, obtained from the GalvaPulse™, show higher values than those obtained from potentiostatic LPR. If the correct polarised area was used, the values were lower and might be similar to what was achieved from the potentiostatic LPR. For this purpose and based on evaluation of the function of the GalvaPulse™, the average values of corrosion current densities measured by the GalvaPulse™ were recalculated assuming that whole length (500 mm) of the steel bar was polarised and the results are shown in Figure 4.44. Comparison between Figures 4.44 and 4.36 shows that this assumption changes values measured by the GalvaPulse™ close to those obtained from the potentiostatic LPR. This point emphasises the importance of using the appropriate polarised area in the calculations.

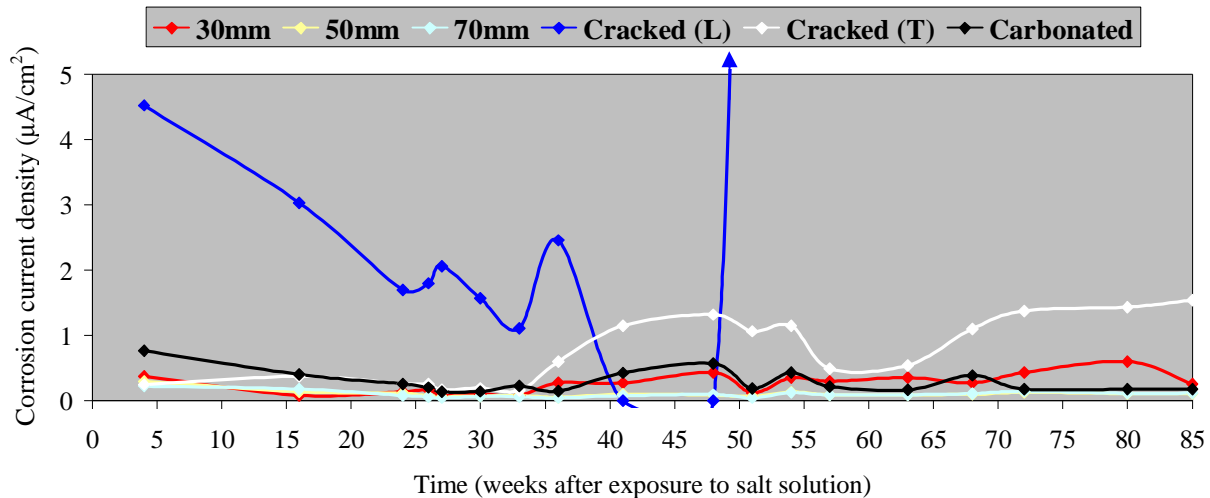


Figure 4. 44. Corrosion current density, measured by the GalvaPulse™. Assumed polarised length of rebar = 500mm

Experiments demonstrated that the GalvaPulse™ is not capable of performing the measurements when the corrosion rate is high ( $>4\mu\text{A}/\text{cm}^2$ ) or it gives unrealistic values, such as  $200\mu\text{A}/\text{cm}^2$ . This is one of the limitations of this equipment.

#### **4.1.2.1.3. Electrochemical impedance spectroscopy**

Figures 4.45 and 4.46 show the Nyquist and Bode plots, obtained by performing EIS on one of the carbonated concrete specimens (S1), 27 weeks after exposure to salt solution. The frequency range was from 2MHz to 0.1mHz. Figure 4.55 indicates that the experimental data could not be fitted in Kramers-Kronig method and there is not sufficient curvature at low frequencies. 78 weeks after exposure to salt solution, impedance spectroscopy test was performed on the same specimen with the frequency range between 1MHz and 0.01 mHz and the results are given in Figures 4.47 and 4.48.

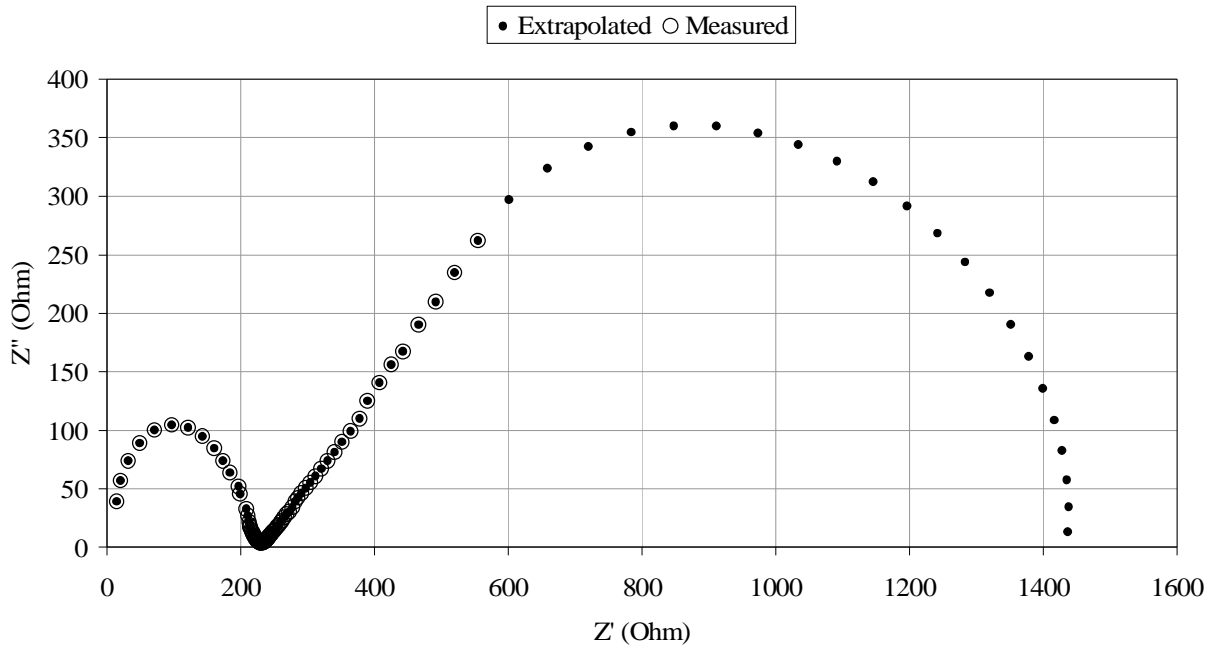


Figure 4. 45. Extrapolated Nyquist plot for one of the carbonated specimens (S1), 27 weeks after exposure to salt solution.

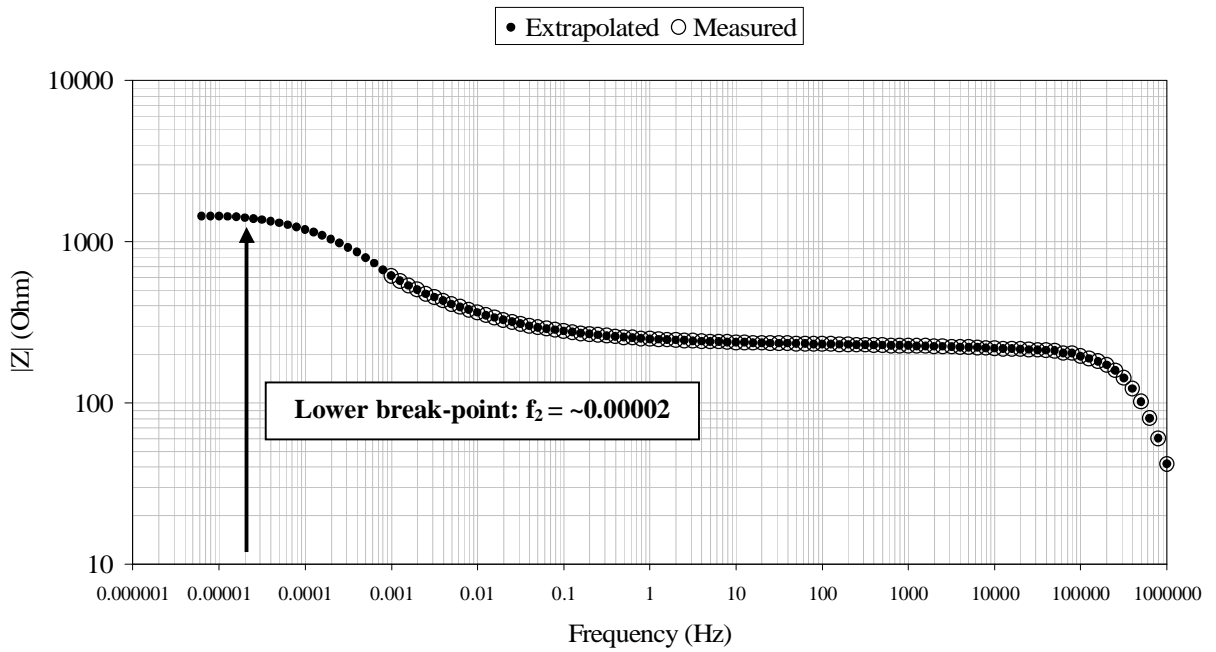


Figure 4. 46. Extrapolated Bode plot for one of the carbonated specimens (S1), 27 weeks after exposure to salt solution.

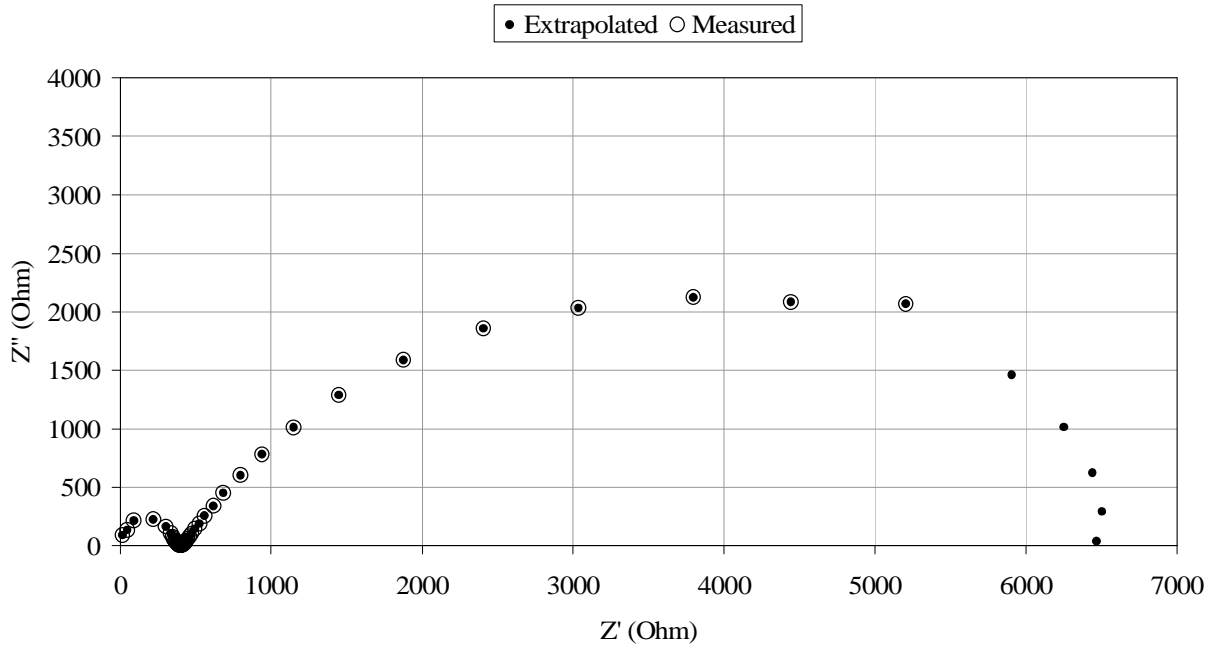


Figure 4. 47. . Extrapolated Nyquist plot for one of the carbonated specimens (S1), 78 weeks after exposure to salt solution.

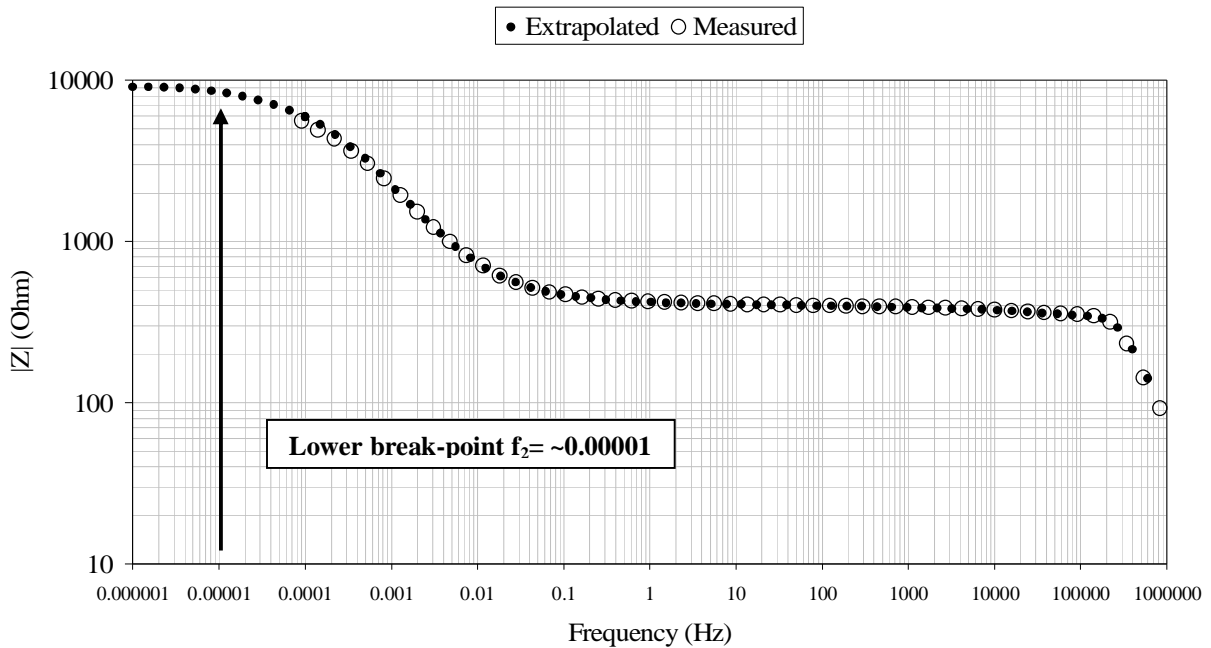


Figure 4. 48. . Extrapolated Nyquist plot for one of the carbonated specimens (S1), 78 weeks after exposure to salt solution.

From Figures 4.46 and 4.48, the lower break point ( $f_2$ ) and consequently, the value of  $f_{\max}$  is calculated and then by using eq. 2.36 the maximum scan rate,  $S_{\max}$ , for performing the cyclic polarization tests can be determined as following:

$$27 \text{ weeks after exposure: } S_{\max} = \pi \cdot \Delta E \cdot f_{\max} < \frac{\pi \cdot \Delta E \cdot f_2}{10} = \frac{3.14 \times 10 \times 0.00002}{10} \approx 0.000063 \text{ mV/s}$$

$$78 \text{ weeks after exposure: } S_{\max} = \pi \cdot \Delta E \cdot f_{\max} < \frac{\pi \cdot \Delta E \cdot f_2}{10} = \frac{3.14 \times 10 \times 0.00001}{10} \approx 0.0000314 \text{ mV/s}$$

From practical point of view choosing 0.00003 or 0.00006 mV/s as the scan rate is not reasonable because a scan would take weeks to be completed. Therefore, 0.006 mV/s was used to perform cyclic polarisation tests and results are given in the next section.

The value of  $R_p$ , can be determined by using Figures 4.45 and 4.47 which is  $\sim 1200 \Omega$  and  $\sim 6000 \Omega$ , and from  $R_p$ ,  $i_{\text{corr}}$  can be calculated as  $\sim 0.2 \mu\text{A}/\text{cm}^2$  and  $1 \mu\text{A}/\text{cm}^2$ , respectively. The similar values obtained from potentiostatic LPR technique at the same time.

#### 4.1.2.2.4. Cyclic polarisation

To illustrate the effect of scan rate on the shape of the cyclic polarisation curve, and consequently the interpretation of the results, different scan rates were selected to perform the test. Figure 4.49 shows the cyclic polarisation curve, performed with 0.006 mV/s scan rate, for one of the specimens with longitudinal crack and Figure 4.50 shows the cyclic polarisation curve for the same sample with 1 mV/s scan rate. In both cases, the scan started at -100 mV below half-cell potential, increased to +900 and decreased to -900 mV versus SCE.

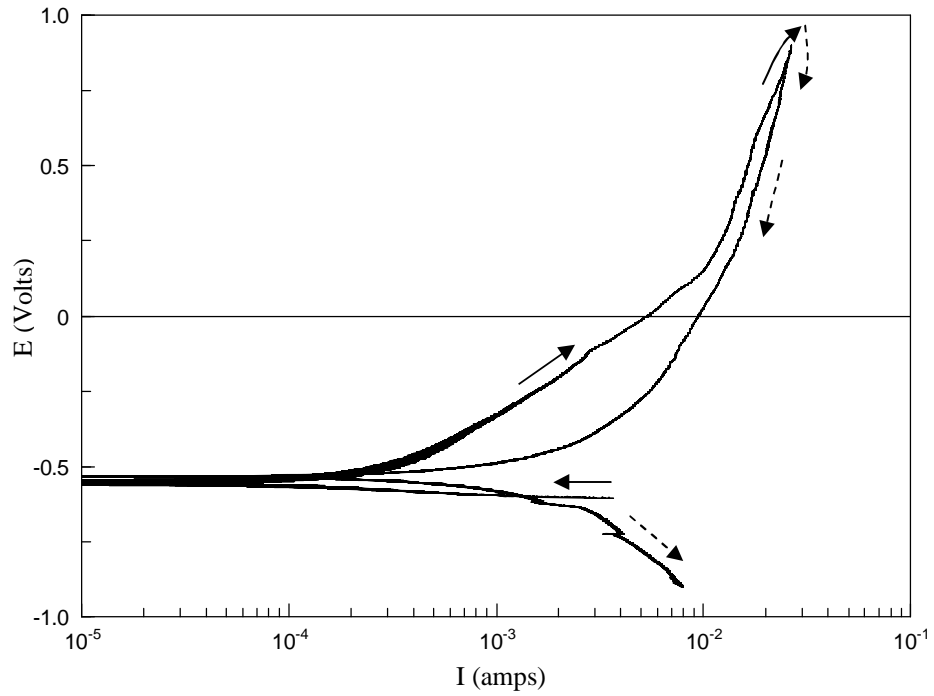


Figure 4. 49. Cyclic polarisation curve with the scan rate of 0.006mV/s, one of the specimens with a longitudinal crack. Solid arrows show the direction of increasing the potential and dotted arrows show the direction of return potential.

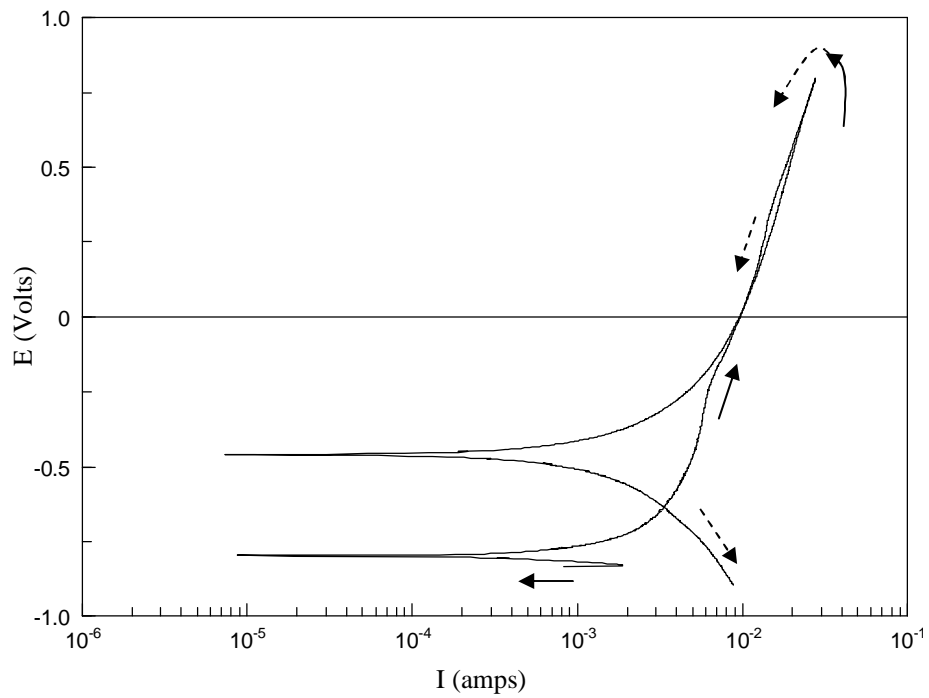


Figure 4. 50. Cyclic polarisation curve with the scan rate of 1mV/s, one of the specimens with a longitudinal crack. Solid arrows show the direction of increasing the potential and dotted arrows show the direction of return potential.



In Figure 4.51, the cyclic polarisation curves for one of the specimens with transverse crack with different scan rates are shown.

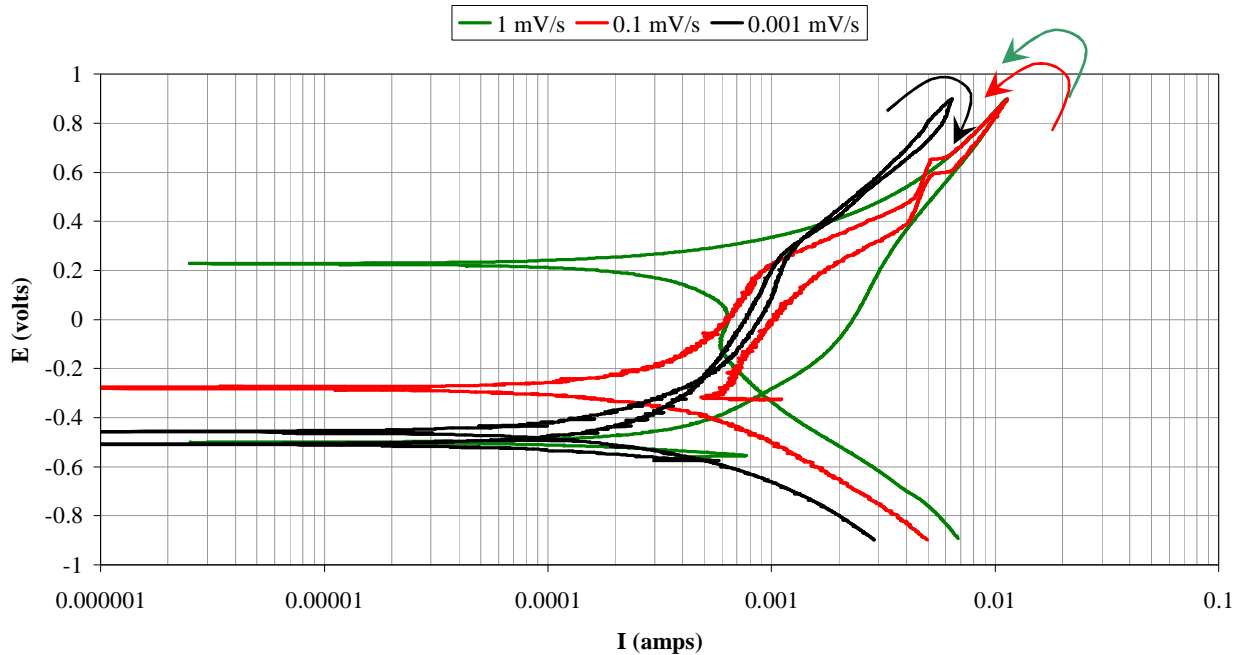


Figure 4. 51. Cyclic polarisation curves with different scan rates for one of the samples with transverse crack. Arrows show the direction of the return potential

If the appropriate scan rate is not chosen, the observed behaviour may mislead the researcher and cause misinterpretation of the results. For example, cyclic polarisation test, performed on the steel bar in one of the specimens with a longitudinal crack at a scan rate of 0.006 mV/s (Figure 4.49) shows that this rebar is corroding actively and also that it is susceptible to pitting corrosion. Furthermore, the second half-cell potential in return section of the curve is very close to the initial half-cell value which means that there is no passive film on the steel to protect it and cause raise in potentials during return. However, the cyclic polarisation curve for the same specimen with the scan rate of 1 mV/s (Figure 4.50) shows completely different behaviour. Figure 4.51 illustrate the same scenario in the specimen with transverse crack.

#### 4.1.2.2.5. Galvanodynamic LPR

The galvanodynamic LPR technique was used to measure the corrosion activity of one specimen of each variable and the results are given in Figure 4.52. Figure 4.53, shows the comparison of the corrosion current densities measured by three different techniques.

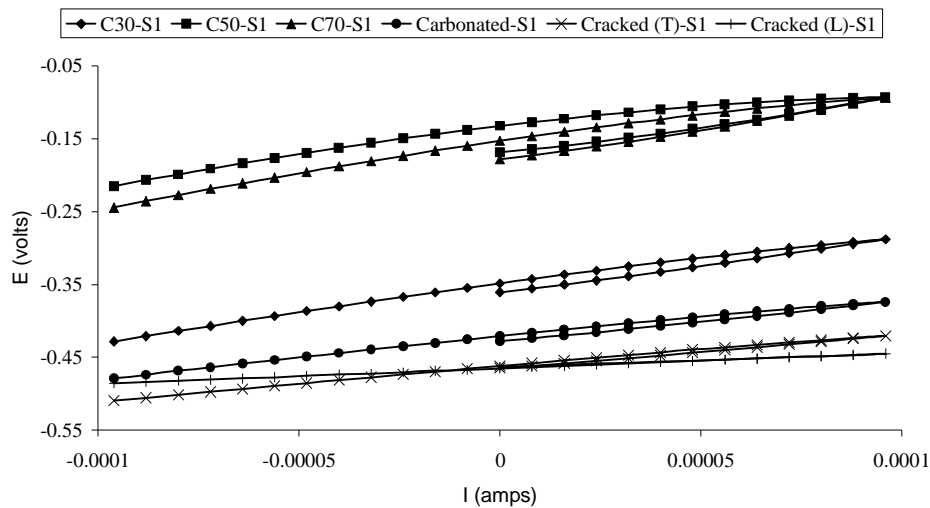


Figure 4. 52. Galvanodynamic LPR curves for one of the specimens of each variable.

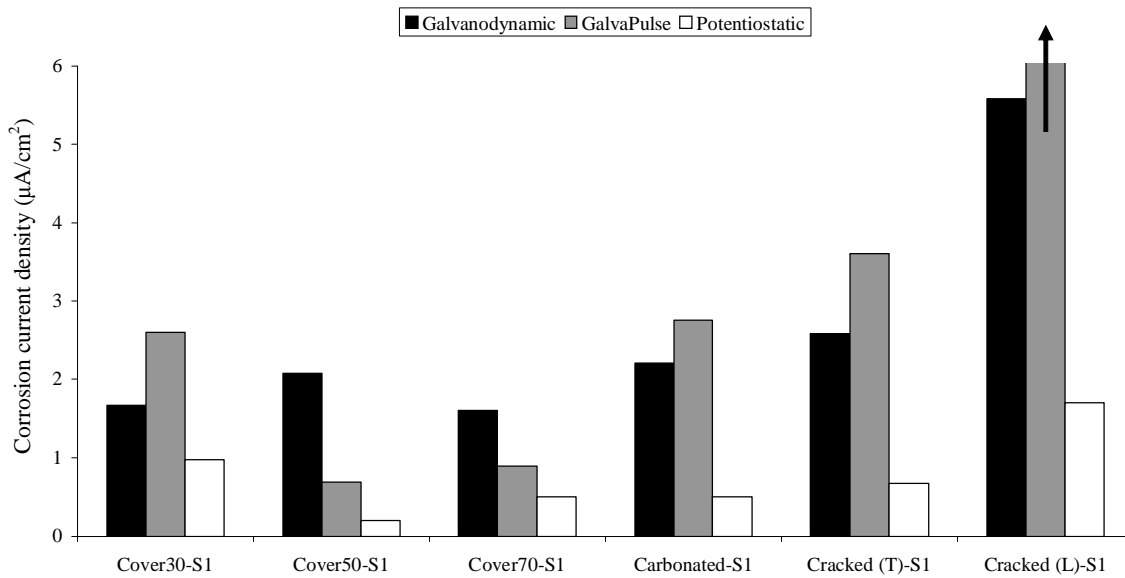


Figure 4. 53. Comparison of the values of corrosion current density of one of the specimens of each variable, measured by three different techniques.

In spite of the fact that the values are higher than those obtained from the potentiostatic LPR test, because is relatively fast and can be used in the field, this technique is recommended for initial evaluations and comparison of corrosion activities between different locations of a structure.

#### **4.1.2.3. Electrical resistance of concrete**

The resistance of concrete specimens was monitored, using the GalvaPulse™ (with and without the guard ring), EIS, galvanostatic pulse technique using the potentiostat, and the Wenner technique. Figure 4.54, shows the concrete resistance for all the specimens, measured using the GalvaPulse™ while the guard ring was on and the average values are given in Figure 4.55. The comparison of the measured values by the GalvaPulse™ and the other techniques was carried out in different times. Figure 4.56 shows the results at obtained 49 weeks after exposure.

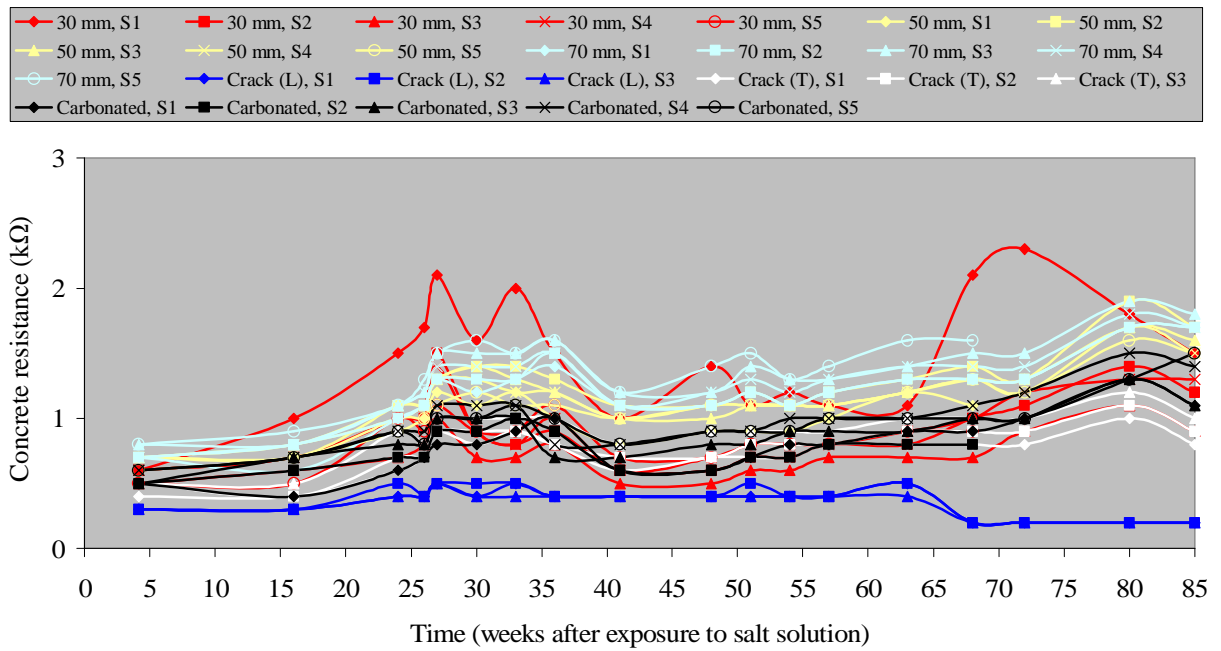


Figure 4. 54. Concrete resistance of all specimens with different variables, measured by the GalvaPulse™, guard ring on.

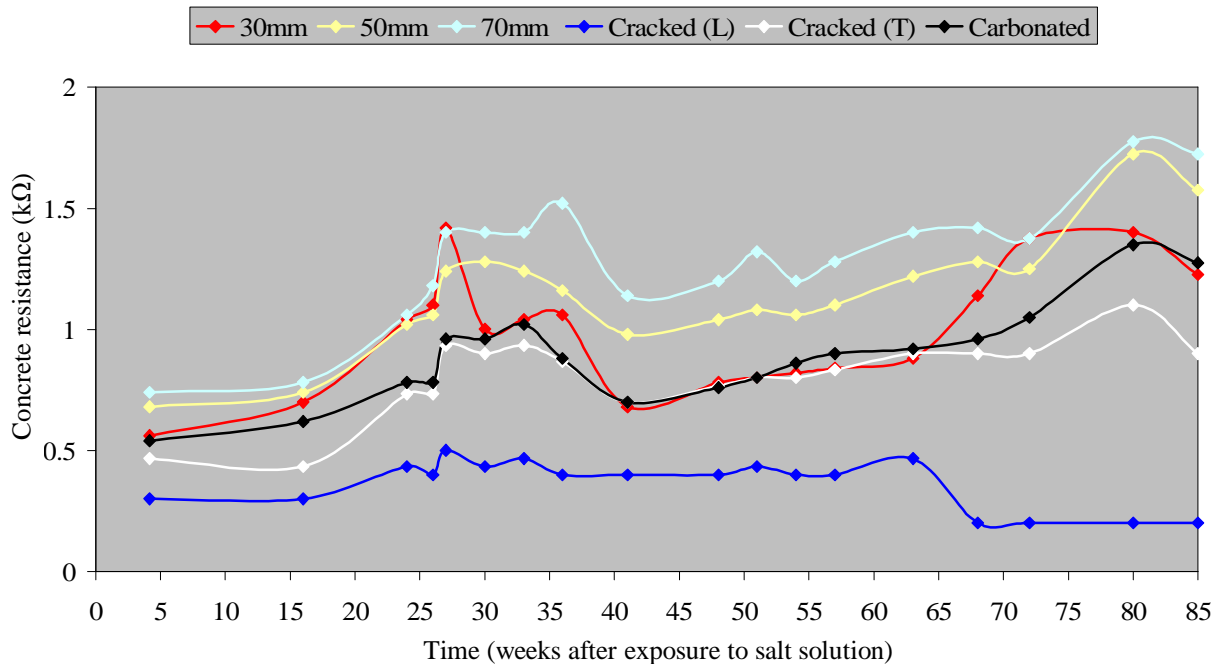


Figure 4. 55. Average values of concrete resistance, specimens with different variables, measured by the GalvaPulse™, guard ring on.

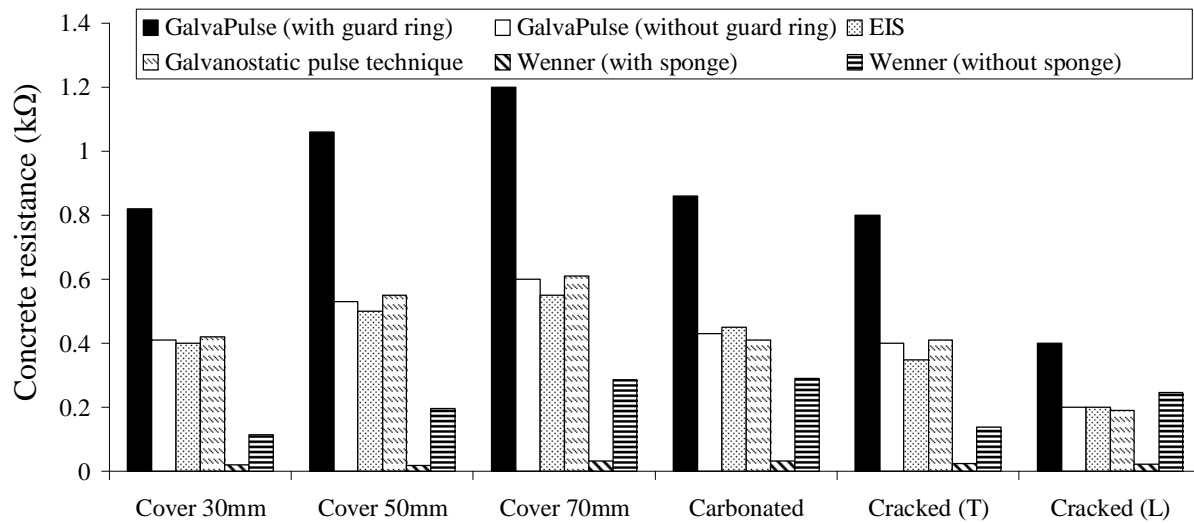


Figure 4. 56. Comparison between concrete resistance, measured by GalvaPulse™ (guard on and off), EIS, galvanostatic pulse technique and Wenner technique, 49 weeks after exposure to salt solution. The shown values are the average of the measured concrete resistances of multiple specimens of each variable.

#### 4.1.3. Chloride content

One of each of the specimens with 30mm cover, 50mm cover, 70mm cover and a carbonated specimen were broken after 70 weeks of exposure to salt solution. Concrete powders were prepared from the location of steel imprint on the broken specimens where corrosion products were observed, if at all. In the specimen with 30mm cover depth, the corrosion products were found in the middle part of the steel. In the specimen with 50mm cover depth, no corrosion products were observed. In specimens with 70mm cover depth and carbonated cover, the corrosion products were found at the border of epoxy coated part of the steel rebars, close to one end of each specimen. In addition to these locations, powders were also collected from the middle part of each broken specimen, 10mm above the location of the steel bar. Chloride

analysis was performed based on ASTM C1152, as described in Section 3.3.1.2 and the results are as following:

Table 4. 2. Results of chloride content analysis

| Specimen            |                                    | mol/ml         | Average | % weight of cement | Average |
|---------------------|------------------------------------|----------------|---------|--------------------|---------|
| cover depth<br>30mm | Steel imprint                      | 0.00158        | 0.0016  | 0.44               | 0.44    |
|                     |                                    | 0.0016         |         | 0.45               |         |
|                     |                                    | 0.00151        |         | 0.42               |         |
|                     | 10mm above<br>the steel<br>imprint | 0.0019         | 0.0018  | 0.53               | 0.51    |
|                     |                                    | 0.00171        |         | 0.48               |         |
|                     |                                    | 0.00185        |         | 0.52               |         |
| cover depth<br>50mm | Steel imprint                      | Not detectable | ----    | Not detectable     | ----    |
|                     |                                    | Not detectable |         | Not detectable     |         |
|                     |                                    | Not detectable |         | Not detectable     |         |
|                     | 10mm above<br>the steel<br>imprint | Not detectable | ----    | Not detectable     | ----    |
|                     |                                    | Not detectable |         | Not detectable     |         |
|                     |                                    | Not detectable |         | Not detectable     |         |
| cover depth<br>70mm | Steel imprint                      | 0.00139        | 0.0014  | 0.39               | 0.39    |
|                     |                                    | 0.00141        |         | 0.4                |         |
|                     |                                    | 0.00133        |         | 0.37               |         |
|                     | 10mm above<br>the steel<br>imprint | Not detectable | ----    | Not detectable     | ----    |
|                     |                                    | Not detectable |         | Not detectable     |         |
|                     |                                    | Not detectable |         | Not detectable     |         |
| Carbonated          | Steel imprint                      | 0.000731       | 0.0007  | 0.21               | 0.21    |
|                     |                                    | 0.000728       |         | 0.2                |         |
|                     |                                    | 0.000742       |         | 0.21               |         |
|                     | 10mm above<br>the steel<br>imprint | Not detectable | ----    | Not detectable     | ----    |
|                     |                                    | Not detectable |         | Not detectable     |         |
|                     |                                    | Not detectable |         | Not detectable     |         |

#### 4.1.4. Effect of the wetness of the surface on half-cell potential measurements

To determine the effect of the wetness of the concrete surface on the half-cell potential values, the half-cell potential of the steel bar in a beam (Figure 4.57) with inconsistent surface wetness was monitored by time. For the measurement, the surface of the beam was wetted thoroughly and a wet sponge was used between the Cu/CuSO<sub>4</sub> reference electrode and the concrete surface. The half-cell potential was monitored every 0.2 second for 90 minutes and the

results are given in Figure 4.58. As can be seen, the starting half-cell potential in a beam was  $\sim -254$  mV vs. CSE which is in uncertainty region based on ASTM C876 recommended guidelines. However, after about 20 minutes, this value reached to  $\sim 318$  which means that the probability of having corrosion is more than 90%! Therefore, to have a reliable half-cell potential value it is essential to keep the surface of the concrete wet, and provide enough time to stabilise the potential.

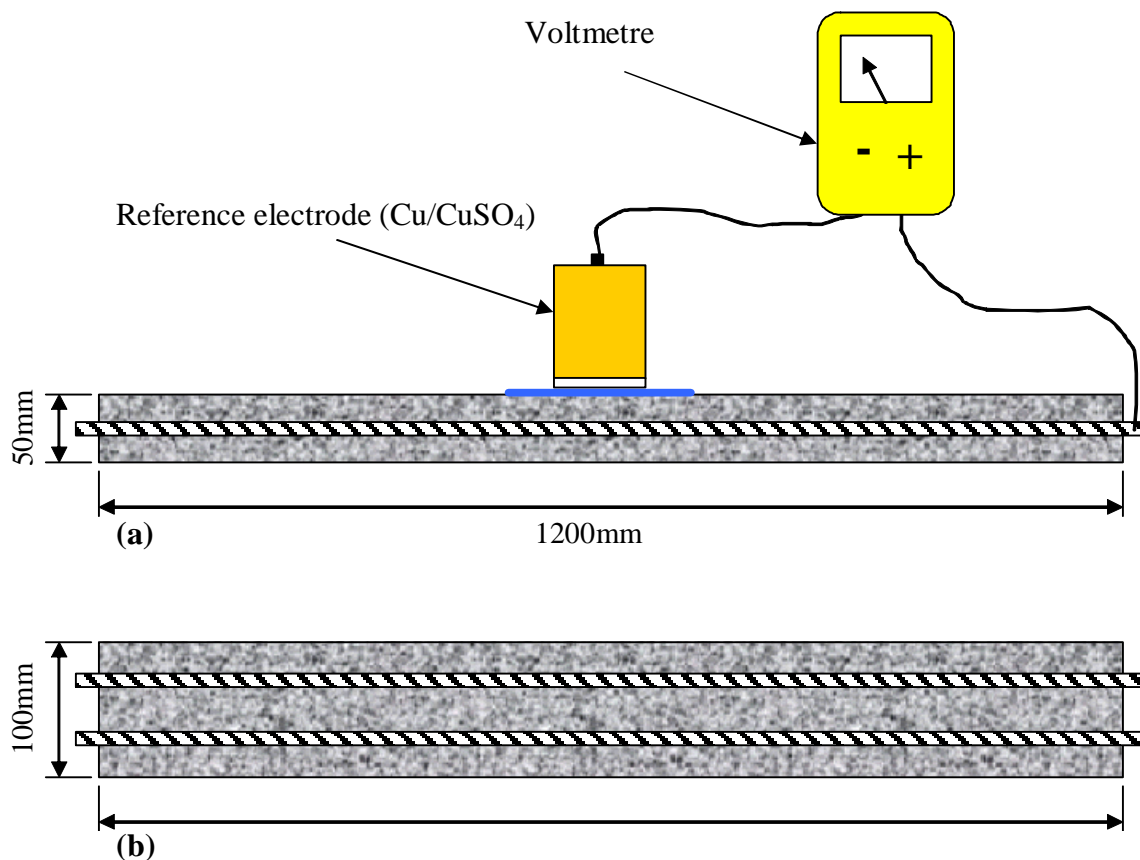


Figure 4. 57. Setup used to monitor the half-cell potential to determine the effect of surface wetness of the measured values; (a) side view and (b) top view.

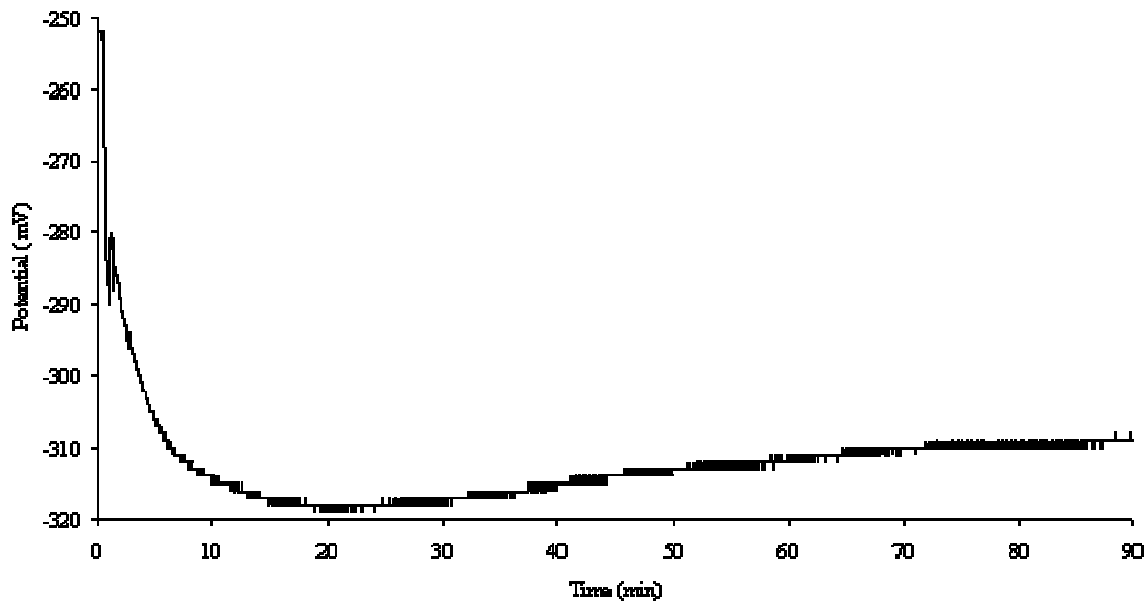


Figure 4. 58. Half-cell potential of the steel bar in a concrete beam, monitored for 90 minutes.

#### 4.1.5. The effect of different counter electrodes on corrosion measurements

The effect of the type of materials, with which the counter electrode is made, and the shape of the counter electrode on the different measurements was tested. For this purpose, three materials and two different shapes were used as given in Table 4.4.

Table 4. 3. Material, shape and the size of the counter electrodes, used to determine the effect of counter electrode on the measurements.

| Material                        | Shape               | Size                    |
|---------------------------------|---------------------|-------------------------|
| Stainless steel                 | Plate (rectangular) | 100 X 180 mm            |
| Stainless steel                 | Ring                | ID = 30mm and OD = 60mm |
| Galvanised steel                | Ring                | ID = 30mm and OD = 60mm |
| GalvaPulse™ measuring unit-Zinc | Ring                | ID = 30mm and OD = 60mm |



The size of all the rings was chosen to match the size of the counter electrodes used in the GalvaPulse™. The GalvaPulse™ measuring unit was also used with a potentiostat to perform potentiostatic and EIS tests. In this case, guard ring was off. Figures 4.59 to 4.61 show the results.

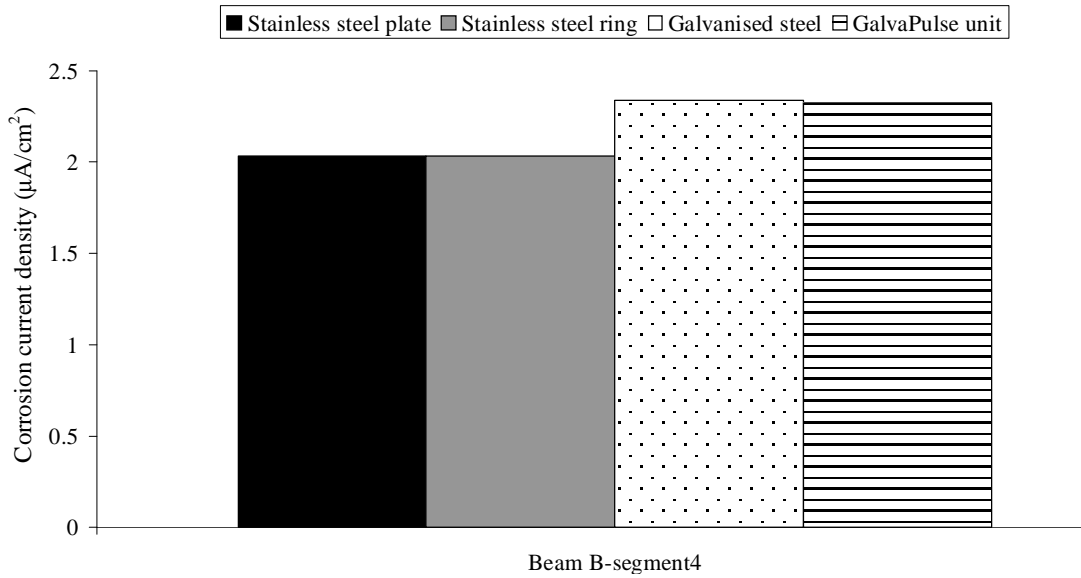


Figure 4. 59. The effect of counter electrode on the corrosion current density values, measured by potentiostatic LPR.

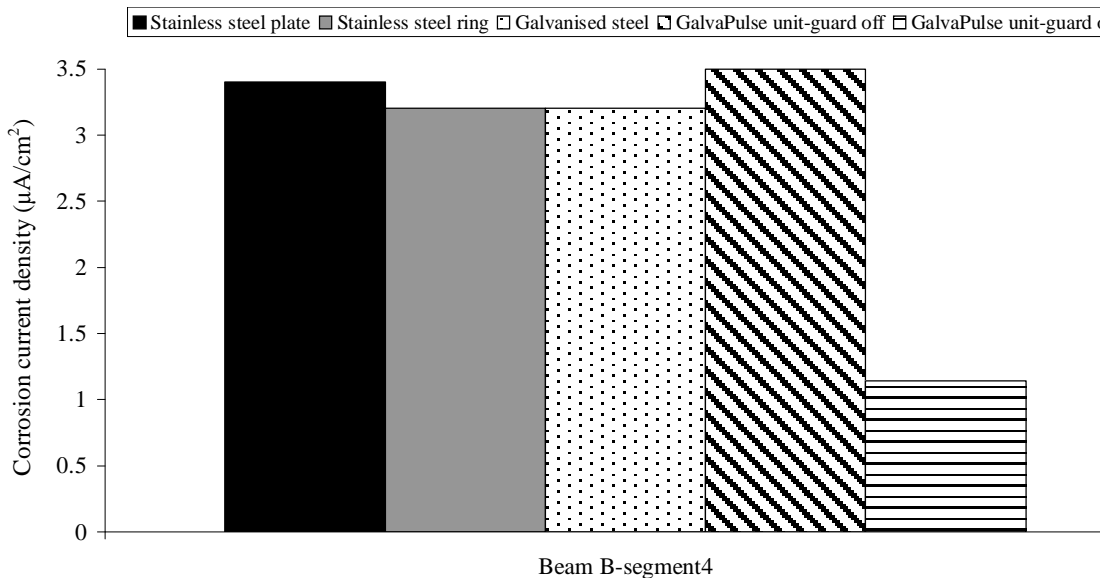


Figure 4. 60. The effect of counter electrode on the corrosion current density values, measured by the GalvaPulse™.

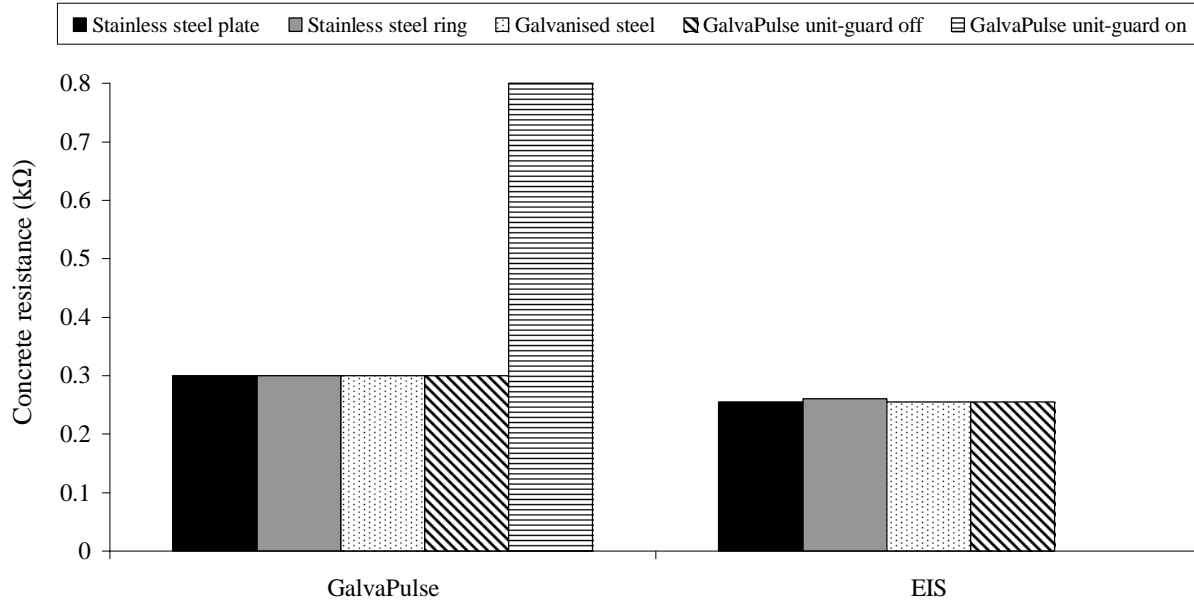


Figure 4. 61. The effect of counter electrode on the concrete resistance values, measured by the GalvaPulse™ and EIS.

Results show that there is no significant difference between different materials, size and different shapes. It should be noted that this conclusion could be only valid for the corrosion measurements of steel in concrete. The results might be different in different solutions due to exchange current density of the oxygen or hydrogen on different materials. The counter electrode should be made of materials that are inert to the electrolyte and they should have high exchange current density. Platinum and graphite are commonly considered as good counter electrode materials. Based on the environment, the organic binder in graphite may leach out and contaminated the electrolyte. This is not a problem in concrete but it should be noticed in other systems.

#### 4.1.6. Function of the GalvaPulse™

To check the function of the GalvaPulse™, its measuring unit and PSION computer were connected to an HP model 34401A digital multimeter and the applied current on the counter and on the guard ring as well as the resultant potential, were measured independently from the PSION computer. For this purpose, one specimen with cover depth of 30 mm and one with the cover depth of 70 mm were used and three different currents were applied: 50  $\mu\text{A}$ , 100  $\mu\text{A}$  and 200  $\mu\text{A}$  while the guard ring was on and off. Figures 4.62 and 4.63 show the measured current on the counter and guard ring, respectively, electrode with different pre-set applied currents.

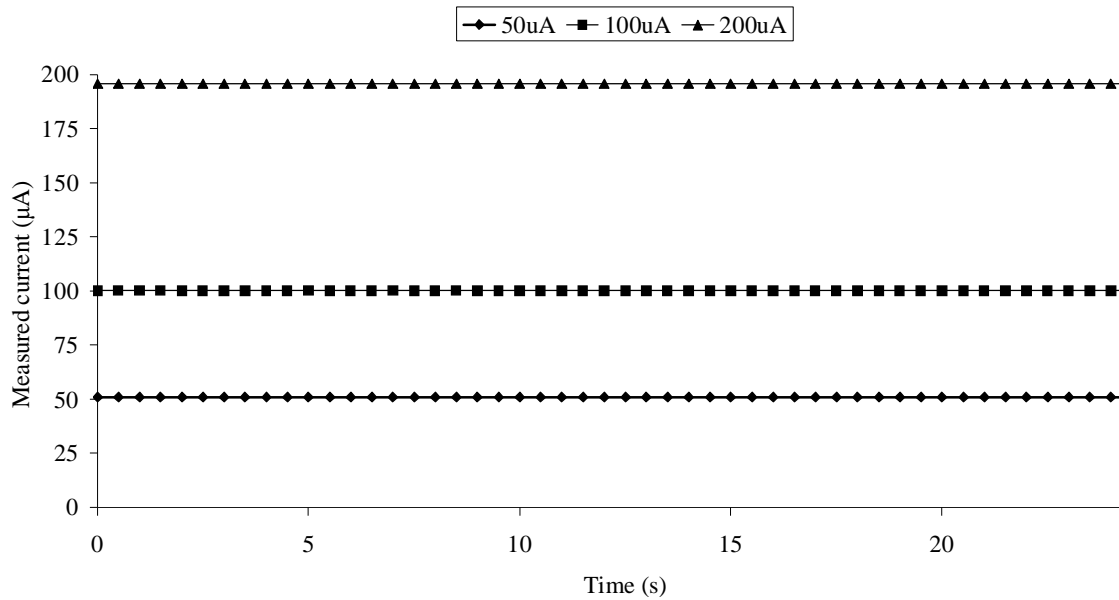


Figure 4. 62. Measured current on the counter electrode of the GalvaPulse™ measuring unit with three pre-set applied current.

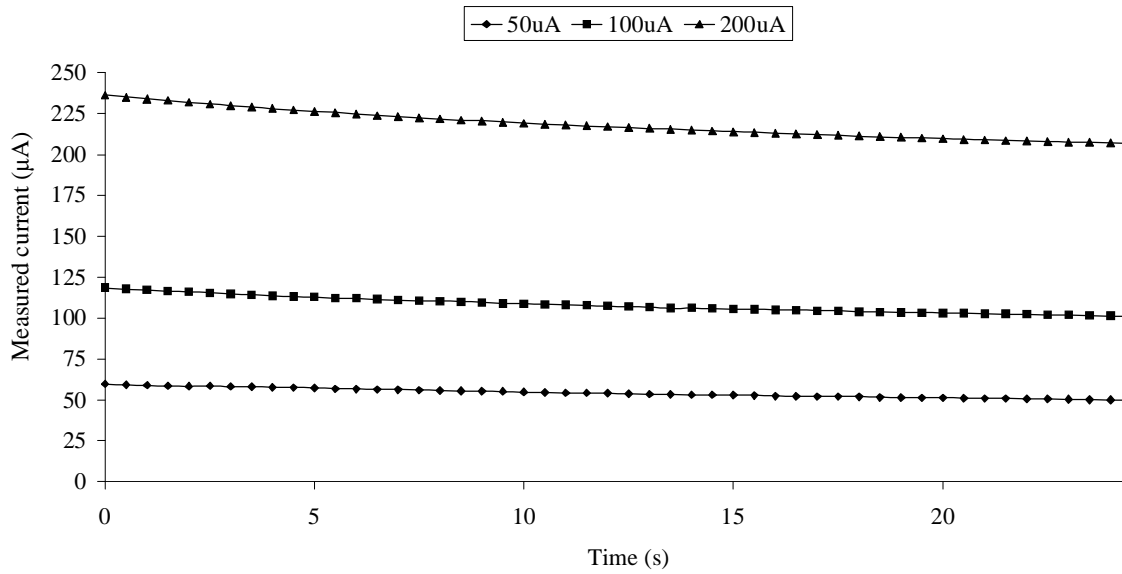


Figure 4. 63. Measured current on the guard ring of the GalvaPulse™ measuring unit with three pre-set applied current.

To ascertain if the guard ring works or not, the current on the guard ring was measured while the guard was off and the result (Figure 4.64) shows that it is working properly and the measured current on the guard ring when the guard is off is almost zero.

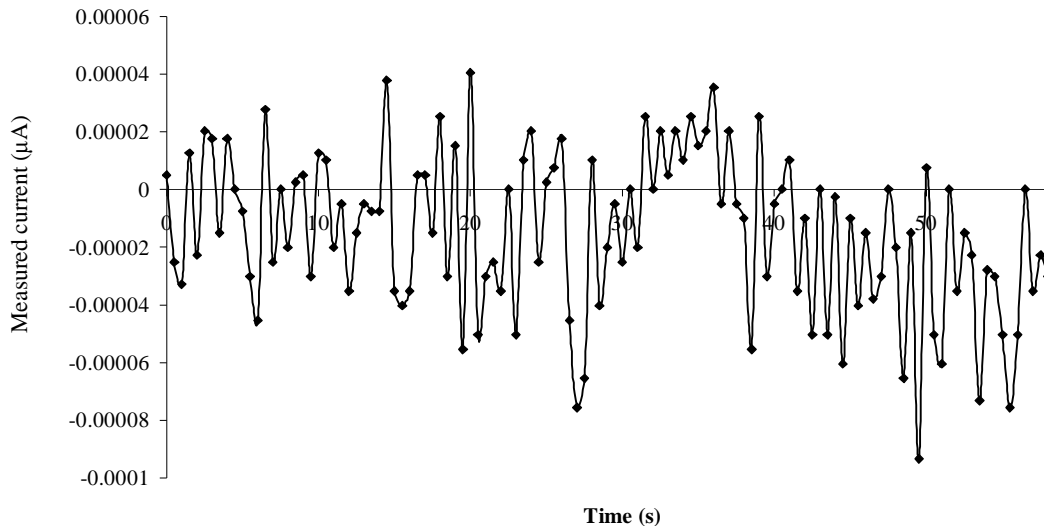


Figure 4. 64. Measured current on the guard ring, while the guard was off. The measured values are almost zero.

In order to verify the calculations of the PSION computer, the resultant potentials were monitored with and without the guard ring. The measurements were performed on one of the specimens with a cover depth of 70 mm and the applied current was 100  $\mu$ A. Results are shown in Figures 4.65 and 4.66.

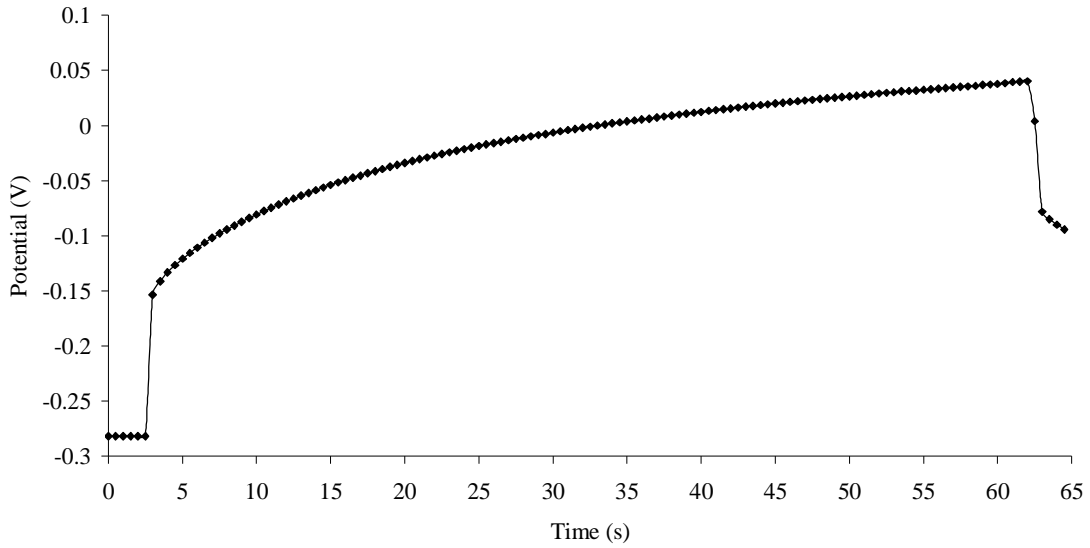


Figure 4. 65. Potential changes, measured by the HP multimeter; guard ring on; applied current =100 $\mu$ A.

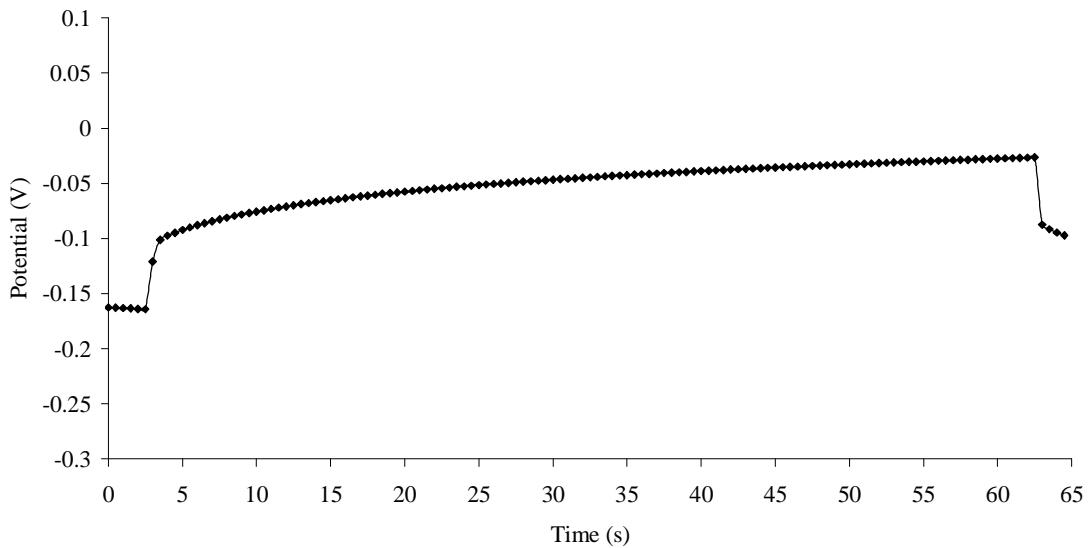


Figure 4. 66. Potential changes, measured by the HP multimeter; guard ring off; applied current =100 $\mu$ A.

From Figures 4.65 and 4.66, the concrete resistance and corrosion current density in both cases are calculated and the results compared to what was calculated by the PSION unit and given in Table 4.4. The calculated value from the obtained results of HP multimeter and PSION computer, are close and the results given by PSION computer are reliable.

Table 4. 4. Comparison between concrete resistance and corrosion current density, calculated using the data in Figures 4.65 and 4.66 and PSION unit.

|                          | Concrete resistance<br>(kΩ),<br>guard on | Concrete resistance<br>(kΩ),<br>guard off | Corrosion current<br>density<br>(μA/cm <sup>2</sup> ), guard on | Corrosion current<br>density<br>(μA/cm <sup>2</sup> ), guard off |
|--------------------------|--|---|---|--|
| <b>Calculated values</b> | 1.28                                     | 0.63                                      | 0.61  | 1.58   |
| <b>PSION computer</b>    | 1.4                                      | 0.7                                       | 0.49  | 1.28   |

Polarised length (and consequently, the polarised area) of the steel bar is an important parameter in corrosion measurement calculations. As described earlier, the goal of the guard ring is to provide uniform polarisation over a limited length of the rebar. To estimate the polarised area, using the GalvaPulse™, a setup shown in Figure 4.67 was used. Before and during actual application of the current by the GalvaPulse™, the half-cell potential of the steel was measured versus a reference electrode (Cu/CuSO<sub>4</sub>) at five different distances: 0 mm, 55 mm, 300 mm, 500 mm and 1000 mm, from the GalvaPulse™ measuring unit. Three applied currents were used: 50 μA, 100 μA and 200 μA. The difference between two measured potentials (before and during the application of current) are plotted versus distance in Figures 4.68 and 4.69 when the guard was on and off, respectively.

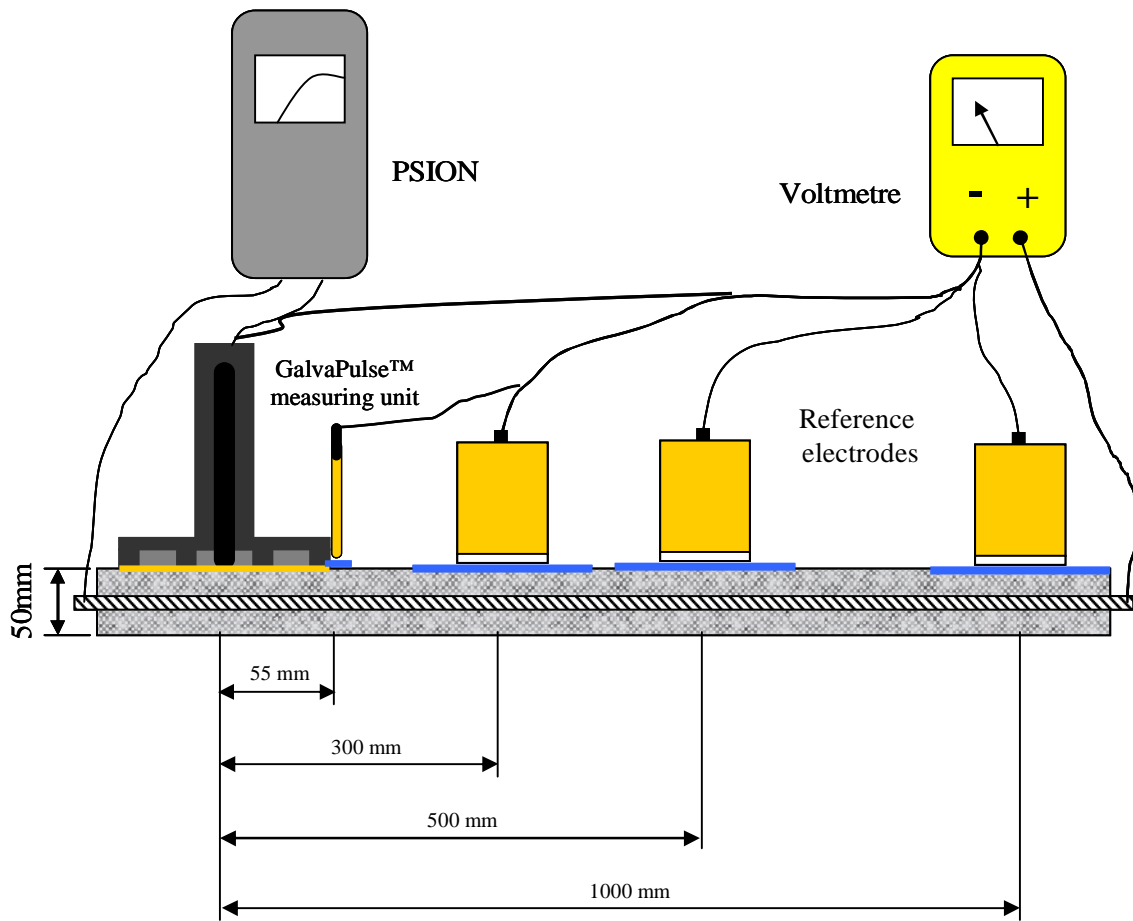


Figure 4. 67. Setup used to estimate the polarised length of the rebar.

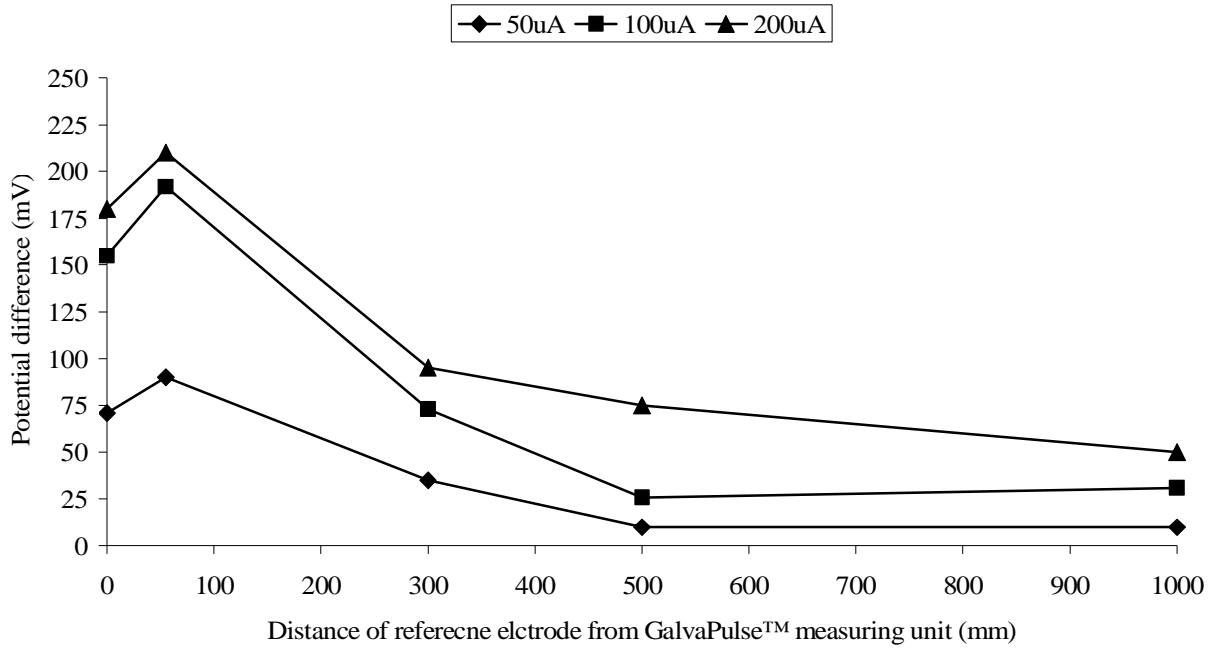


Figure 4. 68. Potential differences between before and at the end of applying the current by GalvaPulse™, guard ring on. Concrete resistance is compensated.

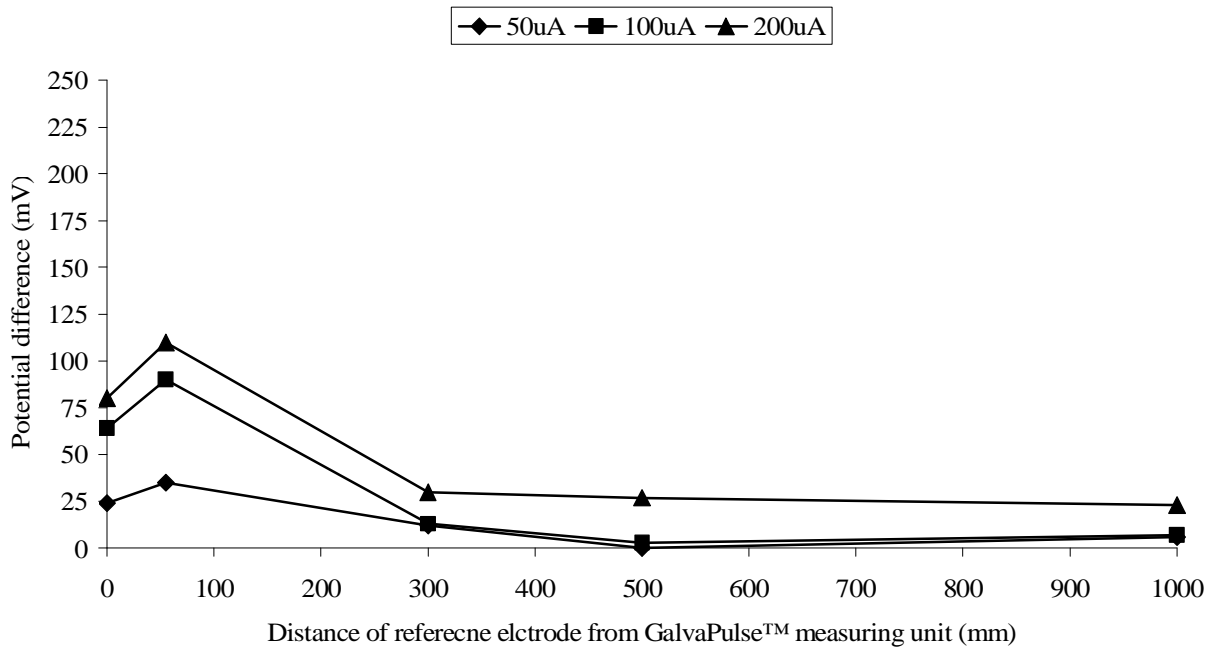


Figure 4. 69. Potential differences between before and at the end of applying the current by GalvaPulse™, guard ring off. Concrete resistance is compensated



As can be seen, when the guard ring is on the steel bar is polarised to a distance of one metre from the GalvaPulse™ measuring unit. However, when the guard ring is off, not only is the polarised distance shorter but the amount of polarisation is also less. In both cases, the potential immediately adjacent to the GalvaPulse™ measuring unit is higher than that immediately under the GalvaPulse™ measuring unit and decays at further distances.

To determine the influence of the guard ring on the current under the counter electrode, a setup shown in Figure 4.70 was used. The applied current under the counter electrode was measured with and without using guard ring with different pre-adjusted currents and the results show that guard ring also doubles the applied current under the counter electrode.

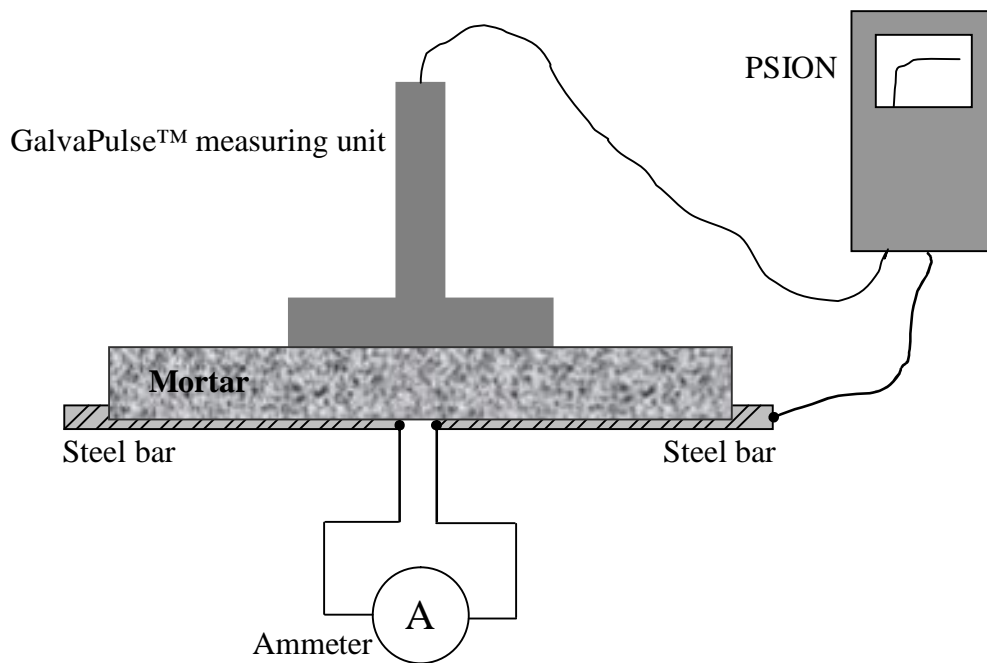


Figure 4. 70. Schematic plan of the setup, used to determine the influence of the guard ring on the current under the counter electrode.

The other important point that should be mentioned about the GalvaPulse™ is its maintenance. The measurement unit must always be cleaned after measurements; this is especially important when one is dealing with salt solutions. The GalvaPulse™ pulse generator unit should be calibrated either monthly or before each use, whichever is the longer period. It has been found that, ignoring this point, causes problem and the results are not reliable.

Results (Figures 4.62 and 4.63) show that the counter and guard electrodes both apply the set current to the surface with the same polarity. The current applied by the guard ring is supposed to limit the polarised area. However, measurements show that by using the guard ring during the test, a greater length of the steel rebar is being polarised (Figures 4.68 and 4.69). The same applied current from both guard and counter electrodes and the larger size of the guard ring are the reasons of such behaviour. As shown, the measured values of corrosion current density and concrete resistance are higher and lower, respectively when the guard ring is off. In all the calculations performed by the GalvaPulse™, the current is considered to be the value which was entered into the PSION computer. However, when the guard ring is on, the value of the current is double the pre-set value. The results given in Table 4.4 are recalculated with considering this point. The new recalculated results (Table 4.5) using the actual applied current, are similar in both cases.

Table 4. 5. Calculation of the corrosion current density and concrete resistance, by using actual applied current; pre-set current:  $I=100\mu\text{A}$ , guard ring off and on.

|  | Concrete resistance<br>( $\text{k}\Omega$ ),<br>guard on | Concrete resistance<br>( $\text{k}\Omega$ ),<br>guard off | Corrosion current<br>density<br>( $\mu\text{A}/\text{cm}^2$ ), guard on | Corrosion current<br>density<br>( $\mu\text{A}/\text{cm}^2$ ), guard off |
|--|--|---|---|--|
| <b>Calculated values<br/>by using actual<br/>applied current</b> | 0.64   | 0.63  | 1.23  | 1.58   |

#### **4.1.7. Reinforcing steel passivation time**

Figures 4.71 and 4.72 show the corrosion current densities measured over a period of 300 hours by the LPR for the samples embedded in mortar and immersed in synthetic pore solution, respectively and their half-cell potential values are plotted in Figures 4.73 and 4.74, respectively. As mentioned earlier, in each case, the mill scale on three of the steel bars was removed by sand blasting and three steel bars had mill scales on them (as received).

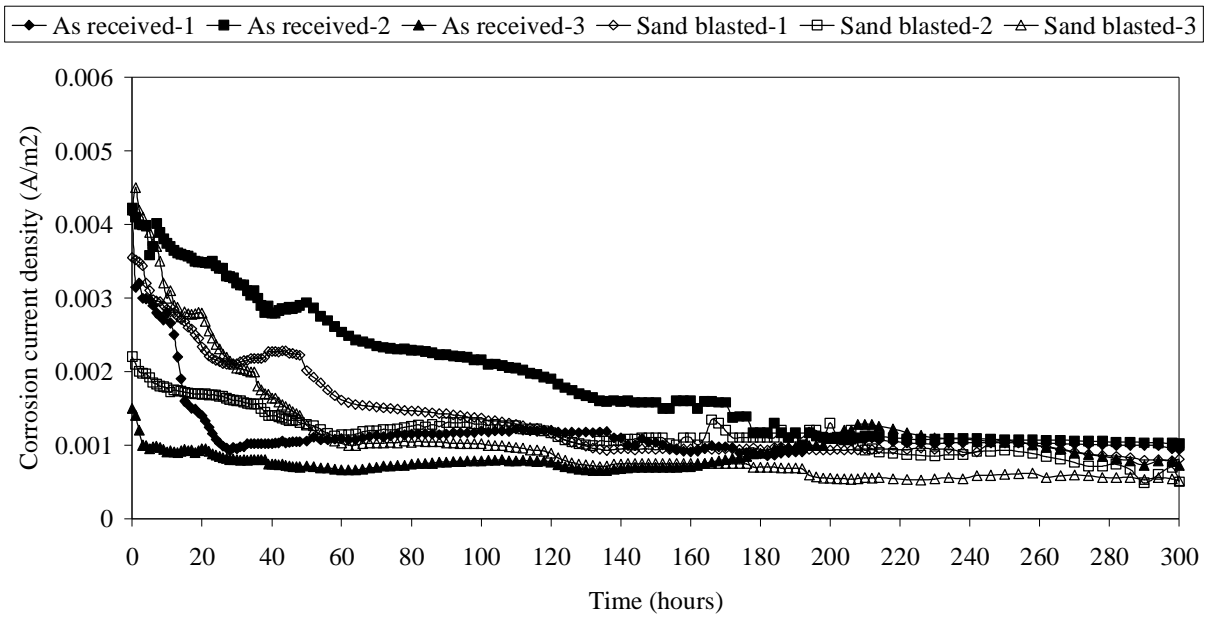


Figure 4. 71. Corrosion current density of steel embedded in mortar for 300 hours.

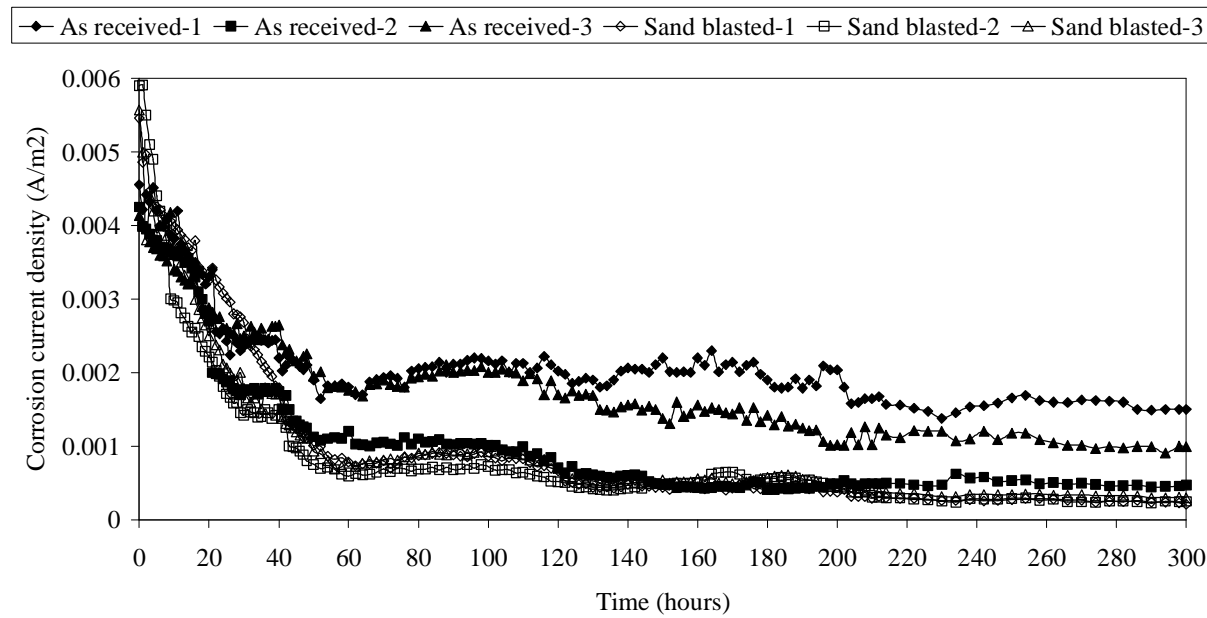
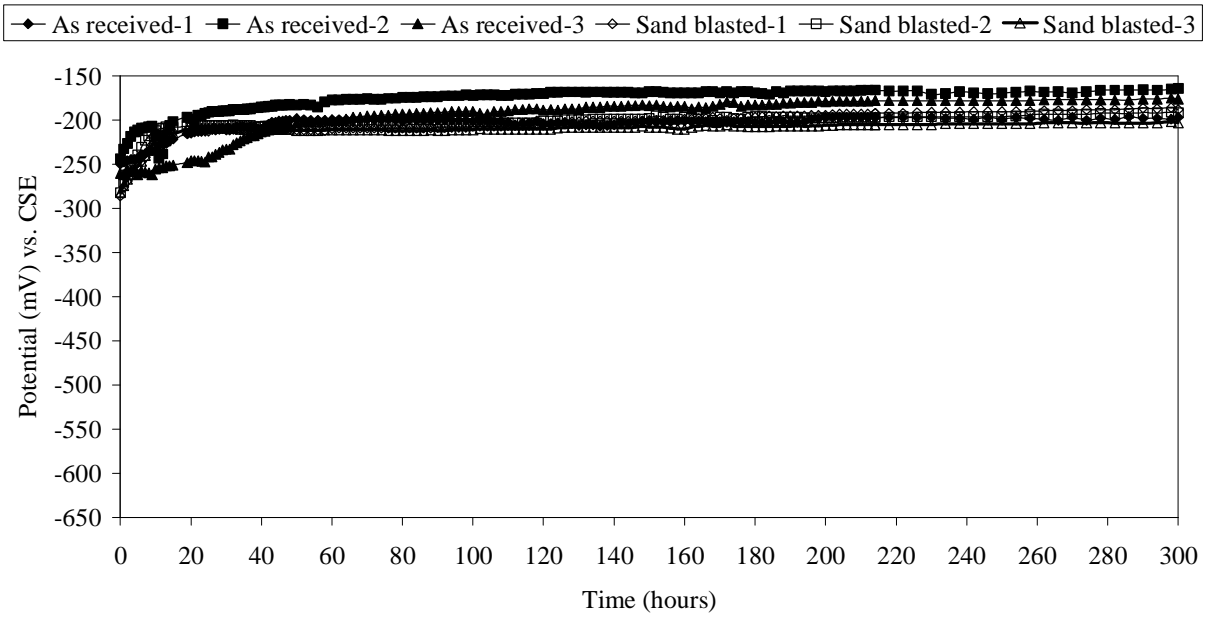
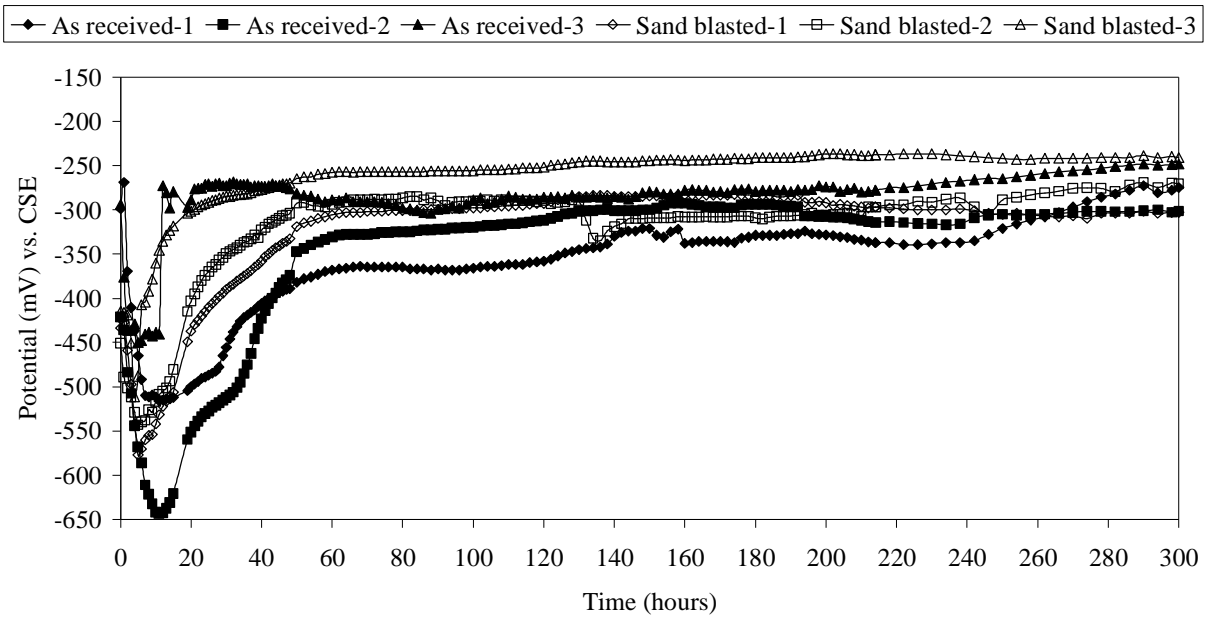


Figure 4. 72. Corrosion current density of steel in synthetic pore solution for 300 hours.



The electrical resistance of mortar of the same proportions as those in Table 3.4, was monitored, by EIS technique, every 30 minutes for 300 hours and the results are shown in Figure 4.75.

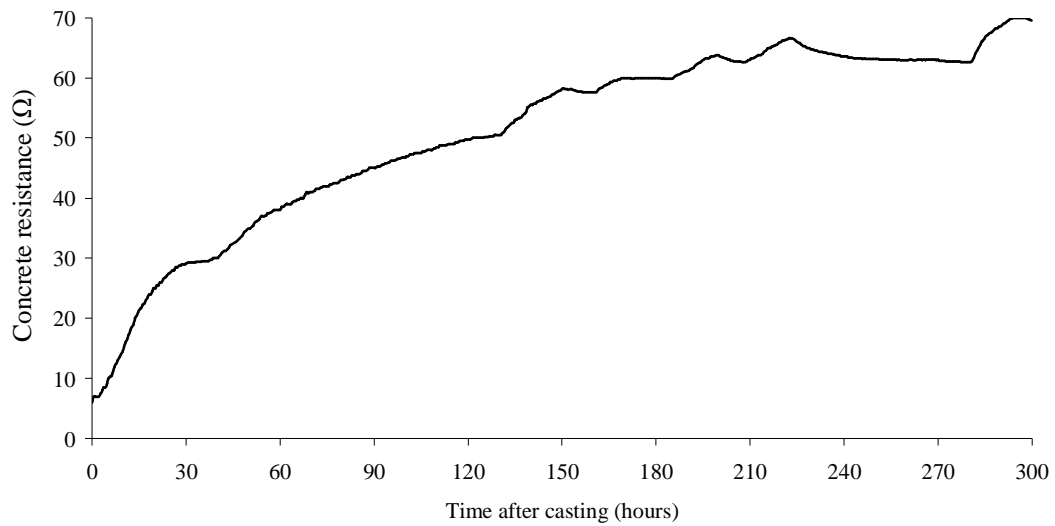


Figure 4. 75. Mortar resistance, measured every 30 minutes for 300 hours.

Results of Raman spectroscopy are shown in Figures 4.76 to 4.78 and the main Raman bands of reference iron oxide compounds are given in Table 4.6.

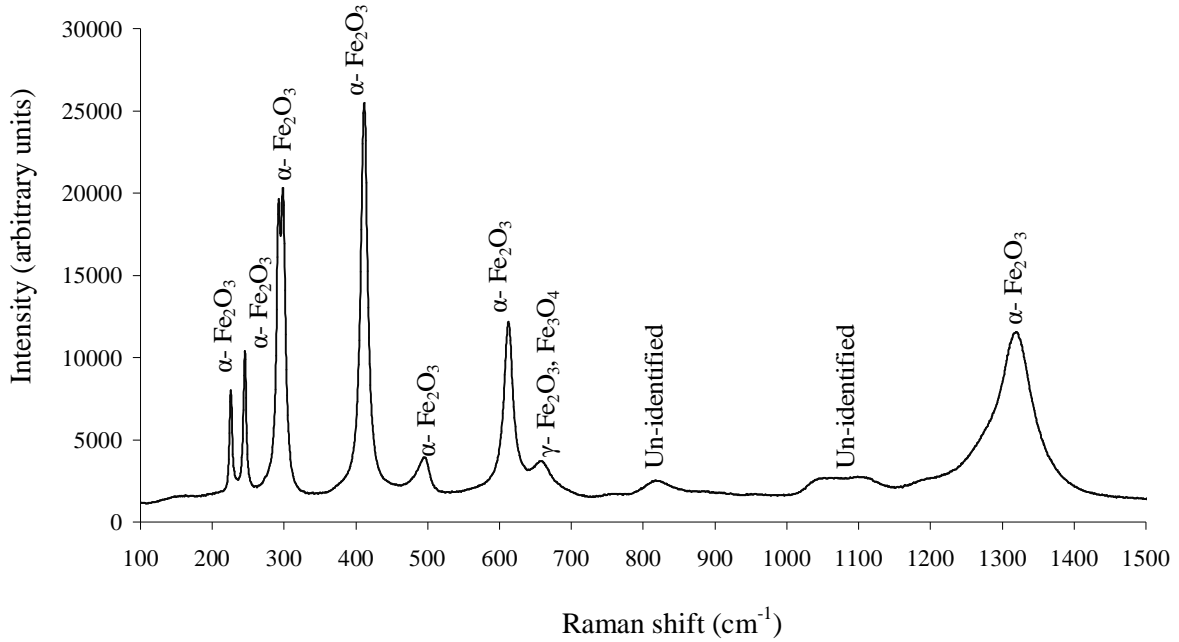


Figure 4. 76. Raman spectra of steel with mill scale, as received.

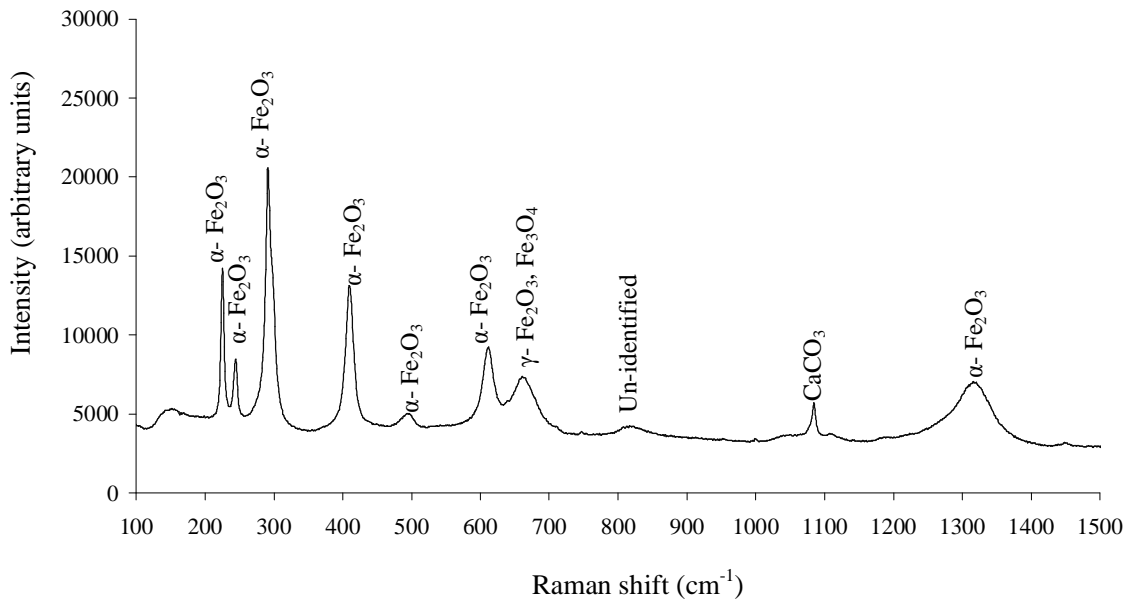


Figure 4. 77. Raman spectra of steel with mill scale , immersed in pore solution for 2 months.

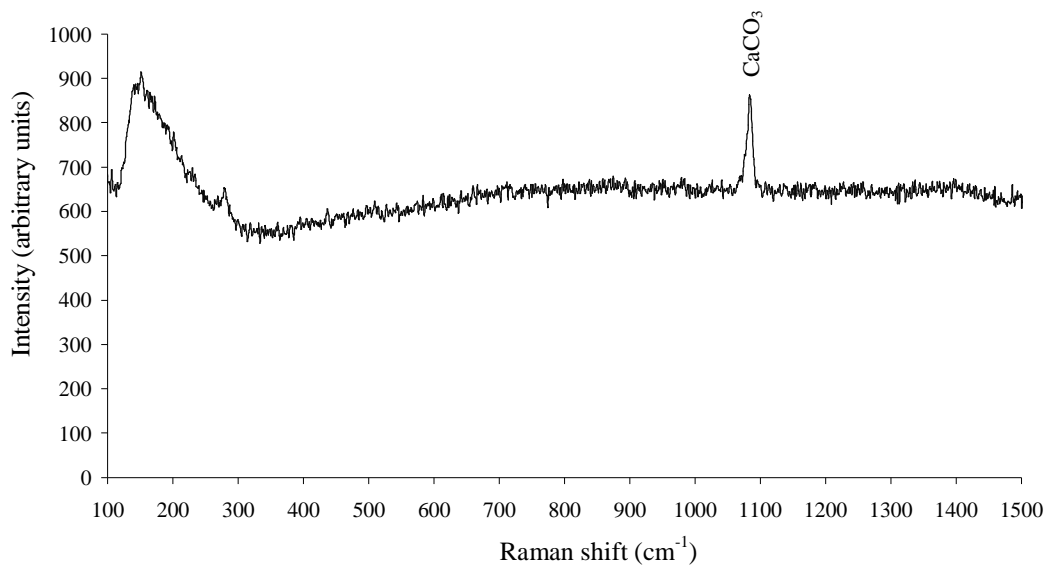


Figure 4. 78. Raman spectra of sand blasted steel , immersed in pore solution for 2 months.

Table 4. 6. Main bands of reference iron oxide compounds (in  $\text{cm}^{-1}$ ) [160-163].

| Magnetite               | Hematite                       | Maghemite                      |
|-------------------------|--------------------------------|--------------------------------|
| $\text{Fe}_3\text{O}_4$ | $\alpha\text{-Fe}_2\text{O}_3$ | $\gamma\text{-Fe}_2\text{O}_3$ |
| 289                     | 225                            | 265                            |
| 319                     | 247                            | 300                            |
| 418                     | 295                            | 350                            |
| 550                     | 412                            | 395                            |
| 670                     | 500                            | 505                            |
|                         | 613                            | 660                            |

The results show that the corrosion current density for both surface treatments drops to the expected value for the passive state ( $10^{-3}$  to  $10^{-4}$   $\text{A/m}^2$ ) [10] and stabilised after about 160 hours ( $\sim 7$  days) in mortar and 70 hours ( $\sim 3$  days) in synthetic pore solution. The half-cell potential values of the specimens embedded in mortar stabilized at about 70 hours ( $\sim 3$  days), while this time for specimens immersed in synthetic pore solution was about 45 hours (2 days). This difference may be attributed to the fact that the pH of the synthetic pore solution was high ( $\sim 13.5$ ) when the bars were immersed, whereas the pH of the mortar mixing water was initially



neutral and increased over time as the mortar hydrated. It has been shown that the passivity of steel increases with increasing pH [18] but, as discussed below, research has indicated that the pH in cement paste or mortar reaches a value of 13 very rapidly [164]. A second factor could be the greater mobility of ions in pore solution than mortar.

The potential values for the specimens embedded in mortar showed dramatic changes within the first ~50 hours (~ 2 days) exhibiting a considerable negative shift in potential during the first ~10 hours, after which the potential rapidly became more anodic over the next ~40 hours and changed only gradually thereafter. This is in contrast to the corrosion data which exhibited only a gradual decrease over a much longer period. It is also in contrast to the variations in half cell potential values for specimens immersed in synthetic pore solution, which did not exhibit a negative shift but increased rapidly in the first ~ 20 hours and continued with a slow anodic shift thereafter.

Several factors have been considered to explain this difference:

- First is the pH of the environment which was constant at ~13.5 in the pore solution but increases from neutral water in the mortar. However, studies [164] have shown that the pore solution in concrete reaches values of ~ 13 within approximately one hour of mixing the concrete.
- Second, the resistivity of the concrete was considered as a factor. Therefore, the electrical resistance of mortar was monitored, as shown in Figure 4.68. It is clear that the mortar resistance increased with a relatively sharp slope within first ~15 hours after casting, after which, the rate of increase decreased. This, by itself, could not explain the half cell behaviour of the steel in mortar but is probably a contributory factor.

- Third, the rise in temperature of the mortar as it hardens was considered as a factor. However, any temperature rise would influence the corrosion rate more than the half cell potential. Again, temperature alone is not likely to be responsible for the observed changes in potential but, again is probably a contributing factor.

A parameter which is dependent on all these factors, relative humidity, temperature, polarity of the environment and the mobility of the ions and charges in the medium, is the relative permittivity on the mortar [165]. The structural and chemical changes monitored by NMR [166, 167], pH measurements and electrical resistance measurements over the initial period of the casting would result in a change in the permittivity of mortar.

The half-cell potential is a measure of the force field existing between the reference electrode, charge  $q_1$  and the rebar, charge  $q_2$ . The potential force between these two electrical charges can be calculated from the following equation:

$$F = k \frac{q_1 q_2}{r^2} \quad \text{eq 4. 1}$$

where  $r$  is the distance between two charges (the cover depth) and  $k$  is called the coulomb constant [168] (which is not constant during hydration). In the present case, it can be assumed that  $q_1$ , and  $r$  are constant and  $q_2$  and  $k$  are changing during hydration process.  $k$  is related to the relative permittivity,  $\epsilon_r$ , which describes how an electric field is disturbed by a dielectric medium of the environment according to the following equation:

$$k = \frac{1}{4\pi\epsilon_r}$$

eq 4. 2

The response of materials to external alternating fields generally depends on the frequency of the field. This frequency dependence reflects the fact that a material does not respond instantaneously to an applied field. For this reason permittivity is often defined as a complex function of the frequency of the applied field. Static permittivity is the response of a medium to static electric fields which can be obtained at low frequencies [169]. At these frequencies the phase shift becomes noticeable and it depends on temperature and the details of the medium such as the polarity of its components and its microstructure [169, 170]

The solution in the pore system mainly determines the dielectric properties concrete. This solution can be a free liquid, for example in the capillary pores, or can be physically bound or chemically bound water. The different dielectric properties of the liquid and solid phases can be used to determine the changes in the microstructure of the cement paste. The moisture content and its distribution is the main factor affecting the dielectric properties of the concrete [171]. For example,  $\epsilon_r$  for water is ~80 and for dry concrete is ~4 [172]. Van Beek et al. [171] measured the permittivity of concrete for 160 hours by using a frequency of 20 MHz to generate an electrical field between two embedded stainless steel rods in concrete with a diameter of 10 mm and a length of 30 mm.

A rapid increase in  $\epsilon_r$  was observed in the first ~16 hours after casting for a concrete with  $w/cm=0.45$ , i.e. the same as in the present work. Their results are shown in Figure 4.79, in which the maximum in permittivity corresponds to the minimum in potential drop observed in Figure 4.73.

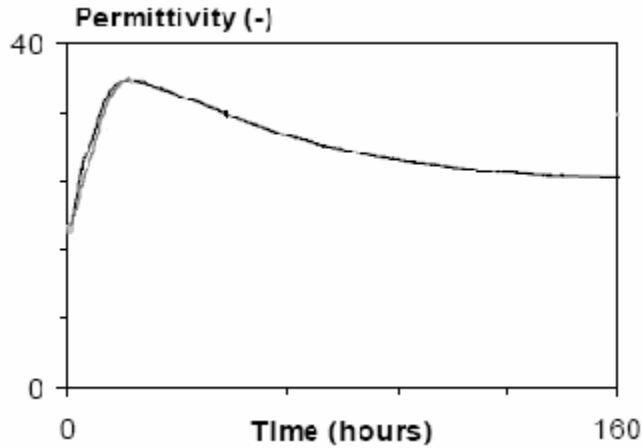


Figure 4. 79. Permittivity of young concrete with ordinary Portland cement [171].

During hydration, the steel passivates in the high pH of the mortar resulting in a decrease in the potential charge,  $q_2$ . However, because a similar decrease in  $q_2$  would be expected for steel in synthetic pore solution, which does not exhibit a major change in half cell potential, it appears that changes in the permittivity with hydration dominate the changes in half cell potential in mortar, and presumably, also in concrete.

The as-received steel (with the mill scale intact) generally shows a higher corrosion rate than sand-blasted steel but there is no consistency in half-cell potential values. Moreover, all  $E_{\text{corr}}$  values are between -350 and -200 mV CSE, which is within the range of “uncertainty of active corrosion” according to the ASTM C876 guidelines for interpretation of half cell potential data [173]. This indicates that the ASTM recommendations are not applicable to potentials in the earliest stages of passivation of the steel while the passive layer is being developed.

It is also important to note that the half-cell potential values appear to reach “steady state” faster than the values of corrosion current density. However, these “steady state” values are far more negative than those normally considered to represent the passive state of steel in

concrete or mortar and indicate that it takes considerably longer for the potential to attain a “true” passive value. This is also the conclusion of observations in the field, where steel has taken more than three months to reach potentials more positive than -200 mV CSE [16]. This implies that it actually takes much longer for the steel to be fully passivated than is suggested by the corrosion rates determined here which, in fact, continued to decrease very slowly even after 300 hours in solution or mortar.

Comparison between Figures 4.75 and 4.76 and data from Table 4.6 reveals that, even after two months immersion in synthetic pore solution, the mill scales still exist on the as-received samples, with no apparent change in their composition. As expected, there is no observable iron oxide on the surface of sand blasted steel bars (Figure 4.77) because a passive film is too thin to be detected by the Raman technique. It should be noted that the scale of intensity axis in Figures 4.75 and 4.76 is different from that in Figure 4.77.

#### **4.1.8. Stern-Geary constant (B)**

As mentioned in section 2.3.2, the constants  $B = 0.026V$  for active and  $B = 0.052V$  for passive corrosion of steel in concrete have been used for many years without questioning them. In this project, values of  $B$  were determined by measuring  $\beta_a$  and  $\beta_c$  in different specimens. To measure the anodic and cathodic Tafel constants, cyclic polarisation results from the measurements on different specimens in the lab were used. While a cathodic Tafel slope could be measured, there is no sensible linearity of the anodic parts in most of the cyclic polarisation experiments; therefore to measure the value of  $\beta_a$  the anodic data were derived from the linear cathodic portion of the curve. The measured values of current which are given on the cyclic

curves are the net value. This means that each point on the cathodic part of the curve is the difference between cathodic and anodic currents ( $i_{\text{net},a}=i_c-i_a$ ) and each point on the anodic part of the curve is the difference between anodic and cathodic currents ( $i_{\text{net},c}=i_a-i_c$ ). To obtain the anodic portion from the cathodic one, the anodic current density ( $i_a$ ) can be calculated as  $i_a=i_{\text{net},c}+i_c$ . In the potential region near half-cell potential, the extrapolated Tafel line gives  $i_c$ , and the measured values (data points) give  $i_{\text{net}}$ . By using this method for a number of potentials, the anodic Tafel slope can be found and then the value of B can be calculated by using eq. 2.12. Figure 4.80, is a schematic illustration of this technique [54].

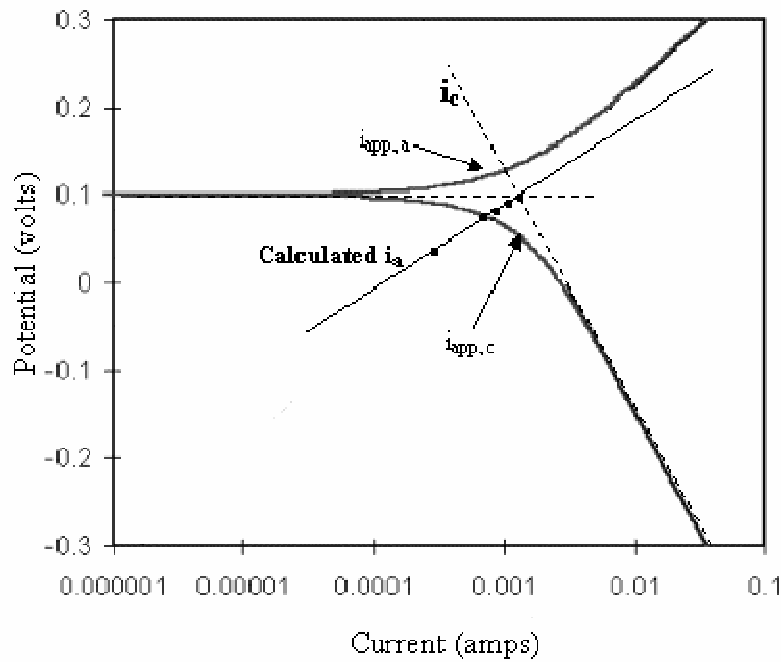


Figure 4. 80. Schematic illustration of obtaining  $i_a$  from  $i_c$  and  $i_{\text{app},c}$ .

By using the aforementioned method, the value of B was calculated for different specimens with different scan rates and the results are shown in Table 4.7.

Table 4. 7. Value of B, calculated for different specimens.

| <b>Specimen</b>                  | <b>Scan rate (mV/s)</b> | <b><math>\beta_a</math>(mV/decade)</b> | <b><math>\beta_c</math>(mV/decade)</b> | <b>B (mV)</b> |
|----------------------------------|-------------------------|--|--|---------------|
| Specimen with transverse crack   | 0.01                    | 486                                    | 271                                    | 76            |
| Specimen with transverse crack   | 0.1                     | 474                                    | 299                                    | 80            |
| Specimen with longitudinal crack | 0.01                    | 480                                    | 263                                    | 74            |
| Specimen with longitudinal crack | 0.1                     | 534                                    | 261                                    | 76            |
| Specimen with longitudinal crack | 0.5                     | 297                                    | 219                                    | 55            |
| Carbonated specimen              | 0.1                     | 247                                    | 466                                    | 70            |
| Segment 1 in beam A              | 0.006                   | 914                                    | 225                                    | 79            |

As shown in Table 4.7, the calculated values for B, based on different conditions, are between 55 and 80 mV. These values are mostly for the steel bars that are actively corroding. These values are higher than 26 mV which is usually used to calculate the active corrosion rate. It should be noted that, originally, the  $B = 26$  mV was validated for steel in saturated  $\text{Ca}(\text{OH})_2$  solution and it was found that this value for mortar is slightly higher [72]. However, the difference between the values in Table 4.7 and those which are traditionally used for the calculations is not large and using the actual values (given in Table 4.7) will not change the results significantly and the error factor would be less than 2 or 3. Therefore, the idea of choosing 26 mV and 52 mV for active and passive corrosion of steel in concrete is considered valid and can be used in the calculations.

## 4.2. RESULTS FROM FIELD MEASUREMENT

### 4.2.1. Bridge at the University of Waterloo

As mentioned in section 3.3.2.1., because epoxy coated rebars are used in the bridge deck, the measurements were only performed on two approaches. The approaches are called A and B as in Figure 4.81. The two approaches are corroded severely and rust areas are visible (Figure 4.82). Also, delaminations and cracks were found in different parts of the two approaches which are shown in Figure 4.83. The location and extent of the delaminations were determined with a chain drag followed by hammering as described in ASTM D 4580 [174]. The half-cell potential of the approaches was measured at six different times and the results are given in Figures 4.84 to 4.89

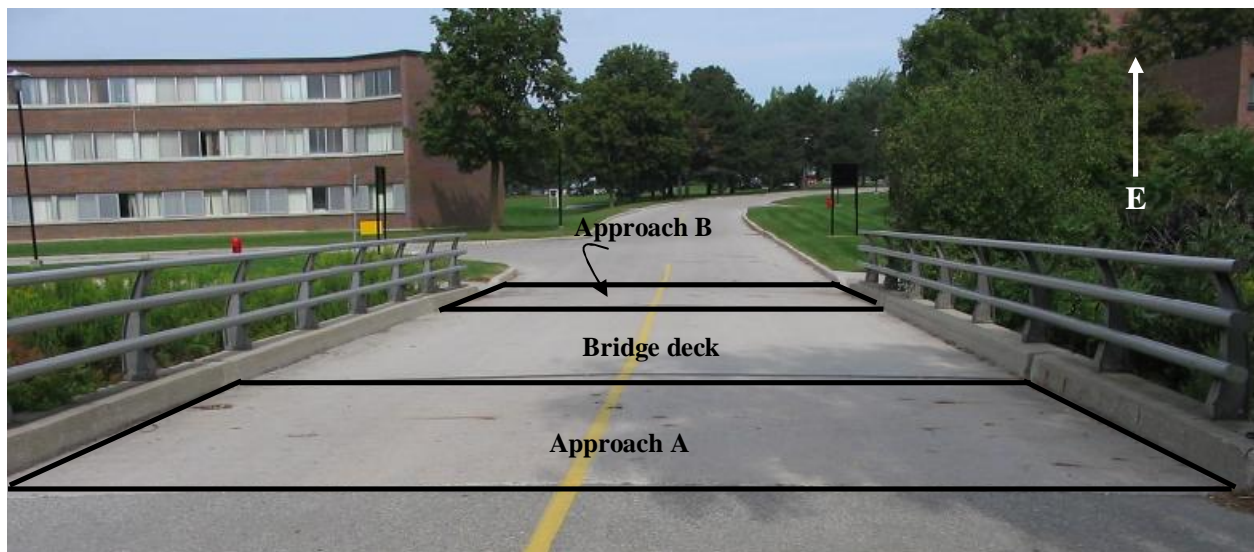


Figure 4. 81. A view of the bridge at the University of Waterloo. Approached are labelled A and B.





Figure 4. 82. Some of the rust spots (marked by black circles) on approach B of the bridge at campus of the University of Waterloo.

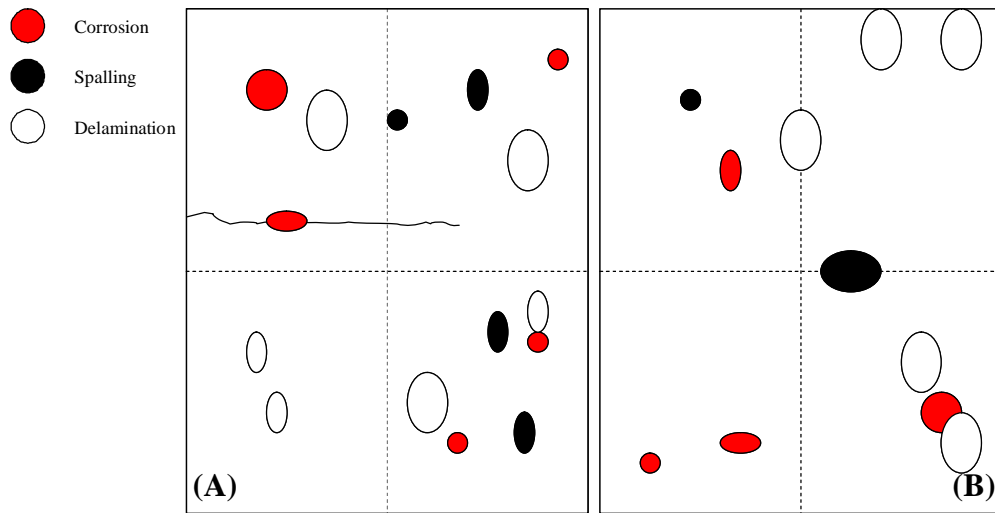


Figure 4. 83. Location of the delaminations and cracks on two approaches.

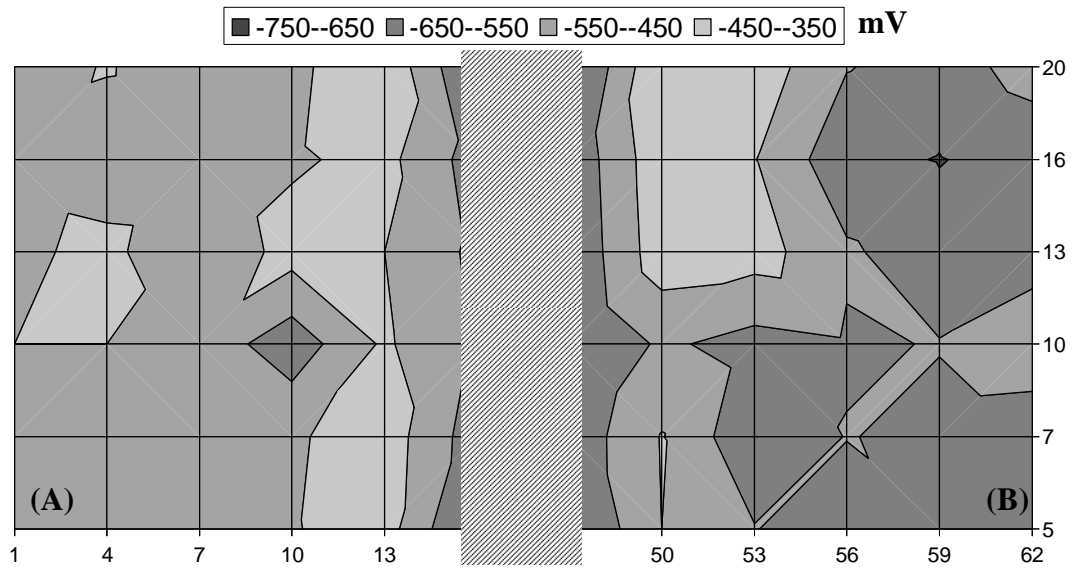


Figure 4. 84. Contour map of the half-cell potential measurements of the approaches A and B of the bridge at the University of Waterloo; March 06, 2005; T = -10°C, RH = 72%, cloudy.

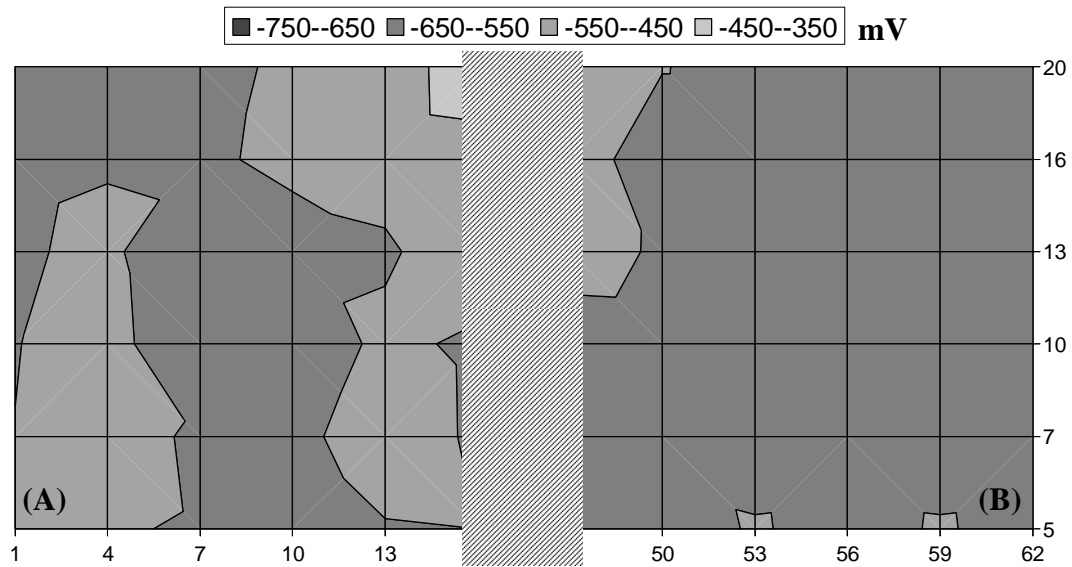


Figure 4. 85. Contour map of the half-cell potential measurements of the approaches A and B of the bridge at the University of Waterloo; May 25, 2005; T = +19°C, RH = 58%, sunny.

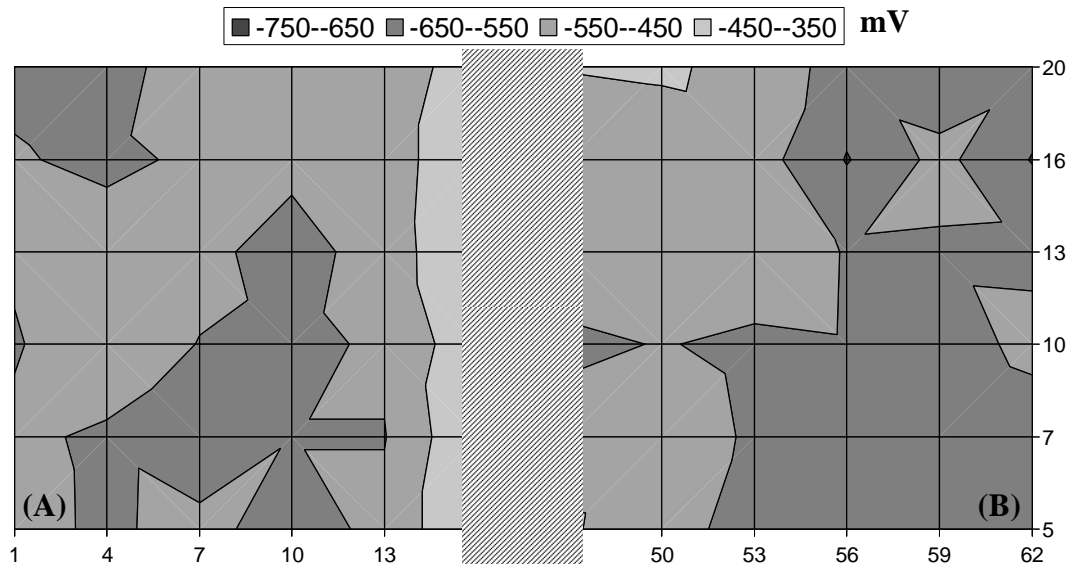


Figure 4. 86. Contour map of the half-cell potential measurements of the approaches A and B of the bridge at the University of Waterloo; August 22, 2005; T = +16°C, RH = 91%, sunny.

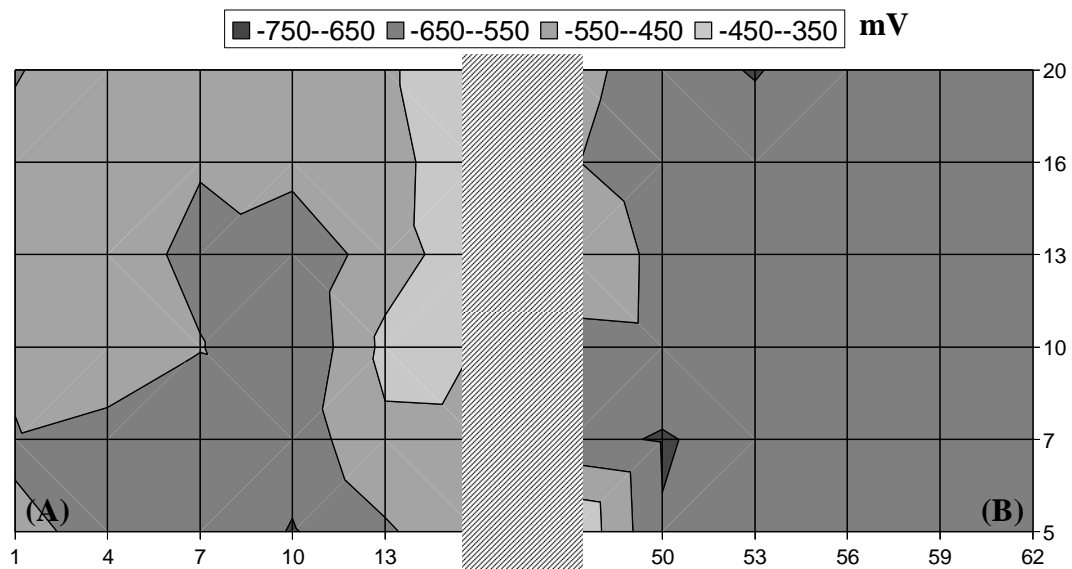


Figure 4. 87. Contour map of the half-cell potential measurements of the approaches A and B of the bridge at the University of Waterloo; April 11, 2006; T = +17°C, RH = 40%, sunny.

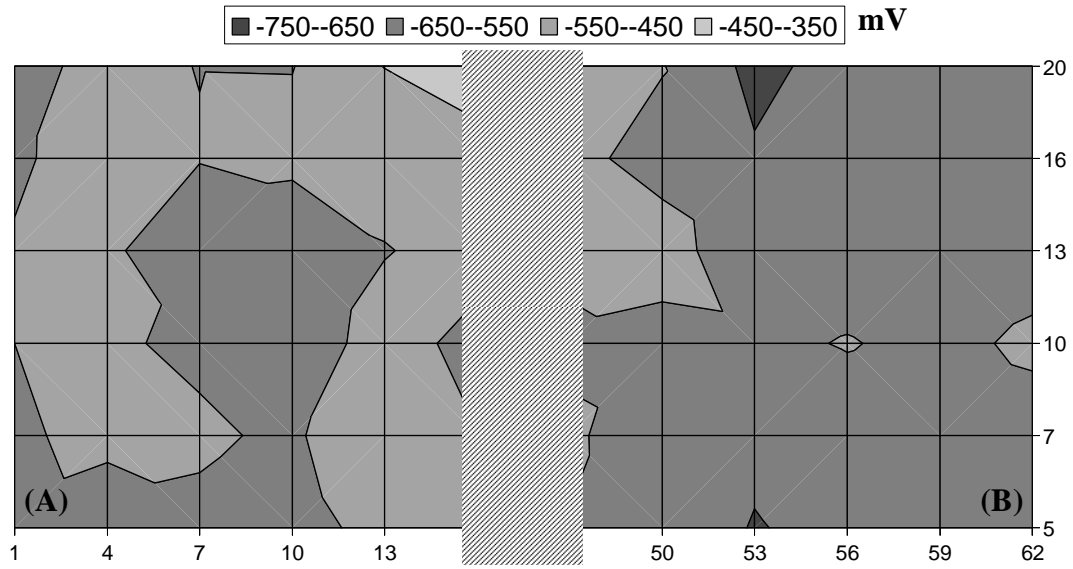


Figure 4. 88. Contour map of the half-cell potential measurements of the approaches A and B of the bridge at the University of Waterloo; May 17, 2006; T = +14°C, RH = 92%, sunny.

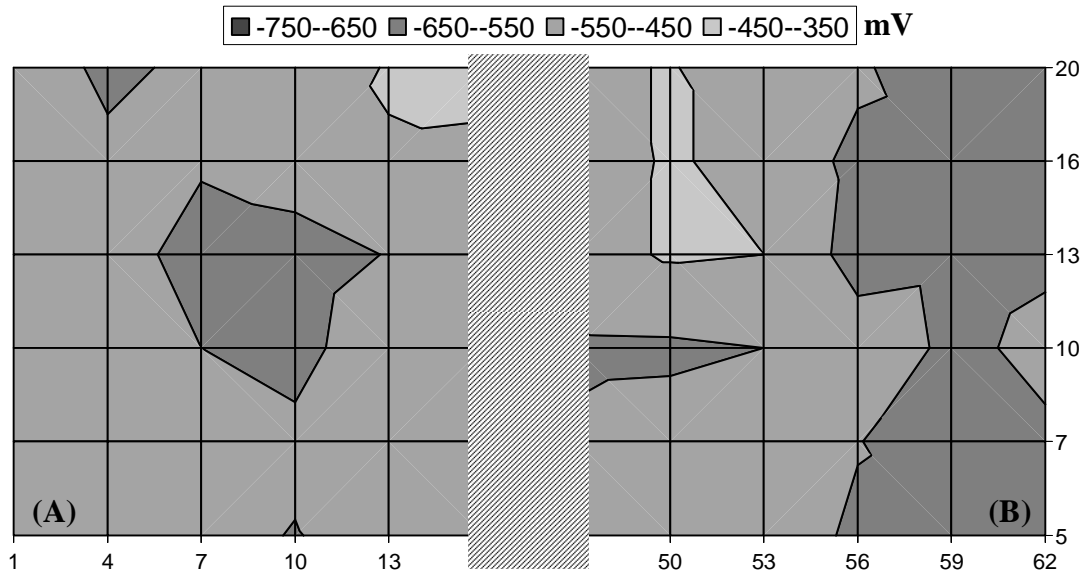


Figure 4. 89. Contour map of the half-cell potential measurements of the approaches A and B of the bridge at the University of Waterloo; August 22, 2006; T = +19°C, RH = 90%, sunny.

In addition to half-cell potential measurements, the corrosion activity of the steel rebars and the concrete resistance in approach B were measured using the GalvaPulse™ at three different times and the results are shown in Figures 4.90 to 4.92. The applied current and the time duration of all measurements were 100  $\mu\text{A}$  and 10 second, respectively.

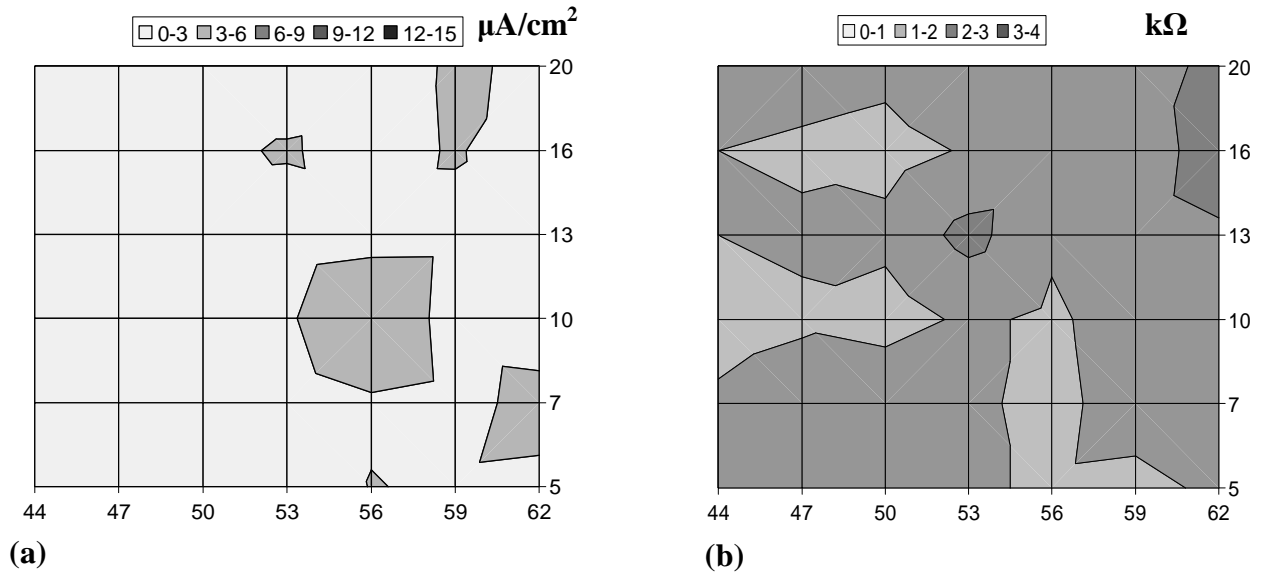


Figure 4. 90. Corrosion current density (a) of the steel bars and concrete resistance (b) of approach B, measured by GalvaPulse™, August 22, 2005.

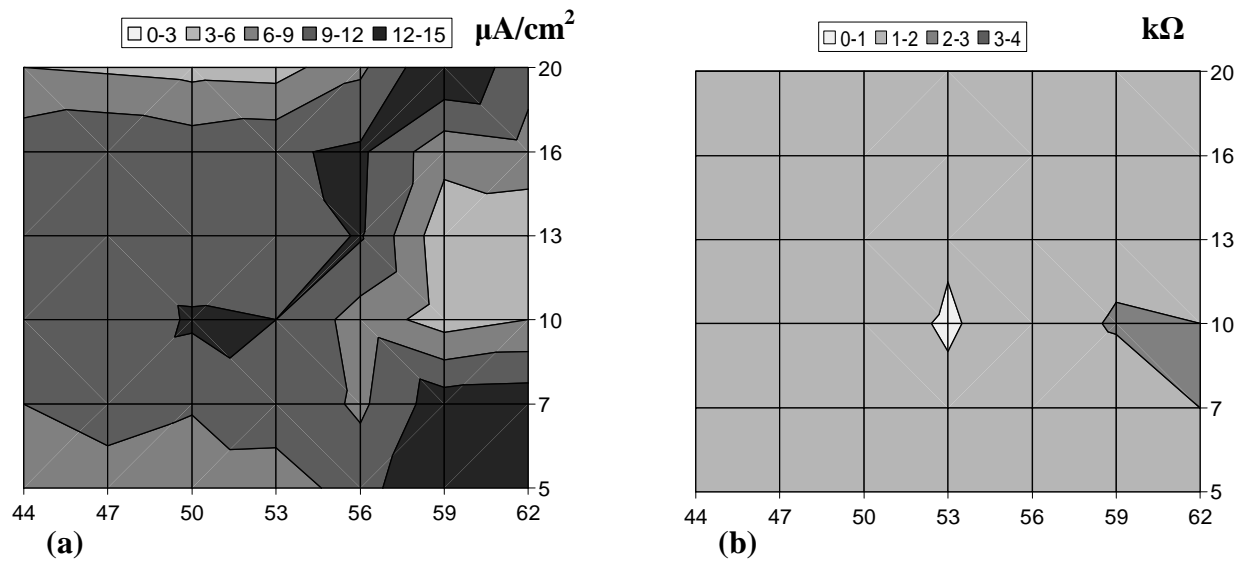


Figure 4. 91. Corrosion current density (a) of the steel bars and concrete resistance (b) of approach B, measured by GalvaPulse™, April 11, 2006.

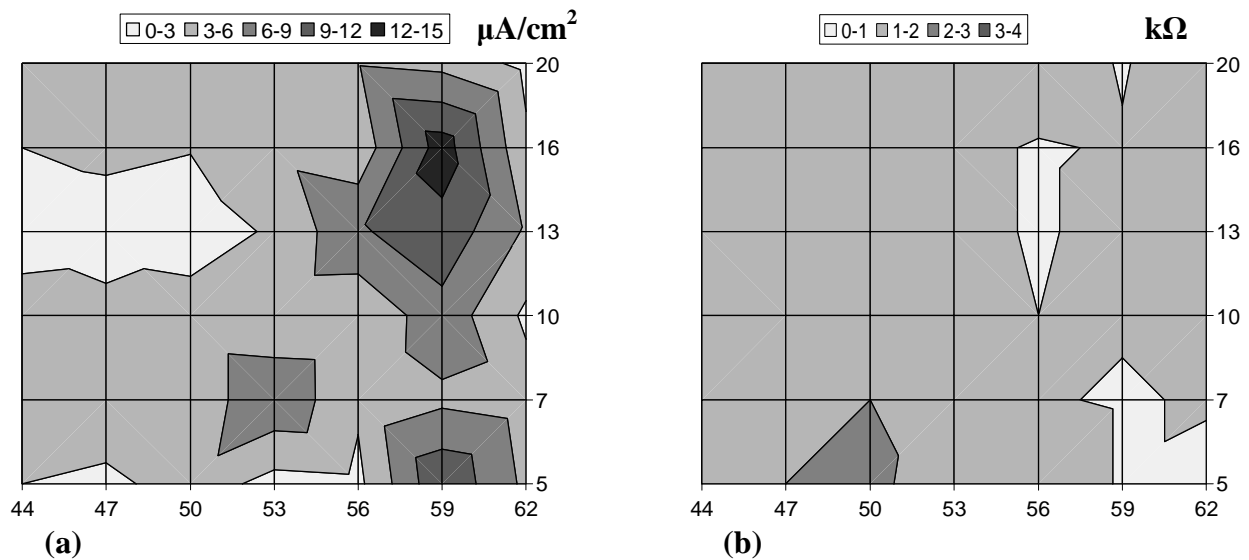


Figure 4. 92. Corrosion current density (a) of the steel bars and concrete resistance (b) of approach B, measured by GalvaPulse™, August 22, 2006.

The half-cell potential contour maps of the steel rebars in the bridge at the University of Waterloo show that the potential map is changing over time. It seems if the measurements performed at the same time in each year, the potential pattern would be more similar. The weather history over the previous period i.e. longer than a few days has an effect on the potential map and it seems that moisture content of the concrete has the major role in term of the weather history of the structure. Also, it should be mentioned that the potential values of all spots were more negative than  $-350\text{mV}$  vs. CSE at all times and the two approaches are actively corroding. Results from visual inspection and delamination tests on approach B show that degree of deterioration of this approach is higher than that of approach A. In spite of the fact that the half-cell potential contour map changes with time, generally, the potential patterns of approach B, shows more corrosion activity. It is important to mention that the ambient temperature is the factor that can change the half-cell potential radically.

The corrosion current density and concrete resistance of approach B were also measured three times by the GalvaPulse™ and there is no consistency between measurements. This can be due to calibration of the GalvaPulse™, because after the first time, it was realised that the GalvaPulse™ needs to be calibrated every month or before each measurement, whichever is the longer period. Also it should be noted that the corrosion rates determined by the GalvaPulse™ are instantaneous rates at that specific moment and they are not constant and change over time.

#### **4.2.2. Victoria Street Bridge, Wingham, Ontario**

As described in section 3.3.2.2, the visited bridge was a 35 years old post-tensioned bridge with galvanised steel rebars. The temperature during tests was about 5°C with 70% relative humidity. Three types of tests were performed on the bridge: visual inspection, chain and hammer tests and corrosion tests.

##### **4.2.2.1. Visual inspection**

Visual inspection showed that there is no serious damage on the bridge deck. Stains caused by corrosion of steel reinforced rebars were observed on the sidewalks. No galvanised steel was used in that part of the bridge. Some longitudinal cracks were observed on the bridge deck. Scaling and pop-outs were also found on the bridge deck. Figures 4.93 to 4.95 show the mentioned results of visual inspection.



Figure 4. 93. Longitudinal cracks on bridge deck.



Figure 4. 94. Pop-outs on the surface of the bridge deck.



Figure 4. 95. Corroded steel rebar in the one of the sidewalks.



#### 4.2.2.2. Delamination

Delaminated areas make a hollow sound when hit lightly by a mechanical device like hammer or chain. In this inspection a heavy chain and a hammer were used to find the location of delaminated areas on the bridge deck according to ASTM D 4580 [174] and the results are shown in Appendix E. Data of the progression of delaminations on the bridge was provided by MTO and is shown in Figure 4.96.

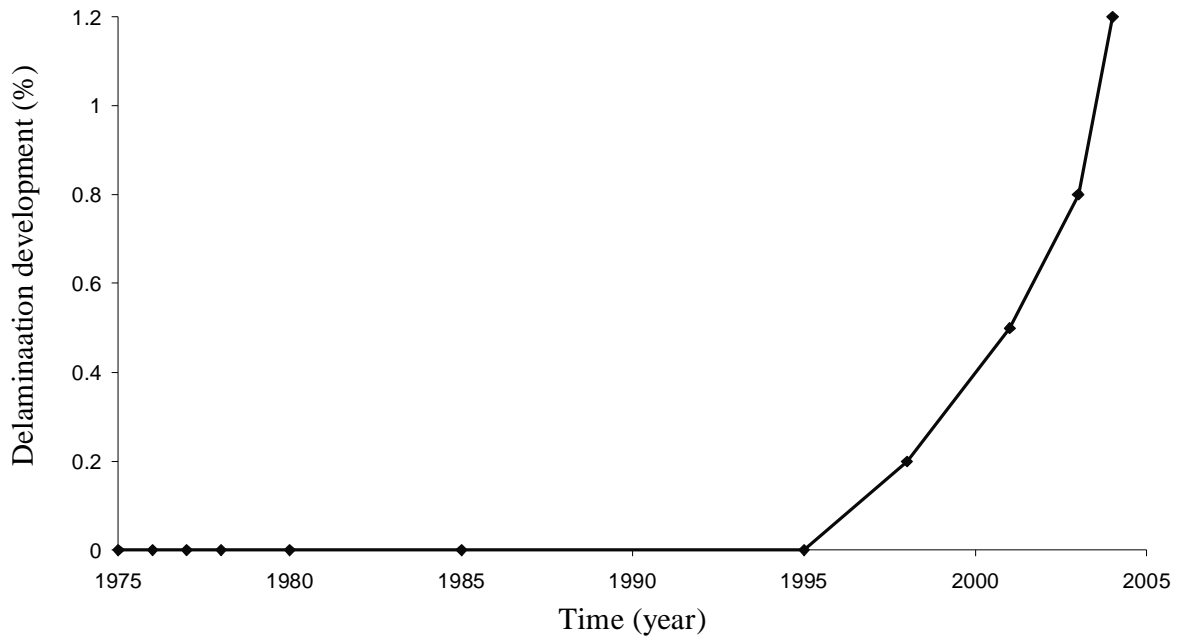


Figure 4. 96. Progression of delaminations on the Victoria St. bridge, Wingham.

#### 4.2.2.2. Corrosion measurement

To evaluate the corrosion condition of the steel bars, half-cell potential (Cu/CuSO<sub>4</sub>) and galvanostatic pulse LPR (using the GalvaPulse™) techniques were used. Also, MTO provided data of half-cell potential measurements which was performed in June, 1998. A grid map was made for the bridge and measurements were done based on the map (Figure 4. 97).

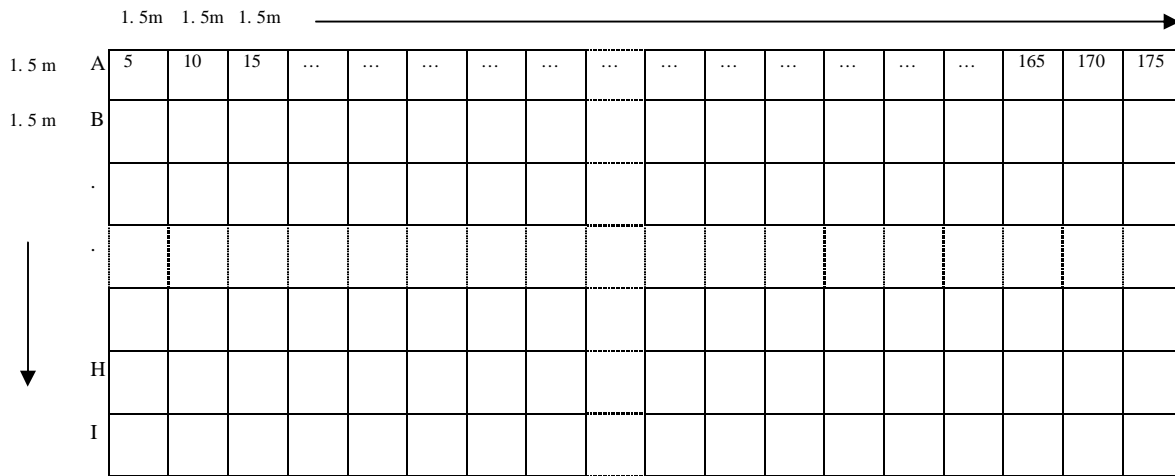


Figure 4. 97. Grid map, used for corrosion measurements

Half-cell potential measurements were carried out only in 3 rows (A, B and C) and 100 metres due to time limitation. LPR measurements with the GalvaPulse™ were done in just one row (row C) up to 100 metres. Data obtained from half-cell in June 1998 by MTO and November 2004 by this author with MTO are presented in Figures 4.98 and 4.99 as contour maps. The measurements are compared in Figure 4.100. Figure 4.101, shows the results of corrosion current density, the concrete resistance measurements and half-cell potential for row C in November 2004. The average of the corrosion potentials measured since 1975 was provided by MTO and is shown in Figure 4.102. The half-cell potential values and the location of the delaminations are shown in Appendix G.

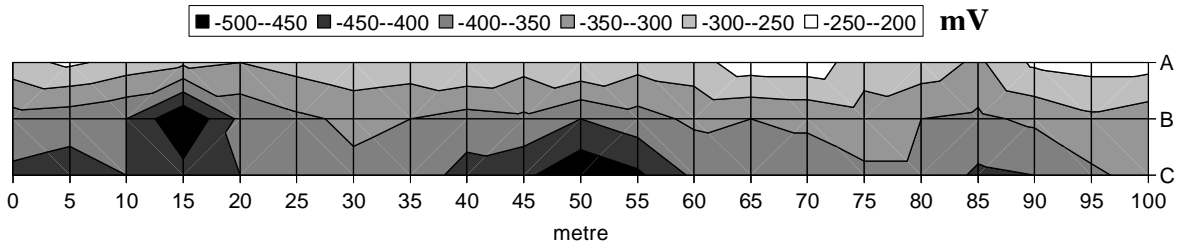


Figure 4. 98. Half-cell potential contour map of galvanised steel rebars, measured vs. CSE, Victoria St Bridge, Wingham, June 16, 1998.

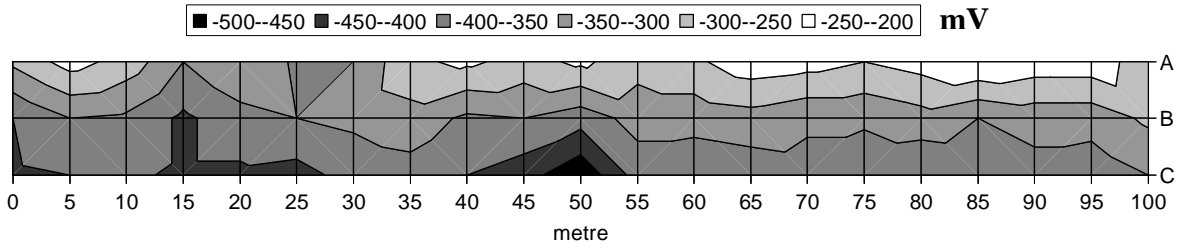


Figure 4. 99. Half-cell potential contour map of galvanised steel rebars, measured vs. CSE, Victoria St Bridge, Wingham, November 22, 2004.

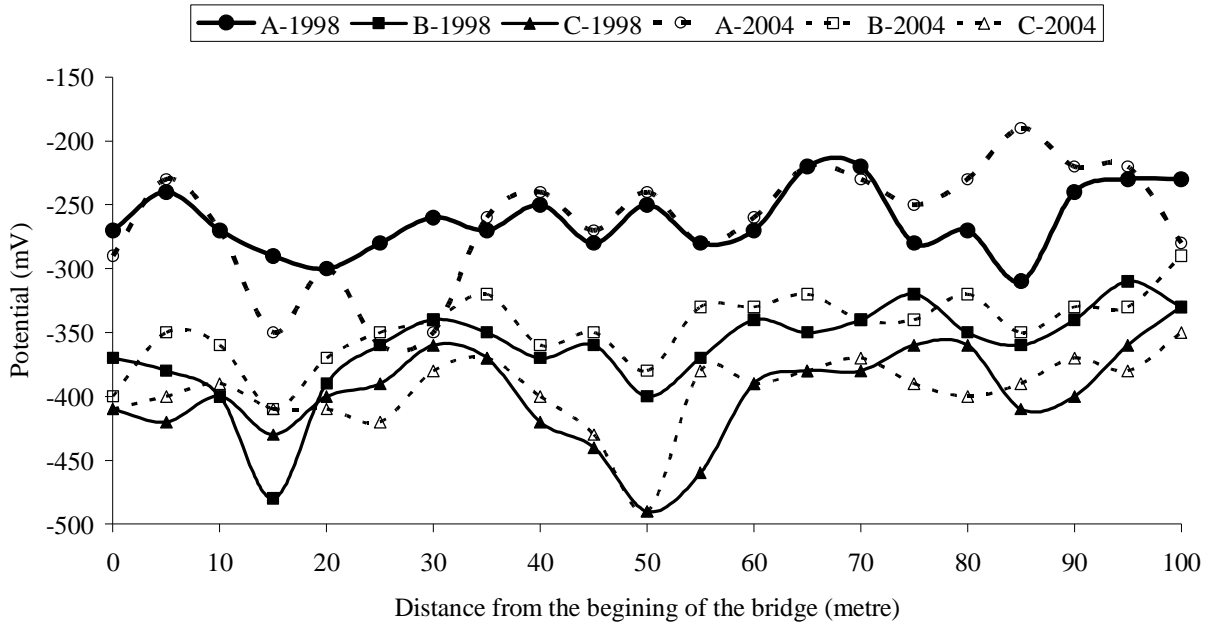


Figure 4. 100. Comparison between half-cell potential measurements (with CSE) in 1998 and 2004.

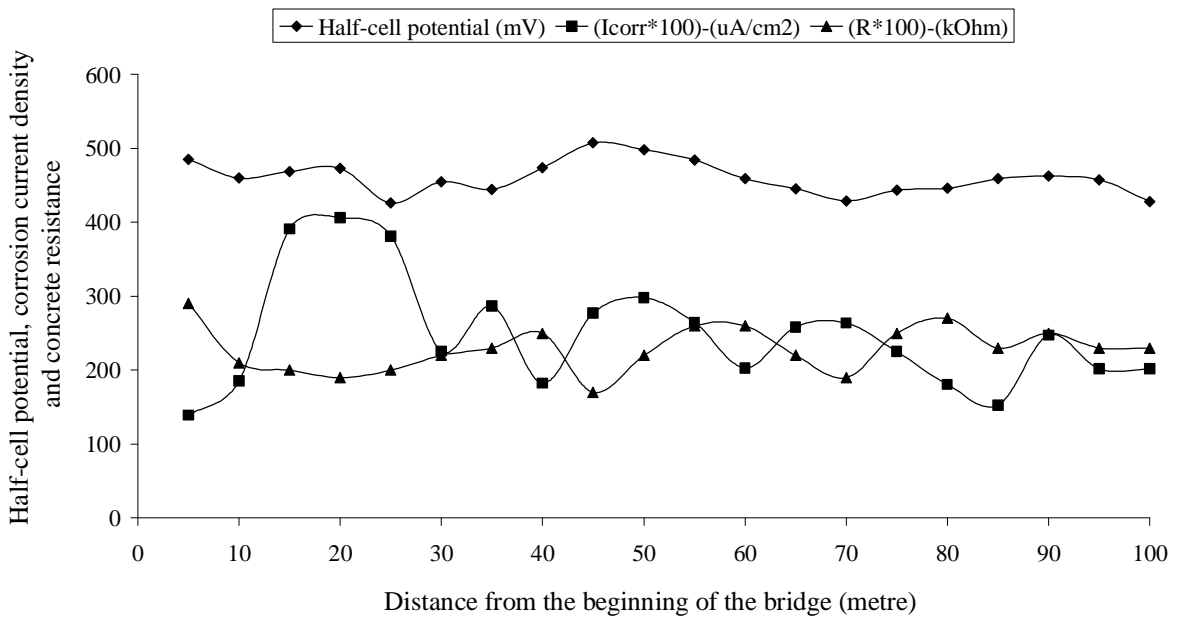


Figure 4. 101. Half-cell potential, corrosion current density and concrete resistance, measured by the GalvaPulse™, row C, November 2004.

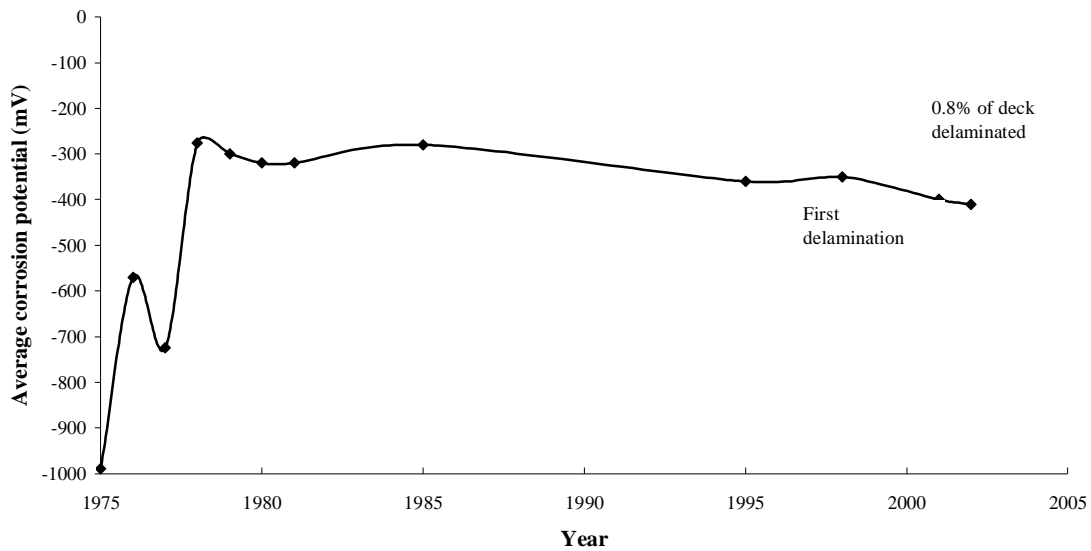


Figure 4. 102. Average corrosion potentials of Victoria St. Bridge, Wingham.

#### 4.2.2.3. Chloride ion content

MTO provided information for chloride ion content in 2004. The test has been done according to MTO test method [175] and results are given in Table 4.8.

Table 4. 8. Total chloride ions content in Victoria St. Bridge, Wingham.

| Distance from the top of the core | Total Chloride Ion Content (%Cl <sup>-</sup> by weight of Concrete) |
|-----------------------------------|---|
| 0-10 mm                           | 0.547   |
| 10-20 mm                          | 0.545   |
| 20-30 mm                          | 0.341   |
| 30-40 mm                          | 0.263   |
| 40-50 mm                          | 0.192   |
| 50-60 mm                          | 0.181   |

Remarks: Reinforcing steel was approximately in the 40-60 mm depth

#### 4.2.2.4. Microscopic observation

A piece of galvanised steel rebar, provided by MTO, was prepared and tested under optical microscope to identify different phases and Zn-Fe alloy layers and under Scanning Electron Microscope (SEM) to obtain more information about morphology, shape and element

analysis. Figure 4.103 shows images from optical microscopy and Figure 4.104 shows the SEM images.

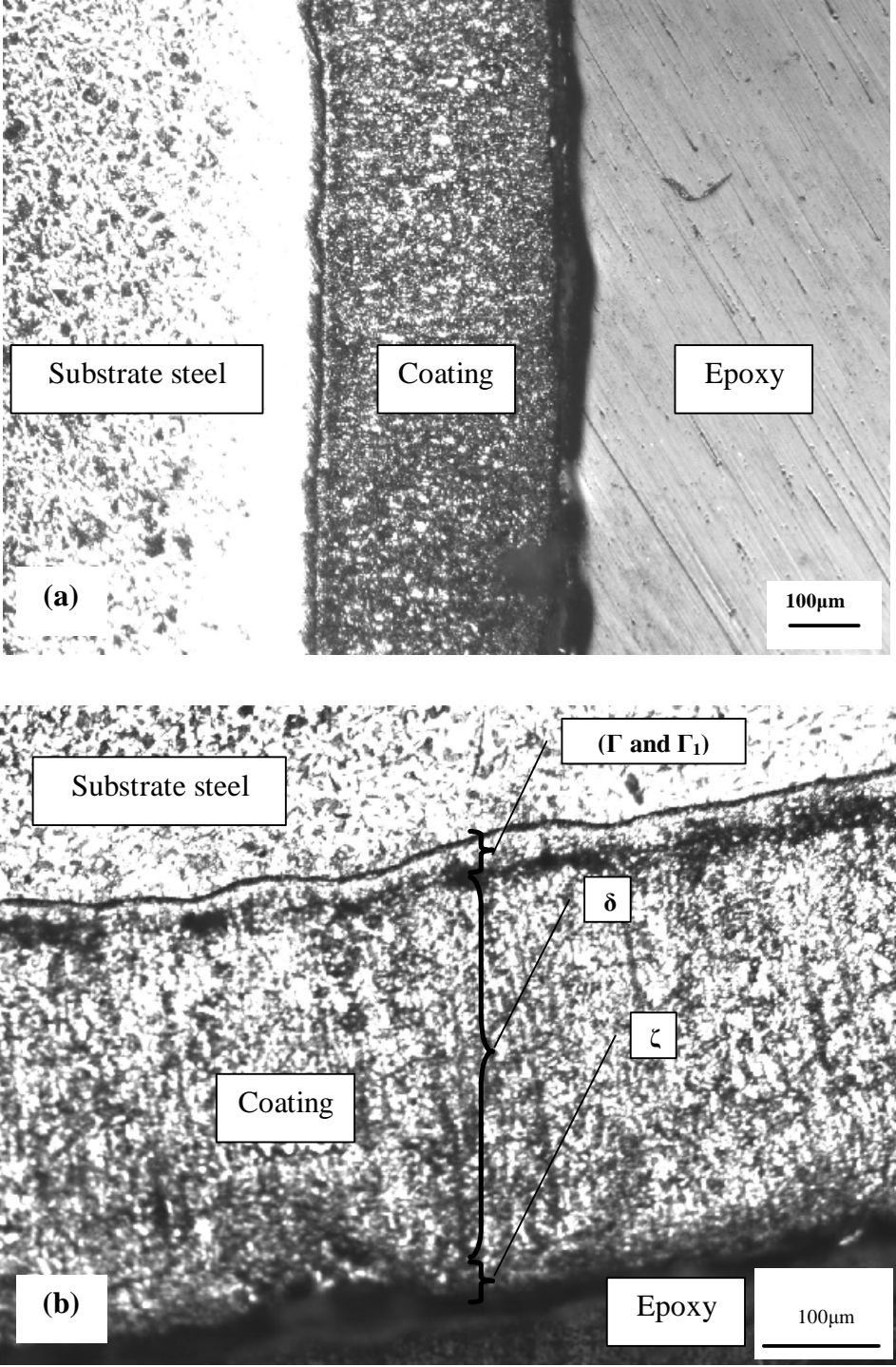


Figure 4. 103. Galvanised steel rebar under optical microscope (a) overview of the galvanised layer (b) different phases.

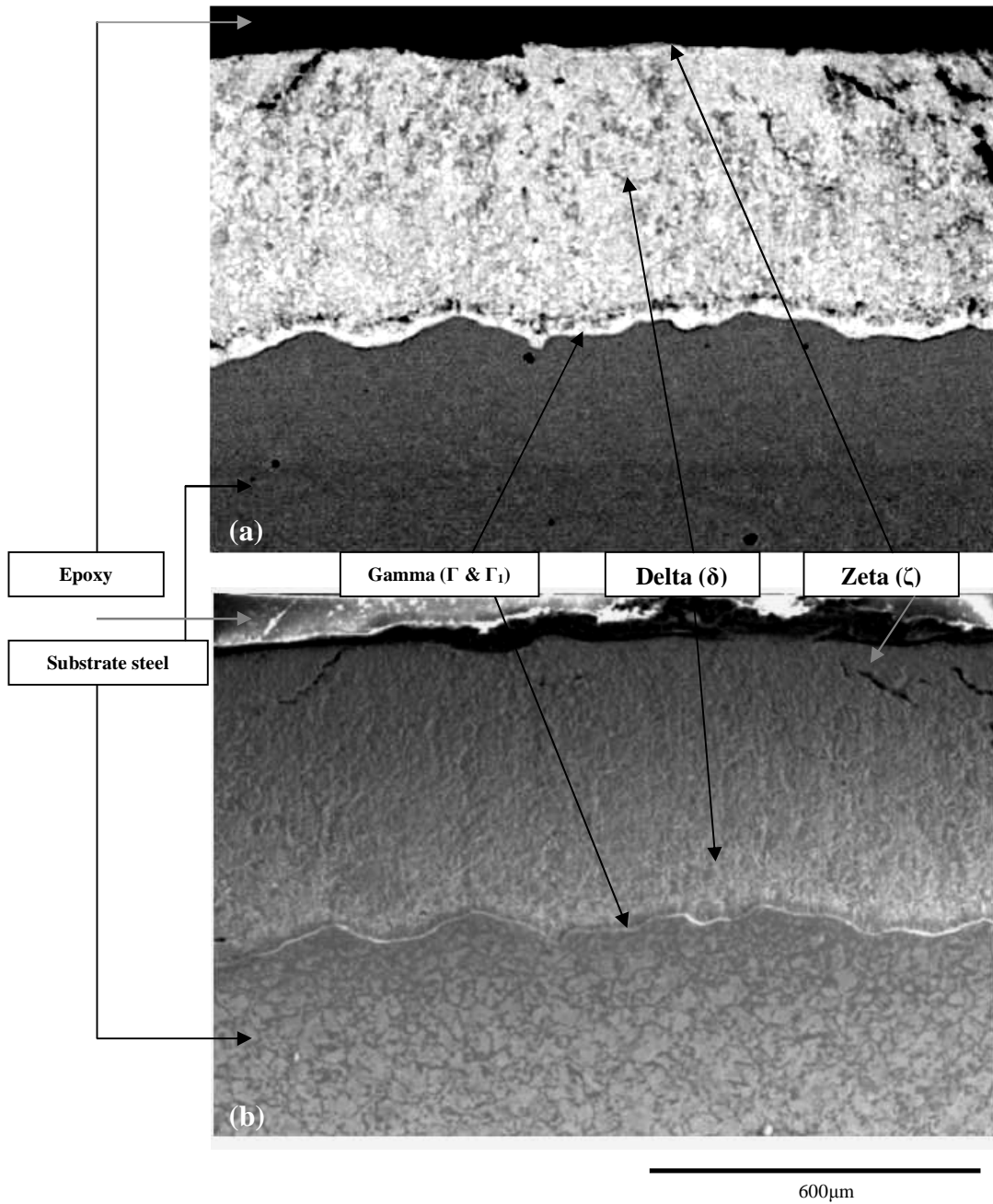


Figure 4. 104. Galvanised steel rebar under SEM, (a) Back Scattered Electron (BSE) mode and (b) secondary electron (SE) mode.

Results from visual inspection show that there is no serious damage on the bridge deck and because the bridge has not been repaired since it has been built, the cracks, scaling, and pop-outs are considered normal and they are not endangering the service life of the bridge.

Results from hammer and chain test revealed that some parts of the bridge are suffering from delaminations and the percentage of the delaminated areas is increasing with time. The development of the delaminated areas should be monitored to prevent the failure of the structure. Figure 4.95 shows that the rate of progression of the delaminations is also increasing.

The most negative measured potential of the steel bars in the Wingham Street Bridge was -490 mV vs. CSE and the most positive measured potential was -190 mV vs. CSE, but, more than 60% of the half-cell potential values were more negative than -350 mV vs. CSE and according to ASTM C876, the probability of corrosion of most steel rebars in the Victoria Street Bridge deck is more than 90%! However, it should be noted the recommended guidelines are for black steel not other types of embedded steel bars. Yeomans [176] did a comparison between potential development in black steel and galvanised steel. He found that at the beginning, both steels were passivated and their half-cell potentials were ~150 mV and -650 mV (versus CSE) for black steel and galvanised steel, respectively. When the potential of black steel reached -550 mV, active corrosion was observed while at the same time the potential of galvanised steel was ~1050 mV. This potential increased to about -600 mV over time. His results indicated that in equivalent concrete exposure conditions, initiation of corrosion in substrate steel in galvanised steel is at least 4 to 5 times slower than the initiation of corrosion in black steel and zinc protects the steel, sacrificially. Therefore, interpretation guidelines, recommended by the ASTM C876 cannot be used for galvanised steel.



Comparison between the half-cell potential measurements performed in 1998 and 2004 shows that the potential values of the rebars in 2004 and 1998 are very similar.

The corrosion current density measured by the GalvaPulse™ show the maximum  $i_{\text{corr}} = \sim 6 \mu\text{A}/\text{m}^2$  and the minimum  $i_{\text{corr}} = \sim 1.4 \mu\text{A}/\text{m}^2$  which are higher than the values usually considered as passive corrosion current density for black steel.

Results of chloride analysis (Table 4.8) show that, generally, the amount of chloride is high in the bridge especially in the areas close to the rebars which is  $\sim 0.18\%$  by weight of concrete. Unfortunately, the mixture design of used in the bridge was not available and most of the data in the literature are based on percent of chloride by weight of cement. If it is assumed that  $\sim 15\%$  of the weight of concrete is cement, then the chloride content of near the surface of the steel would be  $\sim 1.2\%$  by weight of cement. The acid-soluble chloride threshold value for steel in concrete is between 0.2 to 0.4 by weight of cement [27]. The chloride ions can depassivate the zinc and initiate the corrosion, but the chloride threshold in this case is higher than what can be tolerated by black steel. The chloride threshold for corrosion of galvanised steel rebars is at least 4-5 times higher than that in black steel [177, 178]. It means that the chloride content of the Victoria Street Bridge is close to the threshold limit for galvanised steel. Therefore, it is better to monitor the  $\text{Cl}^-$  content of the concrete, more frequently to have up to date information and idea about the internal environment of the concrete.

Results obtained from optical microscopy and SEM show that the thickness of the galvanised coating is around  $400 \mu\text{m}$ . This thickness put the measured galvanised steel coating in grade 100 or more in ASTM A123 [179] which means that the tested galvanised steel rebar has more coating than required by the standard. Metallographical observations confirmed the presence of different metallurgical phases: Gamma ( $\Gamma$ ), Delta ( $\delta$ ) and Zeta ( $\zeta$ ), on the zinc

coating which can provide a tough, metallurgically bonded coating protection to the steel from the environment's corrosive action. The gap seen between Gamma phase and Delta phase is actually the Gamma1 phase ( $\Gamma_1$ ) which can not be identified, clearly. No trace of Etta ( $\eta$ ) phase which is pure zinc was found on the surface of the coating and it is due to corrosion reactions in the concrete environment during 35 years.

#### **4.2.3. Barrier walls, Renfrew**

Corrosion activity of the steel bars in ten barrier walls (with the approximate dimension of 6m X 0.8m for each wall) located on the south part of HWY 17 west of Ottawa, approximately 2 km east of Renfrew, Ontario were checked. On each wall, two points were examined: one in repaired and patched concrete and one in not repaired section of the wall. The half-cell potential of each point was measured, using Cu/CuSO<sub>4</sub> reference electrode and the corrosion current densities of the points were measured by the 3LP and the GalvaPulse™ with the guard ring on. The results are shown in Table 4.9.

Table 4. 9. Results of the corrosion measurements of the steel bars in barrier wall in HWY 17, Renfrew.

| Spot | Concrete condition | Half-cell potential<br>(mV) | Current density ( $\mu\text{A}/\text{cm}^2$ ) |             |
|------|--------------------|-----------------------------|---|-------------|
|      |                    |                             | 3LP   | GalvaPulse™ |
| S1   | Not patched        | -474                        | 14.1  | 21.7        |
|      | Patched            | -495                        | 1.8   | 1.5         |
| S2   | Not patched        | -492                        | 4.3   | 5.2         |
|      | Patched            | -356                        | 1.11  | 1.3         |
| S3   | Not patched        | -555                        | 10.7  | 4.3         |
|      | Patched            | -544                        | 8.9   | 7.4         |
| S4   | Not patched        | -588                        | 14.8  | 10.9        |
|      | Patched            | -594                        | 10  | 9           |
| S5   | Not patched        | -544                        | 10.2  | 22.6        |
|      | Patched            | -439                        | 1.3   | 7.6         |
| S6   | Not patched        | -659                        | 26.2  | 32          |
|      | Patched            | -475                        | 2.3   | 9           |
| S7   | Not patched        | -486                        | 5.4   | 7.6         |
|      | Patched            | -595                        | 6.2   | 17.7        |
| S8   | Not patched        | -482                        | 1   | 4           |
|      | Patched            | -432                        | 0.9   | 0.9         |
| S9   | Not patched        | -620                        | 13.2  | 14          |
|      | Patched            | -351                        | 1.1   | 1.9         |
| S10  | Not patched        | -662                        | 21.4  | 34.5        |
|      | Patched            | -590                        | 16.8  | 7.5         |

The PARSTAT® 2263 was used to perform potentiostatic LPR, galvanostatic pulse technique, EIS and potentiodynamic cyclic polarisation. Due to time limitation, these tests just applied on three spots: S6, S7 and S9 on not-patched areas. However, among these tests, cyclic polarisation and galvanostatic LPR were the only techniques that gave reasonable results. Figure 4.105, shows the cyclic polarisation curve for spot S9. The scan setup for the cyclic polarisation was as follows: 50mV below half-cell potential, up to +500mV vs. reference and return to -900 mV vs. reference with the scan rate of 5 mV/s with IR compensation mode off. The counter electrode used for cyclic polarisation test was a ring with 70 mm diameter and for the calculations of corrosion current densities 70 mm was used as the length of the polarised area of the steel. The comparison between the measured values by different techniques and equipments for spots S6, S7 and S9 are summarised in Table 4.10.

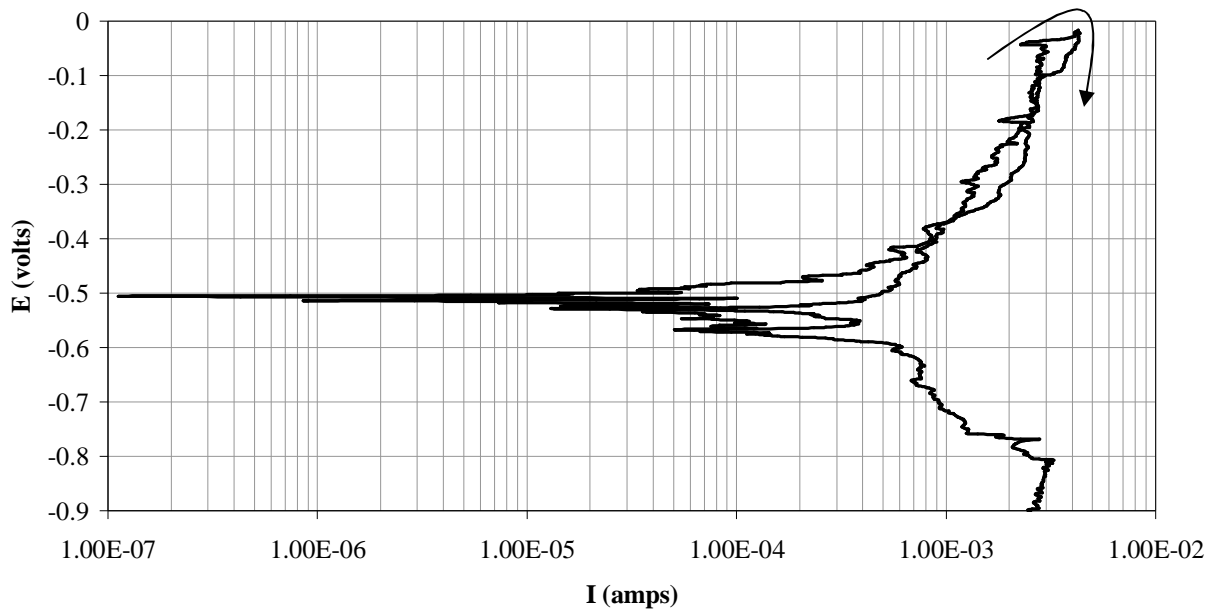


Figure 4. 105. Cyclic polarisation curve for spot S9. Arrow shows the direction of the return part of the curve.

Table 4. 10. Comparison between corrosion current density and concrete resistance, measured by different techniques and equipment.

| Spot | Half-cell potential (mV) | Current density ( $\mu\text{A}/\text{cm}^2$ ) |             |        | Concrete resistance ( $\Omega$ ) |                               |
|------|--------------------------|---|-------------|--------|----------------------------------|-------------------------------|
|      |                          | 3LP   | GalvaPulse™ | Cyclic | GalvaPulse™                      | Galvanostatic pulse technique |
| S6   | -659                     | 26.2  | 32          | 9      | 600                              | 634                           |
| S7   | -480                     | 5.4   | 7.6         | 12     | 800                              | 738                           |
| S9   | -620                     | 13.2  | 14          | 6      | 700                              | 693                           |

The half-cell potential values of the steel bars were all more negative than -350mV vs. CSE. It should be noted the surface of the concrete walls were wetted before measurements, but the time provided for stabilising the potential was about 3-4 minutes which, based on observations in the laboratory, was not long enough. Especially due to high ambient temperature

during the measurement ( $>30^{\circ}\text{C}$ ), more time after wetting was necessary before performing the half-cell potential test.

The concrete resistance of the walls is low, which is reasonable due to exposure of the concrete to the chloride ions, from the splash of cars. The corrosion current densities, measured by three techniques, show extremely high values which is consistent with the very negative potential measurements, and visual observations. The shape and direction of the cyclic polarisation test even with a very fast scan rate (5 mV/s) shows the severity of corrosion of the steel bars. If the corrosion rate is very high, all electrochemical measurements show similar results. Due to high corrosion rates, the GalvaPulse™ was not able to carry out the measurement with the guard ring on. Therefore, all the measurements with the GalvaPulse™ were performed without the guard ring and with an applied current of 200  $\mu\text{A}$ . This is another limitation of this instrument which should be considered. Also, in this case, because of the known history of the structure and visible deterioration, it was obvious that the corrosion rate was very high and identifying the actual and accurate corrosion current densities was not essential. This limitation could be problematic in the case of determining the remaining service life of a structure with no visible and apparent defects.

#### **4.2.4. Island Park Avenue Bridge, Ottawa**

The main purpose of these measurements was to investigate the effectiveness of a Sika FerroGard 903 migration inhibitor, produced by the Sika Company. Based on the information provided by the manufacturer, this inhibitor “is a corrosion inhibiting impregnation coating for hardened concrete surfaces. It is designed to penetrate the surface and then to diffuse in vapour

or liquid form to the steel reinforcing bars embedded in the concrete. Sika FerroGard 903 forms a protective layer on the steel surface which inhibits corrosion caused by the presence of chlorides as well as by carbonation of concrete” [180]. The measurements were carried out at two different times: September 07, 2006 (T=20°C and RH=60%) and October 03, 2006 (T=13°C and RH=95%). A part of the east abutment of the bridge which was selected for the tests. In that part the concrete was intact and no spalling was observed. The measurements were performed on the selected points on the steel rebars shown in Figure 4.106.

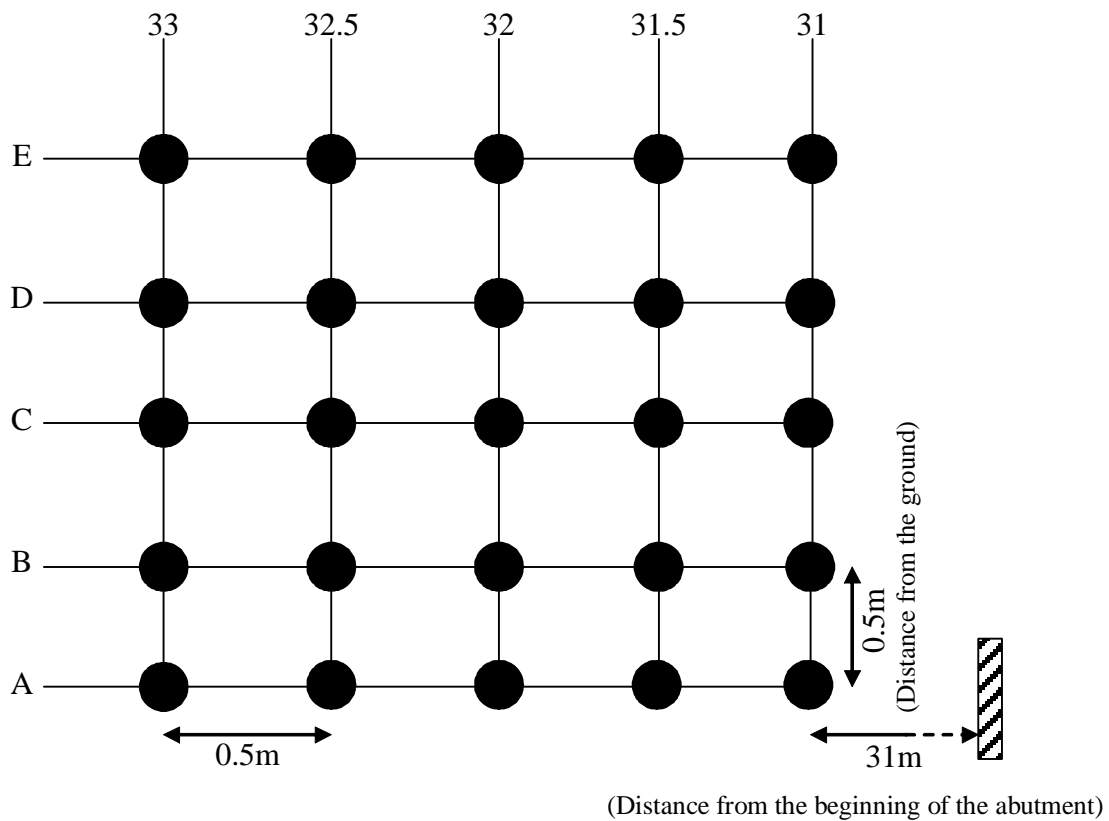


Figure 4. 106. Schematic illustration of the location of the selected points on the east abutment of Island Park Bridge.

The half-cell potential of each point was measured by Cu/CuSO<sub>4</sub> reference electrode and the corrosion current density of five points (B-32, B-33, D-31.5, D-32.5 and D-33) was measured using the 3LP equipment. Attempts were made to use the GalvaPulse™ for the measurements, but due to severe corrosion on the steel bars, the equipment was not able to perform the test. Also, the results obtained from potentiostatic LPR and EIS were not useful and they cannot be analysed. The only other test which was successfully performed was cyclic polarisation. However, because of time limitations, the test was only carried out on point B-32. The scan rate for the test was 5 mV/s. Results of the measurements are given in Table 4.11 and the cyclic polarisation curves are shown in Figure 4.107.

Table 4. 11. Half-cell potential and corrosion current density, obtained by the 3LP, of the selected points of the east abutment of Island Park Bridge, Ottawa.

|        | Half-cell potential |              | Corrosion current density ( $\mu\text{A}/\text{cm}^2$ ) |              |
|--------|---------------------|--------------|---|--------------|
|        | Sep. 07-2006        | Oct. 03-2006 | Sep. 07-2006  | Oct. 03-2006 |
| A-31   | -537                | -533         |   |              |
| A-31.5 | -543                | -550         |   |              |
| A-32   | -464                | -496         |   |              |
| A-32.5 | -454                | -453         |   |              |
| A-33   | -510                | -460         |   |              |
| B-31   | -533                | -522         |   |              |
| B-31.5 | -546                | -533         |   |              |
| B-32   | -483                | -478         | 4.3   | 2.9          |
| B-32.5 | -457                | -481         | 15.4  | 8.6          |
| B-33   | -405                | -429         |   |              |
| C-31   | -522                | -522         |   |              |
| C-31.5 | -494                | -500         |   |              |
| C-32   | -485                | -487         |   |              |
| C-32.5 | -478                | -462         |   |              |
| C-33   | -440                | -449         |   |              |
| D-31   | -522                | -509         | 2.6   | 1.5          |
| D-31.5 | -476                | -475         |   |              |
| D-32   | -478                | -478         |   |              |
| D-32.5 | -468                | -438         | 5   | 4.9          |
| D-33   | -441                | -425         | 23  | 11           |
| E-31   | -502                | -495         |   |              |
| E-31.5 | -467                | -469         |   |              |
| E-32   | -417                | -425         |   |              |
| E-32.5 | -443                | -426         |   |              |
| E-33   | -439                | -430         |   |              |

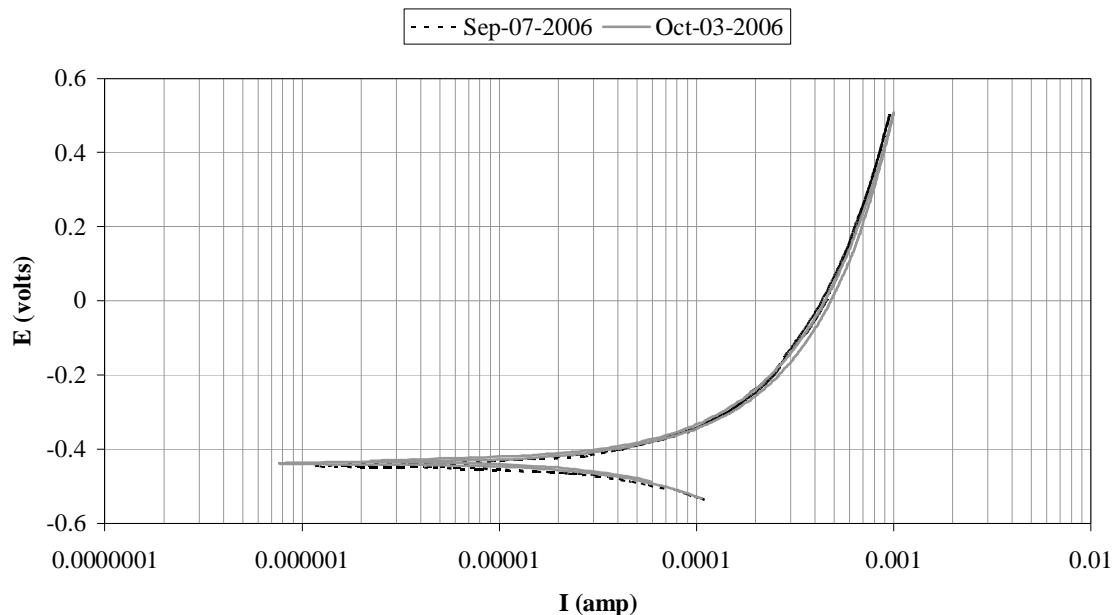


Figure 4. 107. Cyclic polarisation curves for point B-32 with the scan rate of 5mV/s; assumed polarised length of the steel rebar = 70 mm. Based on the obtained curves, the approximated corrosion current densities for both dates are  $\sim 2\mu\text{A}/\text{cm}^2$ .

Visual inspection of the abutments showed spalling in several locations which were due to corrosion of the reinforcing steel bars. The concrete cover depth in some spots was determined to be less than 20 mm. This could be one of the reasons for such extreme deterioration due to steel corrosion.

The half-cell potential values obtained from the measurement performed at two different times are more negative than  $-350\text{mV}$  vs. CSE. The values measured during the second visit are slightly more positive ( $\sim 4\text{ mV}$  on average). This difference is negligible. Also, the difference could be due to the ambient temperature and a relative humidity and precipitation at the time of the measurements. Due to the extremely severe corrosion of the steel rebars, it was not possible to use the GalvaPulse™, even with the guard ring off, to measure the corrosion current density or



concrete resistance. Cyclic polarisation tests were conducted in both visits at one location and the results show similar behaviour in both measurements (Figure 4.108). As mentioned before, this bridge is suffering from severe corrosion and even with the fast scan rate (5 mV/s), used in this experiment, the shape of the curves represent the severity of corrosion. The 3LP equipment, using galvanodynamic LPR technique, was also used to determine the corrosion current density. Results show that, in the second visit (after applying the inhibitor), the current density of most of the selected locations, decreased. This is in contradiction with half-cell potential and cyclic polarisation measurements. However, as mention during the discussion on the laboratory results, the values obtained by galvanodynamic LPR cannot be considered as the actual and accurate values, especially in the 3LP equipment, own by the MTO, which the current should be changed manually and also seems need to be calibrated and checked.

Therefore, based on the obtained results, applying the inhibitor has no positive and protective effect after 3.5 weeks, which was claimed by the manufacturer as the appropriate required time for decreasing the corrosion rate up to 65% [180]. However, it is important to point out again that the Island Park Bridge is suffering from severe corrosion and controlling or reducing such a high corrosion rate is not an easy task. The level of deterioration is critical and the Ministry plans to replace the bridge very soon.

#### **4.2.5. General observations for the field tests**

In general, galvanodynamic LPR (3LP equipment, and PARSTAT<sup>®</sup> 2263) and galvanostatic techniques (GalvaPulse<sup>™</sup> and PARSTAT<sup>®</sup> 2263), were used successfully in the field. The exception was the inability of the GalvaPulse<sup>™</sup> to measure very high corrosion rates.

In these techniques, a current is applied to the rebar and would take the shortest resistance path to the bar rather than attempting to polarise the whole bar.

In contrast, the small amplitude potential-controlled techniques (potentiostatic LPR and EIS), were not successful. For EIS, this is attributed to the area of the polarised steel changing with the frequency and as a result, calculation of the  $R_p$  is not possible [155]. However, another hypothesis applicable for both techniques is the size difference between the counter electrode and the working (which in a structure could be tens of metres of rebars) and consequently, the incapability of the potentiostat to create the required potential difference between the counter and working electrodes. It was possible to obtain a full cyclic potentiodynamic polarisation curve, presumably because a much larger potential signal is applied.

# **CHAPTER 5, SUMMARY, CONCLUSIONS, RECOMMENDATIONS AND FUTURE WORKS**

## **5.1. SUMMARY AND CONCLUSIONS**

- Although, variations in the half-cell potential values of the all specimens in the lab were observed, in most, but not all cases, when the steel bars were corroding actively, the half-cell potential values were more negative than -350 mV vs. CSE. The lack of clear correlation can be attributed to the fact that both half-cell potential and corrosion current density respond differently to the same variables. It has also been reported that the oxide layer composition changes with time and for the same corrosion rate a different age of the oxide layer may cause different half-cell potential [155].
- The half-cell potential measurements in the field show more variations than those in the lab. The potential contour maps of a bridge deck changes significantly due to different weather conditions. It was observed that the potential maps obtained at the same time of the year in different years show relatively similar behaviour but that they were significantly different at different seasons. This was also reported by the MTO staff [181].
- It is essential to wet the concrete surface and provide enough time to stabilise the potential. The estimated time is ~15 minutes. During this period, the surface should be kept completely wet. This is more important in the field with high evaporation rate due to high temperature and wind.
- The distance of the reference electrode to the surface of the steel bar has negligible effect on the measured value of half-cell potential in the laboratory. This is indicative of the relatively

constant environment in the lab which provides low concrete resistance and therefore, this should not be extrapolated to field measurement.

- It is essential to emphasise the ASTM C876 recommended guidelines are for carbon steel (black steel) rebars in concrete and they should not be applied to the other types of steel such as galvanised steel bars. Thermodynamically, the half-cell potential values for galvanised steel could be ~1000 mV vs. CSE in the passive state [18]. This potential may mislead the investigators during the inspection. Therefore, knowledge of the type of reinforcing bar is essential for appropriate interpretation of the potential. Also it is important to mention that the chloride threshold for corrosion of galvanised steel is generally considered 4-5 times higher than that for black steel.
- As mentioned before, relative permittivity is the parameter which is dependent on: relative humidity and the temperature as well as the polarity, mobility and the charge of the ions in the material. Also, corrosion activity alters the half-cell potential value. As a result, changing of these two factors is responsible for the observed potential values. In the case of the approaches to bridge at the campus of University of Waterloo, changing the corrosion condition of the reinforcing bars is not likely to be the main reason of the changes in half-cell potential contour map because the bars were severely corroding at the time of each of the measurements. It is concluded, therefore, that changes in the relative permittivity are the main reason for seasonal variations in the potential map.
- Gravimetry shows that potentiostatic LPR is the most reliable measuring technique compare with the techniques evaluated in the laboratory. Results obtained from the potentiostatic LPR technique have less variation for all specimens.

- Results from corrosion measurements show that steel bar in mortar and pore solution needs time for passivation. This time in mortar is about 7 days and in pore solution is about 3 days. It can be assumed that this time in concrete structures is automatically provided because chloride ions need time to penetrate the cover and reach the surface of the steel. Therefore, even in pore solution, it is recommended that steel be kept for at least a week before adding chloride to the solution.
- It is clear from the data shown in Section 4.1.7 that it is inappropriate to conduct laboratory studies of steel in concrete to which chlorides have been added at the time of mixing. If chlorides are added at the time of mixing, the steel does not have enough time to passivate and consequently, the chloride threshold value, corrosion products and the type of corrosion (localised or more uniform) would be different from those in which  $\text{Cl}^-$  penetrates the hardened concrete. The exception would be when the intention is to study the behaviour of embedded steel in concrete with chloride-contaminated components.
- Generally, as received steel bars with mill scale show higher corrosion current density than sand blasted ones, but there is no such trend in half-cell potential values.
- Since specimens with cracks were actively corroding, no significant difference in potential values was observed during the test period. Half-cell potential values of the specimens with 30 mm cover depth, tended to be more negative.
- The corrosion current density of the steel bars in specimens with different variables measured by the potentiostatic LPR show that those with longitudinal cracks had highest corrosion rate while those with 50 mm and 70 mm cover, remained passive throughout the test period. The carbonated specimens and those with 30 mm cover, showed active corrosion. The autopsy of

the specimens confirmed the results, obtained by the electrochemical measurements. Chloride analysis confirmed the presence of chloride in all the corroded locations.

- The GalvaPulse™ shows higher corrosion rate values compare to the other techniques. Experimental results show that the guard ring not only cannot limit the polarised area, but also it increases the polarised length of the steel. Based on the observations and measurements in the lab, 50  $\mu\text{A}$  applied current, can polarised up to 500 mm of the length of the steel rebar, when the guard ring is off, while this length would about more than a metre with the guard ring on. Therefore using the recommended value of 70 mm as the polarised length is not realistic and will cause error in the calculations. It is also recommended to use the GalvaPulse™ without the guard ring.
- When the corrosion rate is more than 4  $\mu\text{A}/\text{cm}^2$ , (measured by the potentiostatic LPR) the GalvaPulse™ is not capable of performing the measurements and this is one of its major limitations.
- Maintenance of the GalvaPulse™ unit is another important factor without which the results are not reliable. The pulse generator unit of the GalvaPulse™ must be calibrated every month or before each measurement, whichever is the longer period. Also, after each set of measurements, the electrode assembly unit must be cleaned thoroughly, preferably with distilled water, and dried. It is important not to immerse the electrode assembly unit in water because this may damage the electrical connections. Both counter and guard ring are made of zinc and after some time, especially with exposure to salt water, the zinc becomes covered with some white corrosion products. Thus, the surface of the electrodes should be cleaned and the corrosion product removed by sand paper.

- Cyclic polarisation is one of the most informative electrochemical techniques. Information such as half-cell potential, corrosion current density, susceptibility to pitting, prediction of protecting potential and severity of corrosion can be obtained by using this technique. This test was used successfully in the laboratory as well as in the field. However, it is necessary to use a sufficient slow scan rate in order for the detailed features of the corrosion process to be observed. To determine the appropriate scan rate, the second break point in the Bode plot is recommended as described in Chapter 2.
- EIS is the other technique that was used effectively in the laboratory but efforts to perform the test in the field were not successful. EIS can provide unique information about the surface condition of the steel. In this project, in addition to its application for determination of the scan rate for cyclic polarisation test, EIS was used to find the polarisation resistance of the rebar and concrete resistance. This technique gives the concrete resistance in less than one minute with relatively accurate values. The frequencies between 1 MHz and 10 mHz are sufficient for the concrete resistance measurements.
- The galvanodynamic LPR can be used in both laboratory and in the field. This is a relatively fast measurement method; however the measured corrosion current density values are higher than those values measured by the potentiostatic LPR technique. This is a good technique for comparison purpose, but it is not recommended for prediction and modelling the remained service life of the structure.
- The values of Stern-Geary constant were measured during this project for different conditions. Results show that the differences between the measured values and the values used traditionally in the corrosion current density calculations are not significant.

## 5.2. RECOMMENDATIONS

- It is essential to wet the concrete surface thoroughly and provide enough time to stabilise the potential. Also, refreshing the Cu/CuSO<sub>4</sub> reference electrode, as recommended by ASTM C876, is essential.
- It is important to check the half-cell potential contour map and not the actual potential values. This is because a corrosion current flow requires a potential gradient which is most easily detected on a contour map.
- As mentioned before, performing the half-cell potential measurement at the same time in each year provides relatively similar potential map. Therefore, it is recommended to do the regular inspection at the same time, and preferably, in the same weather conditions.
- Because the Wenner technique is very dependant to the surface condition of the concrete, the galvanostatic pulse technique is recommended for measuring the concrete resistance in the field.
- Using the guard ring in the GalvaPulse™ is not recommended. The length of the polarised steel should not be considered 70 mm, as suggested by the GalvaPulse™ manufacturer and it depends on the applied current.
- The unit should be calibrated regularly and kept clean.



### 5.3. FUTURE WORK

- Since no active corrosion was observed on the specimens with 50 mm and 70 mm cover depth, the effect of different cover depths could not be investigated clearly. Also, the specimens in the lab were kept wet during the experiment period. Therefore, performing more measurements may provide useful information regarding the electrochemical techniques, especially, half-cell potential.
- There are tendencies to use different types of steel, such as stainless steel and galvanised steel in reinforced concrete structures. Since the half-cell potential is the most widely used technique for evaluation of the condition of the steel bars, research is necessary to establish guidelines to interpret the results obtained from half-cell potential measurements on different types of steel.
- Relative permittivity involves all the other environmental factors such as temperature, relative humidity, moisture content and concrete resistance; measuring this parameter and correlating it to the half-cell potential measurement through a model could solve the inconsistency of the potential measurements. To correlate the permittivity of concrete of the electrochemical measurements, more reinforced concrete specimens with reasonable size should be cast and the permittivity and corrosion activity of the rebars should be monitored with time.
- To determine the polarised area using the GalvaPulse™, long beams (~ 1.5 metres) can be used with two different covers: (i) typical recommended concrete cover depth which is  $70 \pm 20$  mm on top of the rebar and (ii) a layer of cement paste on the beneath of the steel bar. This design will provide enough length of steel and realistic concrete cover on top. On the

other hand, the small layer of cement paste on the bottom minimised the effect of cover depth on the monitoring process. The half-cell potential and corrosion current density of the different locations of the steel can be monitored by different electrochemical techniques from the side with the thin cement paste layer and the results can be compared with those that will be obtained from using the GalvaPulse™ on the top.

- The uniformity and magnitude of the applied current under the counter electrode of the GalvaPulse™ is the other issue that needs to be investigated in the future.
- Determining the actual corroded area of steel is important in the interpretation of the results from the electrochemical measurements. Research should be conducted to find this area, accurately. Techniques such as infra red spectroscopy, magnetic particle tests, eddy current and ultrasound method have the potential to identify the actual localised corroded areas of the rebar.
- In the GalvaPulse™ the current applied on both guard ring and the counter electrodes has the same sign. Study the behaviour of the polarised area of the steel bar when the current signs change would be very interesting research which may lead to overcome the problem of determining the correct polarised area.
- As mentioned before, the GalvaPulse™ is not capable to perform the measurements when the corrosion rates are high. The reason for this is not known at this time. This is one of the major limitations and needs to be investigated and eliminated.
- Experiments show that the corrosion currents calculated from the results of the galvanodynamic LPR test are generally higher than those obtained from the potentiostatic LPR technique. Since this technique can be used successfully in the field, this problem needs to be investigated and solved.

- The automatic measuring system and software programme developed as part of this project has the capability to be used in the field as well as in the laboratory. The measuring unit can be made embeddable and all the measurements could be done remotely. For that purpose, the software needs to be modified in a way to be able to communicate to the measuring units. Also, by applying some modifications to the programme and by using the LabVIEW PDA<sup>®</sup>, data can be saved in handheld devices. Combining this system with a low price home-made potentiostat could provide an affordable on-site monitoring system for corrosion in reinforced concrete structures. In that case, a wireless system can be designed and installed in a close chamber in the concrete and monitoring can be performed by advanced system such as satellites. This can eliminate the need for wiring which is always problematic in the field.

## REFERENCES

1. H. F. W. Taylor, *Cement Chemistry*. Thomas Telford Services Ltd. 1997.
2. R. H. Bogue, *The chemistry of Portland cement*. 1955: New York, Reinhold Corp.
3. A. M. Neville, *Properties of concrete*. 1990: Longman Scientific & Technical
4. ASTM, *C150-05: Standard Specification for Portland Cement*. 2005.
5. S. H. Kosmatka, B. Kerkhoff, W. C. Panarese, N. F. MacLeod, and M.R. J., *Design and control of concrete mixture*. 2002: EB101, 7th edition, Cement Association of Canada.
6. F. W. Locher, W. Richartz, and S. Sprug, *Setting of Cement-Part I: Reaction and Development of Structure*. ZKG International, 1976. **10**: p. 435-442.
7. P. D. Tennis and H.M. Jennings, *A Model for Two Types of Calcium Silicate Hydrate in the Microstructure of Portland Cement Paste*. Cement and Concrete Research, 2000. **30**: p. 855-863.
8. H. Arup, *European Work on Corrosion of Steel in Concrete*. Glostrup, Denmark, Danish Corrosion Centre, 1983.
9. W. H. Price, *Factors influencing concrete strength*. ACI Materials Journal, 1951. **47**(2): p. 417-432.
10. C. M. Hansson, *Comments on electrochemical measurements of the rate of corrosion of steel in concrete*. Cement and Concrete Research, 1984. **14**: p. 574-584.
11. A. Carnot, I. Frateur, P. Marcus, and B. Tribollet, *Corrosion mechanisms of steel concrete moulds in the presence of a demoulding agent*. Journal of Applied Electrochemistry, 2002. **32**: p. 865-869.

12. M. F. Montemor, A. M. P. Simoes, and M.G.S. Ferreira, *Analytical characterization of the passive film formed on steel in solutions simulating the concrete interstitial electrolyte*. Corrosion, 1998. **54**(5): p. 347-353.
13. T. Zakroczymski, Chwei-Jer Fan, and Z. Szklarska-Smialowska, *Kinetics and mechanism of passive film formation on iron in 0.05M NaOH*. Journal of Electrochemical Society, 1985. **132**(12): p. 2862-2867.
14. T. Zakroczymski, Chwei-Jer Fan, and Z. Szklarska-Smialowska, *Passive film formation on iron and film breakdown in a sodium hydroxide solution containing chloride ions*. Journal of Electrochemical Society, 1985. **132**(12): p. 2868-2871.
15. H. H. Uhlig, *Structure and growth of thin films on metals exposed to oxygen*. Corrosion Science, 1967. **7**: p. 325-339.
16. T. P. Hoar, *The production and breakdown of the passivity of metals*. Corrosion Science, 1967. **7**: p. 341-355.
17. T. D. Marcotte, *Characterization of Chloride-Induced Corrosion Products that form in Steel-Reinforced Cementitious Materials*. PhD thesis, University of Waterloo, 2001.
18. M. Pourbaix, *Atlas of Electrochemical Equilibria in Aqueous Solutions* 1974: Houston, Tex. : National Association of Corrosion Engineers.
19. C. Andrade, P. Merino, X. R. Novoa, M. C. Perez, and L. Solar, *Passivation of reinforcing steel in concrete*. Materials Science Forum, 1995. **192-194**: p. 861-898.
20. F. R. Foulkes and P. McGrath, *A rapid cyclic voltammetric method for studying cement factors affecting the corrosion of reinforced concrete*. Cement and Concrete Research, 1999. **29**: p. 873-883.

21. S. Goni and C. Andrade, *Synthetic Concrete Pore Solution Chemistry and Rebar Corrosion Rate in the Presence of Chlorides*. Cement and Concrete Research, 1990. **20**: p. 525-539.
22. M. Moreno, W. Morris, M.G. Alvarez, and G.S. Duffo, *Corrosion of reinforcing steel in simulated concrete pore solutions Effect of carbonation and chloride content*. Corrosion Science, 2004. **46**: p. 2681–2699.
23. J. Flis and T. Zakroczymski, *Impedance study of reinforcing steel in simulated pore solution with tannin*. Journal of Applied Electrochemistry, 1996. **143**(8): p. 2458-2464.
24. C. V. Raman and K. S. Krishnan, *A new type of secondary radiation* Nature, 1928. **121**: p. 501-502.
25. T. I. Thuresson, *Electrochemical monitoring of the influence of concrete quality on the reinforcing steel corrosion in industrial effluent*. 1996, Queen's University.
26. B. Martin-Perez, H. Zibara, R. D. Hooton, and M.D.A. Thomas, *A study of the effect of chloride binding on service life predictions*. Cement and Concrete Research, 2000. **30**(8): p. 1215-1223.
27. ACI Committee 222, *222R-96: Corrosion of Metals in Concrete*. 1996.
28. R. T. L. Allen and J.A. Forrester, *The investigation and repair of damaged reinforced concrete structures*, A.P. Crane, Editor. 1983, Society of Chemical Industry: London. p. 193-222.
29. NORDTEST, *NT BUILD 357: Concrete, repairing materials and protective coating: UDC 691.32:658.588 carbonation resistance*. 1989: NORDTEST.
30. ASTM, *C856-04: Standard Practice for Petrographic Examination of Hardened Concrete*. Vol. 04.02. 2004.

31. G. J. Verbeck, *Carbonation of Hydrated Portland Cement* Research Department Bulletin RX087, Portland Cement Association, 1995.
32. Germann Instruments Inc., <http://www.germann.org/Pages/Products/index.htm>. 2006.
33. D. H. Campbell, R. D. Sturm, and S.H. Kosmatka, *Detecting Carbonation*. Concrete Technology Today, PL911, [http://www.portcement.org/pdf\\_files?PL911.pdf](http://www.portcement.org/pdf_files?PL911.pdf), 1991. **12**.
34. K. Hong and R.D. Hooton, *Effects of cyclic chloride exposure on penetration of concrete cover*. Cement and Concrete Research, 1999. **29**: p. 1379-1386.
35. I. Soroka, *Portland Cement Paste and Concrete*. 1979, Surrey, England: The Macmillan Press Ltd.
36. T.C. Powers. *Properties of Cement Paste and Concrete*. in *Chemistry of Cement : Fourth International Symposium*. 1960. Washington, D.C. USA: National Bureau of Standards, U.S. Department of Commerce.
37. P. K. Mehta, *Concrete Structure, Properties and Materials*. 1986, Englewood Cliffs, New Jersey, USA: Prentice-Hall Inc.
38. O. M. Jensen, P. F. Hansen, A. M. Coats, and F. P. Glasser, *Chloride Ingress in Cement Paste and Mortar*. Cement and Concrete Research, 1999. **29**(9): p. 1497-1504.
39. S. H. Kosmatka, B. Kerkhoff, W. C. Panarese, N. F. MacLeod, and R. J. McGrath, *Design and Control of Mixtures*. Seventh Canadian Edition ed. Vol. Engineering Bulletin 101. 2002, Ottawa, Ontario, Canada: Cement Association of Canada.
40. B.H. Oh, S. W. Cha, B. S.Jang, and S. Y. Jang, *Development of High-Performance Concrete Having High Resistance to Chloride Penetration*. Nuclear Engineering and Design, 2002. **212**: p. 221-231.

41. P.C. Aïtcin, A.M. Neville, and P. Acker, *Integrated View of Shrinkage Deformation*, in *Concrete International*. 1997. p. 35-41.
42. Y. Lo and H.M. Lee, *Curing effects on carbonation of concrete using a phenolphthalein indicator and Fourier-transform infrared spectroscopy*. *Building and Environment*, 2002. **37**: p. 507 – 514.
43. J. P. Balayssac, Ch. H. Detriche, and J. Grandet, *Effect of curing upon carbonation of concrete*. *Construction and Building Materials*, 1995. **9**(2): p. 91-95.
44. J. M. Khatib and P. S. Mangat, *Influence of high-temperature and low-humidity curing on chloride penetration in blended cement concrete*. *Cement and Concrete Research*, 2002. **32**: p. 1743–1753.
45. M. R. Jones, R. K. Dhir, and J. P. Gill, *Concrete surface treatment: effect of exposure temperature on chloride diffusion resistance*. *Cement and Concrete Research*, 1995. **25**(1): p. 197-208.
46. J. Woo-Yong, Y. Young-Soo, and S. Young-Moo, *Predicting the remaining service life of land concrete by steel corrosion*. *Cement and Concrete Research*, 2003. **33**: p. 663–677.
47. C. Andrade, J. Sarria, and C. Alonzo, *Relative humidity in the interior of concrete exposed to natural and artificial weathering*. *Cement and Concrete Research*, 1999. **29**: p. 1249-1259.
48. J. A. Gonzalez and C. Andrade, *Effect of Carbonation, Chlorides and Relative Ambient Humidity on the Corrosion of Galvanized Rebars Embedded in Concrete*. *British Corrosion Journal*, 1982. **17**(1).



49. S. Ahmed, *Reinforcement corrosion in concrete structure, its monitoring and service life prediction-a review* Cement and Concrete Composite, 2003. **30**(4-5): p. 459-471.
50. Corrosion-club, <http://www.corrosion-club.com/concretecorrosion.htm>. 2004.
51. Corrosion doctors, <http://www.corrosion-doctors.org>. 2005.
52. B. Elsener with contributions from C. Andrade, J. Gulikers, R. Polder, and M. Raupach, *Half-cell potential measurements – Potential mapping on reinforced concrete structures*. Materials and Structures, 2003. **36**.
53. M. G. Fontana, *Corrosion Engineering*. 1987: McGraw-Hill.
54. D. A. Jones, *Principles and Prevention of Corrosion*. 1992: Macmillan Publishing Company.
55. Gamry Instruments, *DC corrosion techniques*. 2005, [http://www.gamry.com/App\\_Notes/DC\\_Corrosion/GettingStartedWithEchemCorrMeasurements.htm](http://www.gamry.com/App_Notes/DC_Corrosion/GettingStartedWithEchemCorrMeasurements.htm): Application Notes.
56. R. F. Stratfull, S., *Laboratory corrosion test of steel in concrete*. 1968, California division of highways, State of California: Sacramento, California.
57. R. F. Stratfull, *Half-cell potential and the corrosion of steel in concrete*. 1972, California division of highways, State of California: Sacramento, California.
58. FORCE Technology, *Evolution of corrosion in reinforced concrete structures*, [www.force.dk/NR/rdonlyres/7A1681DB-71A2-4424-B948-D44EEDC38C35/204/17861en3.pdf](http://www.force.dk/NR/rdonlyres/7A1681DB-71A2-4424-B948-D44EEDC38C35/204/17861en3.pdf). 2004.
59. ASTM-C876-91, *Standard Test Method for Half-cell Potentials of Uncoated Reinforcing Steel in Concrete*. 1999. **03.02**: p. 446-451.

60. O. K. Gepraegs and N. A. Cumming, *Bridge deck evaluation report, Lower Elk Creek Bridge #2531*. 2006, Levelton Consultants Ltd., prepared for Province of British Columbia, Ministry of Transportation, Geotechnical and Materials Engineering, Southern Interior Region.
61. P. Gu and J.J. Beaudoin, *Obtaining Effective Half-Cell Potential Measurements in Reinforced Concrete Structures*. National Research Council of Canada, Construction Technology Update No. 18, 1998.
62. H. R. Soleymani and M.E. Ismail, *Comparing corrosion measurement methods to assess the corrosion activity of laboratory OPC and HPC concrete specimens*. Cement and Concrete Research, 2004. **34**: p. 2037–2044.
63. S. Feliu, J . A. Gonzalez, and C. Andrade, *Electrochemical methods for on-site determination of corrosion rates of rebars*, in *Techniques to assess corrosion activity of steel reinforced concrete structures, ASTM STP 1276*, N. S. Berke, E. Escalante, C. Nmai, and D. Whiting, Editors. 1996, ASTM p. 107-118.
64. J. C. Kliethermes, *Repair of spalling bridge decks*. 1972, Highway Research Record, No. 40. p. 83-92.
65. V. Novokshchenov, *Corrosion Surveys of Prestressed Bridge Members Using a Half-Cell Potential Technique*. Corrosion, 1997. **53**(6): p. 489-498.
66. R. Romagnoli, V. F. Vetere, J. D. Sota, I. T. Lucchini, O. R. Batic, and R.O. Carbonari, *An SEM study of the corrosion process on rebars: an interpretation of the ASTM C876 standard specification*. Corrosion Prevention & Control, 1999. **46**(5): p. 133-140.

67. R. D. Browne, M. P. Geoghegan, and A.F. Baker, *Analysis of structural condition from durability tests*, in *Corrosion of reinforcement in concrete construction*, A.P. Crane, Editor. 1983, Society of Chemical Industry: London. p. 193-222.
68. B. Elsener and H. Bohni, *Potential mapping and corrosion of steel in concrete*, in *Corrosion rates of steel in concrete, ASTM STP 1065*, N. S. Berke, V. Chaker, and D. Whiting, Editors. 1990, ASTM. p. 142-156.
69. J. Cairns and C. Melville, *The effect of concrete surface treatment on electrical measurements of corrosion activity*. *Construction and Building Materials*, 2003. **17**: p. 301-309.
70. *Electrochemistry and corrosion overview and techniques (Application note corr-4)*. 2005, Princeton Application Research, <http://new.ametek.com/content-manager/files/PAR/088.pdf>.
71. M. Stern and A.L. Geary, *Electrochemical polarisation: I. A theoretical analysis of the shape of polarisation curves*. *Journal of the Electrochemical Society*, 1957. **104**(1): p. 56-63.
72. C. Andrade and J.A. González, *Quantitative measurements of corrosion rate of reinforcing steels embedded in concrete using polarization resistance measurements*. *Werkstoffe und Korrosion*, 1978. **29**: p. 515-519.
73. C. Andrade, A. Marcias, S. Feliu, M. L. Escudero, and J.A. Gonzalez, *Quantitative measurement of the corrosion rate using a small counter electrode in the boundary of passive and corroded zones of a long concrete beam*, in *Corrosion Rates of Steel in Concrete, ASTM STP 1065*, N. S. Berke, V. Chaker, and D. Whiting, Editors. 1990, ASTM: Philadelphia, PA.

74. J. A. Gonzalez, C. Andrade, C. Alonso, and S. Feliu, *Comparison of rates of general corrosion and maximum pitting penetration on concrete embedded steel reinforcement*. Cement and Concrete Research, 1995. **25**: p. 257-264.
75. C. Alonso, C. Andrade, M. Castellote, and P. Castro, *Chloride threshold values to depassivated reinforcing bars embedded in a standardised OPC mortar*. Cement and Concrete Research, 2000. **30**: p. 1047-1055.
76. R. B. Polder and W. H. A. Peelen, *Characterisation of chloride transport and reinforcement corrosion in concrete under cyclic wetting and drying electrical resistivity*. Cement & Concrete Composites, 2002. **24**: p. 427-435.
77. O. K. Gepraegs, *Comparison and Evaluation of Electrochemical Techniques and Monitoring Instruments to determine the Corrosion Rate of Steel in Concrete*. 2002, University of Waterloo.
78. C. J. Newton and J.M. Sykes, *A galvanostatic pulse technique for investigation of steel corrosion in concrete*. Corrosion Science, 1988. **28**(11): p. 1051-1074.
79. O. Klinghoffer, *In Situ Monitoring of the Reinforcement Corrosion by Means of Electrochemical Methods*. 1995: Published in Nordic Concrete Research.
80. B. Elsener, O. Klinghoffer, T. Frolund, E. Rislund, Y. Schiegg, and H. Böhni. *Assessment of reinforcement corrosion by means of galvanostatic pulse technique*. in *Repair of Concrete Structures*. 1997. Svolveær, Norway.
81. Germann Instruments Inc., <http://www.germann.org>”, *Products: Galvapulse*. 2004.
82. D. A. Jones and N.D. Greene, *Electrochemical measurement of low corrosion rates*. Corrosion, 1966. **22**: p. 198-204.

83. S. Feliu, J. A. Gonzalez, S. Feliu Jr., and C. Andrade, *Confinement of the electrochemical signal for in-situ measurement of polarization resistance in reinforced concrete*. ACI Materials Journal, 1990. **87**(5): p. 457-460.
84. S. C. Kranc and A. A. Sagues, *Polarization current distribution and electrochemical impedance response of reinforced concrete when using guard ring*. Electrochimica Acta, 1993. **38**(14): p. 2055-2061.
85. S. Feliu, G. J. A. , C. Andrade, and V. Feliu, *On-Site determination of the polarization resistance in a reinforced concrete beam*. Corrosion, 1987. **43**(10): p. 761-767.
86. S. Feliu and J.A. Gonzalez, *Determining polarization resistance in reinforced concrete slabs*. Corrosion Science, 1989. **29**(1): p. 105-113.
87. Germann Instruments Inc., *GalvaPulse© Instruction and Maintenance Manual*. July 1st, 2000.
88. FORCE Technology, [www.force.dk/NR/rdonlyres/336D8F8E-5446-4F40-BFB9-E5974CE0257C/240/19181en3.pdf](http://www.force.dk/NR/rdonlyres/336D8F8E-5446-4F40-BFB9-E5974CE0257C/240/19181en3.pdf). 2005.
89. C. Andrade and C. Alonso, *Corrosion rate monitoring in the laboratory and on-site*. Construction and Building Materials, 1996. **10**: p. 315-328.
90. A. Lasia, *Electrochemical Impedance Spectroscopy and its Applications*, in *Modern Aspects of Electrochemistry*, , B. E. Conway, J. Bockris, and R. E. White, Editors. 1999, Kluwer Academic/Plenum Publishers: New York. p. 143-248.
91. D. C. Silverman, *Simple Models/Practical Answers Using the Electrochemical Impedance Technique*, in *Corrosion Testing and Evaluation*, R. Baboian and W. Dean, Editors. 1990, Silver Anniversary Volume, ASTM.

92. D. C. Silverman, *Primer on the AC impedance technique*, in *Electrochemical techniques for corrosion engineering*, R. Baboian, Editor. 1986, NACE.
93. C. R. Nave, *HyperPhysics*. 2005, Georgia State University: <http://hyperphysics.phy-astr.gsu.edu/hbase/hph.html#hph>.
94. Princeton Applied Research, *Basics of Electrochemical Impedance Spectroscopy, Application Note AC-1*, <http://new.ametek.com/content-manager/files/PAR/078.pdf>.
95. Gamry Instruments, *Basics of Electrochemical Impedance Spectroscopy*. 2006, Gamry Instruments:  
[http://www.gamry.com/App\\_Notes/EIS\\_Primer/EIS%20Primer%202006.pdf](http://www.gamry.com/App_Notes/EIS_Primer/EIS%20Primer%202006.pdf).
96. W. J. Lorenz and F. Mansfeld, *Determination of corrosion rates by electrochemical DC and AC methods*. *Corrosion Science*, 1981. **21**(9): p. 647-672.
97. I. Epelboin, P. Morel, and H. Takenouti, *Corrosion inhibition and hydrogen adsorption in the case of iron in a sulfuric aqueous medium*. *Journal of Electrochemical Society*, 1971. **118**(8): p. 1282-1287.
98. I. Epelboin, C. Gabrielli, M. Kiddam, and H. Takenouti, *A model of the anodic behaviour of iron in sulphuric acid medium*. *Electrochimica Acta*, 1975. **20**: p. 913-916.
99. F. Mansfeld, *Recording and analysis of AC impedance data for corrosion studies*. *Corrosion*, 1981. **36**(5): p. 301-307.
100. Gamry Instruments, *Electrochemical Impedance Spectroscopy Primer*. 2005,  
[http://www.gamry.com/App\\_Notes/EIS\\_Primer/EIS\\_Primer.htm](http://www.gamry.com/App_Notes/EIS_Primer/EIS_Primer.htm): Application Notes.
101. Lemoine, L., F. Wenger, and J. Galland. *Study of the Corrosion of Concrete Reinforcement by Electrochemical Impedance Measurement*. in *Corrosion Rates of Steel in Concrete ASTM STP 1065*. 1990: American Society for Testing and Materials.

102. F. Pruckner, J. Theiner, J. Eri, and E.G. Nauer, *In-situ monitoring of the efficiency of the cathodic protection of reinforced concrete by electrochemical impedance spectroscopy*. *Electrochimica Acta*, 1996. **41**(7/8): p. 1233-1238.
103. L. Dhouibi, E. Triki, and A. Raharinaivo, *The application of electrochemical impedance spectroscopy to determine the long-term effectiveness of corrosion inhibitors for steel in concrete*. *Cement & Concrete Composites*, 2002. **24**: p. 35-43.
104. C. Monticelli, A. Frignani, and G. Trabanelli, *A study on corrosion inhibitors for concrete application*. *Cement and Concrete Research*, 2000. **30**: p. 635-642.
105. G. Trabanelli, C. Monticelli, V. Grassi, and A. Frignani, *Electrochemical study on inhibitors of rebar corrosion in carbonated concrete*. *Cement and Concrete Research*, 2005. **35**: p. 1804-1813.
106. P. Gu, S. Elliott, R. Hristova, J. J. Beaudoin, R. Brousseau, and B. Baldock, *A Study of corrosion inhibitor performance in chloride contaminated concrete by electrochemical impedance spectroscopy*. *ACI Materials Journal*, 1997. **94**(5): p. 385-395.
107. B. B. Hope and A. K. C. Ip, *Corrosion inhibitors for use in concrete*. *ACI Materials Journal*, 1989. **86**(6): p. 602-608.
108. M. Shi, Z. Chen, and J. Sun, *Determination of chloride diffusivity in concrete by AC impedance spectroscopy*. *Cement and Concrete Research*, 1999. **29**(7): p. 1111-1115.
109. C. Aldea, J. Shane, T. Mason, and S.P. Shah, *Assessment of microstructural changes during rapid chloride permeability test using impedance spectroscopy measurements*. *ACI - SP189-19*, 2000. **189**: p. 333-350.
110. M. R. Hansen, M. L. Leming, P. Zia, and S. Ahmad, *Chloride permeability and AC impedance of high performance concrete*. *ACI - SP140-06*, 1993. **140**: p. 121-146.

111. A. Peled, J. M. Torrents, T. O. Mason, S. P. Shah, and E.J. Garboczi, *Electrical impedance spectra to monitor damage during tensile loading of cement composites*. ACI Materials Journal, 2001. **98**(4): p. 313-322.
112. C. Andrade, V. M. Blanco, A. Collazo, M. Keddad, X. R. Novoa, and H. Takenouti, *Cement paste hardening process studies by impedance spectroscopy*. 1999. **44**(24): p. 4313-4318.
113. S. Perron and J. J. Beaudoin, *Freezing of water in Portland cement paste-an ac impedance spectroscopy study*. Cement & Concrete Composite, 2002. **24**(5).
114. ASTM, *G 5-94: Standard Reference Test Method for Making Potentiostatic and Potentiodynamic Anodic Polarization Measurements*. . 1999.
115. ASTM, *G 61-86: Standard Test Method for Conducting Cyclic Potentiodynamic Polarization Measurements for Localized Corrosion Susceptibility Iron-, Nickel-, or Cobalt-Based Alloys*. . 1998.
116. R. A. Corbett, *Laboratory corrosion testing of medical implants*, ASM International: Corrosion Testing Laboratories, Inc., Newark, Delaware, USA.
117. D. C. Silverman, *Tutorial on POLEXPRT and the cyclic potentiodynamic polarization technique*, Argentum Solutions, Inc.:  
[http://www.argentumsolutions.com:80/tutorials/polexpert\\_tutorialpg1.html](http://www.argentumsolutions.com:80/tutorials/polexpert_tutorialpg1.html).
118. F. Mansfeld and M. Kendig, *Concerning the choice of scan rate in polarization measurements*. Corrosion, 1981. **37**(9): p. 545-546.
119. *Laboratory electronics*. 2006, Northern Illinois University:  
[http://www.physics.niu.edu/~labeledc/lab/Le1\\_02lb.pdf](http://www.physics.niu.edu/~labeledc/lab/Le1_02lb.pdf).



120. F. Mansfeld, *Effect of uncompensated resistance on the true scan rate in potentiodynamic experiments*. Corrosion, 1982. **38**(10): p. 556-559.
121. Princeton Applied Research, *Electrochemistry and corrosion overview and techniques, Application Note corr-4*, <http://new.ametek.com/content-manager/files/PAR/088.pdf>.
122. K. R. Gowers and S.G. Millard, *Measurement of concrete resistivity for assessment of corrosion severity of steel using wenner technique*. ACI Materials Journal, 1999(Sep-Oct): p. 536-541.
123. W. Morris, A. Vico, M. Vazquez, and S. R. de Sanchez, *Corrosion of reinforcing steel evaluated by means of concrete resistivity measurements*. Corrosion Science, 2002. **44**: p. 81-99.
124. W. Morris, A. Vico, and M. Vázquez, *Chloride induced corrosion of reinforcing steel evaluated by concrete resistivity measurements*. Electrochimica Acta, 2004. **49**: p. 4447-4453.
125. J. Gulikers, *Theoretical considerations on the supposed linear relationship between concrete resistivity and corrosion rate of steel reinforcement*. Materials and Corrosion, 2005. **56**(6): p. 393-403.
126. C. Alonso, C. Andrade, and J. A. Gonzalez, *Relation between resistivity and corrosion rate of reinforcement in carbonated mortar made with several cement types*. Cement and Concrete Research, 1988. **8**: p. 687-698.
127. B. B. Hope and A. K. Ip, *Corrosion and electrical impedance in concrete*. Cement and Concrete Research, 1985. **15**: p. 525-534.
128. G. K. Glass, C. L. Page, and N. R. Short, *Factors affecting the corrosion rate of steel in carbonated mortars*. Corrosion Science, 1991. **32**(12): p. 1283-1294.

129. R. D. Browne, *Design prediction of the life for reinforced concrete in marine and other chloride environments*. Durability of Building Materials, 1982. **1**: p. 113-125.
130. B. P. Hughes, A. K. O. Soleit, and R. W. Brierley, *New technique for determining the electrical resistivity of concrete*. Magazine of Concrete Research, 1985. **37**(133): p. 243-248.
131. I. L. H. Hansson and C. M. Hansson, *Electrical resistivity measurements of Portland cement based materials*. Cement and Concrete Research, 1983. **13**(5): p. 675-683.
132. H. W. Whittington, J. McCarter, and M. C. Forde, *Conduction of electricity through concrete*. Magazine of Concrete Research, 1981. **33**(114): p. 48-60.
133. N.R. Buenfeld and J.S. Newman, *The resistivity of mortars immersed in sea-water*. Cement and Concrete Research, 1986. **16**: p. 511-524.
134. F. D. Tamas, *Electrical conductivity of cement pastes*. Cement and Concrete Research, 1982. **12**: p. 115-120.
135. F. D. Tamas, E. Farkas, and M. Voros, *low-frequency electrical conductivity of cement, clinker and clinker mineral pastes*. Cement and Concrete Research, 1987. **17**: p. 340-348.
136. P. J. Tamidajski, A. S. Schumacher, S. Perron, P. Gu, and J.J. Beaudoin, *On the relationship between porosity and electrical resistivity of the cementitious systems*. Cement and Concrete Research, 1996. **26**(4): p. 539-544.
137. P. Ghods, M. Chini, M. Hoseini, and R. Alizadeh. *Evaluating the chloride diffusion of concrete by measuring electrical resistivity*. in *International Congress - Global Construction: Ultimate Concrete Opportunities, Proceedings of the International Conference on Young Researchers' Forum*. 2005. Dundee, Scotland, United Kingdom.

138. N. S. Berke and M. C. Hicks, *Estimating the life cycle of reinforced concrete decks and marine piles using laboratory diffusion and corrosion data*. 1992, ASTM ASTM STP 1137. p. 207-231.
139. F. Wenner, *A Method of Measuring Earth Resistivity*. 1916: Bulletin of the Bureau of Standards. p. 469-478.
140. D. A. Whiting and M. A. Nagi, *Electrical Resistivity of Concrete - A Literature Review*. 2003, Portland Cement Association (PCA), PCA R&D Serial No. 2457.
141. S. Feliu, G. J. A. , and C. Andrade, *Electrochemical methods for on-site determinations of corrosion rates of rebars.*, in *Techniques to assess the corrosion activity of steel reinforced concrete structures*, STP 1276, N. Berke, E. Escalante, C. Nmai, and D. Whiting, Editors. 1996, ASTM p. 107–118.
142. J. H. Bungey, *Testing of concrete in structures*. 2nd ed. 1989, New York.: Chapman & Hall.
143. R. S. Barneyback, J. and S. Diamond, *Expression and analysis of pore fluids from hardened cement pastes and mortars*. Cement and Concrete Research, 1981. **11**(2): p. 279-285.
144. L. Mammoliti, *Examination of the Mechanism of Corrosion Inhibition by  $Ca(NO_2)_2$ - and  $Ca(NO_3)_2$ - based Admixtures in Concrete*. PhD thesis in Mechanical Engineering, University of Waterloo, 2001.
145. ASTM, *G1-90: Standard Practice for Preparing, Cleaning, and Evaluating Corrosion Test Specimens*. 1999, ASTM.
146. British Plastics Federation. 2003:  
[www.bpf.co.uk/bpfindustry/plastics\\_materials\\_acrylics\\_PMMA.cfm](http://www.bpf.co.uk/bpfindustry/plastics_materials_acrylics_PMMA.cfm).

147. FORCE Technology, *ECE 20*: <http://www.force.dk/NR/rdonlyres/647207AD-60FC-4665-A13D-E082AFBC76AF/241/19191en2.pdf>.
148. S. Muralidharan, T. Ha, J. Bae, Y. Ha, H. Lee, K. Park, and D. Kim, *Electrochemical studies on the solid embeddable reference sensors for corrosion monitoring in concrete structure*. *Materials Letters*, 2006. **60**(5): p. 651-655.
149. L. L. Swette, M. Manoukian, M. Hamdan, A. LaConti, A. Sohaghpurwala, and W.T. Scannell, *Reference electrode for monitoring steel-in-concrete potential*, U.S. Patent, Editor. 1999: USA.
150. A. Poursaeed, *Automated Corrosion Monitoring Programme (ACMP)*. 2006, Canadian Intellectual Property Office, Registration Number: 1036218, 2006.
151. National Instruments, *What is NI GPIB?*, [http://www.ni.com/gpib/what\\_is.htm](http://www.ni.com/gpib/what_is.htm). 2006.
152. ASTM C1152, *Standard Test Method for Acid-Soluble Chloride in Mortar and Concrete*. 1997, ASTM.
153. C. Alonso, C. Andrade, M. Izquierdo, X. R. Novoa, and M. C. Perez, *Effect of protective oxide scales in the macrogalvanic behaviour of concrete reinforcements*. *Corrosion Science*, 1998. **40**(8): p. 1379-1389.
154. C. Andrade, M. Keddad, X.R. Novoa, M.C. Perez, C.M. Rangel, and H. Takenouti, *Electrochemical behaviour of steel rebars in concrete: influence of environmental factors and cement chemistry*. *Electrochimica Acta*, 2001. **46**: p. 3905–3912.
155. C. Andrade and C. Alonso, *Test methods for on-site corrosion rate measurement of steel reinforcement in concrete by means of the polarisation resistance method*. *Materials and Structures/Materiaux et Constructions*, 2004. **37**: p. 623-643.

156. J. M. Esteban and M. E. Orazem, *On the application of the Kramers-Kronig relations to evaluate the consistency of electrochemical impedance data*. Journal of Electrochemical Society, 1991. **138**(1): p. 67-76.
157. B. Yeum, *ZSimpWin version 3.00 for windows 95/98/2000/NT electrochemical impedance spectroscopy data analysis software*, in *Technical Note 1: Extrapolation using Kramers-Kronig relations*. 2001, Princeton Applied Research.
158. C. Gabrielli, *Use and application of electrochemical impedance technique*, *Technical Report No. 24*. 1997, Solartron Analytical.
159. ASTM, *G 5-94: Standard Reference Test Method for Making Potentiostatic and Potentiodynamic Anodic Polarization Measurements*. . 2004.
160. S. J. Oh, D. C. Cook, and H. E. Townsend, *Characterization of iron oxides commonly formed as corrosion products on steel*. Hyperfine Interactions, 1998. **112**(1-4): p. 59-66.
161. D. S. Dunn, M. B. Bogart, C. S. Brossiaand, and G. A. Cragolino, *Corrosion of iron under alternate wet and dry conditions*. Corrosion, 2000. **56**: p. 470-488.
162. R. Balasubramaniam, A. V. Ramesh Kumar, and P. Dillmann, *Characterization of rust on ancient Indian iron*. Current Science, 2003. **58**(11): p. 1546-1555.
163. J. Dünnwald and A. Otto, *An investigation of phase transitions in rust layers using Raman spectroscopy*. Corrosion Science, 1989. **29**(9): p. 1167-1989.
164. Q. Tan and C. M. Hansson, *The Influence of supplementary cementing materials on the initial corrosion of galvanized steel reinforcing bar*. Unpublished.
165. P. R. Camp and S. Bilotta, *Dielectric properties of Portland cement paste as a function of time since mixing*. Journal of Applied Physics, 1989. **66**(12).

166. J. Greener, H. Peemoeller, C. Choi, R. Holly, C. M. Hansson, and M. M. Pintar, *Monitoring of Hydration of White Cement Paste with Proton NMR Spin-Spin Relaxation*. Journal of American Ceramic Society, 2000. **83**: p. 623-627.
167. S. J. Jaffer, *A study of the hydration and microstructure of cement pastes by NMR, MRI, ESEM and fluorescent microscopy*. MAsc thesis in Mechanical Engineering, University of Waterloo, 2004.
168. D. Halliday and R. Resnick, *Fundamentals of physics* 2005, New Jersey: John Wiley & Sons, Inc.
169. A. Chelkowski, *Dielectric physics*. 1980, New York: Elsevier/North-Holland, Inc.
170. D. R. Askeland, *The science and engineering of materials*. 2006, Toronto: NelsonThomson Learning.
171. A. Van Beek, K. Van Breugel, and M. A. Hilhorst. *Monitoring the hydration in LWA-concrete by dielectric measurements*. in *5th International Symposium on Utilization of High Strength/High Performance Concrete*. 1999. Sandefjord, Norway.
172. D. R. Lide, *CRC Handbook of chemistry and physics*. 1999, New York, NY: CRC Press.
173. ASTM, *C876-91: Standard Test Method for Half-cell Potentials of Uncoated Reinforcing Steel in Concrete*. 1999. p. 446-451.
174. ASTM, *D 4580-03: Standard Practice for Measuring Delamination in Concrete Bridge Decks by Sounding*. 2003.
175. MTO, *LS-417: Determination of total chloride ion in concrete (acid soluble)*. 1996.
176. S.R. Yeomans, *Performance of Black, Galvanized and Epoxy-Coated Reinforcing Steels in Chloride-Contaminated Concrete*. Corrosion, 1994. **50**(1): p. 72-81.

177. D. E. Tonini and S. W. Dean, *Chloride corrosion of steel in concrete*. 1976: ASTM-STP 629.
178. I. Cornet and B. Bresler, *Corrosion of steel and galvanized steel in concrete*. Materials Protection, 1966. 5(5): p. 69-72.
179. ASTM, *A123: Standard Specification for Zinc (Hot-Dip Galvanized) Coatings on Iron and Steel Products*. 2004, ASTM
180. Sika Corporation, *Product Data Sheet: Sika FerroGard® 903*. 2004:  
<http://www.sikaconstruction.com/tds-cpd-SikaFerroGard903-us.pdf>.
181. F. Pianca. 2006: personal communication, Ministry of Transportation Ontario (MTO).
182. R. Doelling, *Potentiostats*. 2000: Bank Elektronik-Intelligent Controls GmbH.
183. R. A. Cottis and A. Llewellyn, *Electrochemistry for corrosion: basics of instrumentation*. 2005, University of Manchester Institute of Science and Technology (UMIST):  
<http://www.cp.umist.ac.uk/lecturenotes/Echem/appendix.html>.
184. T. R. Kuphaldt, *Lessons In Electric Circuits*. Vol. III, Semiconductors. 2001.
185. *Technical user guide*. 2005, Monox: <http://www.monox.com/PDF/MonoxUM0002.pdf>.

## **Appendix (A)**

### **Potentiostat**



The potentiostat has two tasks: To measure the potential difference between working electrode and reference electrode without polarising the reference electrode, and to compare the potential difference to a preset voltage and force a current through the counter electrode towards the working electrode in order to counteract the difference between preset voltage and existing working electrode potential [182].

A simple potentiostat does this by using optional amplifier. The term operational amplifier or "op-amp" refers to a class of high-gain<sup>1</sup> [183] DC coupled amplifiers with two inputs and a single output: an inverting (-) input and a non-inverting (+) one [93]. Figure A.1 shows the general schematic for an op-amp.

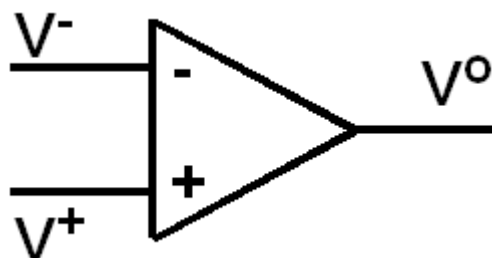


Figure A. 1. General symbol of an optional amplifier [184].

If a voltage (current) feed into a non-inverting input of an op-amp, an amplified voltage (or current) of the same magnitude and sign will be produced by the op-amp. On the other hand,

---

<sup>1</sup>The ratio of the output voltage (relative to the mid-point of the power supply) to the difference between the voltages at the non-inverting and the inverting inputs. The gain is specified for dc voltages (it is typically constant below about 1 Hz), and the gain for ac signals will decrease as the frequency increases.

if a voltage (current) feed into the inverting input, an amplified voltage (or current) of the same magnitude, but of opposite sign will be produced.

To keep the output voltage almost exactly the same as the input voltage, the inverting input and the output should be connected (Figure A.1). [182, 183] This is called unity-gain or buffer op-amp.

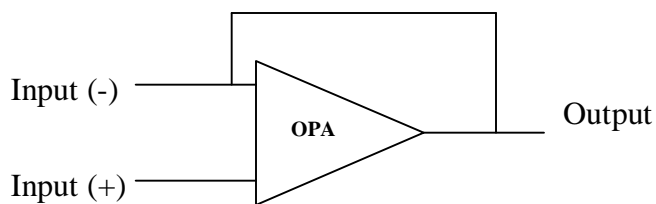


Figure A. 2. Schematic plan of an optional amplifier (op-amp), when the inverting input and output are connected. The output of this circuit will be the input voltage.

The voltage at the output is fed back to the inverting input, so the amplification is controlled by the difference between the  $V_{(+)}$  and the  $V_{(output)}$ . If the  $V_{(+)}$  increased, the difference between  $V_{(+)}$  and  $V_{(-)}$  would become positive, which would cause the output voltage to increase until  $V_{output} = V_{(+)}$ . If  $V_{(+)}$  decreased, the difference between  $V_{(+)}$  and  $V_{(-)}$  would become negative, which would cause the output to decrease. The only stable point for the circuit occurs when  $V_{output} = V_{(+)}$  [184]. Therefore, increasing the voltage on the inverting input (-) forces a corresponding current on the output, which cancels out the input voltage difference. The properties of such an optional amplifier are the basic of potentiostat.

Now, assume that the working, reference and counter electrodes of an electrochemical cell are connected to the non-inverting (+) input, the inverting (-) input and the counter the

output, respectively (Figure A.2). The difference between working and reference electrodes will be amplified and inverted by the op-amp. A matching current is fed to the counter electrode. The control circuit is closed by the cell and the current passes from the counter electrode to the working electrode through the electrolyte. This polarises the working electrode in a way that the difference between the reference electrode input and the working electrode input is set to zero [182].

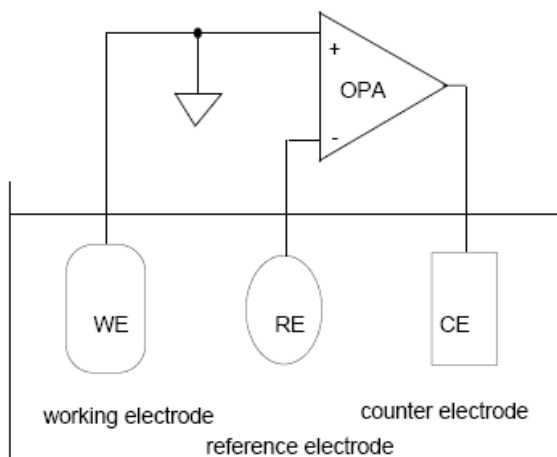


Figure A. 3. Using an optional amplifier as potentiostat [182].

The explained circuit keeps the potential of the working and reference electrodes the same. If a potential shift of the working electrode respect to the reference electrode is required, a known voltage should be applied to the working electrode. To measure the current through the counter electrode, a resistor should be inserted in the counter electrode wiring. A voltage, proportional to the current flowing, can be measured across the resistor.

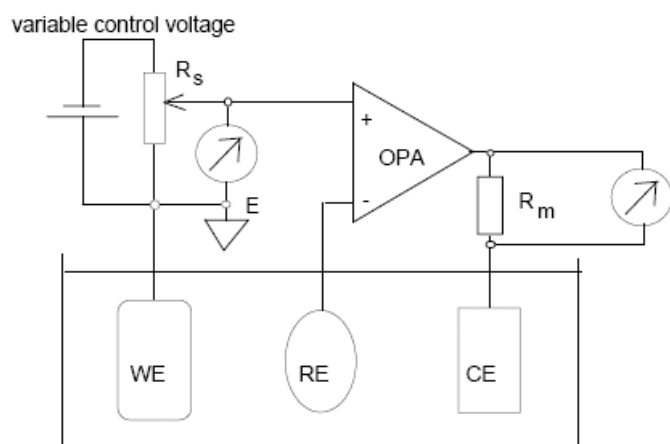


Figure A. 4. A potentiostat with potential control [182].

In a real potentiostat some additional elements are required. The reference electrode input is commonly protected by an input resistor. When the input is open, this resistor protects the reference electrode from being destroyed by static high voltage shocks. Another element which is very important is called a phase correction capacitor. With increasing the frequency, the gain of the amplifier decreases while the phase shift of the amplifier increases. A sine wave fed into the inverting input is counteracted at the output at low frequencies. However, at a critical frequency, the internal phase shift of the amplifier reaches  $180^\circ$ , and as a result, the output signal is in phase with the input signal. The potentiostat then acts as an oscillator, oscillating at full power. The phase correction capacitor prevents this breakdown, by keeping the phase stable within the designated frequency range. Figure A.5, shows a schematic scheme of a potentiostat with aforementioned elements [182].

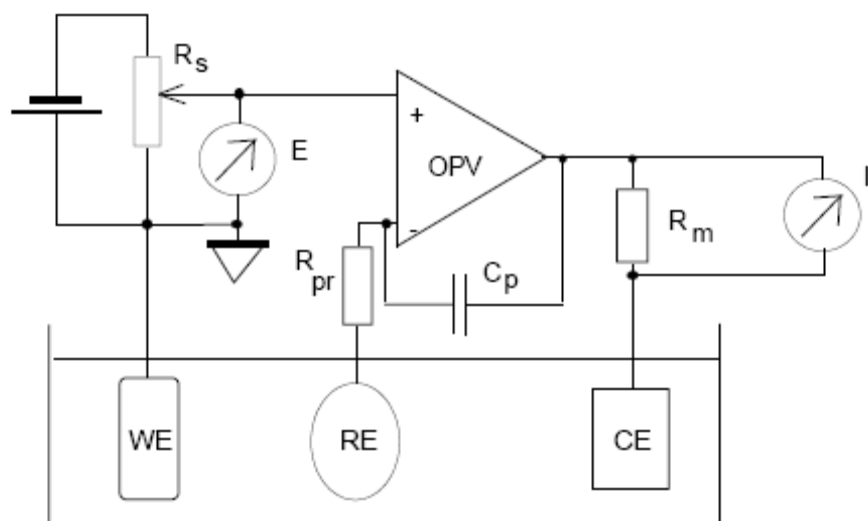


Figure A. 5. Complete scheme of a simple potentiostat [182].

The electronic circuit of a typical standard potentiostat is shown in Figure A.6.

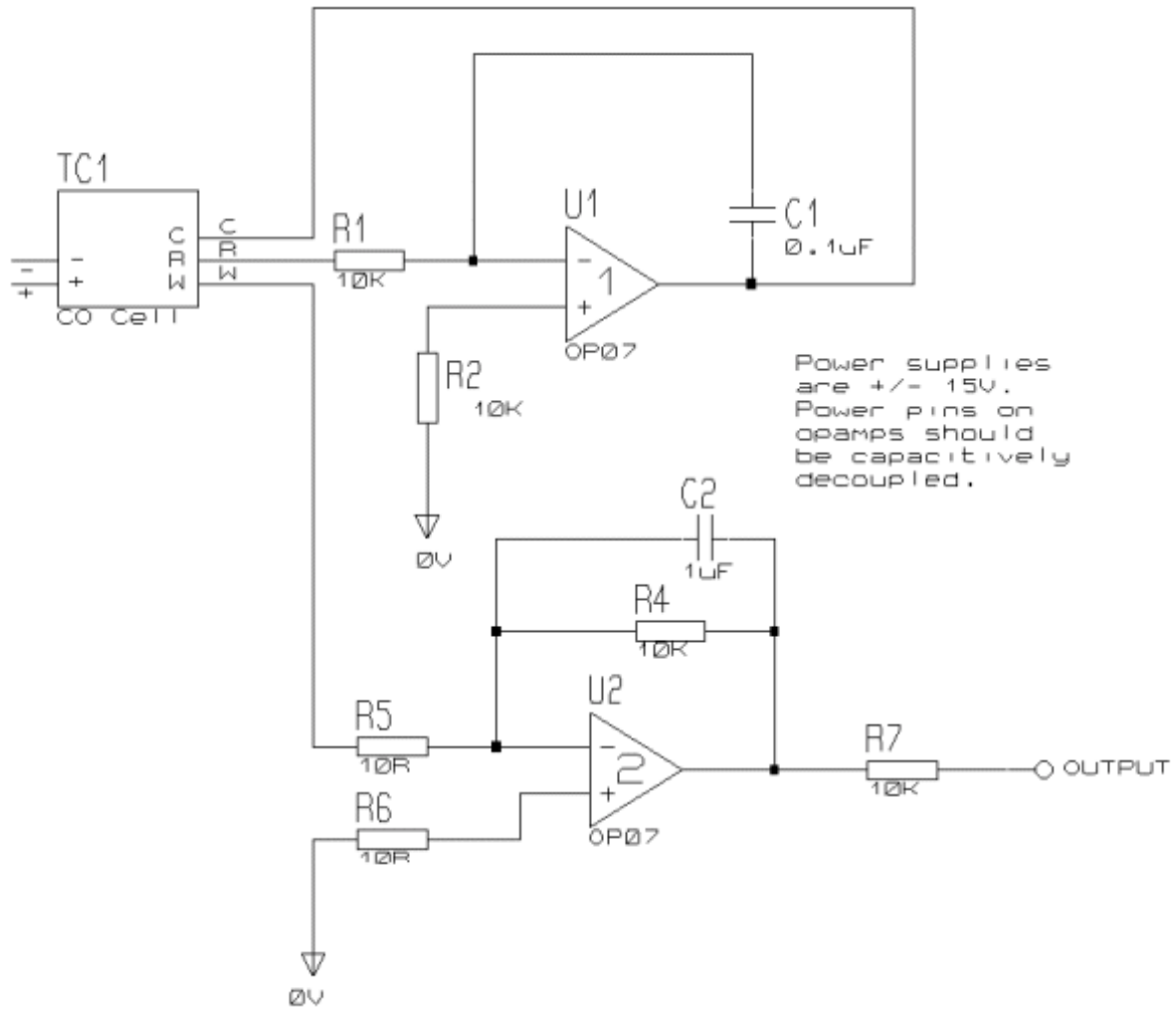


Figure A. 6. A standard potentiostat circuit [185].

## **Appendix (B)**

### **Keithley 2750 Multimeter/Switch system specifications**

# 2750 Multimeter/Switch System

## DC CHARACTERISTICS<sup>1</sup>

CONDITIONS: MED (1 PLC)<sup>2</sup> or 10 PLC or MED (1 PLC) with Digital Filter of 10

| FUNCTION                        | RANGE  | RESOLUTION          | TEST CURRENT<br>±5% OR BURDEN<br>VOLTAGE | INPUT<br>RESISTANCE OR<br>OPEN CKT.<br>VOLTAGE <sup>3</sup> | ACCURACY: ±(ppm of reading + ppm of range)<br>(ppm = parts per million) e.g., 10ppm = 0.001%) |                   |                   | TEMPERATURE<br>COEFFICIENT<br>0°-18°C & 28°-50°C |
|---------------------------------|--|---------------------|--|---|---|-------------------|-------------------|--|
|                                 |  |                     |  |   | 24 Hour <sup>4</sup><br>23°C±1°   | 90 Day<br>23°C±5° | 1 Year<br>23°C±5° |  |
| Voltage <sup>14</sup>           | 100.0000 mV  | 0.1 µV              |  | >10 GΩ  | 15 + 30   | 25 + 35           | 30 + 35           | (1 + 5)°C  |
|                                 | 1.000000 V   | 1.0 µV              |  | >10 GΩ  | 15 + 6  | 25 + 7            | 30 + 7            | (1 + 1)°C  |
|                                 | 10.0000 V  | 10 µV               |  | >10 GΩ  | 10 + 4  | 20 + 5            | 30 + 5            | (1 + 1)°C  |
|                                 | 100.0000 V   | 100 µV              |  | 10 MΩ ± 1%  | 15 + 6  | 35 + 9            | 45 + 9            | (5 + 1)°C  |
|                                 | 1000.000 V <sup>5</sup>  | 1 mV                |  | 10 MΩ ± 1%  | 20 + 6  | 35 + 9            | 50 + 9            | (5 + 1)°C  |
| Resistance <sup>6,8</sup>       | 1.000000 Ω   | 1 µΩ                | 10 mA                                    | 5.9 V   | 80 + 40   | 80 + 40           | 100 + 40          | (8 + 1)°C  |
|                                 | 10.00000 Ω   | 10 µΩ               | 10 mA                                    | 5.9 V   | 20 + 20   | 80 + 20           | 100 + 20          | (8 + 1)°C  |
|                                 | 100.0000 Ω   | 100 µΩ              | 1 mA                                     | 12.2 V  | 20 + 20   | 80 + 20           | 100 + 20          | (8 + 1)°C  |
|                                 | 1.000000 kΩ  | 1 mΩ                | 1 mA                                     | 12.2 V  | 20 + 6  | 80 + 6            | 100 + 6           | (8 + 1)°C  |
|                                 | 10.00000 kΩ  | 10 mΩ               | 100 µA                                   | 6.8 V   | 20 + 6  | 80 + 6            | 100 + 6           | (8 + 1)°C  |
|                                 | 100.0000 kΩ  | 100 mΩ              | 10 µA                                    | 12.8 V  | 20 + 6  | 80 + 10           | 100 + 10          | (8 + 1)°C  |
|                                 | 1.000000 MΩ <sup>23</sup>  | 1.0 Ω               | 10 µA                                    | 12.8 V  | 20 + 6  | 80 + 10           | 100 + 10          | (8 + 1)°C  |
|                                 | 10.00000 MΩ <sup>22,23</sup>   | 10 Ω                | 0.7 µA // 10MΩ                           | 7.0 V   | 150 + 6   | 200 + 10          | 400 + 10          | (70 + 1)°C                                       |
|                                 | 100.0000 MΩ <sup>22,23</sup>   | 100 Ω               | 0.7 µA // 10MΩ                           | 7.0 V   | 800 + 30  | 2000 + 30         | 2000 + 30         | (385 + 1)°C                                      |
|                                 | Dry Circuit<br>Resistance <sup>23</sup>  | 1.000000 Ω          | 1 µΩ                                     | 10 mA   | 20mV  | 80 + 40           | 80 + 40           | 100 + 40   |
| 10.00000 Ω                      |  | 10 µΩ               | 1 mA                                     | 20mV  | 25 + 40   | 80 + 40           | 100 + 40          | (8 + 1)°C  |
| 100.0000 Ω                      |  | 100 µΩ              | 100 µA                                   | 20mV  | 25 + 40   | 90 + 40           | 140 + 40          | (8 + 1)°C  |
| 1.000000 kΩ                     |  | 1 mΩ                | 10 µA                                    | 20mV  | 25 + 90   | 180 + 90          | 400 + 90          | (8 + 1)°C  |
| Continuity (2W) <sup>24</sup>   | 1.000 kΩ   | 100 mΩ              | 1 mA                                     | 12.2 V  | 40 + 100  | 100 + 100         | 100 + 100         | (8 + 1)°C  |
| Current                         | 20.00000 mA  | 10 nA               | <0.2 V                                   |   | 60 + 30   | 300 + 80          | 500 + 80          | (50 + 5)°C                                       |
|                                 | 100.0000 mA  | 100 nA              | <0.1 V                                   |   | 100 + 300   | 300 + 800         | 500 + 800         | (50 + 50)°C                                      |
|                                 | 1.000000 A   | 1.0 µA              | <0.5 V <sup>9</sup>                      |   | 200 + 30  | 500 + 80          | 800 + 80          | (50 + 5)°C                                       |
| 3.000000 A                      | 10 µA  | <1.5 V <sup>9</sup> |  | 1000 + 15   | 1200 + 40   | 1200 + 40         | (50 + 5)°C        |  |
| Channel (Ratio) <sup>19</sup>   | Ratio Accuracy = Accuracy of selected Channel Range + Accuracy of Paired Channel Range   |                     |  |   |   |                   |                   |  |
| Channel (Average) <sup>19</sup> | Average Accuracy = Accuracy of selected Channel Range + Accuracy of Paired Channel Range |                     |  |   |   |                   |                   |  |

## TEMPERATURE<sup>19</sup>

(Display in °C, °F, or K. Exclusive of probe errors.)  
Thermocouples (Accuracy based on ITS-90.)

| Type   | Range           | Resolution | 90 Day/1 Year (23°C ± 5°C)           |                      |            | Temperature<br>Coefficient<br>0°-18°C & 28°-50°C |
|--|-----------------|------------|--------------------------------------|----------------------|------------|--|
|  |                 |            | Relative to<br>Simulated<br>Junction | Using 77xx<br>Module |            |  |
| J  | -200 to +760°C  | 0.001°C    | 0.2°C                                | 1.0°C                | 0.03°C/°C  |  |
| K  | -200 to +1372°C | 0.001°C    | 0.2°C                                | 1.0°C                | 0.03°C/°C  |  |
| N  | -200 to +1300°C | 0.001°C    | 0.2°C                                | 1.0°C                | 0.03°C/°C  |  |
| T  | -200 to +400°C  | 0.001°C    | 0.2°C                                | 1.0°C                | 0.03°C/°C  |  |
| E  | -200 to +1000°C | 0.001°C    | 0.2°C                                | 1.0°C                | 0.03°C/°C  |  |
| R  | 0 to +1768°C    | 0.1°C      | 0.6°C                                | 1.8°C                | 0.03°C/°C  |  |
| S  | 0 to +1768°C    | 0.1°C      | 0.6°C                                | 1.8°C                | 0.03°C/°C  |  |
| B  | +350 to +1820°C | 0.1°C      | 0.6°C                                | 1.8°C                | 0.03°C/°C  |  |
| <b>4-Wire RTD:</b>   |                 |            |                                      |                      |            |  |
| (100Ω platinum [PT100], D100, F100, PT385, PT3916, or user type, Offset compensation On) |                 |            |                                      |                      |            |  |
|  | -200° to 630°C  | 0.01°C     | 0.06°C                               |                      | 0.003°C/°C |  |
| <b>Thermistor: (2.2kΩ, 5kΩ, and 10kΩ)<sup>20</sup></b>                                   |                 |            |                                      |                      |            |  |
|  | -80° to 150°C   | 0.01°C     | 0.08°C                               |                      | 0.002°C/°C |  |

## DC SYSTEM SPEEDS<sup>15,18</sup>

RANGE CHANGES<sup>16</sup>: 50/s (42/s).  
FUNCTION CHANGES<sup>16</sup>: 50/s (42/s).  
AUTORANGE TIME<sup>16</sup>: <30ms.  
ASCII READINGS TO RS-232 (19.2k BAUD): 55/s.  
MAX. INTERNAL TRIGGER RATE: 2000/s.  
MAX. EXTERNAL TRIGGER RATE: 375/s.

## DC MEASUREMENT SPEEDS<sup>15</sup>

Single Channel, 60Hz (50Hz) Operation

| FUNCTION   | DIGITS               | READINGS/s  | PLCs |
|--|----------------------|-------------|------|
| DCV, DCI, Ω (<10M),<br>Thermocouple,<br>Thermistor | 6.5 <sup>12,16</sup> | 5 (4)       | 10   |
|  | 6.5 <sup>16</sup>    | 35 (28)     | 1    |
|  | 6.5 <sup>12,16</sup> | 45 (36)     | 1    |
|  | 5.5 <sup>12,16</sup> | 150 (120)   | 0.1  |
|  | 5.5 <sup>16,17</sup> | 300 (240)   | 0.1  |
|  | 5.5 <sup>17</sup>    | 500 (400)   | 0.1  |
|  | 4.5 <sup>17</sup>    | 2500 (2000) | 0.01 |
| 4WΩ (<10M)   | 6.5 <sup>16</sup>    | 1.4 (1.1)   | 10   |
|  | 6.5 <sup>16</sup>    | 15 (12)     | 1    |
|  | 5.5 <sup>17</sup>    | 33 (25)     | 0.1  |
| 4WΩ 0Comp, RTD <sup>22</sup>                       | 6.5 <sup>16</sup>    | 0.9 (0.7)   | 10   |
|  | 6.5 <sup>16</sup>    | 8 (6.4)     | 1    |
|  | 5.5 <sup>16,17</sup> | 18 (14.4)   | 0.1  |
| Channel (Ratio),<br>Channel (AVG)                  | 6.5 <sup>16</sup>    | 2.5 (2)     | 10   |
|  | 6.5 <sup>16</sup>    | 15 (12)     | 1    |
|  | 5.5 <sup>17</sup>    | 25 (20)     | 0.1  |

## Multiple Channels Into Memory<sup>15,18</sup>

7703 and 7710 Scanning DCV 230/s  
7703 and 7710 Scanning with Limits or Time Stamp On 230/s  
7703 and 7710 Scanning DCV alternating 2WΩ 55/s  
7710 Scanning Temperature (T/C) 90/s  
7700 and 7708 Scanning Temperature (T/C) 50/s

## Multiple Channels Into and Out of Memory<sup>15,16,17,18</sup>

7703 and 7710 Scanning DCV 200/s  
7703 and 7710 Scanning with Limits or Time Stamp On 200/s  
7703 and 7710 Scanning DCV alternating 2WΩ 45/s  
7710 Scanning Temperature (T/C) 85/s  
7702 Scanning DCV 65/s  
7700 and 7708 Scanning Temperature (T/C) 50/s



# 2750 Multimeter/Switch System

## DC SPEED vs. NOISE REJECTION

| Rate | Filter | Readings/s <sup>12</sup> | Digits | RMS Noise    |                      |                    |
|------|--------|--------------------------|--------|--------------|----------------------|--------------------|
|      |        |                          |        | 10V Range    | NMRR                 | CMRR <sup>14</sup> |
| 10   | 50     | 0.1 (0.08)               | 6.5    | <1.2 $\mu$ V | 110 dB <sup>13</sup> | 140 dB             |
| I    | Off    | 15 (12)                  | 6.5    | <4 $\mu$ V   | 90 dB <sup>13</sup>  | 140 dB             |
| 0.1  | Off    | 500 (400)                | 5.5    | <22 $\mu$ V  | —                    | 80 dB              |
| 0.01 | Off    | 2500 (2000)              | 4.5    | <150 $\mu$ V | —                    | 80 dB              |

## DC MEASUREMENT CHARACTERISTICS

### DC Volts

**A-D LINEARITY:** 2.0 ppm of reading + 1.0 ppm of range.

#### INPUT IMPEDANCE:

**100mV-10V Ranges:** Selectable >10G $\Omega$ // with <400pF or 10M $\Omega$   $\pm$ 1%.

**100V, 1000V Ranges:** 10M $\Omega$   $\pm$ 1%.

**Dry Circuit:** 100k $\Omega$   $\pm$ 1% // <1 $\mu$ F.

**INPUT BIAS CURRENT:** <75pA at 23°C.

**COMMON MODE CURRENT:** <500nA at 50Hz or 60Hz.

**AUTOZERO ERROR:** Add  $\pm$ (2ppm of range error +5 $\mu$ V) for <10 minutes and  $\pm$ 1°C.

**INPUT PROTECTION:** 1000V, all ranges, 300V with plug-in modules.

### Resistance

**MAX 4W $\Omega$  LEAD RESISTANCE:** 80% of range per lead (Dry Ckt Mode). 5 $\Omega$  per lead for 1 $\Omega$  range, 10% of range for 10 $\Omega$ , 100 $\Omega$  and 1k $\Omega$  ranges; 1k $\Omega$  per lead for all other ranges.

**OFFSET COMPENSATION:** Selectable on 4W $\Omega$ , 1 $\Omega$ , 10 $\Omega$ , 100 $\Omega$ , 1k $\Omega$ , and 10k $\Omega$  ranges.

**CONTINUITY THRESHOLD:** Adjustable 1 to 1000 $\Omega$ .

**INPUT PROTECTION:** 1000V, all Source Inputs, 350V Sense Inputs, 300V with plug-in modules.

### DC Current

**SHUNT RESISTORS:** 100mA-3A, 0.1 $\Omega$ , 20mA, 5 $\Omega$ .

**INPUT PROTECTION:** 3A, 250V fuse.

### Thermocouples

**CONVERSION:** ITS-90.

**REFERENCE JUNCTION:** Internal, External, or Simulated (Fixed).

**OPEN CIRCUIT CHECK:** Selectable per channel. Open >11.4k  $\pm$ 200 $\Omega$ .

**EARTH ISOLATION:** 500V peak, >10G $\Omega$  and <300pF any terminal to chassis.

## DC Notes

- 20% overrange except on 1000V and 3A.
- Add the following to "ppm of range" uncertainty: 100mV 15ppm, 1V and 100V 2ppm, 1 $\Omega$  and Dry Circuit  $\Omega$  40ppm, 10 $\rightarrow$ <1M $\Omega$  2ppm, 20mA and 1A 10ppm, 100mA 40ppm.
- $\pm$ 2% (measured with 10M $\Omega$  input resistance DMM, >10G $\Omega$  DMM on 10M $\Omega$  and 100M $\Omega$  ranges). For Dry Circuit  $\Omega$ ,  $\pm$ 25% with Input HI connected to Sense HI; with Sense HI disconnected add 30mV.
- Relative to calibration accuracy.
- For signal levels >500V, add 0.02ppm/V uncertainty for portion exceeding 500V.
- Specifications are for 4-wire  $\Omega$ , 1 $\Omega$ , 10 $\Omega$ , and 100 $\Omega$  with offset compensation on. 77xx plug-in modules with LSYNC and offset compensation on. With offset compensation on OPEN CKT. VOLTAGE is 12.8V. For 2-wire  $\Omega$  add 1.5 $\Omega$  to "ppm of range" uncertainty. 1 $\Omega$  range is 4-wire only.
- Must have 10% matching of lead resistance in Input HI and LO.
- Add the following to "ppm of reading" uncertainty when using plug-in modules:

|  | 10 k $\Omega$         | 100 k $\Omega$      | 1 M $\Omega$         | 10 M $\Omega$       | 100 M $\Omega$     |
|--|-----------------------|---------------------|----------------------|---------------------|--------------------|
| <b>All Modules:</b>  |                       |                     |                      | 220 ppm             | 2200 ppm           |
| <b>7701, 7703, 7707, and 7709 Modules:</b>   | 10 ppm                | 100 ppm             | 1000 ppm             | 1%                  | 10%                |
| <b>7706, 7708 Modules:</b>   | 5 ppm                 | 50 ppm              | 500 ppm              | 5000 ppm            | 5%                 |
| <b>7710 Model 23°C <math>\pm</math>5°C:</b>  | 11 ppm                | 110 ppm             | 1100 ppm             | 1.1%                | 11%                |
| <b>7710 Model Temp Coeff. &gt;28<math>^{\circ}</math> <math>\rightarrow</math> 50<math>^{\circ}</math>C:</b> | 0.3 ppm/ $^{\circ}$ C | 3 ppm/ $^{\circ}$ C | 30 ppm/ $^{\circ}$ C | 0.03%/ $^{\circ}$ C | 0.3%/ $^{\circ}$ C |
- Add 1.5V when used with plug-in modules.
- For RATIO, DCV only. For AVERAGE, DCV and Thermocouples only. Available with plug-in modules only.
- Add 6 $\mu$ V to "of range" uncertainty when using Models 7701, 7703, and 7707, 3 $\mu$ V for Models 7706, 7709, and 7710.
- Auto zero off.
- For LSYNC On, line frequency  $\pm$ 0.1%. For LSYNC Off, use 60dB for  $\geq$  1PLC.
- For 1k $\Omega$  unbalance in LO lead, AC CMRR is 70dB.
- Speeds are for 60Hz (50Hz) operation using factory defaults operating conditions (\*RST). Autorange off, Display off, Limits off, Trigger delay = 0.
- Speeds include measurements and binary data transfer out the GPIB (reading element only).
- Sample count = 1000 (into memory buffer), auto zero off.
- Auto zero off, NPLC = 0.01.
- Additional Uncertainty

| Type | Range            | 7710 Module Using CJC |
|------|------------------|-----------------------|
| J    | 0 to +760°C      | 1.5°C                 |
| K    | 0 to +1372°C     | —                     |
| N    | 0 to +1300°C     | 0.5°C                 |
| T    | 0 to +400°C      | 0.5°C                 |
| E    | 0 to +1000°C     | 0.5°C                 |
| R    | -400 to +1768°C  | 0.9°C                 |
| S    | +400 to +1768°C  | 0.9°C                 |
| B    | +1100 to +1820°C | 0.9°C                 |

| Type | Range           | Plug-In Modules                    |                         |                                     |                         |                |                |
|------|-----------------|------------------------------------|-------------------------|-------------------------------------|-------------------------|----------------|----------------|
|      |                 | Front Terminals Sim. Ref. Junction | 7709 Sim. Ref. Junction | 7701, 7703, 7707 Sim. Ref. Junction | 7700 and 7708 Using CJC | 7706 Using CJC | 7710 Using CJC |
| J    | -200 to 0°C     | 0.1                                | 0.1                     | 0.3                                 | 0.8                     | 1.6            | 4.5            |
| K    | -200 to 0°C     | 0.2                                | 0.2                     | 0.4                                 | 0.8                     | 1.6            | 1              |
| N    | -200 to 0°C     | 0.3                                | 0.3                     | 0.6                                 | 0.8                     | 1.6            | 2.5            |
| T    | -200 to 0°C     | 0.2                                | 0.1                     | 0.4                                 | 0.8                     | 1.6            | 2.5            |
| E    | -200 to 0°C     | -                                  | 0.1                     | 0.3                                 | 0.8                     | 1.6            | 2.5            |
| R    | 0 to +400°C     | 0.4                                | 0.6                     | 1.2                                 | 0.5                     | 1.0            | 2.2            |
| S    | 0 to +400°C     | 0.4                                | 0.6                     | 1.2                                 | 0.5                     | 1.0            | 2.2            |
| B    | +350 to +1100°C | 0.8                                | 0.3                     | 1.7                                 | 0.5                     | 1.0            | 2.2            |

20. For lead resistance >0 $\Omega$ , add the following uncertainty/ $\Omega$  for measurement temperatures of:

|                                 |         | 70 $^{\circ}$ -100 $^{\circ}$ C | 100 $^{\circ}$ -150 $^{\circ}$ C |
|---------------------------------|---------|---------------------------------|----------------------------------|
| <b>2.2 k<math>\Omega</math></b> | (44004) | 0.22°C                          | 1.11°C                           |
| <b>5.0 k<math>\Omega</math></b> | (44007) | 0.10°C                          | 0.46°C                           |
| <b>10 k<math>\Omega</math></b>  | (44006) | 0.04°C                          | 0.19°C                           |

- For 4-wire  $\Omega$  only, offset compensation on, LSYNC on.
- For Dry Circuit 1k $\Omega$  range, 2 readings/s max.
- For Front Inputs, add the following to Temperature Coefficient "ppm of reading" uncertainty: 1M $\Omega$  25ppm, 10M $\Omega$  250ppm, 100M $\Omega$  2500ppm. Operating environment specified for 0°C to 50°C and 50%.
- Front panel resolution is limited to 0.1 $\Omega$ .

# 2750 Multimeter/Switch System

## AC SPECIFICATIONS<sup>1</sup>

| Function                          | Range       | Resolution | Calibration Cycle           | Accuracy: ±(% of reading + % of range), 23°C ±5°C                       |                                      |                                      |                |                 |
|-----------------------------------|-------------|------------|-----------------------------|---|--------------------------------------|--------------------------------------|----------------|-----------------|
|                                   |             |            |                             | 3 Hz-10 Hz  | 10 Hz-20 kHz                         | 20 kHz-50 kHz                        | 50 kHz-100 kHz | 100 kHz-300 kHz |
| Voltage <sup>2</sup>              | 100.0000 mV | 0.1 μV     | 90 Days (all ranges)        | 0.35 + 0.03   | 0.05 + 0.03                          | 0.11 + 0.05                          | 0.6 + 0.08     | 4.0 + 0.5       |
|                                   | 1.000000 V  | 1.0 μV     |                             | 1 Year (all ranges)   | 0.35 + 0.03                          | 0.06 + 0.03                          | 0.12 + 0.05    | 0.6 + 0.08      |
|                                   | 10.00000 V  | 10 μV      | (Temp. Coeff.) <sup>3</sup> |   | 0.035 + 0.003                        | 0.005 + 0.003                        | 0.006 + 0.005  | 0.01 + 0.006    |
|                                   | 100.0000 V  | 100 μV     |                             | 3 Hz-10 Hz  | 10 Hz-3 kHz                          | 3 kHz-5 kHz                          |                |                 |
| 750.0000 V                        | 1.0 mV      |            | 0.30 + 0.04                 | 0.10 + 0.04   | 0.14 + 0.04                          |                                      |                |                 |
|                                   |             |            |                             | 0.35 + 0.06   | 0.15 + 0.06                          | 0.18 + 0.06                          |                |                 |
|                                   |             |            |                             | (Temp. Coeff.) <sup>3</sup>   | 0.035 + 0.006                        | 0.015 + 0.006                        |                |                 |
| Current <sup>2</sup>              | 1.000000 A  | 1.0 μA     | 90 Day/1 Yr.                | Accuracy ±(ppm of reading + offset ppm)<br>(3 Hz-500 kHz) (333 ms-2 μs) |                                      |                                      |                |                 |
|                                   | 3.00000 A   | 10 μA      |                             | 100 ppm + 0.333 ppm (SLOW, 1s gate)                                     | 100 ppm + 3.33 ppm (MED, 100ms gate) | 100 ppm + 33.3 ppm (FAST, 10ms gate) |                |                 |
| Frequency <sup>4</sup> and Period | 100 mV      | 0.333 ppm  | 90 Day/1 Yr.                | Accuracy ±(ppm of reading + offset ppm)                                 |                                      |                                      |                |                 |
|                                   | to 750 V    | 3.33 ppm   |                             | 100 ppm + 0.333 ppm (SLOW, 1s gate)                                     | 100 ppm + 3.33 ppm (MED, 100ms gate) | 100 ppm + 33.3 ppm (FAST, 10ms gate) |                |                 |
|                                   |             | 33.3 ppm   |                             |   |                                      |                                      |                |                 |

### Additional Uncertainty ±(% of reading)

| Low Frequency Uncertainty | MED | FAST |
|---------------------------|-----|------|
| 20Hz - 30Hz               | 0.3 | —    |
| 30Hz - 50Hz               | 0   | —    |
| 50Hz - 100Hz              | 0   | 1.0  |
| 100Hz - 200Hz             | 0   | 0.18 |
| 200Hz - 300Hz             | 0   | 0.10 |
| > 300Hz                   | 0   | 0    |

CREST FACTOR<sup>5</sup>:

| Additional Uncertainty: | 1-2  | 2-3  | 3-4  | 4-5  |
|-------------------------|------|------|------|------|
|                         | 0.05 | 0.15 | 0.30 | 0.40 |

Maximum Crest Factor: 5 at full-scale

### AC MEASUREMENT SPEEDS<sup>7,8</sup>

#### Single Channel, 60Hz (50Hz) Operation

| Function          | Digits            | Readings/s | Rate | Bandwidth      |
|-------------------|-------------------|------------|------|----------------|
| ACV, ACI          | 6.5               | 2s/Reading | SLOW | 3 Hz-300 kHz   |
|                   | 6.5               | 1.4 (1.1)  | MED  | 30 Hz-300 kHz  |
|                   | 6.5 <sup>9</sup>  | 40 (32)    | FAST | 300 Hz-300 kHz |
| Frequency, Period | 6.5               | 1 (1)      | SLOW | 3 Hz-300 kHz   |
|                   | 5.5               | 9 (9)      | MED  | 30 Hz-300 kHz  |
|                   | 4.5               | 35 (35)    | FAST | 300 Hz-300 kHz |
|                   | 4.5 <sup>10</sup> | 65 (65)    | FAST | 300 Hz-300 kHz |

## AC MEASUREMENT CHARACTERISTICS

### AC Volts

MEASUREMENT METHOD: AC-coupled, True RMS.

INPUT IMPEDANCE: 1MΩ ±2% // by <100pF.

INPUT PROTECTION: 1000Vp or 400VDC, 300Vrms with plug-in modules.

### AC Current

MEASUREMENT METHOD: AC-coupled, True RMS.

SHUNT RESISTANCE: 0.1Ω.

BURDEN VOLTAGE: 1A <0.5Vrms, 3A <1.5Vrms. Add 1.5Vrms when used with plug-in modules.

INPUT PROTECTION: 3A, 250V fuse.

### Frequency and Period<sup>4</sup>

MEASUREMENT METHOD: Reciprocal Counting technique.

GATE TIME: SLOW 1s, MED 100ms, and FAST 10ms.

### AC General

AC CMRR<sup>6</sup>: 70dB.

VOLT HERTZ PRODUCT: ≤8 × 10<sup>7</sup>.

### Multiple Channel Into Memory<sup>10,11</sup>

7710 SCANNING ACV: 180/s.

7710 Scanning ACV with Auto Delay On: 2s/reading.

### AC SYSTEM SPEEDS<sup>7,11</sup>

RANGE CHANGES<sup>12</sup>: 4/s (3/s).

FUNCTION CHANGES<sup>12</sup>: 4/s (3/s).

AUTORANGE TIME: < 3s.

ASCII READINGS TO RS-232 (19.2k baud): 50/s.

MAX. INTERNAL TRIGGER RATE: 300/s.

MAX. EXTERNAL TRIGGER RATE: 250/s.

### AC Notes

- 20% overrange except on 750V and 3A.
- Specifications are for SLOW mode and sine wave inputs >5% of range. SLOW and MED are multi-sample A/D conversions. FAST is DETECTOR BANDWIDTH 300 with nPLC = 1.0.
- Applies to 0°-18°C and 28°-50°C.
- For square wave inputs >10% of ACV range, except 100mV range, 100mV range frequency must be >10Hz if input is <20mV.
- Applies to non-sine waves >5Hz and <500Hz. (Guaranteed by design for Crest Factors >4.3)
- For 1kΩ imbalance in LO lead.
- Speeds are for 60Hz (50Hz) operation using factory defaults operating conditions (\*RST). Autorange off, Display off, Limits off, Trigger delay=0. Includes measurement and binary data transfer out GPIB (reading element only).
- 0.01% of step settling error. Trigger delay = 400ms.
- Auto Zero off.
- Sample count = 1000.
- DETECTOR BANDWIDTH 300 with nPLC = 0.01.
- Maximum useful limit with trigger delay = 175ms.

# 2750 Multimeter/Switch System

## GENERAL SPECIFICATIONS

**EXPANSION SLOTS:** 5.  
**POWER SUPPLY:** 100V / 120V / 220V / 240V  $\pm$ 10%.  
**LINE FREQUENCY:** 45Hz to 66Hz and 360Hz to 440Hz, automatically sensed at power-up.  
**POWER CONSUMPTION:** 80VA.  
**OPERATING ENVIRONMENT:** Specified for 0°C to 50°C. Specified to 80% RH at 35°C.  
**STORAGE ENVIRONMENT:** -40°C to 70°C.  
**BATTERY:** Lithium battery-backed memory, 3 years @ 23°C.  
**WARRANTY:** 3 years.  
**EMC:** Conforms to European Union Directive 89/336/EEC EN61326-1.  
**SAFETY:** Conforms to European Union Directive 73/23/EEC EN61010-1, CAT I.  
**VIBRATION:** MIL-PRF-28800F Class 3, Random.  
**WARM-UP:** 2 hours to rated accuracy.  
**DIMENSIONS:**  
**Rack Mounting:** 89mm high  $\times$  485mm wide  $\times$  370mm deep (3.5 in.  $\times$  19 in.  $\times$  14.563 in.).  
**Bench Configuration (with handle and feet):** 104mm high  $\times$  485mm wide  $\times$  370mm deep (4.125 in.  $\times$  19 in.  $\times$  14.563 in.).  
**SHIPPING WEIGHT:** 13kg (28 lbs).  
**DIGITAL I/O:** 2 inputs, 1 for triggering and 1 for hardware interlock. 5 outputs, 4 for Reading Limits and 1 for Master Limit. Outputs are TTL compatible or can sink 250mA, diode clamped to 40V.  
**TRIGGERING AND MEMORY:**  
**Window Filter Sensitivity:** 0.01%, 0.1%, 1%, 10%, or Full-scale of range (none).  
**Reading Hold Sensitivity:** 0.01%, 0.1%, 1%, or 10% of reading.  
**Trigger Delay:** 0 to 99 hrs (1ms step size).  
**External Trigger Delay:**  $<$ 1ms.  
**Memory Size:** 110,000 readings.  
**MATH FUNCTIONS:** Rel, Min/Max/Average/Std Dev/Peak-to-Peak (of stored reading), Limit Test, %, 1/x, and mX + b with user defined units displayed.  
**REMOTE INTERFACE:**  
GPIB (IEEE-488.2) and RS-232C.  
SCPI (Standard Commands for Programmable Instruments)  
**ACCESSORIES SUPPLIED:** Model 1751 Safety Test Leads, Product Information CD-ROM, and hardcopy User's Manual. Software CD-ROM with IVI/VISA drivers for VB, VC/C++, LabVIEW, TestPoint, and LabWindows/CVI, and free runtime startup software.  
**ACCESSORIES AVAILABLE:**  
4288-7 Rack Mount Rear Support Kit  
77XX Modules  
Extended Warranty  
ExcellINX-1A (Excel add-in datalogger software)  
TestPoint™ Software Development Package  
**SOFTWARE:** Windows 98, NT, 2000, ME, and XP compatible.

## **Appendix (C)**

**Half-cell potential, corrosion current density and concrete resistance values of the approached of the bridge at the University of Waterloo**

Half-cell potential (mV) measured versus Cu/CuSO<sub>4</sub> reference electrode.

*March 06, 2005, T=-10°C, RH=72%, cloudy*

|           | <b>1</b>          | <b>4</b> | <b>7</b> | <b>10</b> | <b>13</b> | <b>50</b>         | <b>53</b> | <b>56</b> | <b>59</b> | <b>62</b> |
|-----------|-------------------|----------|----------|-----------|-----------|-------------------|-----------|-----------|-----------|-----------|
| <b>5</b>  | -470              | -480     | -500     | -456      | -405      | -450              | -545      | -634      | -563      | -554      |
| <b>7</b>  | -470              | -540     | -520     | -464      | -395      | -445              | -633      | -546      | -576      | -582      |
| <b>10</b> | -450              | -450     | -486     | -609      | -435      | -534              | -586      | -561      | -546      | -517      |
| <b>13</b> | -470              | -425     | -540     | -411      | -450      | -390              | -406      | -536      | -610      | -572      |
| <b>16</b> | -485              | -505     | -514     | -464      | -420      | -379              | -446      | -623      | -654      | -614      |
| <b>20</b> | -500              | -443     | -512     | -476      | -365      | -316              | -390      | -545      | -596      | -512      |
|           | <b>Approach A</b> |          |          |           |           | <b>Approach B</b> |           |           |           |           |



*May 25, 2005; T=+19°C, RH=58%, sunny*

|           | <b>1</b>          | <b>4</b> | <b>7</b> | <b>10</b> | <b>13</b> | <b>50</b>         | <b>53</b> | <b>56</b> | <b>59</b> | <b>62</b> |
|-----------|-------------------|----------|----------|-----------|-----------|-------------------|-----------|-----------|-----------|-----------|
| <b>5</b>  | -546              | -547     | -553     | -649      | -560      | -640              | -533      | -620      | -533      | -620      |
| <b>7</b>  | -549              | -537     | -555     | -591      | -469      | -614              | -646      | -631      | -646      | -631      |
| <b>10</b> | -552              | -525     | -611     | -640      | -520      | -593              | -612      | -573      | -612      | -573      |
| <b>13</b> | -561              | -531     | -636     | -587      | -568      | -563              | -600      | -560      | -600      | -560      |
| <b>16</b> | -567              | -557     | -565     | -530      | -497      | -599              | -596      | -600      | -596      | -600      |
| <b>20</b> | -562              | -557     | -570     | -538      | -495      | -546              | -591      | -553      | -591      | -553      |
|           | <b>Approach A</b> |          |          |           |           | <b>Approach B</b> |           |           |           |           |



*August 22, 2005; T=+16°C, RH=91%, sunny*

|           | <b>1</b>          | <b>4</b> | <b>7</b> | <b>10</b> | <b>13</b> | <b>50</b>         | <b>53</b> | <b>56</b> | <b>59</b> | <b>62</b> |
|-----------|-------------------|----------|----------|-----------|-----------|-------------------|-----------|-----------|-----------|-----------|
| <b>5</b>  | -517              | -567     | -515     | -604      | -519      | -509              | -591      | -625      | -562      | -607      |
| <b>7</b>  | -528              | -568     | -636     | -555      | -555      | -498              | -563      | -585      | -610      | -589      |
| <b>10</b> | -560              | -470     | -554     | -584      | -529      | -544              | -574      | -560      | -584      | -531      |
| <b>13</b> | -534              | -515     | -513     | -608      | -485      | -482              | -465      | -557      | -561      | -564      |
| <b>16</b> | -544              | -565     | -538     | -514      | -493      | -527              | -503      | -656      | -521      | -655      |
| <b>20</b> | -566              | -582     | -507     | -506      | -533      | -431              | -490      | -589      | -624      | -575      |
|           | <b>Approach A</b> |          |          |           |           | <b>Approach B</b> |           |           |           |           |



*April 11, 2006; T=+17°C, RH=40%, sunny*

|           | <b>1</b>          | <b>4</b> | <b>7</b> | <b>10</b> | <b>13</b> | <b>50</b>         | <b>53</b> | <b>56</b> | <b>59</b> | <b>62</b> |
|-----------|-------------------|----------|----------|-----------|-----------|-------------------|-----------|-----------|-----------|-----------|
| <b>5</b>  | -545              | -556     | -568     | -657      | -565      | -644              | -606      | -600      | -599      | -560      |
| <b>7</b>  | -554              | -578     | -631     | -610      | -467      | -658              | -613      | -598      | -605      | -555      |
| <b>10</b> | -538              | -497     | -545     | -648      | -426      | -585              | -587      | -578      | -599      | -580      |
| <b>13</b> | -518              | -500     | -579     | -632      | -496      | -583              | -557      | -576      | -580      | -600      |
| <b>16</b> | -532              | -542     | -542     | -513      | -500      | -621              | -592      | -613      | -574      | -577      |
| <b>20</b> | -554              | -515     | -550     | -536      | -469      | -601              | -658      | -578      | -589      | -592      |
|           | <b>Approach A</b> |          |          |           |           | <b>Approach B</b> |           |           |           |           |



*May 17, 2006; T=+14°C, RH=92%, sunny*

|           | <b>1</b>          | <b>4</b> | <b>7</b> | <b>10</b> | <b>13</b> | <b>50</b>         | <b>53</b> | <b>56</b> | <b>59</b> | <b>62</b> |
|-----------|-------------------|----------|----------|-----------|-----------|-------------------|-----------|-----------|-----------|-----------|
| <b>5</b>  | -572              | -596     | -568     | -591      | -514      | -503              | -555      | -609      | -654      | -628      |
| <b>7</b>  | -560              | -531     | -538     | -564      | -467      | -547              | -534      | -612      | -635      | -607      |
| <b>10</b> | -550              | -540     | -564     | -630      | -495      | -592              | -568      | -587      | -574      | -544      |
| <b>13</b> | -546              | -530     | -632     | -647      | -556      | -503              | -529      | -505      | -626      | -605      |
| <b>16</b> | -557              | -527     | -545     | -520      | -497      | -464              | -523      | -586      | -638      | -631      |
| <b>20</b> | -574              | -528     | -552     | -553      | -449      | -431              | -493      | -545      | -678      | -610      |
|           | <b>Approach A</b> |          |          |           |           | <b>Approach B</b> |           |           |           |           |



*August 22, 2006; T=+19°C, RH=90%, sunny*

|           | <b>1</b>          | <b>4</b> | <b>7</b> | <b>10</b> | <b>13</b> | <b>50</b>         | <b>53</b> | <b>56</b> | <b>59</b> | <b>62</b> |
|-----------|-------------------|----------|----------|-----------|-----------|-------------------|-----------|-----------|-----------|-----------|
| <b>5</b>  | -520              | -530     | -515     | -555      | -500      | -500              | -500      | -565      | -579      | -555      |
| <b>7</b>  | -525              | -525     | -515     | -525      | -450      | -515              | -530      | -545      | -630      | -560      |
| <b>10</b> | -525              | -455     | -550     | -585      | -480      | -565              | -550      | -500      | -565      | -535      |
| <b>13</b> | -535              | -470     | -620     | -600      | -545      | -440              | -450      | -590      | -575      | -560      |
| <b>16</b> | -510              | -540     | -530     | -490      | -460      | -440              | -480      | -575      | -595      | -620      |
| <b>20</b> | -520              | -560     | -540     | -540      | -440      | -440              | -540      | -530      | -643      | -550      |
|           | <b>Approach A</b> |          |          |           |           | <b>Approach B</b> |           |           |           |           |



Corrosion current density ( $\mu\text{A}/\text{cm}^2$ ) and concrete resistance ( $\text{k}\Omega$ ), measured by GalvaPulse™

*August 22, 2005; T=+16°C, RH=91%, sunny*

|  | <b>50</b> | <b>53</b> | <b>56</b> | <b>59</b> | <b>62</b> | <b>50</b>                              | <b>53</b> | <b>56</b> | <b>59</b> | <b>62</b> |
|--|-----------|-----------|-----------|-----------|-----------|--|-----------|-----------|-----------|-----------|
| <b>5</b>                                     | 2.28      | 0.98      | 3.1       | 2.6       | 2.4       | 2.6                                    | 2.2       | 1.8       | 1.7       | 2.2       |
| <b>7</b>                                     | 1.54      | 1.48      | 2.6       | 2         | 4         | 3                                      | 2.2       | 1.7       | 2.5       | 2.3       |
| <b>10</b>                                    | 1.58      | 2.6       | 5.9       | 1.7       | 1.35      | 1.5                                    | 2.2       | 1.8       | 2.6       | 3         |
| <b>13</b>                                    | 1.56      | 1.4       | 1.89      | 1.96      | 1.05      | 2.3                                    | 3.3       | 2.2       | 2.3       | 2.8       |
| <b>16</b>                                    | 2.31      | 3.3       | 1.68      | 3.3       | 0.98      | 1.6                                    | 2.1       | 2.3       | 2.1       | 3.8       |
| <b>20</b>                                    | 1.02      | 1         | 1.56      | 3.4       | 2.5       | 2.3                                    | 3         | 2.1       | 2.3       | 3.41      |
| <b>Approach B, Corrosion current density</b> |           |           |           |           |           | <b>Approach B, Concrete resistance</b> |           |           |           |           |

↑  
N

*April 11, 2006; T=+17°C, RH=40%, sunny*

|  | <b>1</b> | <b>4</b> | <b>7</b> | <b>10</b> | <b>13</b> | <b>50</b>                              | <b>53</b> | <b>56</b> | <b>59</b> | <b>62</b> |
|--|----------|----------|----------|-----------|-----------|--|-----------|-----------|-----------|-----------|
| <b>5</b>                                     | 7        | 6.8      | 10.9     | 15.99     | 12        | 2                                      | 1.5       | 1.2       | 1.2       | 1.5       |
| <b>7</b>                                     | 9.3      | 11.4     | 8.44     | 13.77     | 14        | 1.5                                    | 1.2       | 1.1       | 1.3       | 2         |
| <b>10</b>                                    | 12.5     | 12       | 7.7      | 4.6       | 6         | 1.4                                    | 0.9       | 1.5       | 2.1       | 2         |
| <b>13</b>                                    | 9.25     | 9.6      | 12.3     | 4         | 3.5       | 1.8                                    | 1.1       | 1.1       | 1.7       | 1.5       |
| <b>16</b>                                    | 10.8     | 11.6     | 12.5     | 7         | 8         | 1.3                                    | 1         | 1.1       | 1.2       | 1.4       |
| <b>20</b>                                    | 5        | 4.68     | 8.4      | 15        | 10        | 1.8                                    | 1.6       | 1.2       | 1.1       | 1         |
| <b>Approach B, Corrosion current density</b> |          |          |          |           |           | <b>Approach B, Concrete resistance</b> |           |           |           |           |

↑  
N

*August 22, 2006; T=+19°C, RH=90%, sunny*

|  | <b>1</b> | <b>4</b> | <b>7</b> | <b>10</b> | <b>13</b> | <b>50</b>                              | <b>53</b> | <b>56</b> | <b>59</b> | <b>62</b> |
|--|----------|----------|----------|-----------|-----------|--|-----------|-----------|-----------|-----------|
| <b>5</b>                                     | 4.8      | 1.9      | 2.3      | 11.5      | 5.3       | 2.2                                    | 1.5       | 1.8       | 0.9       | 0.7       |
| <b>7</b>                                     | 4        | 8.4      | 3.5      | 5.4       | 4.4       | 2                                      | 1.6       | 1.1       | 0.9       | 1.1       |
| <b>10</b>                                    | 4        | 3.6      | 3.4      | 7.9       | 2.45      | 1.1                                    | 1.4       | 1         | 1.1       | 1.3       |
| <b>13</b>                                    | 1.84     | 3.3      | 8.6      | 11        | 5.6       | 1.8                                    | 1.3       | 0.9       | 1.3       | 1.2       |
| <b>16</b>                                    | 3.1      | 5        | 4        | 13.5      | 3.6       | 1.5                                    | 1.3       | 0.9       | 1.1       | 1.1       |
| <b>20</b>                                    | 3.9      | 4.9      | 5.8      | 5.1       | 2.2       | 2                                      | 1.5       | 1.8       | 0.9       | 1.9       |
| <b>Approach B, Corrosion current density</b> |          |          |          |           |           | <b>Approach B, Concrete resistance</b> |           |           |           |           |

↑  
N

## **Appendix (D)**

**Calculations of the corrosion current density, using the results from potentiostatic LPR test, and the data obtained for the beams with segmented steel bars and the specimens with different variables**



Figures D.1 and D.2 show the measured current curves for segments A4 and A2, after performing potentiostatic LPR test by applying  $\pm 20$  mV around their  $E_{\text{corr}}$ , respectively.

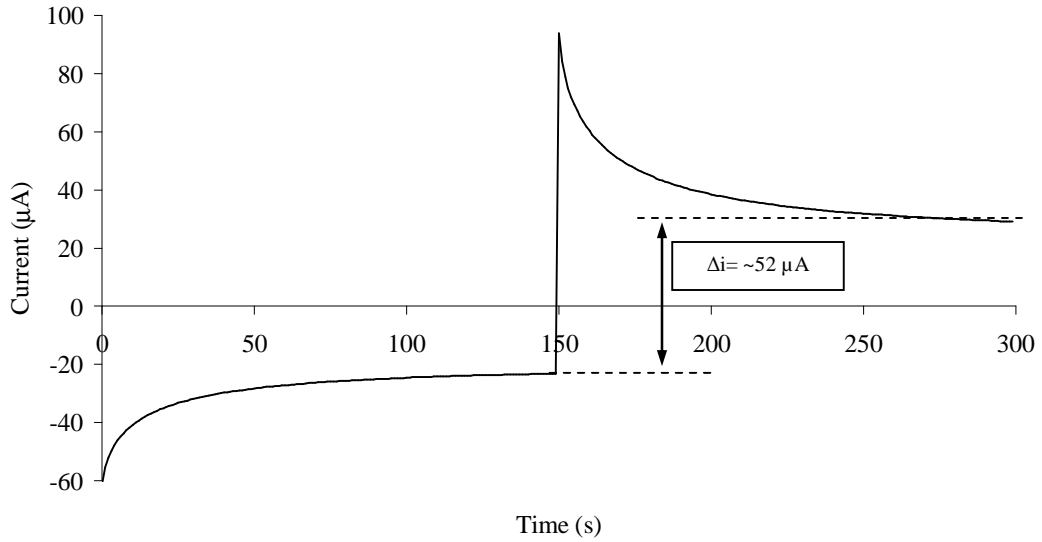


Figure D. 1. Resultant current curve after performing potentiostatic LPR test on segment A4 (active corrosion); 120 weeks after casting.

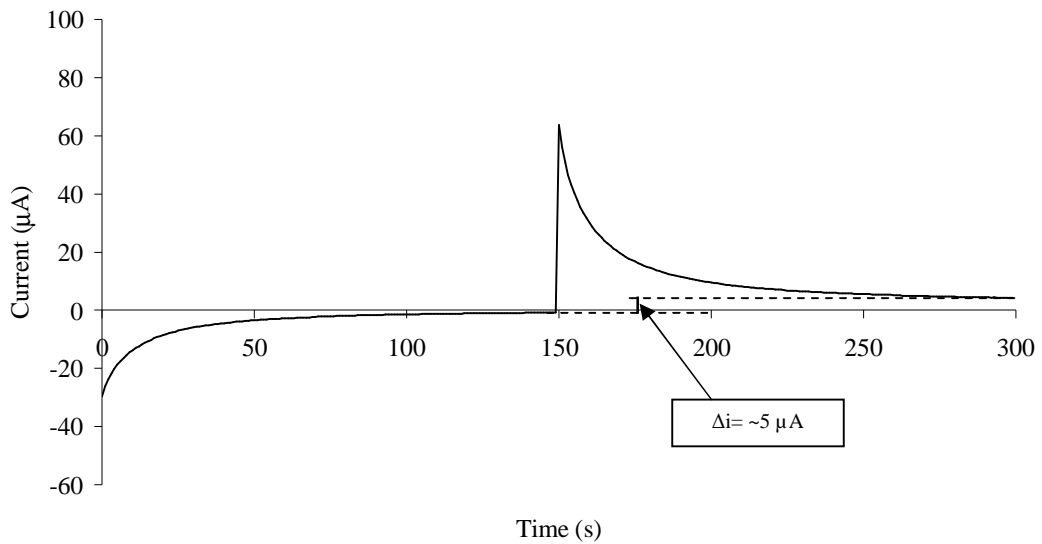


Figure D. 2. Resultant current curve after performing potentiostatic LPR test on segment A4 (passive corrosion); 120 weeks after casting.

The calculations for determining the corrosion current density for these segments are as follows and show the typical calculations that have been used to calculate the corrosion current density in all the potentiostatic LPR measurements.

Segment A4:

$$R_p = \Delta V / \Delta i = 0.04 \text{ V} / 0.000052 \text{ A} = \sim 765.6 \Omega$$

$$\text{Corrosion current} = I = B / R_p = 0.026 / 765.6 = \sim 0.0000034 \text{ A} = 34 \mu\text{A}$$

$$\text{Corrosion current density } i_{\text{corr}} = I / \text{area} = 34 \mu\text{A} / 21.98 \text{ cm}^2 = 1.54 \mu\text{A/cm}^2$$

Segment A2:

$$R_p = \Delta V / \Delta i = 0.04 \text{ V} / 0.000005 \text{ A} = \sim 7871 \Omega$$

$$\text{Corrosion current} = I = B / R_p = 0.052 / 7871 = \sim 0.0000066 \text{ A} = 6.6 \mu\text{A}$$

$$\text{Corrosion current density } i_{\text{corr}} = I / \text{area} = 6.6 \mu\text{A} / 21.98 \text{ cm}^2 = 0.3 \mu\text{A/cm}^2$$

The corrosion current density values for the beams with segmented steel bars and the specimens with different variables are shown in Tables D.1 to D.4.

Table D. 1. Corrosion current density values of steel segments in beams A and B.

| Weeks after casting | Corrosion current density ( $\mu\text{A}/\text{cm}^2$ ) |      |      |      |      |      |      |      |
|---------------------|---|------|------|------|------|------|------|------|
|                     | A1  | A2   | A3   | A4   | B1   | B2   | B3   | B4   |
| 4                   | 1.43  | 0.20 | 1.70 | 1.55 | 0.17 | 1.49 | 1.50 | 1.54 |
| 5                   | 1.20  | 0.24 | 1.78 | 1.50 | 0.15 | 0.86 | 1.50 | 1.81 |
| 6                   | 1.79  | 0.32 | 1.89 | 1.40 | 0.15 | 0.90 | 1.60 | 2.04 |
| 7                   | 1.89  | 0.23 | 1.78 | 1.49 | 0.14 | 0.79 | 1.39 | 1.63 |
| 8                   | 1.50  | 0.20 | 1.70 | 1.50 | 0.12 | 0.75 | 1.50 | 1.70 |
| 9                   | 1.60  | 0.19 | 1.71 | 1.40 | 0.11 | 0.75 | 1.68 | 2.18 |
| 11                  | 1.64  | 0.14 | 1.60 | 1.65 | 0.08 | 0.73 | 2.03 | 1.84 |
| 13                  | 1.74  | 0.14 | 1.61 | 1.30 | 0.12 | 0.80 | 2.00 | 2.10 |
| 15                  | 1.00  | 0.14 | 1.44 | 1.50 | 0.09 | 0.73 | 1.84 | 2.28 |
| 17                  | 0.95  | 0.16 | 1.46 | 1.60 | 0.26 | 0.83 | 1.86 | 2.39 |
| 19                  | 0.86  | 0.07 | 1.67 | 1.63 | 1.63 | 0.54 | 1.59 | 2.08 |
| 23                  | 1.38  | 0.05 | 0.68 | 1.63 | 1.60 | 0.39 | 1.57 | 1.97 |
| 26                  | 1.20  | 0.04 | 1.00 | 1.81 | 1.25 | 0.43 | 1.35 | 1.56 |
| 31                  | 0.57  | 0.03 | 1.56 | 1.80 | 1.80 | 0.38 | 0.78 | 0.97 |
| 37                  | 0.60  | 0.03 | 0.11 | 1.70 | 0.88 | 0.12 | 1.51 | 0.84 |
| 41                  | 0.80  | 0.05 | 0.11 | 1.43 | 1.15 | 0.85 | 1.45 | 1.37 |
| 46                  | 0.98  | 0.04 | 0.08 | 1.39 | 0.72 | 0.74 | 0.92 | 0.96 |
| 52                  | 0.70  | 0.11 | 0.11 | 1.34 | 0.91 | 0.37 | 0.90 | 0.97 |
| 54                  | 0.61  | 0.04 | 0.08 | 1.32 | 0.86 | 0.42 | 1.13 | 0.96 |
| 60                  | 0.47  | 0.04 | 0.06 | 1.29 | 0.76 | 0.28 | 1.45 | 0.88 |
| 61                  | 0.42  | 0.07 | 0.05 | 1.21 | 0.71 | 0.28 | 1.44 | 0.97 |
| 63                  | 0.58  | 0.04 | 0.04 | 1.08 | 0.94 | 0.29 | 1.16 | 1.10 |
| 66                  | 0.72  | 0.03 | 0.04 | 1.12 | 0.71 | 0.24 | 1.30 | 0.86 |
| 69                  | 0.58  | 0.04 | 0.04 | 1.08 | 0.94 | 0.29 | 1.16 | 1.10 |
| 77                  | 0.60  | 0.04 | 0.04 | 1.27 | 0.70 | 0.29 | 1.54 | 1.39 |
| 80                  | 0.56  | 0.06 | 0.04 | 1.24 | 0.67 | 0.23 | 1.48 | 1.72 |
| 84                  | 0.59  | 0.04 | 0.04 | 1.15 | 0.73 | 0.19 | 1.52 | 1.74 |
| 87                  | 0.60  | 0.05 | 0.04 | 1.40 | 0.56 | 0.19 | 1.38 | 1.95 |
| 90                  | 0.55  | 0.05 | 0.04 | 1.28 | 0.90 | 0.22 | 1.57 | 1.76 |
| 93                  | 0.50  | 0.04 | 0.04 | 1.52 | 0.80 | 0.16 | 1.52 | 1.48 |
| 99                  | 0.48  | 0.04 | 0.04 | 1.33 | 0.70 | 0.16 | 1.58 | 1.24 |
| 104                 | 0.40  | 0.04 | 0.03 | 1.26 | 0.80 | 0.15 | 1.55 | 1.06 |
| 108                 | 0.32  | 0.03 | 0.03 | 1.32 | 0.85 | 0.07 | 1.53 | 1.06 |
| 116                 | 0.31  | 0.04 | 0.04 | 1.42 | 0.64 | 0.07 | 1.29 | 1.06 |
| 120                 | 0.34  | 0.02 | 0.04 | 1.54 | 0.49 | 0.06 | 1.41 | 1.04 |

Table D. 2. Corrosion current density values of steel segments in beams C and D.

| Weeks<br>after<br>casting | Corrosion current density ( $\mu\text{A}/\text{cm}^2$ ) |      |      |      |      |      |      |      |
|---------------------------|---|------|------|------|------|------|------|------|
|                           | C1  | C2   | C3   | C4   | D1   | D2   | D3   | D4   |
| 4                         | 0.88  | 0.53 | 0.84 | 0.63 | 0.22 | 0.81 | 0.43 | 0.62 |
| 5                         | 0.58  | 0.70 | 0.78 | 0.82 | 0.96 | 0.07 | 0.59 | 0.13 |
| 6                         | 1.00  | 0.27 | 0.78 | 0.78 | 0.63 | 0.49 | 0.44 | 0.27 |
| 7                         | 0.88  | 0.15 | 0.50 | 0.82 | 0.73 | 0.89 | 0.94 | 0.26 |
| 8                         | 0.69  | 0.12 | 0.45 | 0.96 | 0.62 | 0.22 | 0.81 | 0.19 |
| 9                         | 0.84  | 0.69 | 0.58 | 0.54 | 0.20 | 0.42 | 0.81 | 0.11 |
| 11                        | 0.16  | 0.20 | 0.33 | 1.28 | 0.42 | 0.94 | 0.23 | 0.03 |
| 13                        | 0.40  | 0.21 | 0.28 | 1.28 | 0.99 | 0.40 | 0.04 | 0.06 |
| 15                        | 0.16  | 0.20 | 0.29 | 1.29 | 0.38 | 0.76 | 0.03 | 0.02 |
| 17                        | 0.19  | 0.21 | 0.12 | 1.16 | 0.45 | 0.70 | 0.03 | 0.02 |
| 19                        | 0.06  | 0.07 | 0.23 | 1.04 | 0.15 | 0.13 | 0.18 | 0.01 |
| 23                        | 0.10  | 0.07 | 0.37 | 0.97 | 0.11 | 0.28 | 0.02 | 0.01 |
| 26                        | 0.21  | 0.14 | 2.82 | 0.94 | 0.23 | 0.23 | 0.02 | 0.94 |
| 31                        | 0.16  | 0.04 | 1.80 | 0.45 | 0.24 | 0.23 | 0.01 | 0.64 |
| 37                        | 0.11  | 0.03 | 1.77 | 0.67 | 0.14 | 0.14 | 0.01 | 0.97 |
| 41                        | 0.15  | 0.06 | 2.34 | 0.82 | 0.17 | 0.18 | 0.01 | 1.23 |
| 46                        | 0.09  | 0.05 | 0.91 | 0.82 | 0.14 | 0.14 | 0.01 | 0.96 |
| 52                        | 0.11  | 0.17 | 1.45 | 0.54 | 0.23 | 0.39 | 0.01 | 0.01 |
| 54                        | 0.11  | 0.11 | 1.70 | 1.28 | 0.08 | 0.06 | 1.54 | 0.56 |
| 60                        | 0.10  | 0.10 | 2.12 | 1.34 | 0.05 | 0.05 | 1.03 | 0.51 |
| 61                        | 0.09  | 0.09 | 2.20 | 1.37 | 0.06 | 0.05 | 0.07 | 0.60 |
| 63                        | 0.12  | 0.13 | 1.99 | 1.22 |      |      |      |      |
| 66                        | 0.09  | 0.09 | 1.93 | 1.21 |      |      |      |      |
| 69                        | 0.12  | 0.13 | 1.99 | 1.22 |      |      |      |      |
| 77                        | 0.06  | 0.05 | 0.01 | 1.10 |      |      |      |      |
| 80                        | 0.06  | 0.05 | 0.00 | 1.02 |      |      |      |      |
| 84                        | 0.13  | 0.05 | 0.00 | 1.00 |      |      |      |      |
| 87                        | 0.13  | 0.05 | 0.00 | 1.00 |      |      |      |      |

Table D. 3. Corrosion current density values of steel segments in beam C.

| Weeks<br>after<br>casting | Corrosion current density<br>( $\mu\text{A}/\text{cm}^2$ ) |      |      |      |
|---------------------------|--|------|------|------|
|                           | E1   | E2   | E3   | E4   |
| 4                         | 0.37   | 0.81 | 2.15 | 2.81 |
| 5                         | 0.78   | 0.24 | 2.46 | 2.66 |
| 6                         | 0.77   | 0.68 | 2.42 | 2.50 |
| 7                         | 0.91   | 0.43 | 2.08 | 2.12 |
| 8                         | 0.32   | 0.81 | 2.94 | 2.03 |
| 9                         | 0.95   | 0.40 | 2.28 | 2.99 |
| 11                        | 0.86   | 0.41 | 2.73 | 1.54 |
| 13                        | 0.54   | 0.70 | 2.60 | 1.98 |
| 15                        | 0.92   | 0.27 | 2.64 | 1.71 |
| 17                        | 0.22   | 0.43 | 2.64 | 1.97 |
| 19                        | 0.12   | 0.13 | 2.21 | 1.47 |
| 23                        | 0.45   | 0.25 | 2.59 | 1.55 |
| 26                        | 0.46   | 0.49 | 2.44 | 1.49 |
| 31                        | 0.40   | 0.50 | 1.97 | 1.16 |
| 37                        | 0.16   | 0.17 | 1.62 | 0.90 |
| 41                        | 0.13   | 0.13 | 1.89 | 1.30 |
| 46                        | 0.11   | 0.10 | 1.75 | 1.13 |
| 52                        | 0.24   | 0.23 | 1.75 | 1.25 |
| 54                        | 0.21   | 0.15 | 2.02 | 1.24 |
| 60                        | 0.13   | 0.13 | 1.97 | 1.21 |
| 61                        | 0.80   | 0.16 | 1.94 | 1.12 |
| 63                        | 0.09   | 0.09 | 2.02 | 1.27 |
| 66                        | 0.09   | 0.10 | 2.04 | 1.25 |
| 69                        | 0.13   | 0.15 | 1.95 | 1.18 |
| 77                        | 0.30   | 0.11 | 2.10 | 0.72 |
| 80                        | 0.64   | 0.27 | 1.92 | 1.15 |

Table D. 4. Corrosion current density values of the specimens with different variables.

| Weeks after casting | 4    | 10   | 16   | 24   | 26   | 27   | 30   | 33   | 36   | 40   | 48   | 51   | 54   | 57   | 63   | 68   | 72   | 80   | 85   |
|---------------------|------|------|------|------|------|------|------|------|------|------|------|------|------|------|------|------|------|------|------|
| 30 mm, S1           | 0.25 | 0.20 | 0.29 | 0.24 | 0.25 | 0.27 | 0.22 | 0.24 | 0.51 | 0.48 | 1.28 | 0.93 | 0.52 | 1.21 | 0.98 | 1.09 | 0.53 | 0.51 | 0.52 |
| 30 mm, S2           | 0.03 | 0.03 | 0.03 | 0.02 | 0.03 | 0.03 | 0.03 | 0.03 | 0.12 | 0.10 | 0.18 | 1.00 | 0.97 | 0.42 | 0.38 | 0.46 | 2.03 | 0.37 | 2.10 |
| 30 mm, S3           | 0.14 | 0.13 | 0.11 | 0.12 | 0.14 | 0.13 | 0.12 | 0.17 | 0.41 | 0.40 | 0.64 | 1.44 | 1.24 | 1.06 | 0.97 | 1.50 | 3.11 | 1.56 | 1.50 |
| 30 mm, S4           | 0.09 | 0.06 | 0.08 | 0.07 | 0.08 | 0.07 | 0.08 | 0.08 | 0.48 | 0.38 | 0.30 | 0.87 | 0.23 | 0.47 | 0.63 | 0.44 | 1.76 | 0.45 | 0.90 |
| 30 mm, S5           | 0.09 | 0.10 | 0.10 | 0.10 | 0.10 | 0.10 | 0.11 | 0.11 | 0.10 | 0.10 | 0.36 | 1.00 | 0.97 | 0.63 | 0.41 | 0.40 | 2.58 |      |      |
| 50 mm, S1           | 0.04 | 0.03 | 0.03 | 0.02 | 0.02 | 0.04 | 0.04 | 0.04 | 0.02 | 0.02 | 0.05 | 0.61 | 0.61 | 0.19 | 0.20 | 0.11 | 1.36 |      |      |
| 50 mm, S2           | 0.03 | 0.03 | 0.03 | 0.03 | 0.03 | 0.02 | 0.03 | 0.03 | 0.03 | 0.03 | 0.02 | 0.38 | 0.41 | 0.17 | 0.23 | 0.07 | 1.05 | 0.06 | 0.12 |
| 50 mm, S3           | 0.05 | 0.05 | 0.04 | 0.04 | 0.04 | 0.04 | 0.04 | 0.04 | 0.03 | 0.03 | 0.03 | 0.46 | 0.47 | 0.13 | 0.21 | 0.08 | 1.19 | 0.06 | 0.61 |
| 50 mm, S4           | 0.05 | 0.06 | 0.06 | 0.02 | 0.07 | 0.06 | 0.02 | 0.03 | 0.06 | 0.07 | 0.07 | 0.72 | 0.72 | 0.26 | 0.33 | 0.20 | 1.83 | 0.16 | 0.22 |
| 50 mm, S5           | 0.03 | 0.57 | 0.35 | 0.19 | 0.19 | 0.17 | 0.17 | 0.21 | 0.16 | 0.16 | 0.22 | 0.53 | 0.65 | 0.38 | 0.34 | 0.25 | 1.30 | 0.22 | 0.20 |
| 70 mm, S1           | 0.09 | 0.13 | 0.09 | 0.09 | 0.09 | 0.09 | 0.09 | 0.09 | 0.07 | 0.07 | 0.06 | 0.62 | 0.62 | 0.34 | 0.50 | 0.36 | 0.24 | 0.00 | 0.54 |
| 70 mm, S2           | 0.02 | 0.03 | 0.03 | 0.03 | 0.03 | 0.03 | 0.03 | 0.03 | 0.06 | 0.08 | 0.16 | 0.50 | 0.52 | 0.33 | 0.16 | 0.40 | 1.29 | 0.36 | 0.31 |
| 70 mm, S3           | 0.03 | 0.08 | 0.05 | 0.04 | 0.04 | 0.04 | 0.04 | 0.04 | 0.04 | 0.03 | 0.03 | 0.45 | 0.46 | 0.25 | 0.28 | 0.14 | 1.15 | 0.12 | 0.11 |
| 70 mm, S4           | 0.13 | 0.10 | 0.13 | 0.11 | 0.12 | 0.11 | 0.12 | 0.12 | 0.09 | 0.08 | 0.07 | 0.47 | 0.48 | 0.25 | 0.33 | 0.24 | 1.26 | 0.22 | 0.21 |
| 70 mm, S5           | 0.02 | 0.03 | 0.04 | 0.02 | 0.02 | 0.02 | 0.03 | 0.02 | 0.03 | 0.06 | 0.10 | 0.51 | 0.49 | 0.17 | 0.10 | 0.24 | 1.16 |      |      |
| Carbonated, S1      | 0.69 | 2.48 | 2.07 | 1.54 | 2.19 | 2.13 | 0.52 | 0.48 | 0.59 | 0.64 | 0.79 | 0.97 | 1.11 | 0.84 | 0.51 | 0.57 | 2.58 | 1.03 | 0.74 |
| Carbonated, S2      | 0.53 | 1.83 | 1.89 | 1.10 | 1.07 | 0.94 | 0.52 | 0.49 | 0.64 | 0.67 | 0.78 | 1.16 | 1.42 | 0.83 | 0.57 | 1.61 | 2.79 |      |      |
| Carbonated, S3      | 0.71 | 1.28 | 1.01 | 0.88 | 0.86 | 0.74 | 0.10 | 0.11 | 0.16 | 0.17 | 0.27 | 0.80 | 0.96 | 0.46 | 0.15 | 0.51 | 1.87 | 0.46 | 0.33 |
| Carbonated, S4      | 0.03 | 0.47 | 0.53 | 0.47 | 0.48 | 0.41 | 0.18 | 0.18 | 0.18 | 0.19 | 0.30 | 0.70 | 0.71 | 0.44 | 0.24 | 0.61 | 1.57 | 0.54 | 0.44 |
| Carbonated, S5      | 0.06 | 0.05 | 0.06 | 0.24 | 0.31 | 0.33 | 0.08 | 0.07 | 0.11 | 0.12 | 0.22 | 0.68 | 0.96 | 0.78 | 0.44 | 0.41 | 1.73 | 0.38 | 0.49 |
| Cracked (T), S1     | 0.06 | 0.06 | 0.06 | 0.39 | 0.42 | 0.45 | 0.45 | 0.43 | 0.63 | 0.59 | 0.85 | 0.92 | 0.65 | 0.73 | 0.68 | 2.23 | 2.77 | 2.12 | 1.75 |
| Cracked (T), S2     | 0.76 |      | 0.85 | 0.47 | 0.57 | 0.51 | 0.32 | 0.30 | 0.65 | 0.63 | 0.87 | 0.66 | 0.72 | 0.65 | 0.63 | 1.14 | 2.26 | 2.26 | 2.01 |
| Cracked (T), S3     | 0.62 | 0.90 | 0.80 | 0.50 | 0.58 | 0.54 | 0.46 | 0.49 | 0.62 | 0.62 | 0.71 | 0.75 | 1.66 | 0.59 | 0.56 | 1.73 | 3.92 | 1.72 | 1.89 |
| Cracked (L), S1     | 0.24 | 0.27 | 0.18 | 0.10 | 0.11 | 0.10 | 0.25 | 1.31 | 2.41 | 2.61 | 2.44 | 0.56 | 1.74 | 1.82 | 1.71 | 6.49 | 6.37 | 3.01 | 5.01 |
| Cracked (L), S2     | 0.14 | 0.14 | 0.21 | 0.21 | 0.27 | 0.18 | 1.00 | 0.92 | 1.65 | 1.81 | 2.52 | 2.43 | 1.63 | 2.03 | 1.48 | 6.67 | 6.85 | 5.10 | 5.46 |
| Cracked (L), S3     | 0.06 | 0.33 | 0.21 | 0.07 | 0.07 | 0.06 | 0.83 | 0.76 | 2.28 | 2.44 | 2.67 | 1.03 | 0.84 | 2.56 | 2.06 | 6.98 | 5.87 | 6.03 | 6.01 |
| Mn/MnO2, S1         | 0.05 | 0.05 | 0.06 | 0.05 | 0.05 | 0.05 | 0.04 | 0.04 | 0.05 | 0.05 | 0.04 | 0.39 | 0.40 | 0.32 | 0.04 | 0.10 | 1.03 | 0.10 | 0.10 |
| Mn/MnO2, S2         | 0.02 | 0.03 | 0.02 | 0.04 | 0.02 | 0.01 | 0.01 | 0.02 | 0.03 | 0.02 | 0.02 | 0.25 | 0.30 | 0.12 | 0.19 | 0.28 | 0.84 | 0.54 | 0.05 |
| Mn/MnO2, S3         | 0.11 | 0.12 | 0.11 | 0.11 | 0.11 | 0.11 | 0.11 | 0.11 | 0.10 | 0.09 | 0.06 | 0.61 | 0.52 | 0.74 | 0.21 | 0.47 | 1.59 | 0.46 | 0.32 |

## **Appendix (E)**

**Mass loss obtained from gravimetry test and calculated from electrochemical measurements**

To calculate the mass loss from electrochemical measurement data, the Faraday's law was used as following and the results are given in Tables E1 to E5:

$$m = \frac{S \times a \times A}{n \times F}$$

where:

- $m$  = mass (g)
- $S$  = area under the curve (time  $\times$  current)(second.m<sup>2</sup>)
- $A$  = surface area of the rebar (m<sup>2</sup>)
- $a$  = atomic weight of iron = 55.84 g
- $n$  = number of electrons = 2
- $F$  = Faraday's number (96485 coulomb/mole)



Table E. 1. Mass loss determined by gravimetry and calculated by using electrochemical data, beam A.

| <b>Mass loss (g)</b>      | <b>A1</b> | <b>A2</b> | <b>A3</b> | <b>A4</b> |
|---------------------------|-----------|-----------|-----------|-----------|
| <b>Potentiostatic LPR</b> | 0.34      | 0.03      | 0.19      | 0.65      |
| <b>GalvaPulse™</b>        | 0.84      | 0.21      | 0.5       | 1.16      |
| <b>Gravimetry</b>         | 0.26      | 0.05      | 0.26      | 0.5       |

Table E. 2. Mass loss determined by gravimetry and calculated by using electrochemical data, beam B.

| <b>Mass loss (g)</b>      | <b>B1</b> | <b>B2</b> | <b>B3</b> | <b>B4</b> |
|---------------------------|-----------|-----------|-----------|-----------|
| <b>Potentiostatic LPR</b> | 0.36      | 0.17      | 0.8       | 0.69      |
| <b>GalvaPulse</b>         | 0.46      | 0.36      | 0.95      | 0.76      |
| <b>Gravimetry</b>         | 0.39      | 0.1       | 0.85      | 0.71      |

Table E. 3. Mass loss determined by gravimetry and calculated by using electrochemical data, beam C.

| <b>Mass loss (g)</b>      | <b>C1</b> | <b>C2</b> | <b>C3</b> | <b>C4</b> |
|---------------------------|-----------|-----------|-----------|-----------|
| <b>Potentiostatic LPR</b> | 0.07      | 0.04      | 0.37      | 0.42      |
| <b>GalvaPulse</b>         | 0.2       | 0.18      | 0.95      | 0.54      |
| <b>Gravimetry</b>         | 0.05      | 0.08      | 0.46      | 0.5       |

Table E. 4. Mass loss determined by gravimetry and calculated by using electrochemical data, beam D.

| <b>Mass loss (g)</b>      | <b>D1</b> | <b>D2</b> | <b>D3</b> | <b>D4</b> |
|---------------------------|-----------|-----------|-----------|-----------|
| <b>Potentiostatic LPR</b> | 0.06      | 0.08      | 0.06      | 0.11      |
| <b>GalvaPulse</b>         | 0.27      | 0.28      | 0.22      | 0.29      |
| <b>Gravimetry</b>         | 0.04      | 0.09      | 0.45      | 0.44      |

Table E. 5. Mass loss determined by gravimetry and calculated by using electrochemical data, beam E.

| <b>Mass loss (g)</b>      | <b>E1</b> | <b>E2</b> | <b>E3</b> | <b>E4</b> |
|---------------------------|-----------|-----------|-----------|-----------|
| <b>Potentiostatic LPR</b> | 0.09      | 0.06      | 0.57      | 0.5       |
| <b>GalvaPulse</b>         | 0.2       | 0.21      | 1.1       | 0.95      |
| <b>Gravimetry</b>         | 0.1       | 0.04      | 0.7       | 0.64      |

## **Appendix (F)**

**Photograph of the steel segments, after removing from concrete beams**

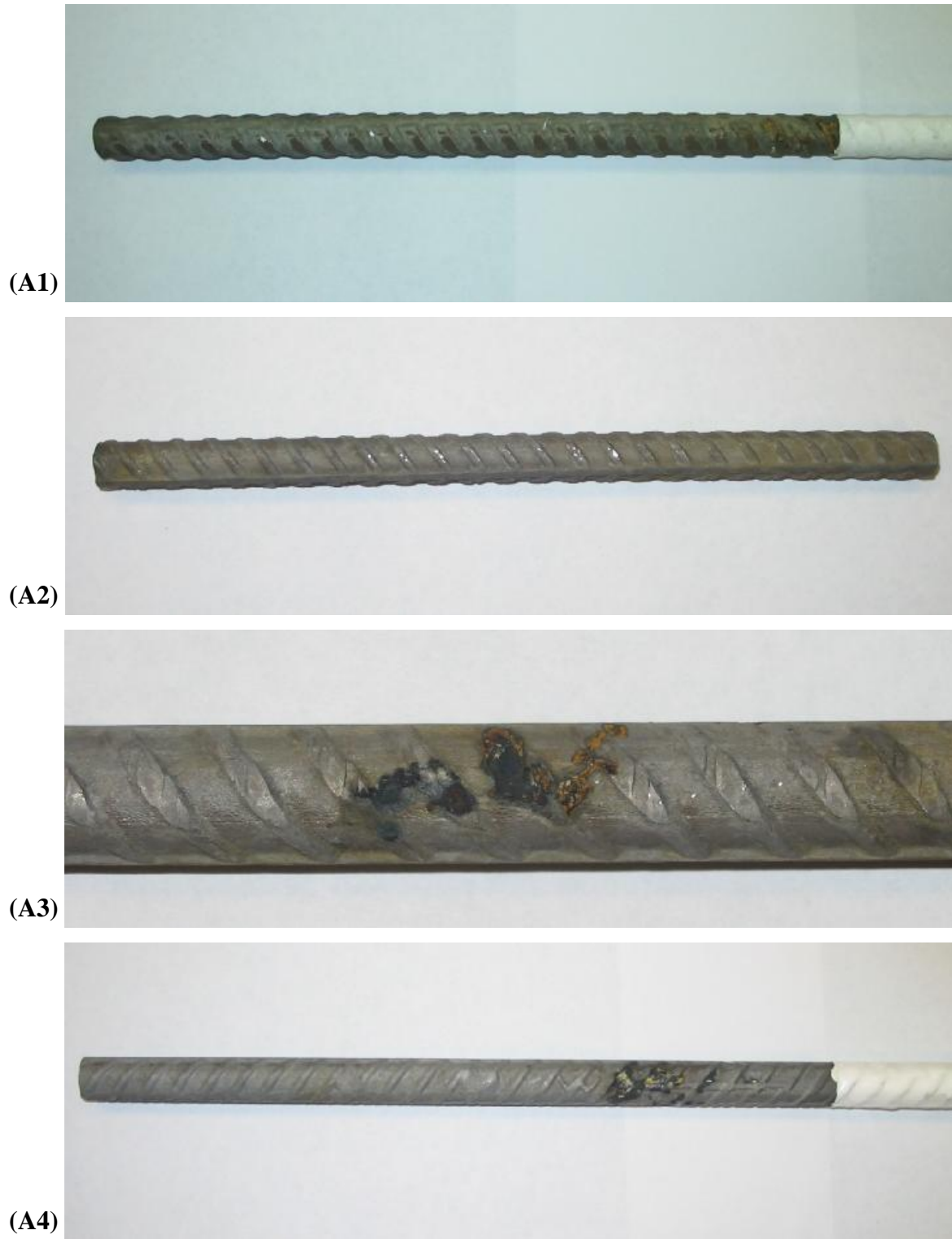


Figure F. 1. Steel segments after cleaning the corrosion products, removed from beam A.

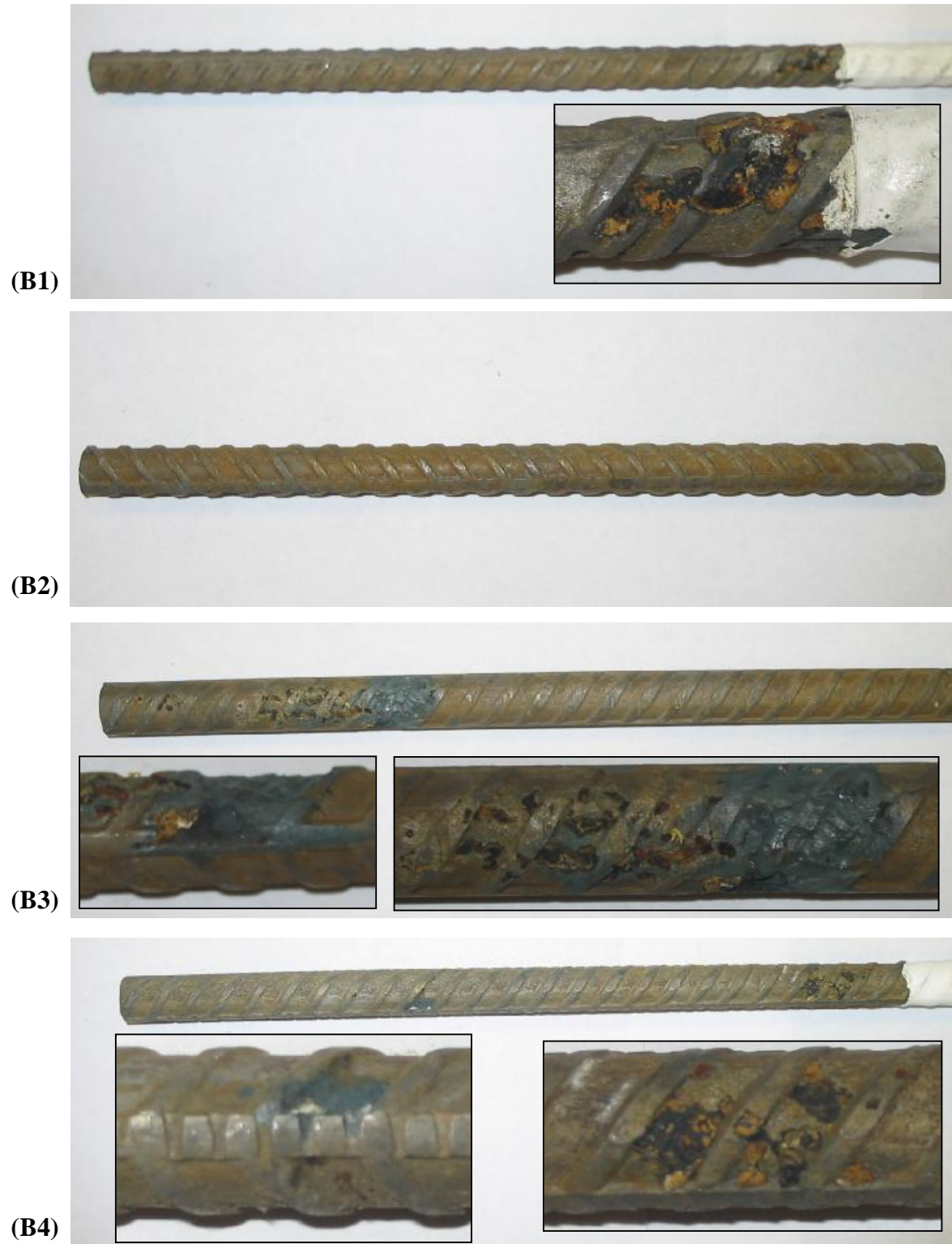


Figure F. 2. Steel segments after cleaning the corrosion products, removed from beam B.

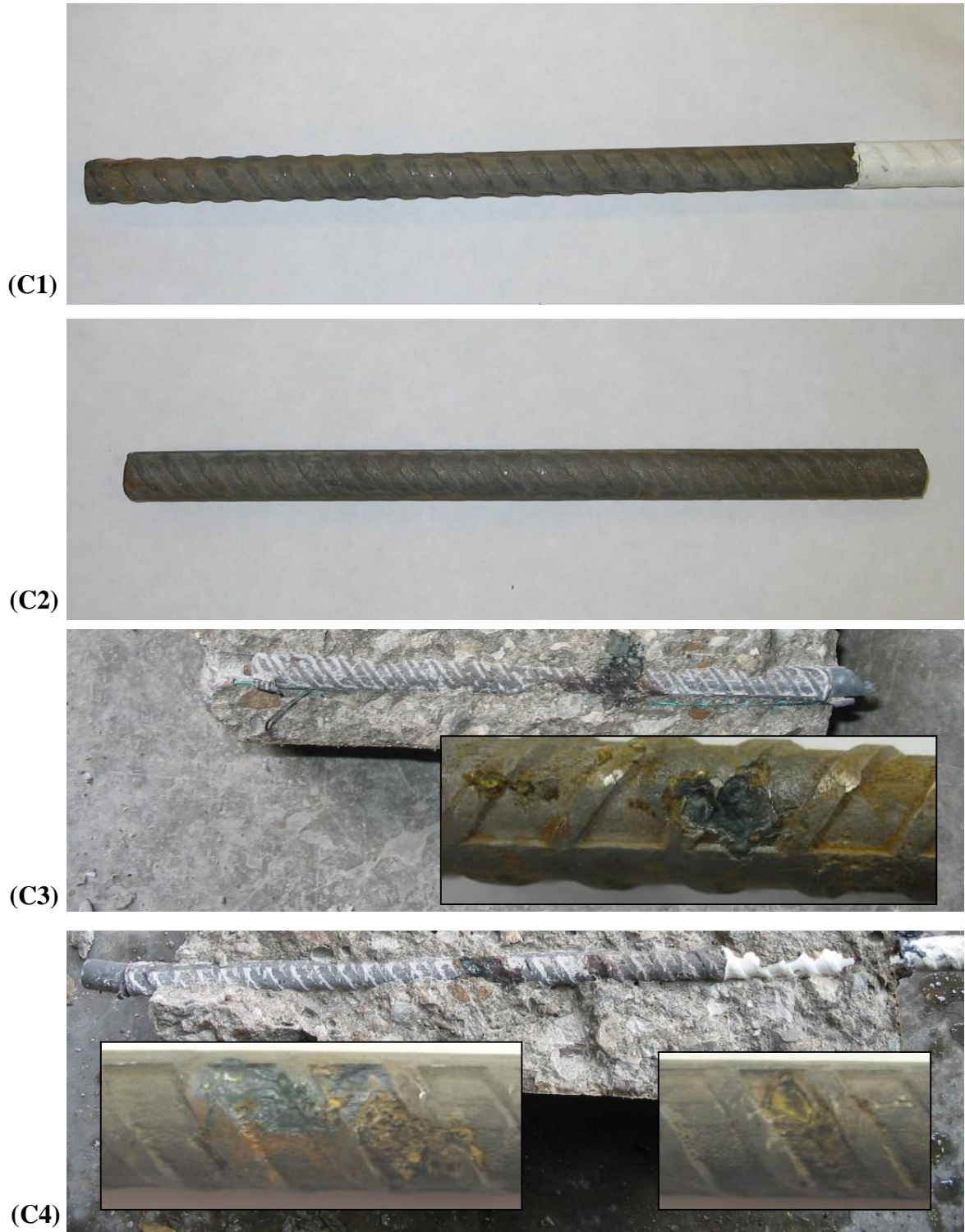


Figure F. 3. Steel segments after cleaning the corrosion products, removed from beam C.

**D1**



**D2**



**D3**



**D4**



Figure F. 4. Steel segments after cleaning the corrosion products, removed from beam D.



**E1**



**E2**



**E3**



**E4**



Figure F. 5. Steel segments after cleaning the corrosion products, removed from beam E.

## **Appendix (G)**

**Data obtained from Victoria Street Bridge, Wingham Ontario**



|   | 0    | 5    | 10   | 15   | 20   | 25   | 30   | 35   | 40   | 45   | 50   | 55   | 60   |
|---|------|------|------|------|------|------|------|------|------|------|------|------|------|
| A | -270 | -240 | -270 | -290 | -300 | -290 | -260 | -270 | -250 | -280 | -250 | -280 | -270 |
| B | -370 | -380 | -400 | -520 | -390 | -360 | -340 | -350 | -370 | -360 | -400 | -370 | -340 |
| C | -410 | -420 | -400 | -430 | -400 | -390 | -360 | -370 | -420 | -440 | -490 | -460 | -390 |
| D | -370 | -400 | -380 | -370 | -390 | -410 | -380 | -400 | -440 | -470 | -460 | -420 | -400 |
| E | -350 | -360 | -370 | -350 | -370 | -390 | -390 | -400 | -440 | -420 | -420 | -400 | -370 |
| F | -360 | -340 | -340 | -320 | -340 | -340 | -350 | -350 | -310 | -320 | -340 | -310 | -320 |
| G | -360 | -380 | -370 | -400 | -310 | -320 | -310 | -300 | -320 | -330 | -360 | -240 | -220 |
| H | -420 | -430 | -470 | -460 | -530 | -500 | -330 | -370 | -330 | -370 | -380 | -350 | -340 |
| I | -540 | -510 | -520 | -540 | -410 | -450 | -370 | -480 | -450 | -460 | -450 | -440 | -400 |

|   | 65   | 70   | 75   | 80   | 85   | 90   | 95   | 100  | 105  | 110  | 115  | 120  | 125  |
|---|------|------|------|------|------|------|------|------|------|------|------|------|------|
| A | -220 | -220 | -280 | -270 | -310 | -240 | -230 | -230 | -220 | -250 | -210 | -210 | -160 |
| B | -350 | -340 | -320 | -350 | -360 | -340 | -310 | -330 | -340 | -260 | -350 | -350 | -330 |
| C | -380 | -380 | -360 | -360 | -410 | -400 | -360 | -330 | -350 | -380 | -380 | -400 | -390 |
| D | -380 | -380 | -400 | -400 | -420 | -430 | -400 | -350 | -400 | -410 | -390 | -450 | -450 |
| E | -340 | -380 | -370 | -400 | -380 | -390 | -370 | -360 | -360 | -370 | -360 | -450 | -410 |
| F | -340 | -320 | -300 | -320 | -330 | -300 | -330 | -300 | -330 | -300 | -310 | -310 | -340 |
| G | -260 | -340 | -350 | -360 | -330 | -360 | -400 | -390 | -340 | -260 | -330 | -300 | -330 |
| H | -320 | -400 | -440 | -420 | -370 | -350 | -390 | -390 | -360 | -330 | 350  | -410 | -380 |
| I | -380 | -450 | -440 | 450  | -400 | -420 | -440 | -410 | -400 | -350 | -330 | -510 | -410 |

|   | 130  | 135  | 140  | 145  | 150  | 155  | 160  | 165  | 170  | 173  |
|---|------|------|------|------|------|------|------|------|------|------|
| A | -190 | -190 | -210 | -200 | -210 | -160 | -210 | -210 | -200 | -210 |
| B | -300 | -300 | -310 | -280 | -280 | -280 | -310 | -290 | -270 | -290 |
| C | -350 | -390 | -370 | -330 | -340 | -350 | -350 | -330 | -320 | -310 |
| D | -370 | -450 | -390 | -350 | -390 | -350 | -370 | -370 | -480 | -430 |
| E | -380 | -400 | -400 | -360 | -380 | -370 | -370 | -380 | -390 | -350 |
| F | -300 | -340 | -330 | -310 | -360 | -330 | -350 | -330 | -340 | -320 |
| G | -430 | -500 | -440 | -410 | -470 | -470 | -450 | -450 | -410 | -480 |
| H | -390 | -440 | -460 | -420 | -470 | -480 | -540 | -460 | -410 | -520 |
| I | -460 | -430 | -450 | -450 | -420 | -470 | -490 | -470 | -420 | -450 |

Figure G. 1. Half-cell potential values of the Victoria Street Bridge deck, Wingham, measured in June 16, 1998; T= 24°C. Hatched regions represent the delaminated areas.

|   | 0    | 5    | 10   | 15   | 20   | 25   | 30   | 35   | 40   | 45   | 50   | 55   | 60   |
|---|------|------|------|------|------|------|------|------|------|------|------|------|------|
| A | -290 | -230 | -270 | -350 | -300 | -260 | -250 | -260 | -240 | -270 | -240 | -280 | -260 |
| B | -400 | -350 | -360 | -410 | -370 | -350 | -340 | -320 | -360 | -350 | -380 | -330 | -330 |
| C | -410 | -400 | -340 | -410 | -410 | -420 | -380 | -370 | -400 | -430 | -490 | -380 | -390 |

|   | 65   | 70   | 75   | 80   | 85   |
|---|------|------|------|------|------|
| A | -220 | -230 | -250 | -230 | -190 |
| B | -320 | -340 | -340 | -320 | -350 |
| C | -380 | -370 | -390 | -400 | -350 |

Figure G. 2. Half-cell potential values of the Victoria Street Bridge deck, Wingham, measured in Nov 24, 2004; T= 5°C